Universidad de Oviedo

Departamento de Ingeniería Química y Tecnología del Medio Ambiente

Programa de Doctorado en Ingeniería Química, Ambiental y Bioalimentaria

OBTENCIÓN DE MONÓMEROS DE BIOPOLÍMEROS A PARTIR DE BIOMASA RESIDUAL

Doctorando:

Paula Rapado Robles

Directores:

Dr. Salvador Ordóñez García

Dr. Laura Faba Peón

Oviedo, diciembre, 2024

Universidad de Oviedo

RESUMEN DEL CONTENIDO DE TESIS DOCTORAL

1.- Título de la Tesis	
Español/Otro Idioma: **Obtención de monómeros de biopolímeros a partir de biomasa residual**	Inglés: **Biopolymer monomers production from biomass waste**

2.- Autor	
Nombre: **Paula Rapado Robles**	
Programa de Doctorado: **Programa de Doctorado en Ingeniería Química Ambiental y Bioalimentaria**	
Órgano responsable: **Centro Internacional de Postgrado de la Universidad de Oviedo**	

RESUMEN (en español)

Esta Tesis Doctoral se centra en el estudio y optimización de las etapas del proceso productivo de ácido 2,5-furandicarboxílico (FDCA), compuesto clave en la producción del furanoato de polietileno (PEF), un polímero sostenible que puede reemplazar al tereftalato de polietileno (PET), uno de los plásticos de mayor producción mundial y cuya producción y posterior gestión como residuos al final de su vida útil, genera graves consecuencias ambientales. La reducción de estos problemas ambientales implica el desarrollo de plásticos sostenibles, utilizando biomasa como materia prima.

El proceso de producción de FDCA implica varias etapas. Inicialmente, la fracción hemicelulósica se somete a hidrólisis ácida para obtener azúcares y, posteriormente, mediante deshidratación, los aldehídos cíclicos, como el furfural (FFL) a partir de las pentosas, y 5-hidroximetilfurfural (HMF) a partir de las hexosas. Para garantizar una buena eficacia en la hidrólisis, la biomasa lignocelulósica residual debe ser pretratada, eliminando la lignina y dañando la estructura recalcitrante de la celulosa. La etapa clave en la formación del FDCA es la oxidación de estos aldehídos. La oxidación de HMF produce directamente el FDCA, pero la ruta a partir de FFL produce ácido furoico (FCA), siendo necesaria una etapa adicional de carboxilación para obtener el FDCA.

Respecto a la primera etapa (hidrólisis-deshidratación), inicialmente se aborda una optimización paramétrica (temperatura, catalizador) y estudio cinético de la reacción para maximizar la obtención de FFL a partir de celulosa microcristalina, considerando un sistema que combina catálisis homogénea (HCl) y heterogénea (zeolita β). Estos resultados se extrapolaron a un sistema real, utilizando serrín de pino como materia prima. En este caso, la presencia de lignina requirió del estudio comparativo de diferentes pretratamientos para favorecer el acceso del catalizador a los polímeros de interés (celulosa y hemicelulosa), eliminando las interferencias de la lignina.

La etapa de oxidación compone la parte más significativa de este trabajo. Inicialmente, se estudia de forma separada para el FFL y el HMF. La obtención de FCA a partir de furfural se aborda considerando dos agentes oxidantes: H_2O_2 y O_2. Los resultados experimentales permiten concluir que la alta reactividad del H_2O_2 da lugar a un proceso complejo y difícil de controlar. En contraste, el oxígeno proporciona un proceso más estable, alcanzando selectividades a FCA sensiblemente superiores.

En base a los resultados de oxidación de FFL, se aborda también la oxidación del HMF. Estos estudios abarcan, además de la optimización de temperatura y presión de oxígeno, el análisis de la influencia del ratio NaOH/HMF ya que, en este caso, la formación de FDCA compite con la oligomerización de HMF y la consiguiente formación de huminas. Considerando que a partir de biomasa lignocelulósica la formación de FFL y HMF ocurriría simultáneamente, se ha explorado la posibilidad de realizar la oxidación de la mezcla de ambos aldehídos.

La última etapa del proceso es la carboxilación del FCA obtenido por oxidación del FFL. La poca bibliografía referente indica que es una reacción sólido fluido condicionada técnicamente por la dificultad para alcanzar un buen contacto entre el CO_2 y el sólido, y económicamente por el elevado coste del cesio, elemento requerido para generar una sal fundente (furoato de cesio), que facilite la interacción sólido-gas. Se evaluó la viabilidad de realizar la reacción a

FOR-MAT-VOA-010 (Reg.2018)

presiones bajas de CO_2 y se plantean ideas para futuras optimizaciones en fase líquida, como la utilización de complejos de cobre como ligandos, o el uso de sistemas binarios considerando disolventes orgánicos polares apróticos.

RESUMEN (en inglés)

This PhD thesis focuses on the study and optimization of the stages of the production process of 2,5-furandicarboxylic acid (FDCA), a key compound in the production of polyethylene furanoate (PEF), a sustainable polymer that can replace polyethylene terephthalate (PET), one of the most widely produced plastics globally whose production and subsequent management as waste at the end of their life cycle generate considerable environmental consequences. Reducing these environmental problems involves the development of sustainable plastics, using biomass as a raw material.

The FDCA production process involves several stages. Initially, the hemicellulose fraction must undergo acid hydrolysis to obtain sugars, which are then dehydrated to form cyclic aldehydes, the platform molecules for this process Specifically, furfural (FFL) is obtained from pentoses, and 5-hydroxymethylfurfural (HMF) from hexoses. To ensure effective hydrolysis, the residual lignocellulosic biomass must be pretreated, removing lignin and disrupting the recalcitrant structure of cellulose. The key stage in the formation of FDCA is the oxidation of these aldehydes. The oxidation of HMF directly produces FDCA, but the route from FFL produces furoic acid (FCA), requiring an additional carboxylation step to obtain FDCA.

Regarding the first stage (hydrolysis-dehydration), a parametric optimization (temperature, catalyst) and kinetic study of the reaction were initially carried out to maximize the production of FFL from microcrystalline cellulose, considering a system that combines homogeneous (HCl) and heterogeneous (beta zeolite) catalysis. These results were extrapolated to a real system, using pine sawdust as a raw material. In this case, the presence of lignin required the comparative study of different pretreatments to favor the access of the catalyst to the polymers of interest (cellulose and hemicellulose), eliminating the interferences of lignin.

The oxidation stage represents the most significant part of this work. Initially, it is studied separately for FFL and HMF. The production of FCA from furfural was approached using two oxidizing agents: hydrogen peroxide and oxygen. These two approaches allowed a comparison between two reaction mechanisms. The experimental results led to the conclusion that the high reactivity of hydrogen peroxide results in a complex process that is difficult to control, with the formation of numerous by-products. In contrast, oxygen provides a more stable process, achieving significantly higher selectivities to FCA.

Based on the results of FFL oxidation, the oxidation of HMF is also addressed. These studies include, not only the optimization of temperature and oxygen pressure but also the analysis of the influence of the NaOH/HMF ratio, as FDCA formation competes with the oligomerization of HMF and the consequent formation of humins. Considering that from lignocellulosic biomass the formation of FFL and HMF would occur simultaneously, the possibility of carrying out the oxidation of the mixture of both aldehydes has been explored.

The last stage of the process is the carboxylation of FCA obtained by oxidation of FFL. The practically non-existent literature indicates that it is a solid-fluid reaction technically conditioned by the difficulty of achieving good contact between CO_2 and the solid, and economically by the high cost of cesium, an element required to generate a molten salt (cesium furoate), which facilitates the solid-gas interaction. The feasibility of carrying out the reaction at low CO_2 pressures was evaluated and ideas are proposed for future optimizations in the liquid phase, such as the use of copper complexes as ligands, or the use of binary systems considering polar aprotic organic solvents.

SR. PRESIDENTE DE LA COMISIÓN ACADÉMICA DEL PROGRAMA DE DOCTORADO EN INGENIERÍA QUÍMICA, AMBIENTAL Y BIOALIMENTARIA

ÍNDICE

RESUMEN

El desarrollo industrial del último siglo ha dependido en gran medida de materias primas de origen fósil, especialmente para la producción de energía y la obtención de productos químicos. Los plásticos constituyen una de las familias más relevantes de derivados del petróleo con amplia implantación en nuestra sociedad. Así, entre el 5-10% de la nafta procesada se destina a la producción de plásticos. Su producción y la posterior gestión como residuos al final de su vida útil, genera importantes consecuencias ambientales. A las emisiones de gases de efecto invernadero inherentes a su proceso productivo, debe añadirse el hecho de que los plásticos son, en su inmensa mayoría, no biodegradables. Por lo tanto, se acumulan en los ecosistemas, particularmente en los océanos, donde se descomponen en microplásticos. Estos microplásticos son ingeridos por los organismos marinos, alterando la cadena alimentaria y la biodiversidad.

La reducción de estos problemas ambientales pasa por el desarrollo de plásticos sostenibles, es decir, utilizar biomasa como materia prima para obtener polímeros de propiedades similares a los de origen fósil. Esta Tesis Doctoral se centra en el estudio y optimización de las diferentes etapas que componen el proceso productivo del ácido 2,5-furandicarboxílico (FDCA, por sus siglas en inglés), compuesto clave en la producción del furanoato de polietileno (PEF). El PEF es el polímero sostenible que puede reemplazar al tereftalato de polietileno (PET), uno de los plásticos de mayor producción mundial. Ambos compuestos poseen propiedades mecánicas similares, principalmente en términos de resistencia y durabilidad.

El proceso de producción de FDCA a partir de biomasa lignocelulósica implica diferentes etapas. Inicialmente, la fracción hemicelulósica debe someterse a hidrólisis ácida para obtener azúcares reductores y, posteriormente, mediante deshidratación, los aldehídos cíclicos que constituyen las moléculas plataforma de este proceso. Concretamente, furfural a partir de las pentosas, y 5-hidroximetilfurfural (HMF) a partir de las hexosas. Para garantizar una buena eficacia en la hidrólisis, la biomasa lignocelulósica residual debe ser pretratada, eliminando la lignina y dañando la estructura recalcitrante de la celulosa. La etapa clave en la formación del FDCA es la oxidación de estos aldehídos. En el caso del HMF, la oxidación produce directamente el FDCA. Por el contrario, la ruta a partir de furfural produce ácido furoico (FCA), siendo necesaria una etapa adicional de carboxilación para obtener el FDCA.

Respecto a la primera etapa (hidrólisis-deshidratación), inicialmente se aborda una optimización paramétrica (temperatura, catalizador) y estudio cinético de la reacción para maximizar la obtención de furfural y HMF a partir de celulosa microcristalina, considerando un sistema que combina catálisis homogénea (HCl) y heterogénea (zeolita β). Estos resultados fueron extrapolados a un sistema real, utilizando serrín de pino como materia prima. En este caso, la presencia de lignina requirió del estudio comparativo de diferentes pretratamientos para favorecer el acceso del catalizador a los polímeros de interés (celulosa y hemicelulosa), eliminando las interferencias de la lignina. Se consideraron pretratamientos oxidativos y reductores, evaluando el efecto de la dosis de los agentes y las condiciones del proceso (tiempo y temperatura).

La etapa de oxidación compone la parte más significativa de este trabajo. Inicialmente, se estudia de forma separada para el furfural y el HMF. La obtención de FCA a partir de furfural se aborda considerando dos agentes oxidantes: el peróxido de hidrógeno y el oxígeno. Estos dos enfoques permiten la comparación entre dos mecanismos de reacción, evaluando si es posible trabajar con un oxidante en fase líquida, lo que implicaría un mejor control teórico de la reacción por encontrarse ambos reactivos en la misma fase. Los resultados experimentales, evaluando diferentes catalizadores y condiciones de operación, permiten concluir que la alta reactividad del peróxido de hidrógeno da lugar a un proceso complejo, difícilmente controlable, con multitud de compuestos laterales (ácido maleico, ácido fórmico, CO_2, etc.), siendo difícil maximizar la producción del FCA, ya que éste se produce mediante la oxidación parcial del furfural. En contraste, el oxígeno proporciona un proceso más estable, alcanzando selectividades a FCA sensiblemente superiores.

En base a los resultados de oxidación de furfural, se aborda también la oxidación del HMF, en este caso considerando únicamente el catalizador Au/TiO_2. Estos estudios abarcan, además de la optimización de temperatura y presión de oxígeno (único oxidante considerado, teniendo en cuenta lo observado con furfural), el análisis de la influencia del ratio NaOH/HMF ya que, en este caso, la formación de FDCA compite con la oligomerización de HMF y la consiguiente formación de huminas (sólidos que desactivan el catalizador por bloqueo de los centros activos).

Finalmente, teniendo en cuenta que a partir de biomasa lignocelulósica la formación de furfural y HMF ocurriría simultáneamente, se ha explorado la posibilidad de realizar la

oxidación de la mezcla de ambos aldehídos, simulando la relación de concentraciones esperable tras un proceso de hidrólisis. Estos estudios, si bien requieren una optimización buscando el equilibrio entre las condiciones óptimas identificadas de forma individual, permiten considerar la etapa de oxidación sin necesidad de extraer selectivamente los aldehídos. Consecuentemente, supone un ahorro considerable en los costes de operación del proceso. Además de la optimización paramétrica, se realiza un estudio cinético para evaluar si las conclusiones extraídas en los estudios individuales son aplicables a la situación de mezcla.

La última etapa del proceso se refiere a la carboxilación del ácido furoico obtenido por oxidación del furfural (la oxidación del HMF ya produce el FDCA deseado). La práctica inexistente bibliografía referente a la carboxilación del ácido furoico indica que es una reacción sólido fluido condicionada técnicamente por la dificultad para alcanzar un buen contacto entre el CO_2 y el sólido, y económicamente por el elevado coste del cesio, elemento requerido para generar una sal fundente (furoato de cesio), que facilite la interacción sólido-gas. En la literatura, estos experimentos se llevan a cabo a elevada presión de CO_2, lo que aleja el proceso de las condiciones esperables para una reacción de valorización de CO_2 atmosférico capturado. Se ha evaluado la viabilidad de realizarlos a menor presión, obteniendo una producción de FDCA no despreciable. Para intentar orientar las modificaciones del proceso que favorecieran su sostenibilidad, se ha realizado un exhaustivo trabajo bibliográfico considerando otras carboxilaciones, trabajo del que se han extraído ideas para futuras optimizaciones en fase líquida, como la utilización de complejos de cobre como ligandos, o el uso de sistemas binarios considerando disolventes orgánicos polares apróticos.

ABSTRACT

The industrial development of the last century has heavily relied on fossil-based raw materials, particularly for energy production and the manufacture of chemicals. Plastics are one of the most significant families of petroleum-derived products, widely integrated into our society. Between 5-10% of processed naphtha is used in the production of plastics. The manufacturing of plastics and their subsequent management as waste at the end of their life cycle have considerable environmental consequences. In addition to the greenhouse gas emissions inherent in their production process, most plastics are non-biodegradable. As a result, they accumulate in ecosystems, particularly in the oceans, where they decompose into microplastics. These microplastics are ingested by marine organisms, disrupting the food chain and biodiversity.

Reducing these environmental problems requires the development of sustainable plastics, meaning the use of biomass as a raw material to produce polymers with properties similar to those derived from fossil sources. This PhD Thesis focuses on the study and optimization of the various stages involved in the production process of 2,5-furandicarboxylic acid (FDCA), a key compound in the production of polyethylene furanoate (PEF). PEF is a sustainable and biodegradable polymer that can replace polyethylene terephthalate (PET), one of the most widely produced plastics globally. Both compounds have similar mechanical properties, particularly in terms of strength and durability.

The production process of FDCA from lignocellulosic biomass involves several stages. Initially, the hemicellulosic fraction must undergo acid hydrolysis to obtain reducing sugars, which are then dehydrated to form cyclic aldehydes, the platform molecules for this process. Specifically, furfural is obtained from pentoses, and 5-hydroxymethylfurfural (HMF) from hexoses. To ensure effective hydrolysis, the residual lignocellulosic biomass must be pretreated, removing lignin and disrupting the recalcitrant structure of cellulose. The key step in FDCA formation is the oxidation of these aldehydes. In the case of HMF, oxidation directly produces FDCA. In contrast, the route starting from furfural yields furoic acid (FCA), requiring an additional carboxylation step to obtain FDCA.

Regarding the first stage (hydrolysis-dehydration), a parametric optimization (temperature, catalyst) and kinetic study of the reaction were initially conducted to maximize the production of furfural and 5-HMF from microcrystalline cellulose, considering a system combining homogeneous (HCl) and heterogeneous (β zeolite) catalysis. These results were extrapolated to a real system using pine sawdust as raw material. In this case, the presence of lignin necessitated a comparative study of different pretreatment methods to facilitate the catalyst's access to the target polymers (cellulose and hemicellulose) by removing lignin interference. Oxidative and reductive pretreatments were considered, evaluating the effects of the agents' dosage and process conditions (time and temperature).

The oxidation stage represents the most significant part of this work. Initially, it was studied separately for furfural and HMF. The production of FCA from furfural was approached using two oxidizing agents: hydrogen peroxide and oxygen. These two approaches allowed a comparison between two reaction mechanisms, evaluating the feasibility of working with a liquid-phase oxidant, which would theoretically provide better control of the reaction since both reactants are in the same phase. The experimental results, evaluating different catalysts and operating conditions, led to the conclusion that the high reactivity of hydrogen peroxide results in a complex process that is difficult to control, with the formation of numerous by-products (maleic acid, formic acid, CO_2, etc.), making it challenging to maximize FCA production, as it is formed through the partial oxidation of furfural. In contrast, oxygen provides a more stable process, achieving significantly higher selectivities for FCA.

Based on the furfural oxidation results, the oxidation of HMF was also addressed, in this case considering only the Au/TiO_2 catalyst. These studies included not only the optimization of temperature and oxygen pressure (the only oxidant considered, given the observations with furfural) but also the analysis of the influence of the NaOH/HMF ratio, as FDCA formation competes with the oligomerization of HMF and the consequent formation of humins (solids that deactivate the catalyst by blocking active sites).

Finally, considering that the formation of furfural and HMF would occur simultaneously from lignocellulosic biomass, the possibility of oxidizing a mixture of both aldehydes was explored, simulating the expected concentration ratio after a hydrolysis process. Although these studies require optimization to balance the individually identified optimal conditions, they allow for the consideration of the oxidation step without the need for selective extraction of the aldehydes. Consequently, this represents a significant reduction in process operating costs. In addition to parametric optimization, a kinetic study was performed to assess whether the conclusions drawn from the individual studies are applicable to the mixed scenario.

The final stage of the process concerns the carboxylation of furoic acid obtained from furfural oxidation (since the oxidation of 5-HMF already produces the desired FDCA). The practically non-existent literature on furoic acid carboxylation indicates that it is a solid-fluid reaction, technically constrained by the difficulty of achieving good contact between CO_2 and the solid, and economically by the high cost of caesium, an element required to generate a molten salt (caesium furoate) that facilitates solid-gas interaction. In the literature, these experiments are conducted under high CO_2 pressure, which distances the process from conditions expected for atmospheric CO_2 valorisation reactions. The feasibility of conducting them at lower pressure was evaluated, yielding a non-negligible FDCA production. To guide process modifications towards greater sustainability, an extensive literature review on other carboxylations was conducted, from which ideas for future liquid-phase optimizations were derived, such as using copper complexes as ligands or considering binary systems with polar aprotic organic solvents.

LISTA DE TABLAS

Table Captions

LISTA DE FIGURAS

Figure Captions

DIFUSIÓN DE LA TESIS DOCTORAL

Dissemination of the PhD Thesis

ARTÍCULOS CIENTÍFICOS

Las publicaciones derivadas de la realización de la presente Tesis Doctoral se enumeran a continuación, siguiendo el orden de discusión en el apartado de resultados:

1. "*Zeolite-assisted acid hydrolysis of cellulose: Optimization of reaction conditions and chemical pretreatments for enhancing HMF yields*", Paula Rapado, Diego Garcés, Laura Faba, Salvador Ordóñez. Industrial Crops and Products 212 (2024) 118309. **Capítulo 4.1.** https://doi.org/10.1016/j.indcrop.2024.118309

2. "*Influence of delignification and reaction conditions in the aqueous phase transformation of lignocellulosic biomass to platform molecules*", Paula Rapado, Laura Faba, Salvador Ordóñez. Bioresource Technology 321 (2021) 124500. **Capítulo 4.2.** https://doi.org/10.1016/j.biortech.2020.124500

3. "*Role of the different catalytic sites in the H_2O_2-mediated aqueous-phase furfural partial oxidation*", Paula Rapado, Laura Faba, Salvador Ordóñez. Journal of Environmental Chemical Engineering 11 (2023) 111466. **Capítulo 4.3.** https://doi.org/10.1016/j.jece.2023.111466

4. "*Selective and stable production of furoic acid by furfural aerobic oxidation at controlled mild-pH conditions*", Paula Rapado, Laura Faba, Salvador Ordóñez. Applied Catalysis A: General 670 (2023) 119536. **Capítulo 4.4.** https://doi.org/10.1016/j.apcata.2023.119536

5. "*Biomass to plastics: from HMF to fructose for the synthesis of 2,5-furandicarboxylic acid over Au/TiO_2*", Paula Rapado, Cristina Lois, Marina Cano, Laura Faba, Salvador Ordóñez. Catalysis Today 445 (2024) 115036. **Capítulo 4.5.** https://doi.org/10.1016/j.cattod.2024.115036

6. "*Carboxylation reaction for integrating CO_2 capture with the production of renewable monomers*", Laura Faba, Paula Rapado, Salvador Ordóñez. Greenhouse Gases: Science and Technology 13 (2022) 227-244. **Capítulo 4.6.** https://doi.org/10.1002/ghg.2175

COMUNICACIONES A CONGRESO

Durante el desarrollo se la presente Tesis Doctoral, se han presentado las siguientes comunicaciones a congresos tanto nacionales como internacionales. Se enumeran en orden cronológico de defensa:

1. *Obtención de ácido furoico mediante oxidación catalítica de furfural*

   Paula Rapado, Laura Faba, Salvador Ordóñez

   Reunión Bienal de la Sociedad Española de Catálisis: SECAT´21. Nuevos retos de la catálisis en química, medido ambiente y energía

   Valencia (España), 18-20 de octubre de 2021

   Tipo de presentación: **Póster**

2. *Comparison of oxygen and hydrogen peroxide as oxidants for obtaining furoic acid from furfural over supported gold catalysts*

   Paula Rapado, Laura Faba, Salvador Ordóñez

   XV European Congress on Catalysis: EUROPACAT´23. Catalysis: A pillar of modern society

   Praga (República Checa), 27 de agosto al 1 de septiembre de 2023

   Tipo de participación: **Short oral**

3. *Oxidation of furfural/5-hydroxymethylfurfural mixtures to furanic acids over Au/*TiO_2*: kinetics and inhibition effects*

   Paula Rapado, Laura Faba, Salvador Ordóñez

   18th ICC - International Congress on Catalysis. Roots and wings for a better world

   Lyon (Francia), 14-19 de julio de 2024

   Tipo de participación: **Póster**

AGRADECIMIENTOS

Acknowledgments

Durante el desarrollo de esta Tesis Doctoral, han sido muchas las personas que me han ofrecido su tiempo, su dedicación y su apoyo de manera de incondicional. Estas líneas van dedicadas a ellos, sin los cuales no hubiera sido imposible llegar hasta aquí.

A mis directores de Tesis, Salvador Ordóñez y Laura Faba, les agradezco sinceramente su compromiso, apoyo y dedicación a lo largo de la realización de este proyecto. Sus conocimientos y su paciencia fueron fundamentales para el éxito de este trabajo. Gracias por creer en mí y acompañarme en este viaje. Sois una inspiración.

A la directora del Centro de Investigación *Fritz-Haber-Institut*, Beatriz Roldán, al *group leader* Thomas Lunkenbein, a Nils Pfister y a todo el grupo de investigación por la hospitalidad recibida durante mi estancia predoctoral. La dedicación incansable que destináis a la excelencia académica es un ejemplo a seguir.

Al programa de Apoyo y Promoción de la Investigación de la Universidad de Oviedo, al Principado de Asturias y al Ministerio de Universidades por la financiación proporcionada durante el desarrollo de mi Tesis Doctoral que me ha permitido dedicarme en exclusividad al mundo de la investigación.

A todos los miembros del grupo Catálisis, Reactores y Control (CRC). En especial a todos mis compañeros de sala con los que he disfrutado todo este tiempo compartiendo experiencias inolvidables. Yoli, Jenni, Mauro y David, nunca olvidaré los días que pasamos juntos en el laboratorio que han servido para forjar una gran amistad. Y mucha suerte a los últimos integrantes Adrián, Sergio e Isabel, el camino es largo, pero merece la pena.

A mi familia y amigos, por el apoyo incondicional que me brindaron durante el arduo proceso. Sus palabras de aliento, comprensión y amor fueron un faro de luz en los momentos más desafiantes.

A Óscar, gracias por ser mi compañero en este viaje, por creer en mí cuando yo dudaba. Aprecio profundamente tu sacrificio y tu comprensión. Tu capacidad para mantener el equilibrio es verdaderamente admirable. Esto solo es una victoria más en nuestro marcador.

Nothing in life is to be feared, it is only to be understood. Now is the time to understand more, so that we may fear less.

Marie Curie (1867-1934)

1. INTRODUCCIÓN

1.1. ANTECEDENTES: DEPENDENCIA DE MATERIAS PRIMAS FÓSILES

El desarrollo industrial del último siglo ha estado intrínsecamente ligado al uso intensivo de materias primas fósiles, no solo para la producción de energía, sino también para la fabricación de productos químicos. La industria petroquímica ha sido el motor del crecimiento global, proporcionando los componentes fundamentales para una amplia gama de productos que van desde plásticos, disolventes y fertilizantes, hasta materiales utilizados en la construcción, la medicina y la tecnología. Sin embargo, este crecimiento también ha sido una de las principales causas de la crisis medioambiental que enfrentamos hoy.

Si nos centramos en la huella de carbono, es decir, en la cantidad total de emisiones de gases de efecto invernadero, especialmente CO_2, que se generan directa o indirectamente durante la fabricación de productos químicos a partir de hidrocarburos fósiles, observamos que esta actividad contribuye significativamente a incrementar dicha huella. La extracción, refino y transformación de petróleo y gas natural liberan cantidades significativas de gases de efecto invernadero (GEI), sobre todo CO_2, contribuyendo al cambio climático (**Figura 1.1**). Además, los procesos de conversión de estos recursos fósiles en productos químicos producen grandes cantidades de residuos, lo que agrava aún más los problemas ambientales.

Un aspecto clave en esta crisis es la producción masiva de plásticos, que ha generado una sobreacumulación de estos residuos en el medio ambiente (**Figura 1.2**). Entre el 5 y el 10% de la nafta procesada en refinerías se destina a la fabricación de diversos tipos de plásticos. Estos materiales no son biodegradables y su resistencia al deterioro, junto con una deficiente gestión como residuos, ha llevado a que grandes cantidades terminen en los océanos y en ecosistemas terrestres, causando daños a la biodiversidad y afectando a las cadenas alimentarias. La combinación de estos factores ha llevado a un punto de inflexión donde es necesario replantear tanto los métodos de producción como los tipos de productos químicos que utilizamos.

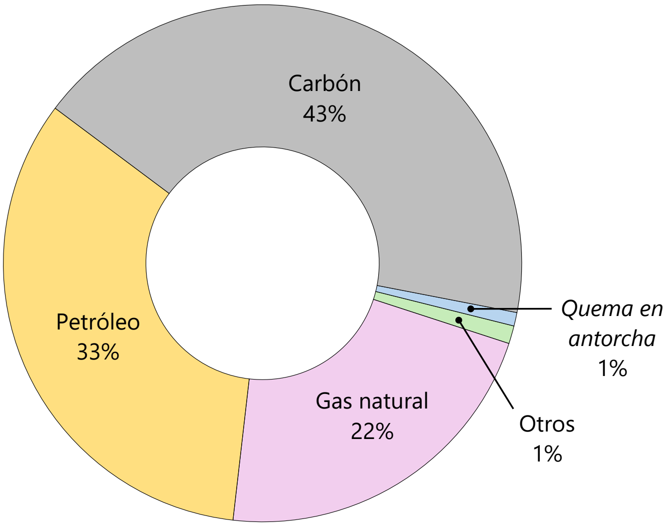

Figura 1.1. Emisiones de CO_2 debidas a la extracción, refino y transformación de materias primas no renovables. [1]

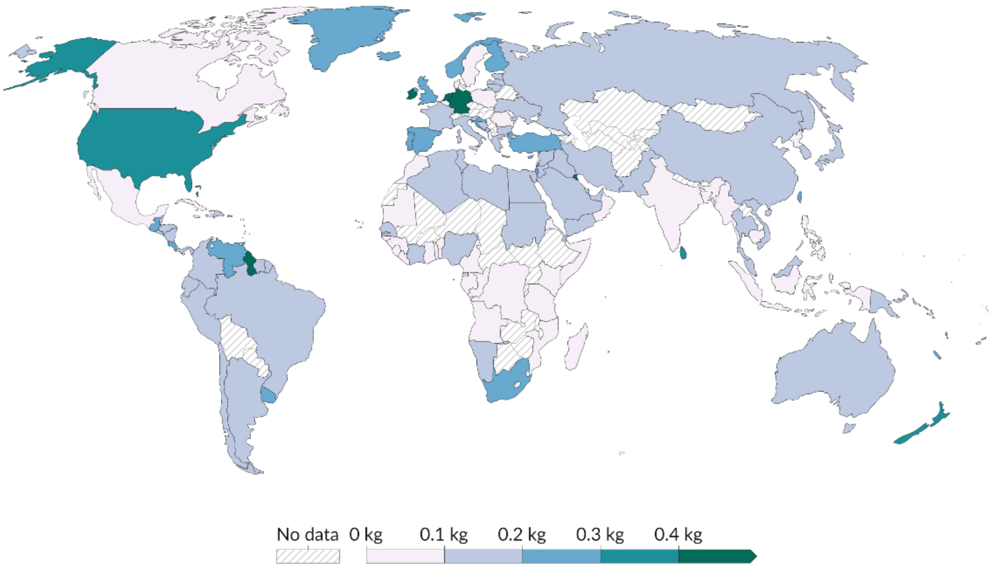

Figura 1.2. Generación de residuos plásticos expresada en kilogramos por persona y día [2]

En respuesta a esta crisis, la industria química se enfrenta a la necesidad de adoptar enfoques más sostenibles. Las regulaciones ambientales cada vez más estrictas y la demanda de productos más ecológicos han motivado la búsqueda de soluciones innovadoras. Esto incluye la química verde, un enfoque que promueve el diseño de productos y procesos que reduzcan o eliminen el uso y generación de sustancias peligrosas. Además, políticas internacionales como los Acuerdos de París y los Objetivos de Desarrollo Sostenible (ODS) de la ONU (**Figura 1.3**) exigen que las industrias reduzcan su impacto ambiental mediante el desarrollo de tecnologías limpias y la transición hacia fuentes de materias primas más sostenibles.

Figura 1.3. Objetivos de Desarrollo Sostenible para alcanzar una huella neutral de carbono [3]

La Conferencia de las Partes (COP), como foro internacional clave en la lucha contra el cambio climático, juega un papel crucial en la formulación de estrategias para mitigar los impactos ambientales. Desde su establecimiento en 1995 bajo la Convención Marco de las Naciones Unidas sobre el Cambio Climático (CMNUCC), las COP han sido fundamentales para coordinar esfuerzos globales. La COP 21 en 2015, por ejemplo, resultó en el Acuerdo de París, para limitar el calentamiento global a menos de 1.5 ºC por encima de los niveles preindustriales [4]. La última COP 28, celebrada en Dubái a finales de 2023, realiza un balance sobre el Acuerdo de Paris concluyendo de que aún estamos muy lejos de limitar el aumento de la temperatura en el valor establecido. Se firmó el Acuerdo de Dubái, que reconoce la necesidad de reducir las emisiones de gases efecto invernadero. A este respecto, este acuerdo sugiere impulsar la búsqueda de materias primas renovables para la producción de plásticos, destacando que solamente el 8.3% de los plásticos empleados corresponden a plásticos reciclados post-consumo y tan solo el 1.5% de los plásticos producidos en 2021 son de origen renovable [5]. Por lo tanto, el desarrollo de un proceso sostenible para la síntesis de plásticos va a jugar un papel clave para alcanzar las emisiones netas de dióxido de carbono cero para 2050 [6].

1.1.1. Cambio climático

El efecto invernadero es un proceso natural que permite que la Tierra mantenga una temperatura adecuada para la vida. Este fenómeno ocurre cuando ciertos gases en la atmósfera, como el dióxido de carbono (CO_2), el metano (CH_4) y el vapor de agua (H_2O), entre otros, atrapan parte de la energía del Sol. La radiación solar atraviesa la atmósfera y calienta la superficie terrestre. Posteriormente, la Tierra emite esta energía en forma de radiación infrarroja, que es parcialmente absorbida y reemitida por los gases de efecto invernadero (GEI), evitando que todo el calor escape al espacio (**Figura 1.4**). Este proceso mantiene la temperatura promedio de la Tierra en unos 15 °C [7].

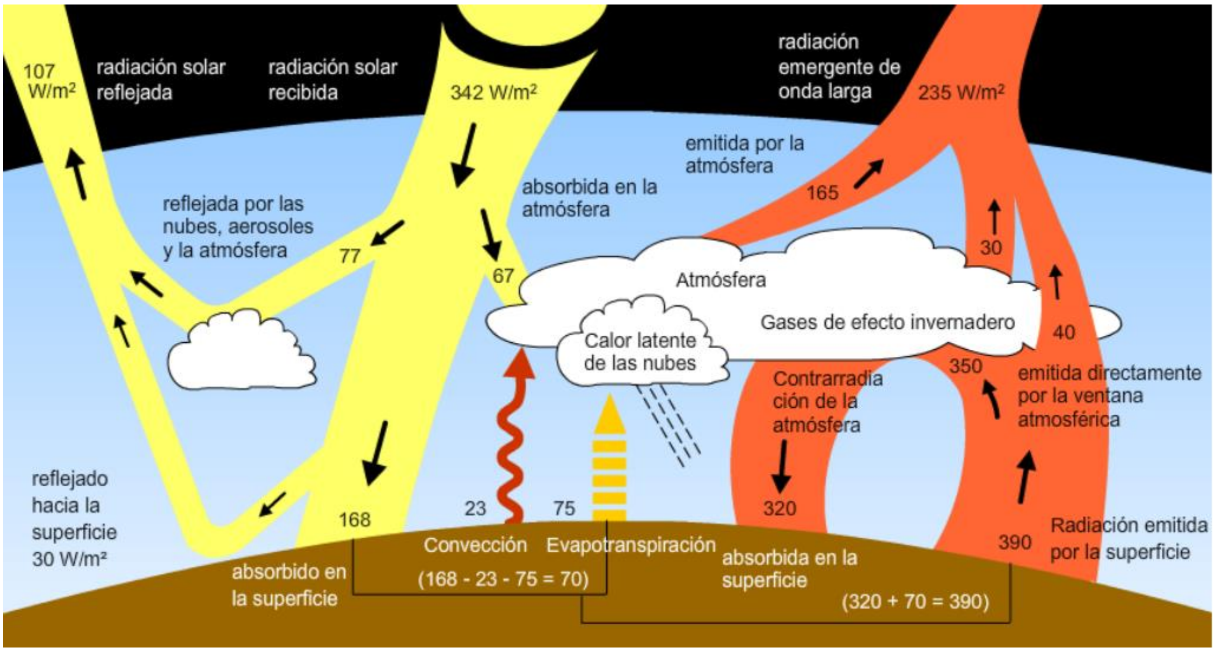

Figura 1.4. Esquema del funcionamiento del efecto invernadero [8]

Sin la capacidad de los gases de efecto invernadero para retener el calor, la temperatura promedio del planeta sería alrededor de -18 °C [9]. Esta diferencia de aproximadamente 33 °C destaca la importancia crítica del efecto invernadero para la vida tal como la conocemos. Sin embargo, el calentamiento global se refiere al aumento gradual de la temperatura promedio de la superficie de la Tierra, especialmente en las últimas décadas del siglo XX y principios del siglo XXI, atribuido principalmente a la actividad humana, especialmente debido al aumento de la concentración de GEI en la atmósfera (**Figura 1.5**).

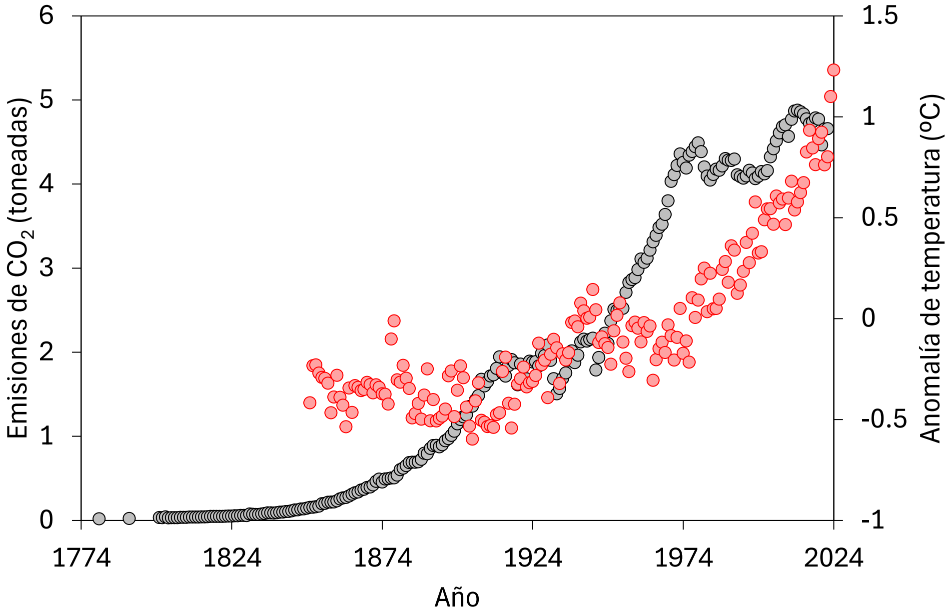

Figura 1.5. Emisiones de CO_2 de origen antropogénico (gris) y variaciones de temperatura (rojo) en relación con la temperatura promedio del período 1961-1990 [10]

Las evidencias del cambio climático son múltiples y variadas, desde cambios en la temperatura atmosférica y oceánica, el deshielo de los casquetes polares y glaciares, el aumento del nivel del mar, la acidificación de los océanos, y cambios en los patrones climáticos, como el aumento de fenómenos meteorológicos extremos. El calentamiento global es un fenómeno complejo y multifacético que representa uno de los mayores desafíos ambientales de nuestro tiempo. Su comprensión y mitigación requieren una colaboración global, políticas efectivas y acciones concertadas a todos los niveles de la sociedad siendo la disminución de GEI y el empleo de material primas renovables las formas más efectivas de disminuir la contribución de origen antropogénico ya que la quema y procesamiento de combustibles fósiles genera emisiones masivas de gases de efecto invernadero. En los últimos años, la producción de productos químicos basada en fuentes fósiles ha sido responsable de una parte significativa de las emisiones globales de CO_2. Procesos como el craqueo de hidrocarburos para producir etileno y propileno, que son los precursores de muchos polímeros plásticos, son altamente intensivos en energía. Esto subraya la necesidad urgente de reducir la dependencia de estas materias primas para disminuir la huella de carbono de la industria.

1.1.2. Inestabilidad derivada del uso de materias primas fósiles

La concentración de materias primas fósiles en ciertas regiones geográficas plantea un desafío significativo para la industria química (**Figura 1.6**). Durante décadas, el petróleo, el gas natural y el carbón han sido las principales fuentes de compuestos químicos base, como hidrocarburos aromáticos, olefinas y alcanos, que se utilizan para sintetizar una amplia variedad de productos. La disponibilidad abundante de estos recursos y su bajo coste relativo permitieron el desarrollo de procesos químicos eficientes que sustentan la producción de plásticos, detergentes, medicamentos, fertilizantes y otros productos esenciales para la vida moderna.

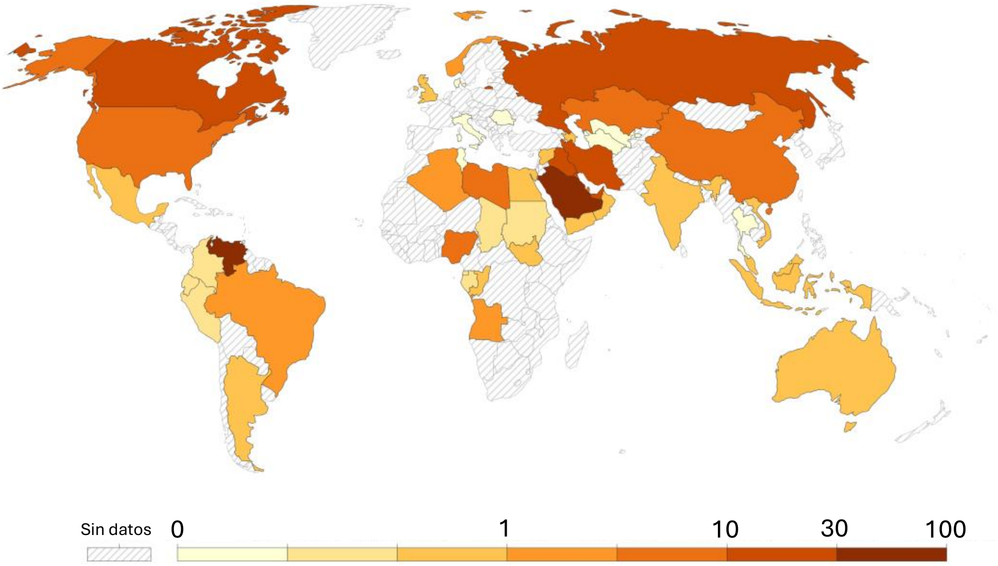

Figura 1.6. Reservas de petróleo en 2022 expresadas en billones de tonadas [11]

No obstante, a medida que se explotan los yacimientos más accesibles, el coste de extracción de estas materias primas aumenta, haciendo que los precios de los productos químicos derivados sean más elevados. La disminución de las reservas de petróleo y gas natural, junto con las fluctuaciones geopolíticas, también incrementa la incertidumbre en torno a la seguridad del suministro. Esto no solo afecta la estabilidad económica de las industrias que dependen de estos insumos, sino que también pone en riesgo la continuidad de la producción de productos químicos esenciales.

Para evitar estos problemas, la industria química está explorando activamente nuevas rutas de síntesis que no dependan de materias primas fósiles. El uso de residuos industriales y el desarrollo de procesos de reciclaje químico avanzado permiten recuperar materiales y reintroducirlos en la cadena de valor, disminuyendo así la necesidad de introducir recursos fósiles nuevos. Asimismo, la captura y reutilización de gases como el CO_2 abre la posibilidad de generar productos químicos con menor impacto ambiental, al transformar un desecho en un recurso fomentando así un modelo económico de economía circular, en el que el reciclaje y la reutilización son los pilares para minimizar los residuos y el impacto ambiental.

La inestabilidad generada por el uso de materias primas fósiles no solo está vinculada a su disponibilidad, sino que también representa un obstáculo significativo para la sostenibilidad de la producción global de productos químicos. Innovar en nuevas fuentes de materias primas y procesos es esencial para asegurar que la industria pueda continuar satisfaciendo la demanda sin comprometer el medio ambiente.

1.1.3. Consumo de plásticos y su impacto ambiental

La producción de plásticos, en particular, ha sido uno de los principales responsables de esta dependencia de las materias primas fósiles. Los polímeros sintéticos, que se derivan principalmente del petróleo y gas natural, han revolucionado la industria debido a su versatilidad, durabilidad y bajo coste. Sin embargo, su masiva producción y el largo tiempo que tardan en degradarse están causando una crisis ambiental sin precedentes (**Figura 1.7**). Si bien los plásticos son esenciales en muchas aplicaciones (empaquetado, automoción, medicina), es evidente que el enfoque actual debe cambiar.

La gestión de los residuos plásticos también es un problema principalmente debido al uso masivo de plásticos de un solo uso. En la **Figura 1.8** se muestran las cantidades de residuos plásticos generados en función de cada polímero. A pesar de los esfuerzos por mejorar las tasas de reciclaje, solo una fracción de los plásticos se recicla efectivamente. De los aproximadamente 400 millones de toneladas de plásticos producidos anualmente, menos del 10% se recicla de manera efectiva, mientras que el resto se destina a vertederos o se libera en el medio ambiente. Esta baja tasa de reciclaje se debe a varios factores, incluyendo la complejidad de los materiales plásticos, la falta de infraestructura adecuada y la degradación de los plásticos durante el reciclaje.

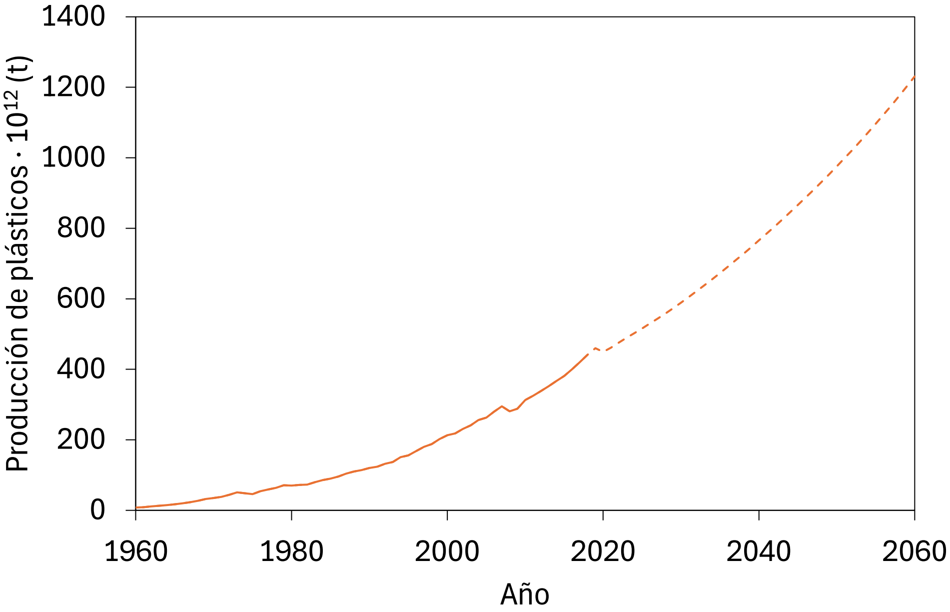

Figura 1.7. Producción de plásticos mundial con previsión hasta 2060 [12]

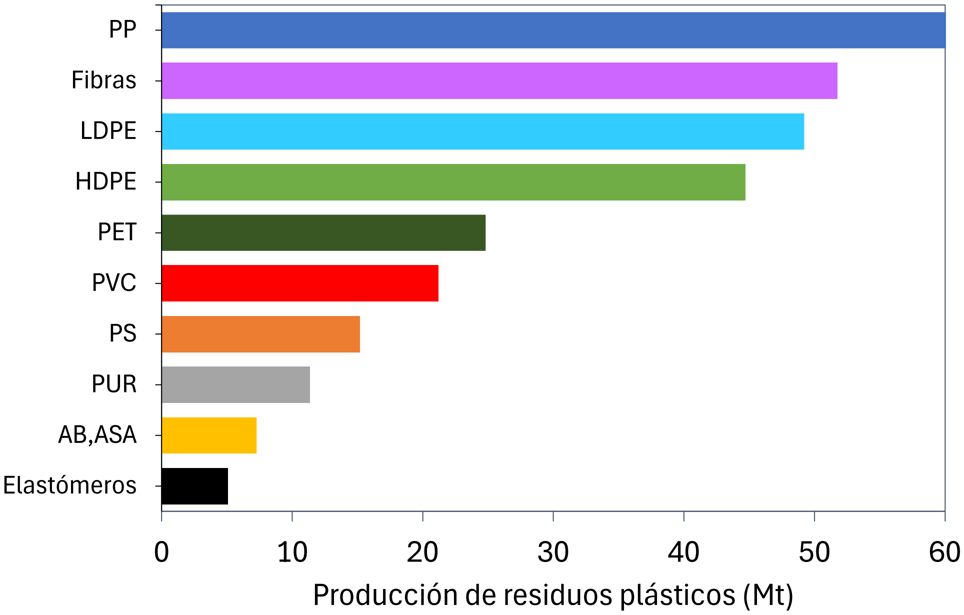

Figura 1.8. Producción global de residuos plásticos en 2019 en función de cada polímero. Leyenda: PP (polipropileno), LDPE (polietileno de baja densidad), HDPE (polietileno de alta densidad), PET (tereftalato de polietileno), PVC (cloruro de polivinilo), PS (poliestireno), PUR (poliuretano), AB (acrilonitrilo butadieno), ASA (acrilonitrilo estireno acrilato) [13]

Además, la persistencia de los plásticos en el medio ambiente es un problema crítico, ya que estos materiales no se degradan fácilmente y pueden permanecer en los ecosistemas durante siglos. La contaminación por plásticos ha alcanzado niveles alarmantes, afectando tanto a ambientes marinos como terrestres. Se estima que aproximadamente 8 millones de toneladas de plásticos terminan en los océanos cada año, causando daños a la vida marina, desde los microplásticos que son ingeridos por organismos marinos hasta grandes fragmentos que pueden atrapar o enredar a las especies [14].

En conclusión, aunque los plásticos siguen siendo materiales irremplazables en muchas aplicaciones debido a sus propiedades únicas, la búsqueda de soluciones sostenibles es esencial para enfrentar los problemas ambientales actuales. La sustitución de plásticos tradicionales por alternativas renovables y la mejora en las prácticas de gestión de residuos representan oportunidades clave para reducir el impacto ambiental y avanzar hacia una industria más sostenible. La producción de plásticos biodegradables y reciclables que mantengan las propiedades clave de los polímeros tradicionales (como resistencia, ligereza y versatilidad) será crucial para asegurar la sostenibilidad del sector. En este sentido, la industria está en una fase de transición hacia un modelo en el que los productos químicos se diseñen para tener un impacto ambiental mínimo durante todo su ciclo de vida.

1.2. ALTERNATIVAS SOSTENIBLES: BIORREFINERÍAS Y FURANOATO DE POLIETILENO

El futuro de la producción de productos químicos depende de la capacidad para sustituir las materias primas fósiles por fuentes alternativas sostenibles. Esta transición es clave no solo para hacer frente al agotamiento de los recursos, sino también para reducir los impactos medioambientales de la industria. El enfoque en este campo abarca varias líneas de investigación que buscan diversificar las fuentes de productos químicos mediante el uso de recursos que sean más accesibles y tengan un menor impacto ambiental. Entre las alternativas más prometedoras se encuentran la valorización de biomasa lignocelulósica residual y los procesos de captura y utilización de CO_2 (CCU), que permiten transformar este gas de efecto invernadero en productos químicos útiles. Actualmente, y como tecnologías emergentes, se está explorando cómo convertir el dióxido de carbono en compuestos como metanol, carbonatos cíclicos y otros precursores químicos, que pueden servir de base para fabricar plásticos y otros materiales. Asimismo, los residuos industriales y subproductos de otros procesos están siendo evaluados como fuentes para la producción de compuestos químicos.

Los procesos de biorrefinería están ganando interés en el desarrollo de alternativas viables para la sustitución tanto de los combustibles fósiles convencionales como para la fabricación de productos químicos de forma sostenible y con baja huella de carbono. El funcionamiento de la una biorrefinería se inspira de las refinerías tradicionales de petróleo, pero utiliza biomasa como materia prima para la producción de una amplia gama de productos químicos, materiales y energía, ya que es la fuente de carbono más abundante después del CO_2 atmosférico [15, 16]. La biomasa incluye desechos orgánicos como residuos agrícolas, subproductos forestales e incluso ciertos tipos de desechos industriales [16]. En la **Figura 1.9** se ilustran algunos de los diferentes productos que pueden obtenerse en una biorrefinería basada en biomasa lignocelulósica.

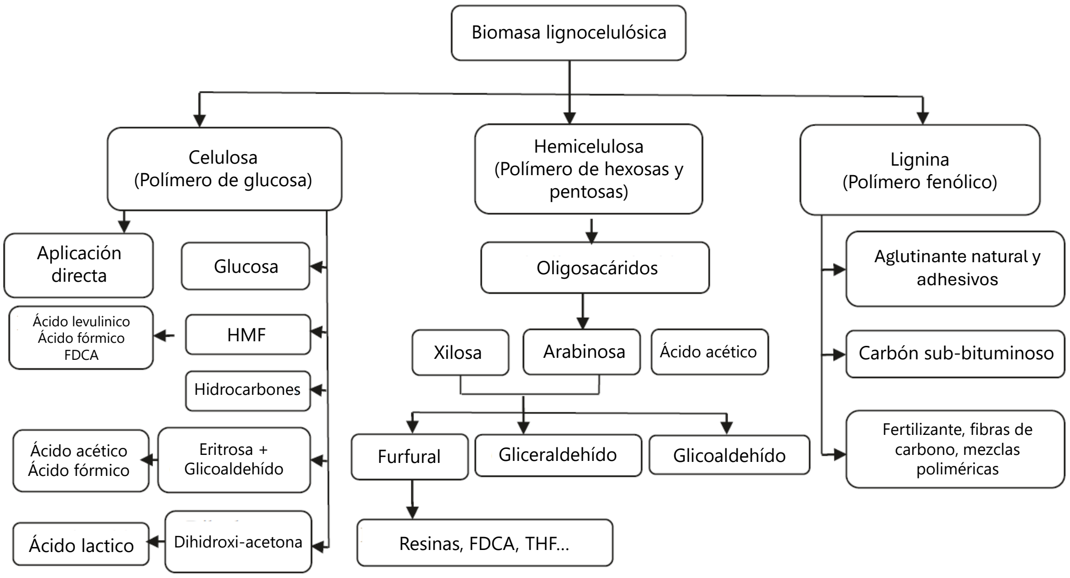

Figura 1.9. Representación de productos obtenidos en una biorrefinería basada en biomasa lignocelulósica. Adaptado de [18]

Comparadas con las refinerías tradicionales de petróleo, las biorrefinerías ofrecen varias ventajas significativas [19, 20]:

- Sostenibilidad ambiental: Las biorrefinerías utilizan recursos renovables y biodegradables (incluso residuos y materiales recuperados de residuos), reduciendo la dependencia de los combustibles fósiles y disminuyendo las emisiones de gases de efecto invernadero.
- Diversificación de productos: Las biorrefinerías pueden producir una amplia gama de productos, desde biocombustibles hasta productos químicos y biomateriales, lo que aumenta la versatilidad y la rentabilidad de la instalación.
- Valorización de residuos: Las biorrefinerías pueden utilizar una variedad de materias primas, incluidos los residuos agrícolas, forestales y alimentarios, convirtiéndolos en productos de valor añadido y reduciendo así la cantidad de residuos enviados a vertederos.
- Menor dependencia de los mercados: Al utilizar recursos renovables y locales, las biorrefinerías pueden reducir la dependencia de los precios volátiles del petróleo y promover la seguridad energética y económica a nivel local y regional.

Una de las vías de valorización de biomasa residual de mayor potencial industrial es la obtención de plásticos. Mediante el desarrollo de polímeros basados en moléculas derivadas de la biomasa es posible reducir la dependencia de los combustibles fósiles, disminuir las emisiones de carbono y contribuir a una economía circular. Este desarrollo es esencial para que la implementación de las políticas gubernamentales (prohibición de plásticos de un solo uso, aumento de la sostenibilidad del sector) sea factible sin suponer una ruptura drástica con el sistema económico actual. Actualmente, existen cuatro familias de plásticos, clasificados en función de su origen y su grado de biodegradabilidad, ver **Figura 1.10**.

La mayor parte de los plásticos tradicionales (polietileno, polipropileno, tereftalato de polietileno, etc.), tienen un origen fósil y son no biodegradables. Estos son los polímeros cuyo análisis de ciclo de vida demuestra un mayor impacto ambiental y, por lo tanto, aquéllos en los que la legislación y la industria deben focalizar los esfuerzos para su sustitución. Existe otra familia que, manteniendo un origen fósil, da lugar a plásticos biodegradables. En este grupo se incluyen, entre otros, los poliésteres alifáticos, plásticos ampliamente utilizados en el sector de paquetería. Ambas familias están llamadas a ser sustituidas por los bioplásticos, entendiendo como tal a todos los que tengan un origen basado en biomasa. Si bien no todos ellos son 100% biodegradables, sí presentan un mayor grado de biodegradabilidad o, al menos, reciclabilidad, respecto a los plásticos convencionales.

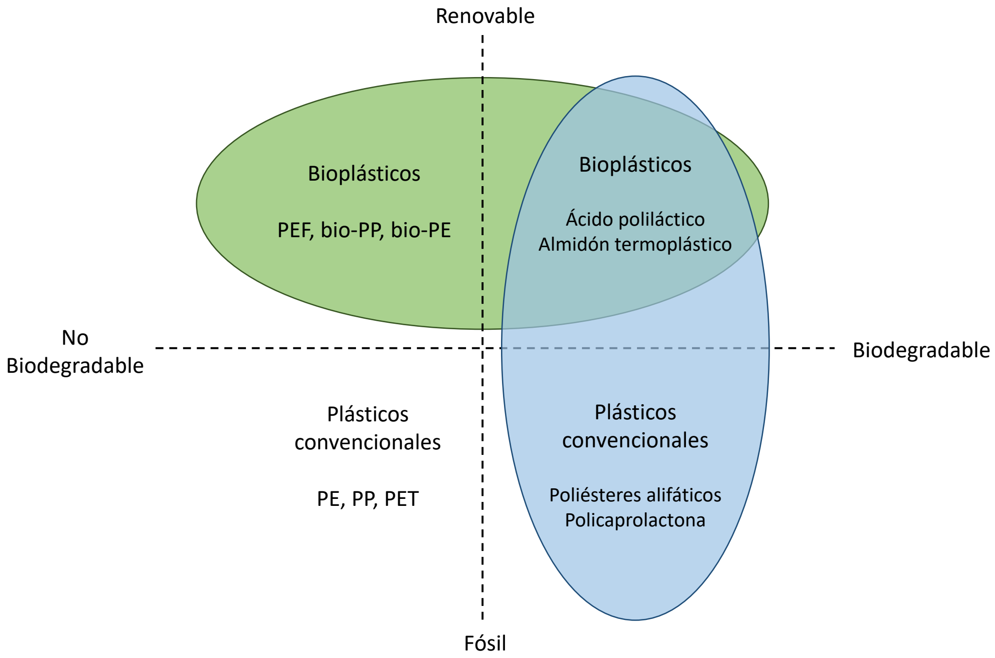

Figura 1.10. Clasificación de plásticos según su origen y capacidad de biodegradación [21]

Un ejemplo claro de sustitución prácticamente directa es el caso del tereftalato de polietileno (PET) y el furanoato de polietileno (PEF) [22]. El PET es un plástico convencional (de origen fósil y no biodegradable) utilizado principalmente para producir botellas y envases y constituye alrededor del 20% de la producción de plásticos a nivel mundial [22-24].

En la actualidad, el PET se produce utilizando etileno y xileno, ambos derivados de procesos de refinado del petróleo orientados principalmente a la producción de combustibles fósiles. Sin embargo, a medida que se impulsa la transición hacia un modelo de transporte más sostenible, donde se promueve el uso de vehículos eléctricos y se fomenta el transporte colectivo, la demanda de gasolina y gasóleo se verá reducida. Todo esto conllevará a una disminución en el refino de petróleo, lo que resultará en una menor disponibilidad de olefinas y aromáticos como el etileno y el xileno. La disminución de estos subproductos podría plantear desafíos para la industria de los plásticos convencionales, aumentando la necesidad de alternativas sostenibles que no dependan del refino de combustibles fósiles.

El furanoato de polietileno (PEF) surge como una alternativa renovable que, debido a su similitud estructural (**Figura 1.11**), genera un polímero de propiedades similares al PET y significativas ventajas medioambientales.

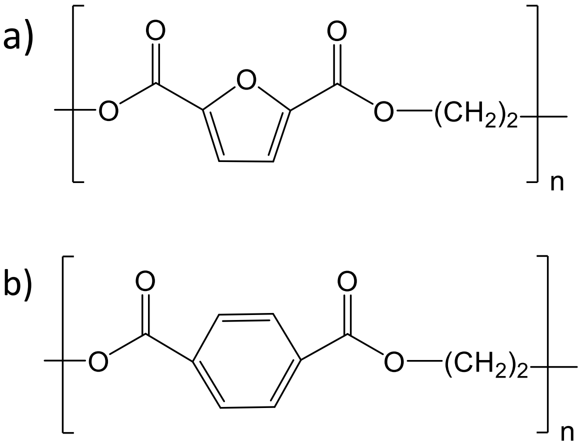

Figura 1.11. Comparación de la estructura de (a) PEF y (b) PET

El PEF se obtiene mediante la policondensación del bio-etilenglicol y el ácido 2,5-furandicarboxílico (FDCA). Ambos compuestos se obtienen a partir de biomasa lignocelulósica (**Figura 1.12**).

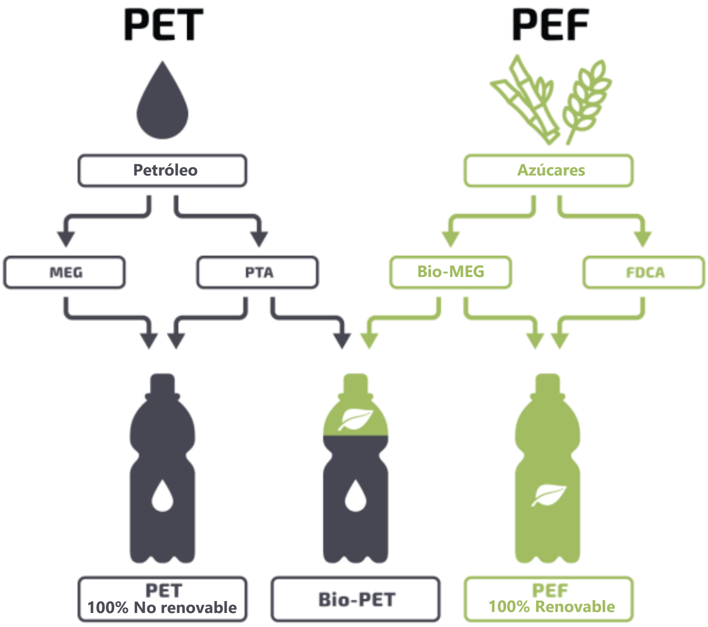

Figura 1.12. Composición de botellas de PEF, botellas multicapa de PEF y PET y botellas de PET

El FDCA y el ácido tereftálico (PTA), utilizado en la síntesis de PET y de origen no renovable, tienen propiedades químicas similares, lo que permite que el FDCA se utilice como un reemplazo directo en la síntesis de poliésteres [25]. Los poliésteres fabricados con FDCA pueden tener características comparables o incluso mejoradas. Destaca sobre todo la resistencia mecánica del PEF (comparable a la del PET) haciéndolo adecuado para aplicaciones que requieren durabilidad y robustez. Además, el PEF presenta excelentes propiedades de barrera frente a gases como oxígeno y dióxido de carbono, lo que lo convierte en una opción superior para el envasado de alimentos y bebidas, al preservar los alimentos frescos y extender la vida útil del producto.

Aunque el PEF no es completamente biodegradable en todas las condiciones, su capacidad para descomponerse en entornos específicos puede ayudar a mitigar la acumulación de residuos plásticos en el medio ambiente. También es reciclable, lo que facilita su integración en los sistemas de reciclaje existentes, ofreciendo una solución más sostenible en comparación con el PET. Además, su síntesis a partir de biomasa lignocelulósica representa un paso importante hacia una economía más sostenible y basada en recursos renovables.

1.3. BIOMASA LIGNOCELULÓSICA

La biomasa lignocelulósica está constituida principalmente por celulosa (40-60%), hemicelulosa (10-40%) y lignina (15-30%) formando un material compuesto que es resistente a la conversión química, un fenómeno comúnmente conocido como carácter recalcitrante de la biomasa (**Figura 1.13**) [26, 27].

La holocelulosa considera celulosa y hemicelulosa, es decir, engloba la parte de carbohidratos y contiene entre un 40-60% de oxígeno. La presencia de oxígeno hace que la biomasa sea una materia prima atractiva para producir productos químicos oxigenados de interés industrial que son costosos de sintetizar a partir de materias primas derivadas del petróleo [26].

Actualmente, uno de los mayores retos de la ingeniería química es avanzar hacia una industria capaz de implementar una conversión catalítica eficiente de la biomasa, transformando esta materia prima renovable en productos químicos, combustibles y energía de utilidad. Estos compuestos se pueden generar mediante procesos como la pirólisis y gasificación, así como a través de fermentación o rutas quimio-catalíticas avanzadas [27]. A largo plazo, el desarrollo de estas tecnologías promete contribuir a la creación de una economía más sostenible y menos dependiente de los recursos fósiles.

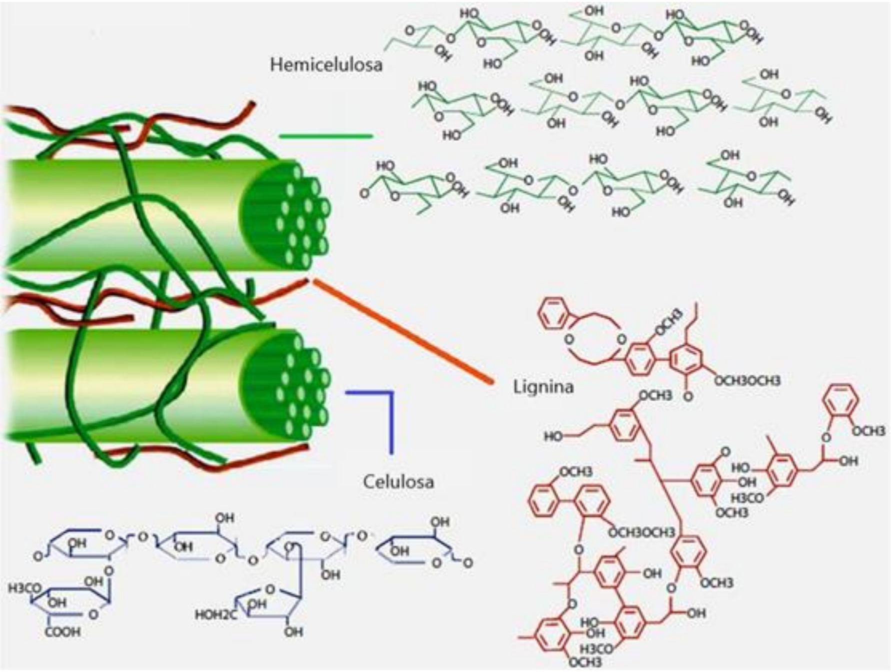

Figura 1.13. Representación esquemática de los constituyentes de la biomasa lignocelulósica

1.3.1. Celulosa

La celulosa es el polímero natural más abundante en la Tierra y se encuentra en la pared celular de las plantas. Es un homopolímero lineal compuesto por unidades repetidas de D-glucosa unidas mediante enlaces β-1,4-glucosídicos. Esta estructura confiere a la celulosa una alta resistencia y una naturaleza hidrofílica debido a los grupos hidroxilo presentes en sus enlaces. La celulosa tiene una complejidad química considerable, lo que dificulta su aislamiento y separación de otros componentes de la biomasa, como la hemicelulosa y la lignina [27].

La celulosa tiene múltiples aplicaciones industriales, como la producción de papel, textiles y productos químicos como el 5-hidroximetilfurfural (HMF) y el ácido levulínico (LA). La celulosa se obtiene principalmente a través de procesos de pretratamiento mecánico y químico que permiten su separación de otros componentes de la biomasa. Estos procesos incluyen el uso de disoluciones ácidas, alcalinas y enzimas para romper los enlaces entre la celulosa y otros biopolímeros [29].

1.3.2. Hemicelulosa

La hemicelulosa es un heteropolímero ramificado compuesto por una variedad de monosacáridos, incluyendo pentosas (como xilosa, arabinosa y ribosa) y hexosas (como glucosa, fructosa, galactosa y manosa), siendo la xilosa el componente predominante [30]. Este biopolímero se encuentra en la pared celular vegetal, donde está unida a la celulosa a través de enlaces de hidrógeno. La hemicelulosa es menos resistente a la hidrólisis en comparación con la celulosa, lo que facilita su degradación.

La hemicelulosa tiene aplicaciones potenciales en la producción de biocombustibles y productos químicos derivados de biomasa. Sin embargo, su desarrollo a nivel industrial presenta desafíos ya que su estructura compleja y heterogénea dificulta una conversión selectiva, y actualmente no posee un valor añadido elevado en comparación con otros biopolímeros [31]. La obtención de hemicelulosa implica el uso de métodos de pretratamiento y extracción específicos, como la hidrólisis ácida o alcalina, que permiten su separación de la celulosa y la lignina presentes en la biomasa lignocelulósica [30].

1.3.3. Lignina

La lignina es el principal componente polimérico restante en la biomasa lignocelulósica, representando aproximadamente el 20% en peso. Es un biopolímero polifenólico tridimensional que se encuentra en la pared celular de las plantas, proporcionando rigidez y resistencia estructural.

Tradicionalmente la lignina se quema para generar calor y energía ya que su conversión en coproductos adicionales sigue siendo un reto debido a su estructura altamente ramificada y aleatoria, lo que contribuye a su carácter recalcitrante y dificulta su conversión en productos útiles mediante técnicas convencionales [32]. Sin embargo, tiene potencial para ser utilizada en la producción de biocompuestos, productos químicos y materiales avanzados mediante procesos de valorización más innovadores [33]. La obtención de lignina implica métodos de extracción durante el proceso de *pulping*, como el método Kraft, que permiten su separación de la celulosa y la hemicelulosa [34].

1.4. VALORIZACIÓN DE RESIDUOS DE BIOMASA LIGNOCELULÓSICA

La Ley 7/2022, de 8 de abril, de residuos y suelos contaminados para una economía circular, define valorización como cualquier operación cuyo resultado principal sea que un residuo adquiera una finalidad útil, ya sea sustituyendo a otros materiales que se habrían utilizado para cumplir una función específica o preparándolo para cumplir esa función en un proceso industrial o en la economía en general. En este contexto, se están desarrollando cuatro tecnologías clave para la valorización de biomasa lignocelulósica: gasificación, pirólisis, licuefacción e hidrólisis [35, 36].

1.4.1. Gasificación

La gasificación es un proceso de oxidación parcial que convierte la alimentación orgánica en monóxido de carbono, dióxido de carbono e hidrógeno, por medio de una reacción a elevadas temperaturas (>700 ºC), sin que tenga lugar la combustión y controlando la cantidad de oxígeno o de vapor empleada. El resultado es un gas llamado gas de síntesis o *syngas* [35].

El gas de síntesis puede ser sometido a una combustión para la recuperación de energía térmica en forma de calor y/o vapor y electricidad. La energía derivada de la gasificación, mediante la combustión del gas de síntesis, se considera como una fuente de energía renovable si se emplea biomasa como materia prima. Por otro lado, el gas de síntesis puede ser utilizado para obtener diferentes productos químicos, destacando cinco rutas alternativas de valorización [38, 39]:

- Síntesis Fischer-Tropsch. Se trata de un proceso catalítico que ha sido utilizado desde 1920 para la producción de combustibles líquidos a partir del gas de síntesis derivado del carbón y del gas natural.
- Síntesis de alcoholes. Es también un proceso catalítico utilizado para producir metanol a partir del gas de síntesis derivado del reformado de vapor del gas natural o gas de síntesis a partir de carbón.
- Síntesis de alcoholes mixtos. Es un proceso catalítico que produce una mezcla de metanol, etanol, propanol, butanol y pequeñas cantidades de alcoholes más pesados.
- Síntesis de dimetil éter (DME). El dimetil éter se forma por eterificación de dos moléculas de metanol, con lo que se integra con la producción de este. Es un proceso catalítico a través del cual se consigue obtener un nuevo combustible que permite una combustión limpia debido a sus propiedades fisicoquímicas, como el alto índice de cetano y las bajas emisiones de combustión de hollín, CO, hidrocarburos y NO_x.

- Fermentación del gas de síntesis. Es un proceso biológico que utiliza microorganismos anaeróbicos para fermentar el gas de síntesis y producir etanol y otros compuestos químicos.

1.4.2. Pirólisis

La pirólisis es la despolimerización térmica de la materia orgánica en ausencia de oxígeno a temperaturas en torno a 500 ºC. El requerimiento de calor para la pirólisis de materias primas lignocelulósicas se encuentra en el rango de 207-434 kJ/kg [40]. En este proceso se genera una mezcla compleja de productos gaseosos, líquidos y sólidos. El principal beneficio sobre la gasificación es que el combustible líquido generado puede almacenarse y transportarse fácilmente [41].

El calentamiento rápido de la biomasa en dicha atmósfera inerte da como resultado la producción de vapor orgánico compuesto por fragmentos de polímeros de celulosa, hemicelulosa y lignina. Estos vapores se pueden condensar para dar un líquido orgánico, comúnmente conocido como bio-aceite. Los gases no condensables abandonan el sistema de reacción y pueden usarse para proporcionar calor para la pirólisis. El sólido restante, conocido como bio-char, posee un alto contenido en carbono. La distribución del producto depende predominantemente de la composición de la biomasa lignocelulósica. El aceite de pirólisis es un material muy complejo (fuertemente ácido, muy heterogéneo) y precisa un refino técnicamente complicado para ser utilizado como combustible, por lo que debe acondicionarse para emplearse en los motores actuales [40, 42].

1.4.3. Licuefacción

La licuefacción es una vía alternativa para la producción de bio-aceite, consiste en la descomposición térmica catalítica de moléculas grandes a especies inestables más cortas que se polimerizan nuevamente en un bio-aceite [43]. La biomasa se mezcla con agua y catalizadores básicos como el carbonato de sodio, y el proceso se lleva a cabo a temperaturas más bajas que la pirólisis (250-450 ºC) pero presiones más altas (5-20 atm). Estos factores se combinan para hacer que la licuefacción sea un proceso más costoso. El producto líquido obtenido contiene menos oxígeno (12-14%) que el bio-aceite producido por la pirólisis y generalmente requiere un procesamiento menos extenso [27, 44].

1.4.4. Hidrólisis

La hidrólisis en comparación con técnicas como la gasificación, pirólisis o licuefacción se lleva a cabo a temperaturas más bajas (100-250 °C) en fase acuosa. Su objetivo es romper las cadenas de celulosa y hemicelulosa para llegar a la unidad monomérica, en este caso, azúcares como la glucosa y la xilosa, principalmente [45]. Posteriormente, a través de diferentes técnicas catalíticas, se pueden transformar esos azúcares en productos plataforma, es decir, en compuestos que son la base para la obtención de otros más complejos de interés industrial, como HMF y furfural (FFL).

Como se indica anteriormente en el **apartado 1.3.1**, la celulosa es un polímero de glucosa ampliamente presente en las plantas, y representa una de las materias primas más abundantes y renovables para la producción de bioproductos. Se trata de un material higroscópico e insoluble en agua [46]. Sin embargo, la hidrólisis es uno de los procesos clave para la conversión de celulosa en productos químicos de valor añadido [47], ya que implica la ruptura de los enlaces glucosídicos que unen las unidades de glucosa en la cadena polimérica, generando así productos de menor peso molecular. Esta reacción puede llevarse a cabo mediante diversos métodos, como la hidrólisis ácida o la enzimática.

La hidrólisis enzimática se basa en la acción de enzimas celulolíticas, como las celulasas y hemicelulasas, que catalizan la descomposición de la celulosa en azúcares fermentables [48]. Por otro lado, la hidrólisis ácida utiliza ácidos diluidos, como el ácido sulfúrico o el ácido clorhídrico, para catalizar la ruptura de los enlaces glucosídicos, lo que genera la formación de azúcares monoméricos como la glucosa, así como productos secundarios como ácidos orgánicos y aldehídos [47].

Aunque la hidrólisis enzimática tiene ventajas en términos de selectividad y eficiencia energética, su implementación a gran escala puede verse limitada por los elevados costes asociados a la producción y purificación de las enzimas. En cambio, la hidrólisis ácida presenta menores costes, ya que la producción de los ácidos utilizados como catalizadores es considerablemente más económica, y su velocidad de reacción es mayor, lo que permite completar el proceso en menos tiempo y con equipamientos más pequeños [49]. Además, se han investigado estrategias de pretratamiento de la celulosa para mejorar su accesibilidad a los agentes hidrolíticos, así como métodos de recuperación y reciclaje de los catalizadores ácidos [50].

Es importante destacar que la hidrólisis de la celulosa proporciona la base para el desarrollo de procesos más complejos que implican la utilización de biomasa lignocelulósica. A diferencia de la celulosa pura, la biomasa lignocelulósica contiene no solo celulosa, sino también hemicelulosa y lignina, lo que añade una complejidad adicional debido a la heterogeneidad de la materia prima y la necesidad de descomponer y valorizar múltiples componentes. Además, el sistema no ideal de la biomasa lignocelulósica introduce consideraciones adicionales en términos de cinética de reacción y transferencia de calor y materia, lo que requiere un enfoque integrado y multidisciplinario para su conversión eficiente.

1.5. OBTENCIÓN DE ÁCIDO 2,5-FURANDICARBOXÍLICO A PARTIR DE BIOMASA

Tras haber contextualizado la problemática medioambiental derivada de la sobreproducción de plásticos de origen fósil y la urgente necesidad de desarrollar alternativas sostenibles, en esta Tesis Doctoral se detallan las distintas etapas del proceso de producción de FDCA (precursor de PEF) a partir de residuos de biomasa lignocelulósica.

Las etapas del proceso incluyen la hidrólisis de la biomasa tras su pretratamiento, obteniendo azúcares simples (glucosa, xilosa) y, posteriormente, aldehídos furánicos, FFL y HMF. La oxidación de estos aldehídos produce FDCA y ácido furóico (FCA), que a su vez es sometido a una etapa adicional de carboxilación para completar la síntesis de FDCA.

Este proceso integrado permite la conversión de un residuo abundante en un producto de alto valor añadido, alineándose con los principios de la economía circular y la sostenibilidad industrial. Las distintas etapas del proceso se muestran esquematizadas en la **Figura 1.14.**

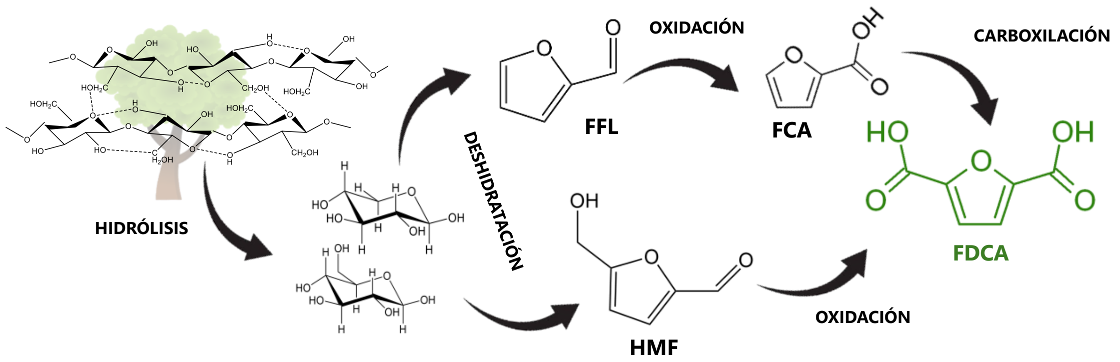

Figura 1.14. Secuencia de las diferentes etapas necesarias para la transformación de biomasa en FDCA.

1.5.1. Tratamientos previos de la biomasa lignocelulósica

La estructura recalcitrante de la biomasa lignocelulósica hace que su conversión directa hacia otros productos sea compleja. Por lo tanto, los pretratamientos son necesarios para permitir la separación efectiva de sus componentes y su posterior valorización independiente [51]. Entre los pretratamientos más comunes se encuentran la hidrólisis ácida, la hidrólisis alcalina, la explosión de vapor (*Steam Explosion*), la oxidación con oxígeno y el tratamiento con disolventes orgánicos [52].

- Hidrólisis ácida: En este proceso, la biomasa se trata con ácidos fuertes, como ácido sulfúrico o ácido clorhídrico, en condiciones controladas de temperatura y presión. El ácido rompe los enlaces químicos que mantienen unidas las fibras de celulosa, hemicelulosa y lignina, liberando así azúcares fermentables y compuestos fenólicos. Este método es efectivo para descomponer la hemicelulosa en azúcares simples, como la xilosa y la arabinosa, que luego pueden ser utilizados en la producción de biocombustibles o productos químicos [53].
- Hidrólisis alcalina: Similar a la hidrólisis ácida, este proceso implica el tratamiento de la biomasa con soluciones alcalinas, como hidróxido de sodio o hidróxido de potasio. La alcalinidad rompe los enlaces éster entre la lignina y los carbohidratos, facilitando la separación de la lignina de la celulosa y la hemicelulosa. Además, la hidrólisis alcalina puede facilitar la despolimerización de la lignina en compuestos fenólicos de menor peso molecular, que son más fáciles de recuperar y utilizar en aplicaciones químicas [54].

- Explosión de vapor (*Steam Explosion*): En este proceso, la biomasa se somete a altas temperaturas y presiones en presencia de vapor de agua. La rápida expansión y contracción resultante de la liberación de la presión provoca la ruptura de las estructuras lignocelulósicas, aumentando la accesibilidad de los componentes de la biomasa. Este método es particularmente efectivo para la separación de la lignina de la celulosa y la hemicelulosa, sin degradar significativamente los azúcares fermentables [55].

- Pretratamientos oxidativos: En este proceso, la biomasa se trata con oxígeno a alta temperatura y presión en presencia de catalizadores metálicos. La oxidación química descompone los componentes de la biomasa, especialmente la lignina, en compuestos más simples y reactivos. Este método puede mejorar la extracción de lignina y aumentar la concentración de azúcares fermentables en la biomasa tratada [56].

- Tratamiento con disolventes orgánicos: En este proceso, la biomasa se trata con disolventes orgánicos, como etanol, metanol o acetona, que tienen afinidad con componentes específicos de la biomasa, como la lignina. Los disolventes disuelven selectivamente la lignina sin dañar significativamente la celulosa y la hemicelulosa, permitiendo su posterior recuperación y valorización [57].

La lignina, una vez separada de la celulosa y la hemicelulosa, puede ser sometida a diversos procesos para su valorización. Por ejemplo, la lignina se puede utilizar como materia prima para la producción de biocombustibles líquidos mediante procesos de pirólisis o gasificación. También puede ser transformada en productos químicos de alto valor mediante procesos de despolimerización, hidrogenación u oxidación controlada [32]. Sin embargo, todos estos procesos se encuentran fuera los objetivos de esta Tesis Doctoral.

1.5.2. Producción de furfural y 5-hidroximetilfurfural

El FFL es uno de los productos químicos renovables más antiguos producidos por el ser humano, cuya estructura se compone de un anillo de furano y un grupo aldehído, lo que lo convierte en una molécula reactiva y versátil. Tradicionalmente, ha sido utilizado en la fabricación de resinas, especialmente en tecnologías de fundición, y como disolvente en la producción de lubricantes. Además, el FFL es una molécula plataforma clave para la síntesis de productos químicos basados en furanos, como el alcohol furfurílico, alcohol metilfurfurílico, furano, ácido furóico, furfurilamina y metilfurano (**Figura 1.15**). Estos derivados tienen un alto potencial en aplicaciones industriales, incluyendo la producción de biocombustibles, resinas y disolventes sostenibles [58]. Dada la baja valorización de esta fracción, las rutas centradas en el FFL ofrecen una ventaja adicional tanto desde la perspectiva de la economía circular como de la sostenibilidad [58].

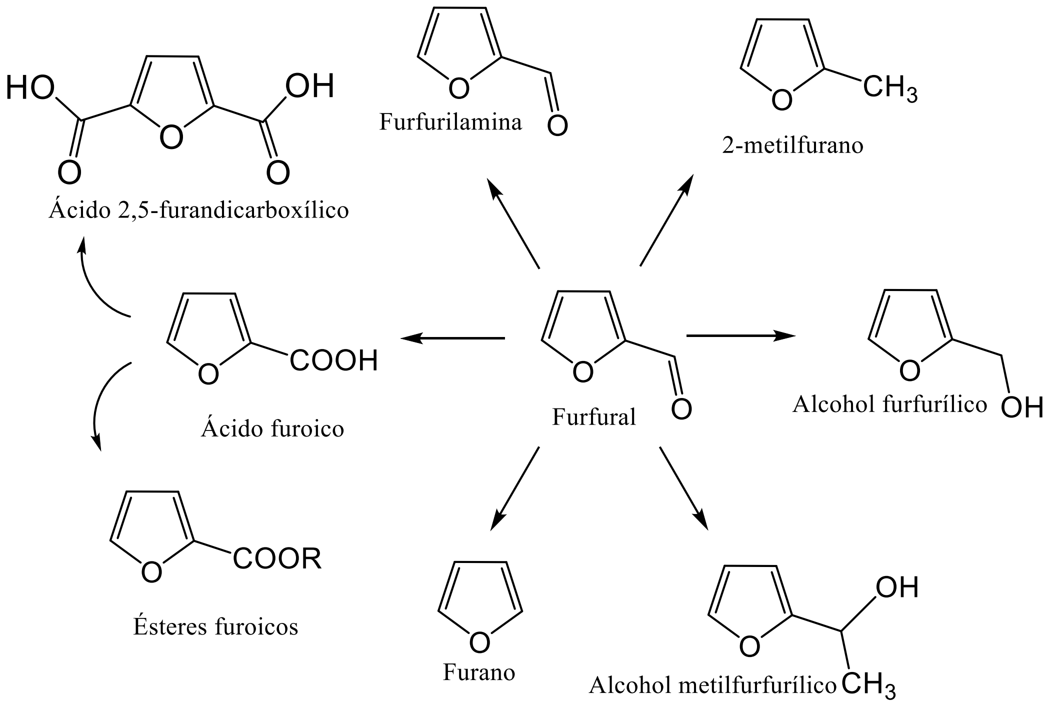

Figura 1. 15. Ejemplos de productos químicos derivados del furfural

El HMF, por su parte, presenta una estructura similar, con un anillo de furano al que están unidos un grupo aldehído y un grupo hidroxilo, lo que le confiere una gran reactividad. Puede transformarse en varios productos químicos y combustibles importantes debido a la presencia de los grupos funcionales C=O, C-O y el anillo de furano (**Figura 1.16**). El HMF es utilizado como materia prima para la síntesis de compuestos clave como el diformilfurano (DFF) y el FDCA, a través de procesos de oxidación. Tanto el DFF como el FDCA son fundamentales para la fabricación de productos farmacéuticos, fungicidas y polímeros de furano. Como se indica anteriormente, el FDCA es de gran interés industrial por su papel en la producción de PEF, un polímero renovable que tiene el potencial de sustituir al PET en la industria de los plásticos [59].

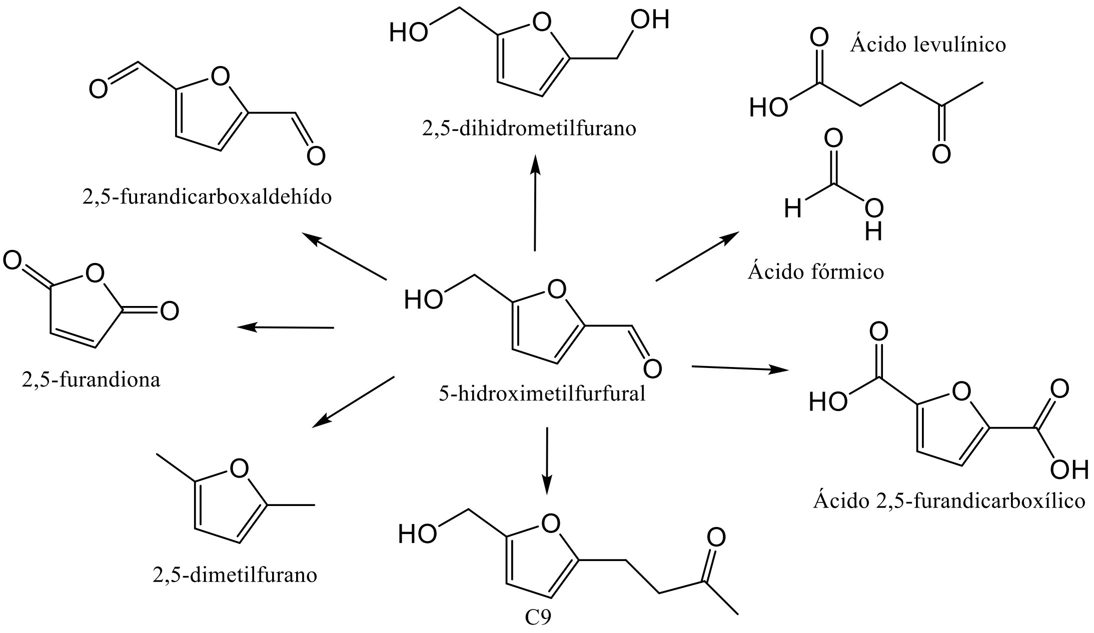

Figura 1. 16. Ejemplos de productos químicos derivados del 5-hidroximetilfurfural

La producción de FFL y HMF comienza con la hidrólisis de la biomasa hemicelulósica. Como se explica en el **apartado 1.4.4**, esta etapa puede llevarse a cabo mediante diferentes enfoques, incluyendo tratamientos ácidos, enzimáticos o combinados [60]. Una vez liberados los azúcares, el FFL y el HMF se generan mediante reacciones de deshidratación y condensación junto con el ácido levulínico (LA) y fórmico (FA) [26]. El FFL se produce a partir de la deshidratación de pentosas (principalmente xilosa) presente en la hemicelulosa, mientras que el HMF se forma a partir de la deshidratación de hexosas (principalmente glucosa) derivada de la celulosa (**Figura 1.17**) [53].

El FFL y el HMF emergen como un pilar en la valorización de la biomasa por su capacidad para transformarse en diferentes compuestos de alto valor añadido. La investigación en este campo continúa explorando nuevas rutas catalíticas y mejorando la eficiencia de los procesos, con el objetivo de maximizar el rendimiento y la pureza de los productos derivados de la hidrólisis, lo que podría tener un impacto significativo en la industria de los materiales sostenibles. En la literatura se han propuesto diferentes catalizadores para llevar a cabo la hidrólisis, incluidos ácidos orgánicos e inorgánicos, sales, ácidos de Lewis y resinas de intercambio iónico [47], concluyendo que la isomerización de glucosa a fructosa (catalizada por ácidos de Lewis) es el paso limitante en la velocidad de reacción. Además de los cloruros metálicos (catálisis homogénea), se han probado zeolitas como ZSM-5 modificado con metales, zeolita Y o mordenita para obtener una buena actividad de isomerización [61, 62].

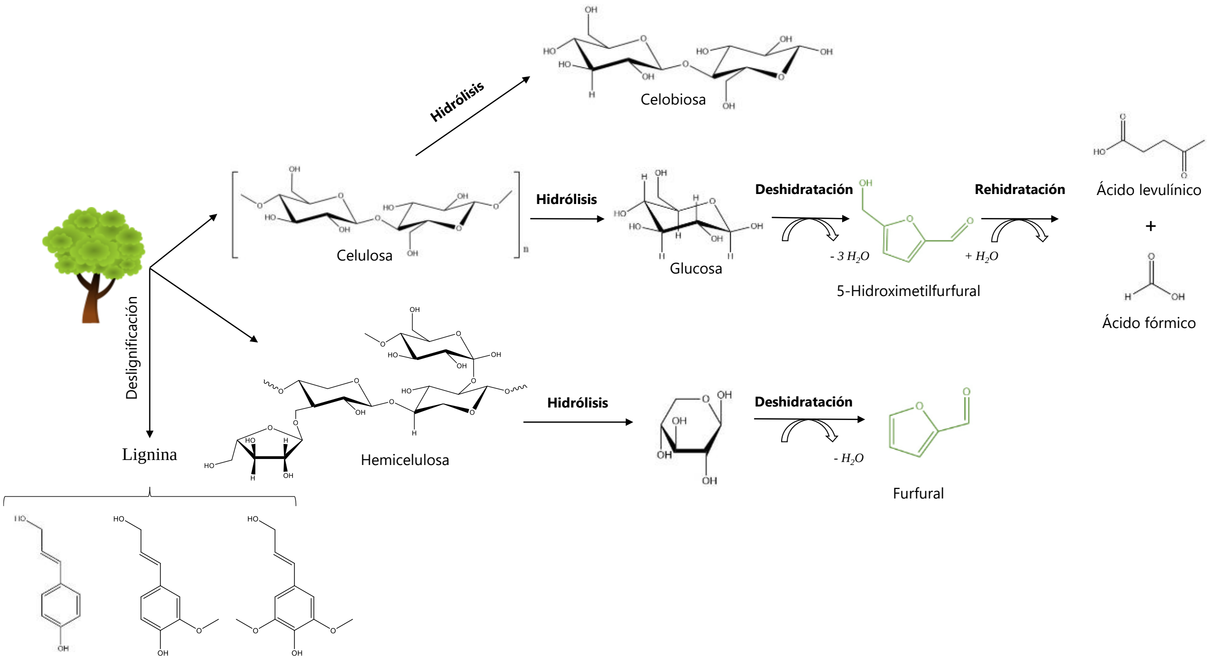

Figura 1.17. Esquema del proceso de hidrolisis de biomasa lignocelulósica

Por otro lado, cuando se utilizan ácidos de Brønsted, esta isomerización no tiene lugar y la deshidratación cíclica es termodinámicamente menos favorable. Además, la acidez de Brønsted promueve la degradación del HMF (ruptura del ciclo y rehidratación), obteniéndose LA y FA [61]. Por ello, las condiciones de reacción deben equilibrarse para optimizar la producción de aldehídos [26, 63]. En la **Tabla 1.1** se detallan las condiciones de operación y los tipos de catalizadores empleados en hidrolisis de diferentes tipos de biomasa lignocelulósica encontrados en la literatura. En este punto, el uso combinado de zeolitas y ácidos minerales ha mostrado muy buenos resultados para transformar glucosa en HMF [62], pero su efecto en aquellas reacciones que combinan hidrólisis y deshidratación (como la obtención de HMF a partir del polímero) aún no ha sido estudiado, siendo una de las principales novedades de esta Tesis Doctoral.

Tabla 1.1. Revisión de condiciones y resultados obtenidos en hidrólisis ácida de biomasa en la literatura.

Sustrato	Disolvente	Catalizador	T (ºC)	t(h)	η glucosa (%)	η xilosa (%)	η HMF (%)	η FFL (%)	Ref.
MCC	H_2O	$CP\text{-}SO_3H$	120	10	93	-	-	-	[65]
Almidón	H_2O	$CP\text{-}SO_3H$	120	2	100	-	-	-	[65]
MCC	H_2O	H_2SO_4	120	2	1	-	-	-	[65]
MCC molido	H_2O	$Si_{33}C_{66}.823\text{-}SO_3H$	150	24	50	-	0	-	[66]
MCC molido	H_2O	Sucrosa sulfonatada	150	24	27	-	1	-	[66]
Haya	H_2O	H_2SO_4	145	1	76	74	2	6	[67]
Álamo	H_2O	H_2SO_4	145	1	78	82	2	8	[67]
Algodón	$[C_2mim]Cl$	HCl	105	3	87	-	6	-	[68]
Maíz	$[C_2mim]Cl$	HCl	105	3	70	79	-	-	[68]
MCC	$[C_4mim]Cl$	H_2SO_4	100	0.75	38	-	-	-	[69]
Eucalipto	$[C_4mim]Cl$/ChCl/oxálico	-	120	10	48	-	4	-	[70]
MCC de pino			120	10	50	-	6	-	[70]
Maíz			100	2	54	35	10	-	[70]
Maíz	$ZnCl_2{\cdot}4.25H_2O$	HCl	120	1	61	-	30	22	[71]
Algas	$ZnCl_2{\cdot}4.25H_2O$	HCl	120	1	49	-	35	29	[71]
Xilanos	ChCl/cítrico/MIBK	$AlCl_3$	140	0.5	-	-	-	69	[72]
Madera	ChCl/oxálico/MIBK	-	100	5	0	0	1	55	[73]

MCC, celulosa microcristalina; ChCl, Cloruro de colina
$[C_2mim]Cl$, 1-etil-3-metilimidazolium
$[C_4mim]Cl$, 1-butil-3-metilimidazolium

A pesar de la gran cantidad de estudios en este campo, no se han abordado los efectos que conllevan los pretratamientos previos de la biomasa o de la celulosa en los resultados finales de la hidrólisis.

1.5.3. Oxidación de furfural para la obtención de ácido furoico

La producción industrial actual de FCA se basa en la reacción de Cannizzaro. Este método de síntesis está lejos de cumplir con los Principios de la Química Verde ya que se realiza en medios básicos fuertes, utilizado NaOH como catalizador básico de Brønsted, con todos los problemas derivados del uso de un catalizador homogéneo. El alcohol furfurílico (FOH) y el furoato de sodio se forman como resultado de esta reacción de desproporción por lo que esta ruta limita la selectividad máxima del FCA al 50% [74] (**Figura 1.18**). La adición de un ácido es necesaria para neutralizar la solución y obtener ácido furóico, generalmente se emplea ácido sulfúrico y como resultado, se forma bisulfato de sodio. La temperatura óptima se encuentra en torno a 150 ºC y debe controlarse meticulosamente porque la reacción de Cannizzaro es altamente exotérmica. La oligomerización del furfural en condiciones de Cannizzaro (pH muy alto, 150 ºC) también es un inconveniente relevante [75].

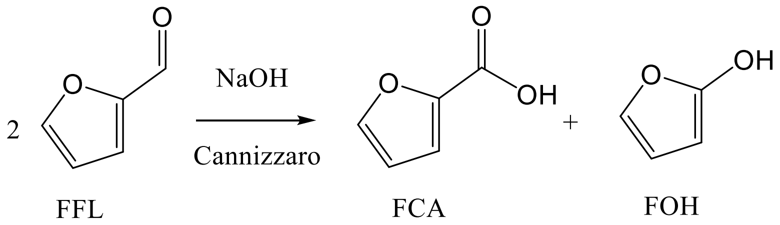

Figura 1.18. Esquema de la reacción de Cannizzaro

Como posibles alternativas al proceso industrial de síntesis de FCA, se han propuesto dos rutas prometedoras: la oxidación catalítica con peróxido de hidrógeno y la oxidación con aire u oxígeno.

Oxidación con peróxido de hidrógeno

El peróxido de hidrógeno es considerado un oxidante verde que no produce ningún residuo indeseado y que permite llevar a cabo la reacción de oxidación a temperaturas bajas ya que ambos reactivos (FFL y H_2O_2) se encuentran en fase líquida. La descomposición del H_2O_2 conduce a un proceso autocatalítico, aún más potenciado por los ácidos generados durante la oxidación (catálisis homogénea) [76]. Estas ventajas, así como el significativo crecimiento de la producción industrial de H_2O_2 en las últimas décadas y la posibilidad de generación *in situ* mediante métodos fotocatalíticos o electrocatalíticos justifican el creciente interés en la investigación de nuevos procesos de producción más verdes y nuevas aplicaciones de este oxidante industrial verde [77].

La oxidación del furfural utilizando H_2O_2 ha sido estudiada en la literatura, describiendo un complejo mecanismo de reacción caracterizado por una combinación de etapas paralelas y secuenciales (**Figura 1.19**). La literatura previa se ha centrado principalmente en la síntesis de ácido maleico [78, 79] y succínico [80], y, en menor medida, 2-(5H)-furanona (FN) [81] y ácido furóico [82].

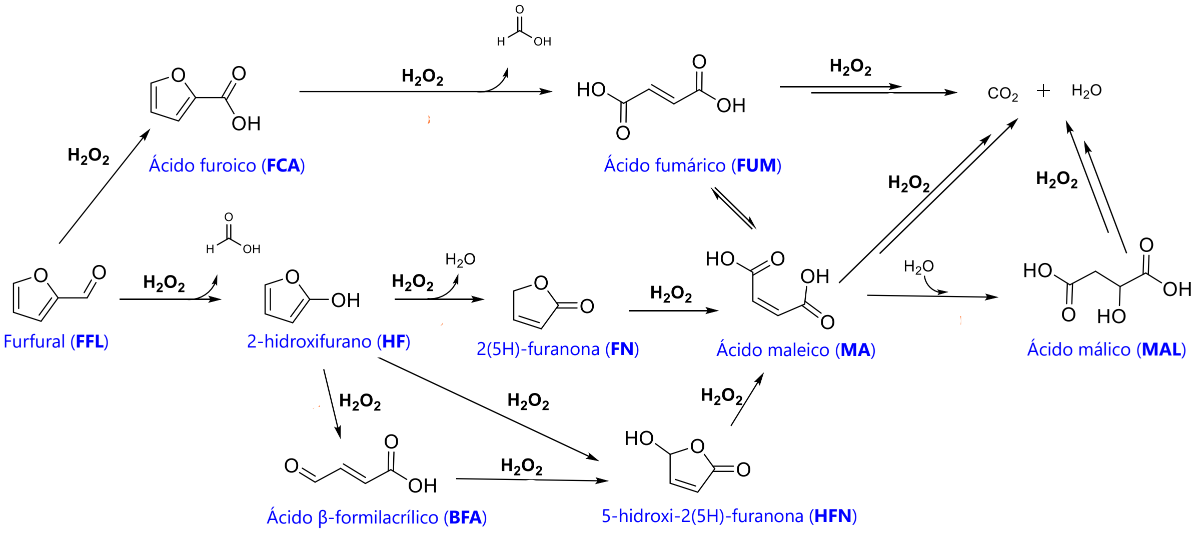

Figura 1.19. Esquema del mecanismo de reacción para la oxidación de FFL empleando H_2O_2

Entre los catalizadores basados en zeolitas, Palai *et al.* obtiene un rendimiento del 53% para producir ácido succínico al utilizar H_2O_2 como agente oxidante empleando como catalizador zeolita Sn-Beta. En este estudio se identificó la 2-(3H)-furanona como un intermedio clave. La zeolita Sn-Beta fue reutilizada durante varios ciclos, y los depósitos orgánicos producidos se eliminan fácilmente calcinando el material. Sin embargo, en este estudio, la zeolita TS-1 fue más selectiva hacia la producción de ácido maleico (58%) [80].

Por otro lado, Murzin y colaboradores, en presencia de peróxido de hidrógeno, también tuvieron como producto principal el ácido succínico, mostrando una selectividad 50% frente a otros ácidos orgánicos como el FA y el MA utilizando como catalizador un ácido sulfónico soportado en un polímero fibroso (Smopex-101) [83]. En un estudio análogo con aluminosilicatos mesoporosos, Murzin y colaboradores obtienen un 19.5% de rendimiento de ácido succínico con 3MMAS. Con otros catalizadores como ZSM-5 y AlSi-SBA-15 tuvieron rendimientos de 17.8% y 16.4%, respectivamente [84].

En la mayoría de estos casos, se tienen selectividades inferiores al 5% de FCA, debido a la alta reactividad del H_2O_2, a la coexistencia de diferentes rutas de reacción y a la naturaleza ácida de los catalizadores. En esta Tesis Doctoral, se evalúa otro enfoque mediante el uso de diferentes catalizadores con propiedades básicas para intentar favorecer la producción de FCA empleando una disolución tampón para minimizar la acción de los ácidos. Este nuevo enfoque no presenta bibliografía previa por lo que se considera un enfoque novedoso y prometedor. Se evalúan varios materiales como posibles catalizadores para la oxidación parcial del furfural utilizando H_2O_2. Se utilizaron cuatro óxidos con diferentes propiedades catalíticas: TiO_2 y CeO_2, que representan materiales redox, y MgAl y MgZr, como óxidos mixtos típicos con sitios ácido-básicos. Para mejorar la actividad catalítica, se prepararon materiales bifuncionales incorporando Au, Pd y Pt, tres de los metales más activos para oxidaciones [85, 86]. Estos cuatro soportes elegidos han sido propuestos previamente en diferentes estudios utilizando moléculas de plataforma lignocelulósica. Así, el CeO_2 ha sido probado con éxito en la oxidación selectiva de HMF, destacando el estrecho contacto entre el metal y el soporte obtenido, y el papel crucial de los defectos del soporte en la oxidación [87, 88]. El TiO_2 ha sido ampliamente utilizado como soporte para catalizadores bifuncionales en oxidaciones de HMF, revelando una fuerte interacción con las nanopartículas metálicas que altera las propiedades originales, aumentando el área de superficie y la concentración de sitios activos, lo que contribuye a una alta actividad, selectividad y estabilidad [89, 90]. También se consideraron óxidos mixtos derivados de hidrotalcitas (MgAl) y otros óxidos (incluidos Mg y Zr) para la oxidación de HMF [91, 92], principalmente utilizando Rh como fase activa.

A pesar de la escasa literatura sobre estos materiales en oxidaciones, se utilizan ampliamente en otras reacciones que involucran furfural, como la condensación [93] o la hidrogenación [94]. Por lo tanto, una buena actividad en esta reacción podría ampliar su versatilidad, aumentando el espectro de reacciones relacionadas con moléculas derivadas de biomasa que pueden catalizar.

Oxidación con aire u oxígeno

Al emplear oxígeno molecular para esta oxidación la selectividad hacia FCA es mucho más alta y el entorno es más fácilmente controlable debido a la oxidación selectiva. Sin embargo, esta reacción puede verse limitada por la transferencia de masa de oxígeno entre las fases gas-líquido, requiriendo condiciones más severas y necesitando catalizadores heterogéneos para la activación del oxígeno [95]. Para prevenir la desactivación catalítica inducida por ácidos, estas reacciones suelen llevarse a cabo en un medio básico fuerte (NaOH). La presencia de NaOH promueve las reacciones de Cannizzaro, mientras que el material sólido cataliza tanto la oxidación directa del aldehído como la oxidación secuencial del alcohol furfurílico a aldehído y del aldehído a ácido. Este enfoque requiere un control estricto de la temperatura para prevenir la oligomerización del FFL, que probablemente ocurra en condiciones muy básicas. Entre otros trabajos, Verdeguer y colaboradores muestran que se pueden lograr altas selectividades de FCA (92%) en presencia de un catalizador bimetálico PbPt [96]. Dowthwaite *et al.* obtiene rendimientos superiores al 93% con 1% AuPd/Mg(OH), un valor ligeramente superior al 76% obtenido con Au/MnO [97]. Sha y colaboradores logran altas selectividades (92%) hacia FCA con Ag_2O/CuO [98]. Un trabajo reciente propone diferentes catalizadores Au/Nb_2O_5, obteniendo conversiones moderadas (<50%) [99]. Como conclusión general de estos trabajos, se propone que Au es el metal noble óptimo para la oxidación de FFL, siendo más estable en un medio acuoso oxidante que Pt o Pd, y evitando rutas radicales de degradación de FFL, con el efecto positivo inherente en la selectividad y estabilidad del proceso [100].

A pesar de estos resultados prometedores, esta ruta sigue siendo contraria a los Principios de la Química Verde debido al uso de NaOH. Un enfoque alternativo considera trabajar en condiciones homogéneas sin base (pH no controlado). Varios trabajos obtienen mejoras claras concluyendo que la ausencia de NaOH debe ser compensada utilizando soportes básicos (MgO, CaO o materiales derivados de hidrotalcitas) para potenciar el rendimiento catalítico [101, 102]. Como alternativa a este concepto, otros autores sugieren añadir un segundo metal (catalizadores bimetálicos) o desarrollar materiales tipo núcleo-corona, aumentando la complejidad del sistema catalítico [103, 104].

Sin embargo, existen dos inconvenientes relevantes relacionados con la estabilidad: la continua lixiviación del soporte debido a la formación de ácidos orgánicos y la desactivación de Au por la adsorción irreversible de ácido fórmico. Ambos problemas podrían ser minimizados utilizando una solución tampón que neutralice los ácidos obtenidos. Para lo cual no existe literatura previa sobre este enfoque, a pesar del equilibrio óptimo entre actividad, estabilidad y sostenibilidad que podría representar.

En esta Tesis Doctoral se aborda la oxidación parcial de FFL a FCA con O_2 utilizando catalizadores heterogéneos bifuncionales basados en Au como metal activo sobre dos soportes diferentes, MgAl y TiO_2. Además, se evitan las condiciones básicas fuertes sustituyéndolas por una disolución tampón.

1.5.4. Oxidación de 5-hidroximetilfurfural para la obtención de FDCA

La síntesis de FDCA a partir de HMF se ha estudiado principalmente a través de rutas electroquímicas y fotocatalíticas [105, 106], destacando el catalizador Au/TiO_2 como uno de los más prometedores debido a su alta actividad, estabilidad y selectividad debido a su capacidad para activar el oxígeno y adsorber HMF [107, 109]. En cuanto a la ruta termo-catalítica, se ha investigado utilizando oxígeno molecular en presencia de catalizadores heterogéneos basados en Pt, Pd o Ru. Sin embargo, estos sistemas presentan una estabilidad o selectividad insuficiente [109-111]. En cambio, los catalizadores de oro, entre ellos el Au/TiO_2, son activos y más estables que el Pt y el Pd, alcanzando una selectividad casi total con conversiones de HMF superiores al 80% [112, 113].

La oxidación catalítica de HMF se define como un proceso de dos pasos, que sigue dos mecanismos diferentes según el grupo funcional que sufra la primera oxidación, transformándose en ácido 5-hidroximetil-2-furancarboxílico (HMFCA) en el caso del grupo aldehído, o 2-diformilfurano (DFF) si se trata del grupo hidroxilo (**Figura 1.20**). La prevalencia de las rutas HMFCA o DFF está condicionada por diferentes factores, como el metal utilizado (Au promueve la ruta de HMFCA, en cambio otros metales nobles promueven la ruta de DFF [112]) y el disolvente (los disolventes orgánicos polares apróticos promueven la ruta de DFF, el agua y el entorno básico promueven la ruta de HMFCA) [111, 114].

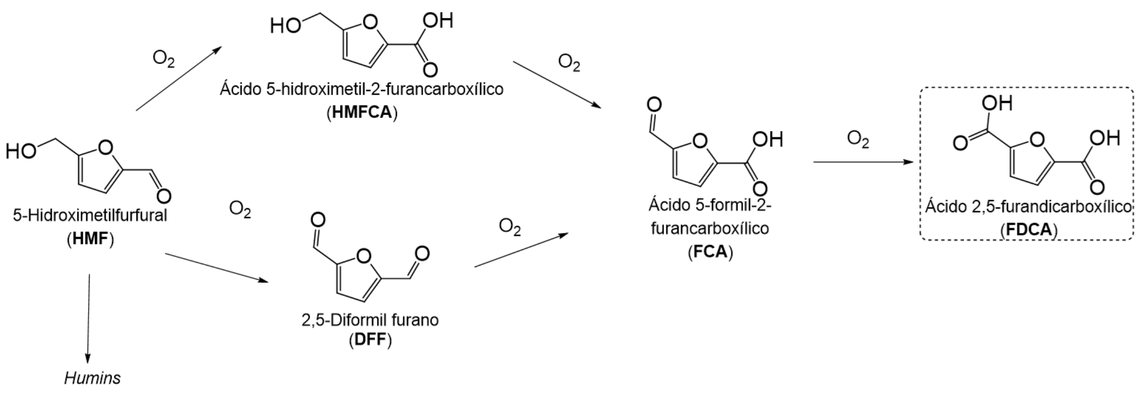

Figura 1.20. Mecanismo general de la oxidación de HMF para producir FDCA. Adaptado de [115].

Estudios previos demuestran los efectos positivos de la adición de bases homogéneas en el rendimiento de la oxidación de HMF, tanto activando el HMF para producir HMFCA [116, 117] como aumentando la solubilidad de los productos de reacción. Sin embargo, el entorno básico lleva a la formación de subproductos que no pueden ser fácilmente identificados, generalmente conocidos como huminas, con el subsiguiente efecto negativo en la selectividad y, en el caso de utilizar un catalizador heterogéneo, en la estabilidad [118]. A pesar de la influencia esperada de las condiciones de reacción en la formación de huminas, existe una brecha relevante en la literatura sobre estos aspectos. Los únicos estudios que abordan la prevención de huminas en la oxidación de HMF sugieren el uso de disolventes orgánicos [119], lo que plantea preocupaciones sobre la sostenibilidad del proceso.

La viabilidad económica es otro cuello de botella de esta ruta, ya que está restringida por la dificultad de aislar el HMF en la hidrólisis de biomasa ya que se trata de n aldehído inestable en un medio acuoso que tiende a descomponerse en ácido levulínico y ácido fórmico como productos finales [120, 121]. El desarrollo de un proceso en un solo paso que permita la oxidación in situ de HMF sería de gran interés, evitando su descomposición y reduciendo los costes totales del proceso. Sin embargo, las propiedades catalíticas opuestas requeridas para la hidrólisis de azúcares (un proceso catalizado por ácido [122, 123]) y la oxidación de HMF (catálisis *redox* en condiciones alcalinas) hacen que este enfoque sea difícil. Algunos autores proponen un sistema bifásico donde la deshidratación de azúcares tiene lugar en medios acuosos y el HMF se extrae a una fase orgánica donde se lleva a cabo la oxidación, lo que implica desarrollos complejos de reactores y un control del proceso complicado [124]. Además, la mayoría de estos estudios proponen sistemas catalíticos complejos [125], o la oxidación se limita a producir DFF en lugar de FDCA [126].

En esta Tesis Doctoral se realiza un análisis integral del impacto de varias condiciones de reacción, incluyendo temperatura, presión de oxígeno, relación NaOH y concentración inicial de HMF, en la oxidación de HMF a FDCA sobre Au/TiO_2.

Por otro lado, la literatura explora extensamente la oxidación de FFL o HMF por separado, pero, como se mencionó anteriormente, en la reutilización directa de residuos lignocelulósicos, el HMF y el FFL se producen juntos generalmente en una relación de 1:2 [127, 128]. Además, ambos aldehídos tienen puntos de ebullición cercanos y polaridades similares, lo que complica su separación durante los procesos de extracción y purificación [129, 130]. El FFL, a pesar de ser producido a partir de la fracción minoritaria de hemicelulosa presente en la biomasa, es mucho más estable. Por el contrario, el HMF bajo condiciones de hidrólisis generalmente se descompone en LA y ácido fórmico. Este hecho abre una posible ruta inexplorada para la transformación conjunta de HMF y FFL mediante oxidación en ácidos furánicos como el FCA y FDCA utilizando un catalizador heterogéneo. Dado que, desde la perspectiva de la implementación industrial de la utilización de residuos de biomasa lignocelulósica, el estudio de la oxidación simultánea de FFL y HMF juega un papel clave, en esta Tesis Doctoral también se estudia la oxidación conjunta de ambos aldehídos a diferentes proporciones de NaOH utilizando Au/TiO_2.

1.5.5. Carboxilación de ácido furoico

En la búsqueda continua de métodos sostenibles y eficientes para la síntesis de compuestos orgánicos de alto valor añadido, los procesos de carboxilación se han convertido en una herramienta importante en la química moderna. Estos procesos permiten la introducción de grupos carboxilo (-COOH) en sustratos orgánicos, generando productos con una amplia gama de aplicaciones industriales, que van desde la fabricación de polímeros hasta la síntesis de productos farmacéuticos.

La carboxilación también ha ganado interés en el contexto de la captura y utilización de dióxido de carbono (CO_2), un importante gas de efecto invernadero. Al convertir el CO_2 en compuestos orgánicos mediante procesos de carboxilación, no solo se puede mitigar su impacto ambiental al capturarlo, sino que también se puede transformar en productos químicos de valor añadido, contribuyendo así a la economía circular y a la reducción de la dependencia de recursos fósiles [131].

La incorporación de CO_2 en moléculas orgánicas se propuso por primera vez hace más de 100 años, como una aplicación particular de la Reacción de Grignard (**Figura 1.21**) [132]. Sin embargo, la disponibilidad limitada de los reactivos originales, así como su reactividad química y manipulación compleja, hacen que la fijación de CO_2 mediante este método sea poco atractiva para su implementación industrial.

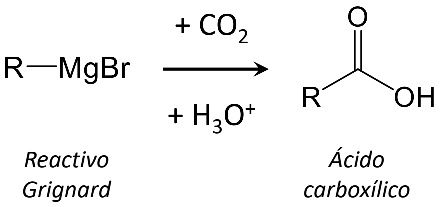

Figura 1.21. Esquema de la reacción de Grignard con CO_2

En este contexto, la producción de FDCA a partir de FCA es un proceso clave en la síntesis de polímeros de alto rendimiento y productos químicos bio-renovables. Este proceso puede llevarse a cabo mediante, carboxilación enzimática, carboxilación en discontinuo o carboxilación en lecho fijo.

Carboxilación enzimática de ácido furoico

La producción de FDCA a través de las rutas biocatalíticas ha ganado relevancia en los últimos años. La actividad carboxilativa de algunas enzimas de la familia de las descarboxilasas se identificó como una conclusión secundaria de los estudios de biodegradación [133, 134]. Estos resultados fueron el punto de partida para el estudio de Payne y colaboradores, que demostró la capacidad de las enzimas HmF para carboxilar y producir FDCA [135]. Los resultados no son muy prometedores (0.3 % de rendimiento tras 12 h) y la reacción requiere un control estricto de las condiciones de reacción, ya que es muy sensible a la temperatura (50 ºC es el óptimo), al pH (casi nula actividad fuera del rango neutro) y a la presión de CO_2 (se requieren 32 bar para observar resultados). Sin embargo, la sostenibilidad inherente de las reacciones enzimáticas, así como las posibilidades de recombinación e ingeniería de ADN, definen esta ruta biocatalítica como un campo prometedor para futuros estudios.

Carboxilación de ácido furoico en discontinuo

La carboxilación del FCA usando CO_2 y una base como reactivo se propuso por primera vez en 2016 [131]. Esta reacción es una aplicación particular de la síntesis de Kolbe-Schmitt, posiblemente la síntesis orgánica más antigua que usa CO_2, reportada en 1860. La reacción de Kolbe-Schmitt es una reacción en estado sólido que generalmente se lleva a cabo poniendo en contacto CO_2 con compuestos aromáticos activados por sustituyentes donadores de electrones, como cationes alcalinos. Aunque esta reacción se ha desarrollado para aromáticos de hidrocarburos, su mecanismo podría extenderse a otros compuestos heterocíclicos con características aromáticas, como piridinas o furano [136].

El trabajo pionero de Kanan y colaboradores [131] establece los pilares para estudios futuros, obteniendo conclusiones muy relevantes sobre el mecanismo y las condiciones de reacción. Investigaciones previas demuestran que los carbonatos pueden desprotonar enlaces C-H con valores de pKa de hasta 27 usando disolventes orgánicos y altas temperaturas [137, 138]. Considerando el alto pKa del C-H en la posición 5 del furano-2-carboxilato (≈35), la formación de FDCA mediante carboxilación con CO_2 es termodinámicamente desfavorable. Este inconveniente se soluciona mediante la formación inicial de un furoato metálico por la reacción del ácido furoico con una sal alcalina. Así, la reacción involucra dos sólidos y se lleva a cabo en condiciones sin disolvente. Estos sólidos deben fundirse para permitir la movilidad iónica necesaria para la correcta interacción entre los diferentes iones involucrados. Por lo tanto, el punto de fusión de los carbonatos es un aspecto crítico para evitar la descomposición de los compuestos orgánicos (ácido furoico y productos intermedios de reacción o compuestos secundarios). En este contexto, la mayoría de las sales alcalinas se descartan (temperaturas mucho mayores de 200 ºC para fundirse), proponiendo Cs_2CO_3 como la mejor opción. Esta desprotonación da lugar a un átomo de carbono nucleofílico fuerte que podría reaccionar con el CO_2 débilmente electrófilo. Los mecanismos de reacción propuestos (**Figura 1.22**) resultan en un consumo neto de un equivalente de CO_2 por cada $C\text{-}CO^{2-}$ producido. Trabajar con una alta concentración de carbonatos garantiza la estabilización de la base conjugada de FDCA mediante apareamiento iónico. El FDCA se obtiene por protonación con HCl, mientras que el carbonato se recupera por electrodiálisis.

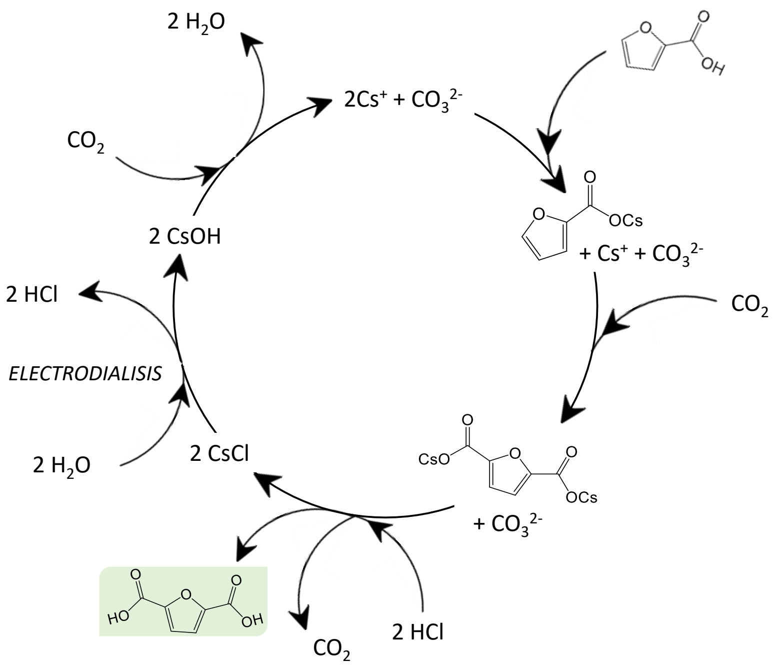

Figura 1.22. Esquema del mecanismo de reacción para obtener FDCA de manera selectiva mediante la carboxilación de ácido furoico y CO_2

Los mejores resultados propuestos en este trabajo corresponden a un rendimiento del 76% de $FDCA^{2-}$ después de 12 h al calentar a 260 ºC bajo un flujo de CO_2 de 40 $mL \cdot min^{-1}$, utilizando un 10% de exceso de Cs_2CO_3. El acetato y el malonato se identifican como los principales productos de descomposición, limitando su producción al trabajar en un reactor por lotes presurizado (89% de rendimiento de $FDCA^{2-}$ después de 7 h a 200 ºC con 8 bar de CO_2) [131]. El papel limitado del Cs^+ (solo para reducir el punto de fusión de la sal) se corrobora al sustituir este alcalino por sales de potasio (carbonato y carboxilato de potasio como co-sal). Empleando potasio se alcanzaron rendimientos superiores al 60% (por lo que Cs^+ no tiene un papel específico en el mecanismo), pero a temperaturas mucho más altas (320 ºC) a las que las reacciones de descomposición no pueden ser evitadas. Como se esperaba debido al estado semilíquido del reactivo, la reacción ocurre en la interfaz gas-sólido. Los estudios de cambio de escala (de 1-10 a 100 mmol) resultan en rendimientos más bajos debido a la menor relación área superficial-volumen obtenida [131]. Estos resultados se justifican por problemas de transferencia del CO_2 hacia la sal y la eliminación del H_2O.

En un enfoque diferente, Nocito y colaboradores comparan la actividad de diferentes carbonatos más baratos, tratando de obtener más evidencias del mecanismo de reacción y los intermediarios involucrados, concluyendo que los carbonatos inorgánicos, especialmente aquellos con cationes monovalentes, son las especies más activas, observando una actividad creciente a medida que la densidad de carga en los cationes disminuye [139]. Este estudio también demuestra la correlación de actividad-punto de fusión de los carbonatos y propone el uso de difuroato de cobre ($Cu(F)_2$) como una alternativa al Cs. Una comparación completa entre la carboxilación de $Cu(F)_2$ y FCA demuestra un mayor rendimiento al usar el complejo de cobre (selectividad del 89% frente al 70%, después de 6 h a 220 ºC, 6 MPa de CO_2).

Por otro lado, otros autores proponen la carboxilación de derivados del furano utilizando catálisis homogénea, empleando sales de Cu y Pd. Sin embargo, este enfoque se basa en la síntesis de FDCA a través de un proceso multietapa que involucra reacciones en cascada: bromación, esterificación, carboxilación e hidrólisis. Los principales avances en este tema se resumen en una revisión de Drault *et al.* [140].

Carboxilación de ácido furoico en lecho fijo

Tratando de mejorar estos resultados y garantizar la escalabilidad del proceso, Dick y colaboradores llevaron a cabo la carboxilación del furoato en un reactor de lecho fijo utilizando carbonato con diferentes mezclas de cationes. Se obtuvieron resultados muy prometedores a pequeña escala utilizando una mezcla en relación 2:1 de K^+/Cs^+, alcanzando un 89 % de selectividad de FDCA después de 24 horas a 260-285°C con 8 bares de CO_2 [141]. Estos resultados son relevantes para mejorar la rentabilidad del proceso, ya que emplea K^+ cuyo precio es más asequible que el Cs^+, a pesar de la recuperación teórica propuesta mediante electrodiálisis. La reacción equivalente bajo presión estática no fue eficiente, produciendo una mezcla enriquecida en productos de descomposición. Se concluyó que la eliminación de H_2O suprime la descomposición y mejora el rendimiento de FDCA [131].

En base a estos resultados, Zhou y colaboradores propusieron en 2019 la producción directa de FDCA a partir de HMF y FFL [142]. Desarrollaron un catalizador metálico soportado (complejo de Co/Zn-lignina sobre un *single-atom* de Co soportado en carbono dopado con nitrógeno, Co SAs/N@C) que, en presencia de Cs_2CO_3, produce la oxidación simultánea de HMF y FFL, obteniendo FDCA y FCA, respectivamente. Dado que el Cs_2CO_3 actúa como base facilitando la deshidrogenación oxidativa del furfural (no se observa reacción en ausencia de este carbonato), se utilizó el mismo sistema para transformar directamente el FCA en FDCA. Después de 36 horas a 260°C, se obtuvo un rendimiento del 71.1 % de FDCA a partir del producto de oxidación de FFL con una selectividad cercana al 83 %. Estos resultados muestran una alta similitud con aquellos optimizados al usar FCA puro.

Wang y colaboradores realizaron un estudio completo sobre las condiciones de reacción en reactores de flujo de lecho fijo, analizando el efecto de Cs_2CO_3 y la relación FA-Cs, la temperatura, el tiempo de reacción y la presión de CO_2 sobre el rendimiento de FDCA [143], obteniendo resultados prometedores en concordancia con los valores reportados por otros autores. En este estudio, se alcanza un máximo de producción de FDCA con una relación molar de 3:5 (FDCA: Cs_2CO_3) (50.6 % de rendimiento a 270°C después de 3 horas), mientras que con excesos superiores la actividad se reduce. Los resultados por encima de 270°C muestran una descomposición de FCA-Cs en acetato, malonato y otros compuestos. El tiempo de reacción también es relevante, ya que a tiempos prolongados se genera tanta agua en el sistema de reacción que afecta la disociación de los reactivos, mientras que parte del Cs_2CO_3 se disuelve. Ambos fenómenos dificultan la reacción, definiendo un máximo a 3 horas cuando la reacción se lleva a cabo a 280°C con 8 bares de CO_2.

En resumen, diferentes estudios demuestran que la carboxilación heterogénea del ácido furóico es factible en ausencia de disolvente. Además de las ventajas mencionadas, esta reacción en fase sólido-gas se recomienda sobre la de fase líquida, ya que el uso de sales de metales alcalinos en lugar de catalizadores de metales de transición permite realizar la reacción utilizando CO_2 de pureza relativamente baja (calidad industrial), debido a que las sales de metales alcalinos son mucho más tolerantes a las impurezas que los metales de transición. Sin embargo, según el estado actual de la técnica, el proceso debe mejorarse sustituyendo del cesio por un elemento más económico o regenerando completamente la sal carbonatada para garantizar su total reutilización. Además, para una producción a escala industrial más grande, se deben mejorar las cinéticas de reacción, así como el control de algunos parámetros, como la transferencia de materia. Este tema se ha desarrollado en **Capítulo 4.7** de esta Tesis Doctoral.

Sin embargo, a pesar de los avances significativos en los procesos de carboxilación y la captura de CO_2, aún persisten desafíos importantes que deben abordarse de cara a futuro. Estos incluyen la mejora de la selectividad hacia los productos deseados, la optimización de la eficiencia energética y la escalabilidad de los procesos a nivel industrial.

1.6. REFERENCIAS

[1] Annual emissions of carbon dioxide (CO_2) by fuel or industry type (https://ourworldindata.org/emissions-by-fuel) Acceso: Agosto 2024

[2] Per capita plastic waste (https://ourworldindata.org/plastic-pollution) Acceso: Agosto 2024

[3] Objetivos de desarollo sostenible (https://www.un.org/sustainabledevelopment/es/2015/09/la-asamblea-general-adopta-la-agenda-2030-para-el-desarrollo-sostenible/) Acceso: Agosto 2024

[4] Naciones unidas: Acción por el clima (https://www.un.org/es/climatechange/paris-agreement) Acceso: Agosto 2024

[5] Plásticos - Situacion en 2022 (https://plasticseurope.org/es/wp-content/uploads/sites/4/2023/02/PLASTICOS-SITUACION-2022-esp.pdf) Acceso: Agosto 2024

[6] COP 28: What Was Achieved and What Happens Next? (https://unfccc.int/cop28/5-key-takeaways) Acceso: Agosto 2024

[7] Ollila, The Greenhouse Effect Definition, *Physical Science International Journal* **2019** (23) 1-5. https://doi.org/10.9734/psij/2019/v23i230149

[8] El efecto invernadero – Un modelo sobre el cambio climático (https://crea-portaldemedios.siemens-stiftung.org/vieworig/107114). Acceso: Agosto 2024

[9] K. Md. Zulfequar Ahmad, Causes and Consequences of Greenhouse Effect & Its Catastrophic Problems for Earth, *International Journal of Sustainability Management and Information Technologies* **2017** (3) 34-39. https://doi.org/10.11648/j.ijsmit.20170304.11

[10] CO2 and Greenhouse gas emissions (https://ourworldindata.org/co2-and-greenhouse-gas-emissions) Acceso: Julio 2024

[11] Statistical Review of World Energy (https://ourworldindata.org/grapher/oil-proved-reserves?time=latest) Acceso: Agosto 2024

[12] Annual plastic production between 1950 and 2019 and plastic use projections (https://ourworldindata.org/grapher/global-plastic-production-projections) Acceso:

[13] Global Plastics Outlook - Plastics waste in 2019 by region, polymer and application (https://ourworldindata.org/grapher/plastic-waste-polymer) Acceso: Julio 2024

[14] M.G. Kibria, N.I. Masuk, R. Safayet, H.Q. Nguyen, M. Mourshed, Plastic Waste: Challenges and Opportunities to Mitigate Pollution and Effective Management, *International Journal of Environmental Research* **2023** (17) 20. https://doi.org/10.1007/s41742-023-00507-z

[15] T. Chaturvedi, A.I. Torres, G. Stephanopoulos, M.H. Thomsen, J.E. Schmidt, Developing Process Designs for Biorefineries—Definitions, Categories, and Unit Operations, *Energies* **2020** (13). https://doi.org/10.3390/en13061493

[16] J.M.R. Gallo, M.A. Trapp, The chemical conversion of biomass-derived saccharides: An overview, *Journal of the Brazilian Chemical Society* **2017** (28) 1586-1607. https://doi.org/10.21577/0103-5053.20170009

[17] Y. Duan, A. Tarafdar, V. Kumar, P. Ganeshan, K. Rajendran, B. Shekhar Giri, R. Gómez-García, H. Li, Z. Zhang, R. Sindhu, P. Binod, A. Pandey, M.J. Taherzadeh, S. Sarsaiya, A. Jain, M. Kumar Awasthi, Sustainable biorefinery approaches towards circular economy for conversion

of biowaste to value added materials and future perspectives, *Fuel* **2022** (325) 124846. https://doi.org/10.1016/j.fuel.2022.124846

[18] A.F. Ferreira, Biorefinery Concept, *Biorefineries: Targeting Energy, High Value Products and Waste Valorisation*, **2017**, 1-20. https://doi.org/10.1007/978-3-319-48288-0_1

[19] E. de Jong, G. Jungmeier, Chapter 1 - Biorefinery Concepts in Comparison to Petrochemical Refineries, *Industrial Biorefineries & White Biotechnology*, **2015**, 3-33. https://doi.org/10.1016/B978-0-444-63453-5.00001-X

[20] Gupta, T. Sahni, S. Kumar, Biorefineries: An Analogue to Petroleum Refineries, *Paddy Straw Waste for Biorefinery Applications*, **2024**, 1-29. https://doi.org/10.1007/978-981-99-8224-0_1

[21] Bio-based and biodegradable plastics (https://plasticseurope.org/sustainability/climate/circular-feedstocks/bio-based-and-biodegradable-plastics/). Acceso: Agosto 2024

[22] L. Dai, O. Karakas, Y. Cheng, K. Cobb, P. Chen, R. Ruan, A review on carbon materials production from plastic wastes, *Chemical Engineering Journal* **2023** (453) 139725. https://doi.org/10.1016/j.cej.2022.139725

[23] G. Tang, W. Qiao, Z. Wang, F. Liu, L. He, M. Liu, W. Huang, H. Wu, C. Liu, Waste plastic to energy storage materials: a state-of-the-art review, *Green Chemistry* **2023** (25) 3738-3766. http://doi.org/10.1039/D2GC04927A

[24] Q.-L. Li, R. Shan, S.-X. Wang, H.-R. Yuan, Y. Chen, Production of carbon nanotubes via catalytic pyrolysis of waste plastics over Ni/Al2O3 catalyst: The influence of plastic types, *Journal of Analytical and Applied Pyrolysis* **2024** (177) 106318. https://doi.org/10.1016/j.jaap.2023.106318

[25] H. Zhou, Y. Ren, B. Yao, Z. Li, M. Xu, L. Ma, X. Kong, L. Zheng, M. Shao, H. Duan, Scalable electrosynthesis of commodity chemicals from biomass by suppressing non-Faradaic transformations, *Nature Communications* **2023** (14) 5621. http://doi.org/10.1038/s41467-023-41497-y

[26] G. Gómez Millán, S. Hellsten, J. Llorca, R. Luque, H. Sixta, A.M. Balu, Recent Advances in the Catalytic Production of Platform Chemicals from Holocellulosic Biomass, *ChemCatChem* **2019** (11) 2022-2042. https://doi.org/10.1002/cctc.201801843

[27] D.M. Alonso, J.Q. Bond, J.A. Dumesic, Catalytic conversion of biomass to biofuels, *Green Chemistry* **2010** (12) 1493-1513. https://doi.org/10.1039/C004654J

[28] K. Huang, W. Won, K.J. Barnett, Z.J. Brentzel, D.M. Alonso, G.W. Huber, J.A. Dumesic, C.T. Maravelias, Improving economics of lignocellulosic biofuels: An integrated strategy for coproducing 1,5-pentanediol and ethanol, *Applied Energy* **2018** (213) 585-594. https://doi.org/10.1016/j.apenergy.2017.11.002

[29] F. Hussin, N.N. Hazani, M. Khalil, M.K. Aroua, Environmental life cycle assessment of biomass conversion using hydrothermal technology: A review, *Fuel Processing Technology* **2023** (246) 107747. https://doi.org/10.1016/j.fuproc.2023.107747

[30] J. Rao, Z. Lv, G. Chen, F. Peng, Hemicellulose: Structure, chemical modification, and application, *Progress in Polymer Science* **2023** (140) 101675. https://doi.org/10.1016/j.progpolymsci.2023.101675

[31] C. T, S. Das, P. Das, V.D. Veeranki, A.A. Prabhu, Re-routing the hemicellulosic fraction of lignocellulosic biomass toward value added products: A pragmatic bio refinery approach,

Journal of Environmental Chemical Engineering **2024** (12) 111971. https://doi.org/10.1016/j.jece.2024.111971

[32] R. Saini, A. Kaur, J.K. Saini, A.K. Patel, S. Varjani, C.-W. Chen, R.R. Singhania, C.-D. Dong, Trends in Lignin Biotransformations for Bio-Based Products and Energy Applications, *BioEnergy Research* **2023** (16) 88-104. https://doi.org/10.1007/s12155-022-10434-0

[33] C.G. Yoo, X. Meng, Y. Pu, A.J. Ragauskas, The critical role of lignin in lignocellulosic biomass conversion and recent pretreatment strategies: A comprehensive review, *Bioresource Technology* **2020** (301) 122784. https://doi.org/10.1016/j.biortech.2020.122784

[34] R.-C. Sun, Lignin Source and Structural Characterization, *ChemSusChem* **2020** (13) 4385-4393. https://doi.org/10.1002/cssc.202001324

[35] I.U. Haq, K. Qaisar, A. Nawaz, F. Akram, H. Mukhtar, X. Zohu, Y. Xu, M.W. Mumtaz, U. Rashid, W.A. Ghani, T.S. Choong, Advances in Valorization of Lignocellulosic Biomass towards Energy Generation, *Catalysts* **2021** (11). https://doi.org/10.3390/catal11030309

[36] F. Güleç, A. Parthiban, G.C. Umenweke, U. Musa, O. Williams, Y. Mortezaei, H. Suk-Oh, E. Lester, C.C. Ogbaga, B. Gunes, J.A. Okolie, Progress in lignocellulosic biomass valorization for biofuels and value-added chemical production in the EU: A focus on thermochemical conversion processes, *Biofuels, Bioproducts and Biorefining* **2024** (18) 755-781. https://doi.org/10.1002/bbb.2544

[37] Ö. Tezer, N. Karabağ, A. Öngen, C.Ö. Çolpan, A. Ayol, Biomass gasification for sustainable energy production: A review, *International Journal of Hydrogen Energy* **2022** (47) 15419-15433. https://doi.org/10.1016/j.ijhydene.2022.02.158

[38] M. Ram, M.K. Mondal, Chapter 13 - Biomass gasification: a step toward cleaner fuel and chemicals, *Biofuels and Bioenergy*, **2022**, 253-276. https://doi.org/10.1016/B978-0-323-85269-2.00008-3

[39] L.J.R. Nunes, Biomass gasification as an industrial process with effective proof-of-concept: A comprehensive review on technologies, processes and future developments, *Results in Engineering* **2022** (14) 100408. https://doi.org/10.1016/j.rineng.2022.100408

[40] V. Dhyani, T. Bhaskar, A comprehensive review on the pyrolysis of lignocellulosic biomass, *Renewable Energy* **2018** (129) 695-716. https://doi.org/10.1016/j.renene.2017.04.035

[41] A.N. Amenaghawon, C.L. Anyalewechi, C.O. Okieimen, H.S. Kusuma, Biomass pyrolysis technologies for value-added products: a state-of-the-art review, *Environment, Development and Sustainability* **2021** (23) 14324-14378. https://doi.org/10.1007/s10668-021-01276-5

[42] Y. Zhang, Y. Liang, S. Li, Y. Yuan, D. Zhang, Y. Wu, H. Xie, K. Brindhadevi, A. Pugazhendhi, C. Xia, A review of biomass pyrolysis gas: Forming mechanisms, influencing parameters, and product application upgrades, *Fuel* **2023** (347) 128461. https://doi.org/10.1016/j.fuel.2023.128461

[43] M. El Bast, N. Allam, Y. Abou Msallem, S. Awad, K. Loubar, A review on continuous biomass hydrothermal liquefaction systems: Process design and operating parameters effects on biocrude, *Journal of the Energy Institute* **2023** (108) 101260. https://doi.org/10.1016/j.joei.2023.101260

[44] E. Ocampo, V.V. Beltrán, E.A. Gómez, L.A. Ríos, D. Ocampo, Hydrothermal liquefaction process: Review and trends, *Current Research in Green and Sustainable Chemistry* **2023** (7) 100382. https://doi.org/10.1016/j.crgsc.2023.100382

[45] R. Agrawal, A. Verma, R.R. Singhania, S. Varjani, C. Di Dong, A. Kumar Patel, Current understanding of the inhibition factors and their mechanism of action for the lignocellulosic biomass hydrolysis, *Bioresource Technology* **2021** (332) 125042. https://doi.org/10.1016/j.biortech.2021.125042

[46] T.H. Mokhothu, M.J. John, Review on hygroscopic aging of cellulose fibres and their biocomposites, *Carbohydrate Polymers* **2015** (131) 337-354. https://doi.org/10.1016/j.carbpol.2015.06.027

[47] S. Kang, J. Fu, G. Zhang, From lignocellulosic biomass to levulinic acid: A review on acid-catalyzed hydrolysis, *Renewable and Sustainable Energy Reviews* **2018** (94) 340-362. https://doi.org/10.1016/j.rser.2018.06.016

[48] A.A. Vaidya, K.D. Murton, D.A. Smith, G. Dedual, A review on organosolv pretreatment of softwood with a focus on enzymatic hydrolysis of cellulose, *Biomass Conversion and Biorefinery* **2022** (12) 5427-5442. http://doi.org/10.1007/s13399-022-02373-9

[49] C.A. Hubbell, A.J. Ragauskas, Effect of acid-chlorite delignification on cellulose degree of polymerization, *Bioresource Technology* **2010** (101) 7410-7415. https://doi.org/10.1016/j.biortech.2010.04.029

[50] Z. Zhou, D. Liu, X. Zhao, Conversion of lignocellulose to biofuels and chemicals via sugar platform: An updated review on chemistry and mechanisms of acid hydrolysis of lignocellulose, *Renewable and Sustainable Energy Reviews* **2021** (146) 111169. https://doi.org/10.1016/j.rser.2021.111169

[51] X. Shen, R. Sun, Recent advances in lignocellulose prior-fractionation for biomaterials, biochemicals, and bioenergy, *Carbohydrate Polymers* **2021** (261) 117884. https://doi.org/10.1016/j.carbpol.2021.117884

[52] W. Schutyser, T. Renders, S. Van den Bosch, S.F. Koelewijn, G.T. Beckham, B.F. Sels, Chemicals from lignin: an interplay of lignocellulose fractionation, depolymerisation, and upgrading, *Chemical Society Reviews* **2018** (47) 852-908. http://doi.org/10.1039/C7CS00566K

[53] K. Świątek, S. Gaag, A. Klier, A. Kruse, J. Sauer, D. Steinbach, Acid Hydrolysis of Lignocellulosic Biomass: Sugars and Furfurals Formation, *Catalysts* **2020** (10). https://doi.org/10.3390/catal10040437

[54] V. Oriez, J. Peydecastaing, P.-Y. Pontalier, Lignocellulosic Biomass Mild Alkaline Fractionation and Resulting Extract Purification Processes: Conditions, Yields, and Purities, *Clean Technologies* **2020** (2) 91-115. https://doi.org/10.3390/cleantechnol2010007

[55] Y. Yu, J. Wu, X. Ren, A. Lau, H. Rezaei, M. Takada, X. Bi, S. Sokhansanj, Steam explosion of lignocellulosic biomass for multiple advanced bioenergy processes: A review, *Renewable and Sustainable Energy Reviews* **2022** (154) 111871. https://doi.org/10.1016/j.rser.2021.111871

[56] H. Luo, E.P. Weeda, M. Alherech, C.W. Anson, S.D. Karlen, Y. Cui, C.E. Foster, S.S. Stahl, Oxidative Catalytic Fractionation of Lignocellulosic Biomass under Non-alkaline Conditions, *Journal of the American Chemical Society* **2021** (143) 15462-15470. https://doi.org/10.1021/jacs.1c08635

[57] P. Paulsen Thoresen, H. Lange, U. Rova, P. Christakopoulos, L. Matsakas, Role and importance of solvents for the fractionation of lignocellulosic biomass, *Bioresource Technology* **2023** (369) 128447. https://doi.org/10.1016/j.biortech.2022.128447

[58] M. Kabbour, R. Luque, Chapter 10 - Furfural as a platform chemical: From production to applications, *Biomass, Biofuels, Biochemicals*, **2020**, 283-297. https://doi.org/10.1016/B978-0-444-64307-0.00010-X

[59] H. Xia, S. Xu, H. Hu, J. An, C. Li, Efficient conversion of 5-hydroxymethylfurfural to high-value chemicals by chemo- and bio-catalysis, *RSC Advances* **2018** (8) 30875-30886. http://doi.org/10.1039/C8RA05308A

[60] E. Cousin, K. Namhaed, Y. Pérès, P. Cognet, M. Delmas, H. Hermansyah, M. Gozan, P.A. Alaba, M.K. Aroua, Towards efficient and greener processes for furfural production from biomass: A review of the recent trends, *Science of The Total Environment* **2022** (847) 157599. https://doi.org/10.1016/j.scitotenv.2022.157599

[61] C. Moreau, R. Durand, A. Roux, D. Tichit, Isomerization of glucose into fructose in the presence of cation-exchanged zeolites and hydrotalcites, *Applied Catalysis A: General* **2000** (193) 257-264. https://doi.org/10.1016/S0926-860X(99)00435-4

[62] Galadima, A. Masudi, O. Muraza, Conversion of cellulose to glucose and further transformation into fuels over solid acid catalysts: A mini review, *Microporous and Mesoporous Materials* **2022** (336) 111846. https://doi.org/10.1016/j.micromeso.2022.111846

[63] D. Garcés, E. Díaz, S. Ordóñez, Aqueous Phase Conversion of Hexoses into 5-Hydroxymethylfurfural and Levulinic Acid in the Presence of Hydrochloric Acid: Mechanism and Kinetics, *Industrial & Engineering Chemistry Research* **2017** (56) 5221-5230. https://doi.org/10.1021/acs.iecr.7b00952

[64] D. Garcés, L. Faba, E. Díaz, S. Ordóñez, Aqueous-Phase Transformation of Glucose into Hydroxymethylfurfural and Levulinic Acid by Combining Homogeneous and Heterogeneous Catalysis, *ChemSusChem* **2019** (12) 924-934. https://doi.org/10.1002/cssc.201802315

[65] L. Shuai, X. Pan, Hydrolysis of cellulose by cellulase-mimetic solid catalyst, *Energy & Environmental Science* **2012** (5) 6889-6894. https://doi.org/10.1039/C2EE03373A

[66] S. Van de Vyver, L. Peng, J. Geboers, H. Schepers, F. de Clippel, C.J. Gommes, B. Goderis, P.A. Jacobs, B.F. Sels, Sulfonated silica/carbon nanocomposites as novel catalysts for hydrolysis of cellulose to glucose, *Green Chemistry* **2010** (12) 1560-1563. https://doi.org/10.1039/C0GC00235F

[67] M.D. Kaufman Rechulski, M. Käldström, U. Richter, F. Schüth, R. Rinaldi, Mechanocatalytic Depolymerization of Lignocellulose Performed on Hectogram and Kilogram Scales, *Industrial & Engineering Chemistry Research* **2015** (54) 4581-4592. https://doi.org/10.1021/acs.iecr.5b00224

[68] J.B. Binder, R.T. Raines, Fermentable sugars by chemical hydrolysis of biomass, *Proceedings of the National Academy of Sciences* **2010** (107) 4516-4521. https://doi.org/10.1073/pnas.0912073107

[69] C. Li, Z.K. Zhao, Efficient Acid-Catalyzed Hydrolysis of Cellulose in Ionic Liquid, *Advanced Synthesis & Catalysis* **2007** (349) 1847-1850. https://doi.org/10.1002/adsc.200700259

[70] Bodachivskyi, U. Kuzhiumparambil, D. Bradley G. Williams, High Yielding Acid-Catalysed Hydrolysis of Cellulosic Polysaccharides and Native Biomass into Low Molecular Weight Sugars in Mixed Ionic Liquid Systems, *ChemistryOpen* **2019** (8) 1316-1324. https://doi.org/10.1002/open.201900283

[71] Bodachivskyi, U. Kuzhiumparambil, D.B.G. Williams, The role of the molecular formula of ZnCl2·nH2O on its catalyst activity: a systematic study of zinc chloride hydrates in the catalytic valorisation of cellulosic biomass, *Catalysis Science & Technology* **2019** (9) 4693-4701. https://doi.org/10.1039/C9CY00846B

[72] R. Brière, P. Loubet, E. Glogic, B. Estrine, S. Marinkovic, F. Jérôme, G. Sonnemann, Life cycle assessment of the production of surface-active alkyl polyglycosides from acid-assisted ball-

milled wheat straw compared to the conventional production based on corn-starch, *Green Chemistry* **2018** (20) 2135-2141. https://doi.org/10.1039/C7GC03189K

[73] Bodachivskyi, U. Kuzhiumparambil, D.B.G. Williams, Catalytic Valorization of Native Biomass in a Deep Eutectic Solvent: A Systematic Approach toward High-Yielding Reactions of Polysaccharides, *ACS Sustainable Chemistry & Engineering* **2020** (8) 678-685. https://doi.org/10.1021/acssuschemeng.9b06528

[74] F. Deng, A.S. Amarasekara, Catalytic upgrading of biomass derived furans, *Industrial Crops and Products* **2021** (159) 113055. https://doi.org/10.1016/j.indcrop.2020.113055

[75] Sádaba, M. Ojeda, R. Mariscal, J.L.G. Fierro, M.L. Granados, Catalytic and structural properties of co-precipitated Mg–Zr mixed oxides for furfural valorization via aqueous aldol condensation with acetone, *Applied Catalysis B: Environmental* **2011** (101) 638-648. https://doi.org/10.1016/j.apcatb.2010.11.005

[76] S. Eaimsumang, S. Wongkasemjit, S. Pongstabodee, S.M. Smith, S. Ratanawilai, N. Chollacoop, A. Luengnaruemitchai, Effect of synthesis time on morphology of CeO2 nanoparticles and Au/CeO2 and their activity in oxidative steam reforming of methanol, *Journal of Rare Earths* **2019** (37) 819-828. https://doi.org/10.1016/j.jre.2018.11.010

[77] R. Ciriminna, L. Albanese, F. Meneguzzo, M. Pagliaro, Hydrogen Peroxide: A Key Chemical for Today's Sustainable Development, *ChemSusChem* **2016** (9) 3374-3381. https://doi.org/10.1002/cssc.201600895

[78] D.Y. Murzin, E. Bertrand, P. Tolvanen, S. Devyatkov, J. Rahkila, K. Eränen, J. Wärnå, T. Salmi, Heterogeneous Catalytic Oxidation of Furfural with Hydrogen Peroxide over Sulfated Zirconia, *Industrial & Engineering Chemistry Research* **2020** (59) 13516-13527. https://doi.org/10.1021/acs.iecr.0c02566

[79] Q. Yu, R. Bai, F. Wang, Q. Zhang, Y. Sun, Y. Zhang, L. Qin, Z. Wang, Z. Yuan, A sustainable system for maleic acid synthesis from biomass-derived sugar, *Journal of Chemical Technology & Biotechnology* **2020** (95) 751-757. https://doi.org/10.1002/jctb.6260

[80] Y.N. Palai, A. Shrotri, A. Fukuoka, Selective Oxidation of Furfural to Succinic Acid over Lewis Acidic Sn-Beta, *ACS Catalysis* **2022** (12) 3534-3542. https://doi.org/10.1021/acscatal.1c05348

[81] V. Zvarych, A. Nakonechna, M. Marchenko, O. Khudyi, V. Lubenets, L. Khuda, O. Kushniryk, V. Novikov, Hydrogen Peroxide Oxygenation of Furan-2-carbaldehyde via an Easy, Green Method, *Journal of Agricultural and Food Chemistry* **2019** (67) 3114-3117. http://doi.org/10.1021/acs.jafc.8b06284

[82] J. Thuriot-Roukos, R. Khadraoui, S. Paul, R. Wojcieszak, Raman Spectroscopy Applied to Monitor Furfural Liquid-Phase Oxidation Catalyzed by Supported Gold Nanoparticles, *ACS Omega* **2020** (5) 14283-14290. http://doi.org/10.1021/acsomega.0c00091

[83] D.Y. Murzin, F. Saleem, J. Warnå, T. Salmi, Kinetic modelling of heterogeneous catalytic oxidation of furfural with hydrogen peroxide to succinic acid, *Chemical Engineering Journal* **2020** (382) 122811. https://doi.org/10.1016/j.cej.2019.122811

[84] N.D. Shcherban, R.Y. Barakov, S.A. Sergiienko, K. Eränen, J. Wärnå, D.Y. Murzin, Furfural Oxidation with Hydrogen Peroxide Over ZSM-5 Based Micro-Mesoporous Aluminosilicates, *Catalysis Letters* **2022** (152) 2920-2932. https://doi.org/10.1007/s10562-021-03899-9

[85] C. Ampelli, G. Centi, C. Genovese, G. Papanikolaou, R. Pizzi, S. Perathoner, R.J. van Putten, K.J.P. Schouten, A.C. Gluhoi, J.C. van der Waal, A Comparative Catalyst Evaluation for the Selective Oxidative Esterification of Furfural, *Topics in Catalysis* **2016** (59) 1659-1667. https://doi.org/10.1007/s11244-016-0675-y

[86] T. Pirmohamed, J.M. Dowding, S. Singh, B. Wasserman, E. Heckert, A.S. Karakoti, J.E.S. King, S. Seal, W.T. Self, Nanoceria exhibit redox state-dependent catalase mimetic activity, *Chemical Communications* **2010** (46) 2736-2738. https://doi.org/10.1039/B922024K

[87] Lolli, R. Amadori, C. Lucarelli, M.G. Cutrufello, E. Rombi, F. Cavani, S. Albonetti, Hard-template preparation of Au/CeO2 mesostructured catalysts and their activity for the selective oxidation of 5-hydroxymethylfurfural to 2,5-furandicarboxylic acid, *Microporous and Mesoporous Materials* **2016** (226) 466-475. https://doi.org/10.1016/j.micromeso.2016.02.014

[88] O. Casanova, S. Iborra, A. Corma, Biomass into Chemicals: Aerobic Oxidation of 5-Hydroxymethyl-2-furfural into 2,5-Furandicarboxylic Acid with Gold Nanoparticle Catalysts, *ChemSusChem* **2009** (2) 1138-1144. https://doi.org/10.1002/cssc.200900137

[89] T. Xie, S. Yue, T. Su, M. Song, W. Xu, Y. Xiao, Z. Yang, C. Len, D. Zhao, High selective oxidation of 5-hydroxymethyl furfural to 5-hydroxymethyl-2-furan carboxylic acid using Ag-TiO2, *Molecular Catalysis* **2022** (525) 112353. https://doi.org/10.1016/j.mcat.2022.112353

[90] Y. Cao, X. Liu, S. Iqbal, P.J. Miedziak, J.K. Edwards, R.D. Armstrong, D.J. Morgan, J. Wang, G.J. Hutchings, Base-free oxidation of glucose to gluconic acid using supported gold catalysts, *Catalysis Science & Technology* **2016** (6) 107-117. https://doi.org/10.1039/C5CY00732A

[91] Y.Y. Gorbanev, S. Kegnæs, A. Riisager, Effect of Support in Heterogeneous Ruthenium Catalysts Used for the Selective Aerobic Oxidation of HMF in Water, *Topics in Catalysis* **2011** (54) 1318. https://doi.org/10.1007/s11244-011-9754-2

[92] F. Nocito, M. Ventura, M. Aresta, A. Dibenedetto, Selective Oxidation of 5-(Hydroxymethyl)furfural to DFF Using Water as Solvent and Oxygen as Oxidant with Earth-Crust-Abundant Mixed Oxides, *ACS Omega* **2018** (3) 18724-18729. https://doi.org/10.1021/acsomega.8b02839

[93] L. Faba, E. Díaz, S. Ordóñez, Aqueous-phase furfural-acetone aldol condensation over basic mixed oxides, *Applied Catalysis B: Environmental* **2012** (113-114) 201-211. https://doi.org/10.1016/j.apcatb.2011.11.039

[94] R. López-Asensio, J.A. Cecilia-Buenestado, C. Herrera-Delgado, M.Á. Larrubia-Vargas, C. García-Sancho, P.J. Maireles-Torres, R. Moreno-Tost, Mixed Oxides Derived from Hydrotalcites Mg/Al Active in the Catalytic Transfer Hydrogenation of Furfural to Furfuryl Alcohol, *Catalysts* **2023** (13). https://doi.org/10.3390/catal13010045

[95] M. Douthwaite, X. Huang, S. Iqbal, P.J. Miedziak, G.L. Brett, S.A. Kondrat, J.K. Edwards, M. Sankar, D.W. Knight, D. Bethell, G.J. Hutchings, The controlled catalytic oxidation of furfural to furoic acid using AuPd/Mg(OH)2, *Catalysis Science & Technology* **2017** (7) 5284-5293. https://doi.org/10.1039/C7CY01025G

[96] P. Verdeguer, N. Merat, L. Rigal, A. Gaset, Optimization of experimental conditions for the catalytic oxidation of furfural to furoic acid, *Journal of Chemical Technology & Biotechnology* **1994** (61) 97-102. https://doi.org/10.1002/jctb.280610203

[97] C.P. Ferraz, A.G. Da Silva, T.S. Rodrigues, P.H. Camargo, S. Paul, R. Wojcieszak, Furfural Oxidation on Gold Supported on MnO2: Influence of the Support Structure on the Catalytic Performances, *Applied Sciences* **2018** (8). https://doi.org/10.3390/app8081246

[98] Q. Tian, D. Shi, Y. Sha, CuO and Ag2O/CuO Catalyzed Oxidation of Aldehydes to the Corresponding Carboxylic Acids by Molecular Oxygen, *Molecules* **2008** (13) 948-957. http://doi.org/10.3390/molecules13040948

[99] M. Lin, C. Mochizuki, T. Ishida, Y. Zhang, M. Haruta, T. Murayama, Effect of poly(N-vinylpyrrolidone) ligand on catalytic activities of Au nanoparticles supported on Nb2O5 for CO

oxidation and furfural oxidation, *Catalysis Today* **2023** (410) 143-149. https://doi.org/10.1016/j.cattod.2022.03.034

[100] R. Wojcieszak, C.P. Ferraz, J. Sha, S. Houda, L.M. Rossi, S. Paul, Advances in Base-Free Oxidation of Bio-Based Compounds on Supported Gold Catalysts, *Catalysts* **2017** (7). http://doi.org/10.3390/catal7110352

[101] Z. Ren, Y. Yang, S. Wang, X. Li, H. Feng, L. Wang, Y. Li, X. Zhang, M. Wei, Pt atomic clusters catalysts with local charge transfer towards selective oxidation of furfural, *Applied Catalysis B: Environmental* **2021** (295) 120290. https://doi.org/10.1016/j.apcatb.2021.120290

[102] C.P. Ferraz, S. Navarro-Jaén, L.M. Rossi, F. Dumeignil, M.N. Ghazzal, R. Wojcieszak, Enhancing the activity of gold supported catalysts by oxide coating: towards efficient oxidations, *Green Chemistry* **2021** (23) 8453-8457. https://doi.org/10.1039/D1GC02889H

[103] Y. Wu, Z. Guo, C. Sun, Y. Yang, Q. Li, Integrated experimental and DFT analysis on the efficient and green upgrading of agroforestry biomass derived furan chemicals over NiMoO4-CNTs-CF electrocatalyst with bi-catalytic sites, *Industrial Crops and Products* **2022** (187) 115492. https://doi.org/10.1016/j.indcrop.2022.115492

[104] F. Nocito, N. Ditaranto, D. Linsalata, M. Naschetti, R. Comparelli, M. Aresta, A. Dibenedetto, Selective Aerobic Oxidation of Furfural into Furoic Acid over a Highly Recyclable MnO2@CeO2 Core–Shell Oxide: The Role of the Morphology of the Catalyst, *ACS Sustainable Chemistry & Engineering* **2022** (10) 8615-8623. https://doi.org/10.1021/acssuschemeng.2c02341

[105] H. Luo, J. Barrio, N. Sunny, A. Li, L. Steier, N. Shah, I.E.L. Stephens, M.-M. Titirici, Progress and Perspectives in Photo- and Electrochemical-Oxidation of Biomass for Sustainable Chemicals and Hydrogen Production, *Advanced Energy Materials* **2021** (11) 2101180. https://doi.org/10.1002/aenm.202101180

[106] C. Xu, E. Paone, D. Rodríguez-Padrón, R. Luque, F. Mauriello, Recent catalytic routes for the preparation and the upgrading of biomass derived furfural and 5-hydroxymethylfurfural, *Chemical Society Reviews* **2020** (49) 4273-4306. https://doi.org/10.1039/D0CS00041H

[107] W. Yu, Y. Wang, H. Zhang, Q. Zhang, S. Wang, Z. Liu, G. Yang, F. Peng, Mechanistic Insights into the Selective Oxidation of 5-Hydroxymethylfurfural over Au/TiO2 Catalysts under Photoexcited and Dark States, *ACS Sustainable Chemistry & Engineering* **2023** (11) 13116-13125. https://doi.org/10.1021/acssuschemeng.3c03289

[108] H. Li, S. Wang, M. Wang, Y. Gao, J. Tang, S. Zhao, H. Chi, P. Zhang, J. Qu, F. Fan, C. Li, Enhancement of Plasmon-Induced Photoelectrocatalytic Water Oxidation over Au/TiO2 with Lithium Intercalation, *Angewandte Chemie International Edition* **2022** (61) e202204272. https://doi.org/10.1002/anie.202204272

[109] X. Wan, C. Zhou, J. Chen, W. Deng, Q. Zhang, Y. Yang, Y. Wang, Base-Free Aerobic Oxidation of 5-Hydroxymethyl-furfural to 2,5-Furandicarboxylic Acid in Water Catalyzed by Functionalized Carbon Nanotube-Supported Au–Pd Alloy Nanoparticles, *ACS Catalysis* **2014** (4) 2175-2185. https://doi.org/10.1021/cs5003096

[110] S. Hameed, L. Lin, A. Wang, W. Luo, Recent Developments in Metal-Based Catalysts for the Catalytic Aerobic Oxidation of 5-Hydroxymethyl-Furfural to 2,5-Furandicarboxylic Acid, *Catalysts* **2020** (10). https://doi.org/10.3390/catal10010120

[111] P. Verdeguer, N. Merat, A. Gaset, Oxydation catalytique du HMF en acide 2,5-furane dicarboxylique, *Journal of Molecular Catalysis* **1993** (85) 327-344. https://doi.org/10.1016/0304-5102(93)80059-4

[112] Villa, M. Schiavoni, S. Campisi, G.M. Veith, L. Prati, Pd-modified Au on Carbon as an Effective and Durable Catalyst for the Direct Oxidation of HMF to 2,5-Furandicarboxylic Acid, *ChemSusChem* **2013** (6) 609-612. https://doi.org/10.1002/cssc.201200778

[113] C.A. Antonyraj, N.T.T. Huynh, S.-K. Park, S. Shin, Y.J. Kim, S. Kim, K.-Y. Lee, J.K. Cho, Basic anion-exchange resin (AER)-supported Au-Pd alloy nanoparticles for the oxidation of 5-hydroxymethyl-2-furfural (HMF) into 2,5-furan dicarboxylic acid (FDCA), *Applied Catalysis A: General* **2017** (547) 230-236. https://doi.org/10.1016/j.apcata.2017.09.012

[114] L. Yu, H. Chen, Z. Wen, M. Jin, Z. Ma, X. Ma, Y. Sang, M. Chen, Y. Li, Highly selective oxidation of 5-hydroxymethylfurfural to 2,5-diformylfuran over an α-MnO2 catalyst, *Catalysis Today* **2021** (367) 9-15. https://doi.org/10.1016/j.cattod.2020.10.037

[115] Z. Li, L. Zhao, B. Li, S. Bian, J. Wang, H. Zhang, C. Zhao, Base metal catalyzed oxidation of 5-hydroxy-methyl-furfural to 2,5-furan-dicarboxylic acid: A review, *Catalysis Today* **2023** (408) 64-72. https://doi.org/10.1016/j.cattod.2022.09.002

[116] B.N. Zope, D.D. Hibbitts, M. Neurock, R.J. Davis, Reactivity of the Gold/Water Interface During Selective Oxidation Catalysis, *Science* **2010** (330) 74-78. https://doi.org/10.1126/science.1195055

[117] T. Mallat, A. Baiker, Oxidation of Alcohols with Molecular Oxygen on Solid Catalysts, *Chemical Reviews* **2004** (104) 3037-3058. https://doi.org/10.1021/cr0200116

[118] D. Yan, J. Xin, Q. Zhao, K. Gao, X. Lu, G. Wang, S. Zhang, Fe–Zr–O catalyzed base-free aerobic oxidation of 5-HMF to 2,5-FDCA as a bio-based polyester monomer, *Catalysis Science & Technology* **2018** (8) 164-175. https://doi.org/10.1039/C7CY01704A

[119] S. Liu, Y. Zhu, Y. Liao, H. Wang, Q. Liu, L. Ma, C. Wang, Advances in understanding the humins: Formation , prevention and application, *Applications in Energy and Combustion Science* **2022** (10) 100062. https://doi.org/10.1016/j.jaecs.2022.100062

[120] P. Rapado, D. Garcés, L. Faba, S. Ordóñez, Zeolite-assisted acid hydrolysis of cellulose: Optimization of reaction conditions and chemical pretreatments for enhancing HMF yields, *Industrial Crops and Products* **2024** (212) 118309. https://doi.org/10.1016/j.indcrop.2024.118309

[121] R. Wojcieszak, I. Itabaiana, Engineering the future: Perspectives in the 2,5-furandicarboxylic acid synthesis, *Catalysis Today* **2020** (354) 211-217. https://doi.org/10.1016/j.cattod.2019.05.071

[122] Q.N.B. Nguyen, H.A.N. Le, P.D. Ly, H.B. Phan, P.H. Tran, One-step synthesis of 2,5-diformylfuran from monosaccharides by using lanthanum(iii) triflate, sulfur, and DMSO, *Chemical Communications* **2020** (56) 13005-13008. https://doi.org/10.1039/D0CC05582D

[123] W. Wei, G. Lyu, W. Jiang, Z. Chen, S. Wu, High-efficiency synthesis of 5-hydroxymethylfurfural and 2,5-diformylfuran from fructose over magnetic separable catalysts, *Journal of Colloid and Interface Science* **2021** (602) 146-158. https://doi.org/10.1016/j.jcis.2021.05.161

[124] G. Yi, S.P. Teong, Y. Zhang, The Direct Conversion of Sugars into 2,5-Furandicarboxylic Acid in a Triphasic System, *ChemSusChem* **2015** (8) 1151-1155. https://doi.org/10.1002/cssc.201500118

[125] F. Wang, L. Jiang, J. Wang, Z. Zhang, Catalytic Conversion of Fructose and 5-Hydroxymethylfurfural into 2,5-Diformylfuran over SBA-15 Supported Ruthenium Catalysts, *Energy & Fuels* **2016** (30) 5885-5892. https://doi.org/10.1021/acs.energyfuels.6b01148

[126] Z. Yang, W. Qi, R. Su, Z. He, 3D Flower-like Micro/Nano Ce–Mo Composite Oxides as Effective Bifunctional Catalysts for One-Pot Conversion of Fructose to 2,5-Diformylfuran, *ACS Sustainable Chemistry & Engineering* **2017** (5) 4179-4187. https://doi.org/10.1021/acssuschemeng.7b00175

[127] D. Steinbach, A. Kruse, J. Sauer, Pretreatment technologies of lignocellulosic biomass in water in view of furfural and 5-hydroxymethylfurfural production- A review, *Biomass Conversion and Biorefinery* **2017** (7) 247-274. https://doi.org/10.1007/s13399-017-0243-0

[128] Y. Zhao, K. Lu, H. Xu, L. Zhu, S. Wang, A critical review of recent advances in the production of furfural and 5-hydroxymethylfurfural from lignocellulosic biomass through homogeneous catalytic hydrothermal conversion, *Renewable and Sustainable Energy Reviews* **2021** (139) 110706. https://doi.org/10.1016/j.rser.2021.110706

[129] S.P. Verevkin, V.N. Emel’yanenko, E.N. Stepurko, R.V. Ralys, D.H. Zaitsau, A. Stark, Biomass-Derived Platform Chemicals: Thermodynamic Studies on the Conversion of 5-Hydroxymethylfurfural into Bulk Intermediates, *Industrial & Engineering Chemistry Research* **2009** (48) 10087-10093. https://doi.org/10.1021/ie901012g

[130] V.N. Emel'yanenko, A. Dabrowska, M.O. Hertel, H. Scheuren, K. Sommer, Vapor Pressures, Enthalpies of Vaporization, and Limiting Activity Coefficients in Water at 100 °C of 2-Furanaldehyde, Benzaldehyde, Phenylethanal, and 2-Phenylethanol, *Journal of Chemical & Engineering Data* **2007** (52) 468-471. https://doi.org/10.1021/je060406c

[131] Banerjee, G.R. Dick, T. Yoshino, M.W. Kanan, Carbon dioxide utilization via carbonate-promoted C–H carboxylation, *Nature* **2016** (531) 215-219. https://doi.org/10.1038/nature17185

[132] D.M. Dalton, T. Rovis, C–H carboxylation takes gold, *Nature Chemistry* **2010** (2) 710-711. https://doi.org/10.1038/nchem.815

[133] M.M. Cajnko, U. Novak, M. Grilc, B. Likozar, Enzymatic conversion reactions of 5-hydroxymethylfurfural (HMF) to bio-based 2,5-diformylfuran (DFF) and 2,5-furandicarboxylic acid (FDCA) with air: mechanisms, pathways and synthesis selectivity, *Biotechnology for Biofuels* **2020** (13) 66. https://doi.org/10.1186/s13068-020-01705-z

[134] B. Lupa, D. Lyon, M.D. Gibbs, R.A. Reeves, J. Wiegel, Distribution of genes encoding the microbial non-oxidative reversible hydroxyarylic acid decarboxylases/phenol carboxylases, *Genomics* **2005** (86) 342-351. https://doi.org/10.1016/j.ygeno.2005.05.002

[135] K.A.P. Payne, S.A. Marshall, K. Fisher, M.J. Cliff, D.M. Cannas, C. Yan, D.J. Heyes, D.A. Parker, I. Larrosa, D. Leys, Enzymatic Carboxylation of 2-Furoic Acid Yields 2,5-Furandicarboxylic Acid (FDCA), *ACS Catalysis* **2019** (9) 2854-2865. https://doi.org/10.1021/acscatal.8b04862

[136] J.A. Gibson, W. Kynaston, A.S. Lindsey, The infrared spectra of some pyridones and quinolones and their behaviour in the Kolbe–Schmitt reaction, *Journal of the Chemical Society (Resumed)* **1955** 4340-4344. https://doi.org/10.1039/JR9550004340

[137] Y. Dingyi, Z. Yugen, The direct carboxylation of terminal alkynes with carbon dioxide, *Green Chemistry* **2011** (13) 1275-1279. https://doi.org/10.1039/C0GC00819B

[138] K. Kudo, M. Shima, Y. Kume, F. Ikoma, S. Mori, N. Sugita, Carboxylation of Cesium 2-Naphthoate in the Alkali Metal Molten Salts of Carbonate and Formate with CO2 under High Pressure, *Journal of the Japan Petroleum Institute* **1995** (38) 40-47. https://doi.org/10.1627/jpi1958.38.40

[139] F. Nocito, N. Ditaranto, A. Dibenedetto, Valorization of C5 polyols by direct carboxylation to FDCA: Synthesis and characterization of a key intermediate and role of carbon dioxide, *Journal of CO2 Utilization* **2019** (32) 170-177. https://doi.org/10.1016/j.jcou.2019.04.013

[140] F. Drault, Y. Snoussi, S. Paul, I. Itabaiana Jr, R. Wojcieszak, Recent Advances in Carboxylation of Furoic Acid into 2,5-Furandicarboxylic Acid: Pathways towards Bio-Based Polymers, *ChemSusChem* **2020** (13) 5164-5172. https://doi.org/10.1002/cssc.202001393

[141] G.R. Dick, A.D. Frankhouser, A. Banerjee, M.W. Kanan, A scalable carboxylation route to furan-2,5-dicarboxylic acid, *Green Chemistry* **2017** (19) 2966-2972. https://doi.org/10.1039/C7GC01059A

[142] H. Zhou, H. Xu, X. Wang, Y. Liu, Convergent production of 2,5-furandicarboxylic acid from biomass and CO2, *Green Chemistry* **2019** (21) 2923-2927. https://doi.org/10.1039/C9GC00869A

[143] Y.-G. Wang, C.-Y. Guo, J. Shen, Y.-Q. Sun, Y.-X. Niu, P. Li, G. Liu, X.-Y. Wei, A sustainable and green route to furan-2,5-dicarboxylic acid by direct carboxylation of 2-furoic acid and CO2, *Journal of CO2 Utilization* **2021** (48) 101524. https://doi.org/10.1016/j.jcou.2021.101524

2. OBJETIVOS

El objetivo de esta Tesis Doctoral es el desarrollo y optimización de un proceso catalítico que permita la obtención de ácido 2,5-furandicarboxílico a partir de biomasa residual mediante una secuencia de tres etapas en serie que incluye la hidrólisis ácida de biomasa, la oxidación de los aldehídos y la carboxilación del ácido furoico. Dada la complejidad del proceso a estudiar, se han establecido objetivos parciales (agrupados según las etapas del proceso) que, conjuntamente, permiten avanzar en la comprensión y aplicación de procesos sostenibles para la producción de materiales biodegradables y biocompatibles, en este caso un monómero para la obtención de bioplásticos, a partir de materias primas renovables e incluyendo una última etapa de captura de CO_2.

Hidrólisis ácida de biomasa lignocelulósica:

- Optimización de las condiciones de operación para maximizar la obtención de 5-HMF a partir de celulosa microcristalina. Se utilizará este polímero comercial como estándar para determinar el mecanismo y el modelo cinético del proceso de hidrólisis con catálisis homogénea y heterogénea, mediante un estudio riguroso sobre la influencia de la temperatura, concentración de catalizador y tiempo de reacción. Igualmente, se analizará la influencia de diferentes pretratamientos que permitan una degradación parcial de la estructura recalcitrante de la celulosa, favoreciendo la producción del 5-HMF.
- Optimización de las condiciones de operación para maximizar la obtención de furfural y 5-HMF a partir de serrín de pino. Se evaluará la extrapolación de las condiciones óptimas

definidas con anterioridad a una matriz real, serrín de pino. En base a los resultados experimentales, se estudiará en profundidad la influencia de los principales parámetros de operación en la productividad de los aldehídos de interés (pretratamientos, temperatura, carga catalítica), haciendo hincapié en las diferencias obtenidas respecto a los estudios previos con celulosa, de forma que se determine el papel de la lignina y la hemicelulosa en el proceso.

Oxidación de furfural y 5-HMF:

- Desarrollo del mecanismo de reacción y optimización de las condiciones de operación para maximizar la obtención de ácido furoico a partir de furfural. Se llevará a cabo un estudio sistemático y detallado de la oxidación catalítica de furfural empleando dos tipos de oxidantes, peróxido de hidrógeno y oxígeno molecular. La actividad de diversos catalizadores de metales nobles soportados sobre materiales con diferentes propiedades ácidas, básicas y redox se analizará en función de las condiciones de reacción (temperatura, presión, concentración de furfural y pH), permitiendo determinar el mecanismo y las etapas cinéticamente controlantes en este proceso.

- Optimización de las condiciones de operación para maximizar la obtención de ácido 2,5-furandicarboxílico a partir de 5-hidroximetilfurfural y fructosa. Los estudios referidos a la oxidación del HMF partirán de las conclusiones obtenidas durante la oxidación de furfural (catalizador y agente oxidante). En este caso, dada la mayor inestabilidad química del HMF (formación de huminas, tendencia a la descomposición), se reevaluarán las condiciones de operación (temperatura, presión), con especial atención al pH. Una vez optimizada esta etapa, se explorará la posibilidad de obtener el FDCA directamente a partir de fructosa, mediante un proceso en una sola etapa, analizando la aplicabilidad de los mecanismos y resultados cinéticos obtenidos en los estudios individuales de hidrólisis y oxidación.

- Producción simultánea de ácido furoico y FDCA a partir de mezclas de furfural y HMF. Se evaluará la oxidación simultánea de ambos aldehídos, en un avance hacia un sistema realista en el cual se pudiera prescindir de la etapa de purificación tras la hidrólisis. Tomando como punto de partida los resultados obtenidos en las optimizaciones individuales, se realizarán las adaptaciones necesarias en términos de composición de la mezcla (ratio furfural/HMF y grado de dilución) y condiciones de operación.

Carboxilación de ácido furoico:

- Selección de rutas químicas para la carboxilación de FCA a FDCA. Se llevará a cabo un análisis crítico de las diferentes rutas y condiciones de reacción para llevar a cabo la carboxilación de ácido furoico haciendo hincapié en las ventajas y desventajas de cada enfoque. Ello permitirá identificar posibles oportunidades para desarrollar estrategias de mejora que permitan aumentar la eficacia del proceso o simplificar las condiciones de operación para aumentar la sostenibilidad de esta etapa.
- Desarrollo de nuevas estrategias para la carboxilación. Se plantearán experimentos a baja presión para facilitar el acople de la reacción a un sistema de captura de CO_2. En otra línea de trabajo, se propondrá una configuración en fase líquida, evaluando posibles disolventes y planteando la posible sustitución total o parcial del cesio, metal utilizado en bibliografía para generar la sal fundente que encarece significativamente el proceso.

3. METODOLOGÍA EXPERIMENTAL

3.1. REACTIVOS Y CATALIZADORES COMERCIALES

Para el desarrollo de esta Tesis Doctoral se han empleado diferentes reactivos y catalizadores comerciales. Como reactivos se emplean: celulosa microcristalina (Sigma Aldrich, CAS: 9004-34-6), serrín de pino (carpintería local), fructosa (≥99.5%, Panreac Applichem), furfural (≥99%, Sigma Aldrich), 5-hidroximetilfurfural (≥99%, Sigma Aldrich), ácido furoico (≥98%, Sigma Aldrich) y carbonato de cesio (≥99%, Sigma Aldrich). Como catalizadores se emplean: HCl (49-51%, Panreac Applichem) y zeolita β (Zeolyst International, CP814E, SiO_2/Al_2O_3=25).

3.2. SÍNTESIS DE CATALIZADORES

En este apartado de la Tesis Doctoral se describen las síntesis de los catalizadores no comerciales utilizados a lo largo de la tesis, agrupados por apartados según las etapas del proceso en las que son utilizados (hidrólisis y oxidación).

3.2.1. Catalizadores empleados en las reacciones de hidrólisis

En los experimentos de hidrólisis se emplea zeolita β comercial. Esta zeolita comercial se suministra en su forma catiónica NH_4^+, la cual no es activa desde el punto de vista catalítico. Para activarla, se somete a un tratamiento térmico en mufla con un gradiente de temperatura de 1 °C min^{-1} hasta 550 °C, manteniendo esta temperatura constante durante 12 horas para eliminar los grupos funcionales NH_4^+ y obtener así la forma protonada y activa para este tipo de reacciones. Este protocolo de activación ha sido previamente utilizado por otros autores en la bibliografía [1].

3.2.2. Catalizadores empleados para los estudios de oxidación

Para llevar a cabo las reacciones de oxidación de FFL, se ha realizado una selección de catalizadores bifuncionales (metal + soporte) sintetizados en el laboratorio. En concreto, en base a la bibliografía se utilizan cuatro soportes con diferentes propiedades catalíticas: TiO_2 y CeO_2 como ejemplos de materiales redox [2,3], y MgAl y MgZr como óxidos mixtos típicos con sitios ácidos y básicos [4,5]. Para potenciar la actividad catalítica, se preparan materiales bifuncionales (con una carga metálica de un 1% en peso) con Au, Pd y Pt, tres de los metales más utilizados en oxidaciones [6,7]. En base a los resultados obtenidos, se selecciona Au/TiO_2 como el catalizador con mejores resultados sobre el cual se continua la investigación de oxidación de HMF. A continuación, se detalla el protocolo seguido para la síntesis de los soportes y el procedimiento experimental utilizado para la impregnación de los metales en la superficie de estos.

- Óxido de titanio (TiO_2). El óxido de titanio utilizado para llevar a cabo estas reacciones posee un 25% de la fase cristalina rutilo y un 75% de anatasa, se trata de un material comercial con un 99% de pureza adquirido en Sigma Aldrich. Para activar la superficie del material se somete a un proceso de calcinación en flujo de aire durante 2h con una rampa de 5°C min^{-1} hasta 500°C [8].

- Óxido de cerio (CeO_2). El óxido de cerio se sintetiza de acuerdo con el procedimiento propuesto por Eaimsumang *et al.* a partir de una sal precursora, en este caso nitrato de amonio y cerio (IV) [9]. Junto a esta sal, se utiliza un surfactante catiónico, el bromuro de hexadeciltrimetilamonio (CTAB), que ayuda a la correcta síntesis del óxido de cerio. Se utiliza una mezcla con una relación molar 2:3 respectivamente. Esta mezcla se disuelve en agua y amoniaco en disolución al 28%, empleándose un ratio volumétrico 5:1. La disolución resultante se introduce en un reactor discontinuo de tanque agitado (Autoclave Engineers EZE Seal), donde se le somete a agitación suave y se aumenta la temperatura hasta 100°C durante 2 h. El sólido resultante se lava con agua desionizada y acetona y se filtra para posteriormente secarse durante 24 h en un horno a 80 °C. El material una vez seco se tamiza y se calcina en una mufla a 400 °C durante 4h para así obtener el CeO_2.

- Óxido mixto de magnesio y aluminio ($MgO-Al_2O_3$). La síntesis de este soporte se realiza siguiendo un procedimiento de co-precicipitación a sobresaturación (pH 10-12) controlada con ultrasonidos desarrollado por Larina *et al.* [10]. Se emplea un reactor de vidrio que posee un encamisado de agua suspendido sobre un baño de ultrasonidos. Se añaden gota a gota disoluciones 1 M de $Mg(NO_3)_2 \cdot 6H_2O$ (Sigma Aldrich, 98%) y $Al(NO_3)_3 \cdot 9H_2O$ (Sigma Aldrich, 99%) en proporción 2:1 sobre 200 ml de una disolución tampón que contiene NaOH 1.6 M y Na_2CO_3 0.1 M bajo agitación vigorosa a una temperatura de 85°C. Posteriormente, la mezcla se somete a un proceso de envejecimiento a 85°C durante 24 h en un baño con agitación leve. El sólido resultante se filtra y se lava para eliminar los restos de sales o iones Na^+ y se tamiza entre 50-80 μm. Las hidrotalcitas resultantes se calcinan a 700 ºC durante 5 h en flujo de aire para obtener óxidos mixtos.

- Óxido mixto de magnesio y zirconio ($MgO-ZrO_3$). Este soporte se sintetiza empleando la técnica sólido-gel propuesta por Aramendía y colaboradores [11]. Se disuelven 51 g de $Mg(NO_3)_2 \cdot 6H_2O$ y 4g de $Zr(NO_3)_2$ (Sigma Aldrich, 98%) en agua desionizada lo que supone una relación Mg/Zr=4. La mezcla se agita a temperatura ambiente y se agrega NaOH (25% en peso) hasta alcanzar un pH de 10 mientras se forma un sólido blanquecino. El gel resultante se envejece a 85 ºC durante 24h en un baño con agitación leve y posteriormente se filtra y se lava hasta obtener un pH de 7 para eliminar todos los iones de las disoluciones empleadas que hayan podido quedar retenidos sobre la superficie del catalizador. El gel obtenido se seca a 100 °C durante 24h y se tamiza para obtener un tamaño de partícula homogéneo (50-80μm). Finalmente, se calcina el sólido en un flujo de aire en exceso hasta 600 °C con una rampa de 5 °C min^{-1} que se mantiene durante 3h.

Impregnación de la fase metálica: Pd, Pt y Au

Los catalizadores modificados con Pd y Pt (1% en peso como carga metálica teórica) se preparan utilizando el método de impregnación seca. Esta técnica se basa en disolver el precursor metálico en un volumen de agua desionizada igual al volumen de poros del material utilizado como soporte. La adicción se hace gota a gota y agitando el catalizador constantemente para evitar sobresaturaciones locales del metal. Sin necesidad de lavado previo, el sólido resultante se seca en una estufa a 100°C durante 24h. Concretamente, se utiliza $Pd(NH_3)_4(NO_3)_2$ como precursor de Pd y $Pt(NH_3)_4(NO_3)_2$ como precursor de Pt (ambos adquiridos por Sigma Aldrich, >99.99%). Los catalizadores obtenidos se calcinan en aire a la misma temperatura que se calcina cada soporte previamente y se reducen en flujo de H_2 a 400 ºC durante 4h (en todos los casos, temperatura se alcanza con una rampa de 5 $ºC\cdot min^{-1}$)

El Au se deposita con una concentración de un 1% en peso en los diferentes soportes mediante el método de deposición-precipitación utilizando $HAuCl_4\cdot 3H_2O$ (Sigma Aldrich, 99%) como precursor en presencia de urea [8]. Todos los catalizadores se calcinan durante 3 h a la misma temperatura que sus correspondientes soportes (es decir, 400, 500, 600 y 700°C para CeO_2, TiO_2, MgZr y MgAl, respectivamente). Para garantizar la reducción del metal, los catalizadores se reducen en H_2 durante 4 h, a 300 ºC con una rampa de 5 $ºC\cdot min^{-1}$ [12].

3.3. TÉCNICAS DE CARACTERIZACIÓN DE LOS MATERIALES UTILIZADOS

Una vez preparados los diferentes materiales se debe proceder con su caracterización para relacionar sus propiedades morfológicas, superficiales y fisicoquímicas con su actividad catalítica. Para ello, se emplean diversas técnicas espectroscópicas y analíticas cuyo fundamento teórico se detalla a continuación junto la descripción del equipo y del procedimiento experimental empleado en cada caso.

3.3.1. Técnicas de adsorción-desorción

Cuando una molécula de gas se encuentra con una superficie sólida, puede rebotar o quedar fijada sobre la superficie, es decir, sufrir adsorción. Se define la adsorción como el proceso de unión de una molécula gaseosa sobre la superficie de un sólido. Por el contrario, la desorción es el proceso inverso a la adsorción. Se distingue entre dos comportamientos en la adsorción: la fisisorción y quimisorción. En la adsorción física o fisisorción, las moléculas del gas se mantienen unidas a la superficie del sólido por medio de fuerzas de Van der Waals (interacciones dipolares). Este hecho define todas las características propias de la fisisorción ya que se trata de una interacción débil. Es un proceso exotérmico en el que las moléculas fisisorbidas mantienen su naturaleza química. Además, la fisisorción se puede producir en multicapas, es decir, sobre una capa de gas fisisorbida puede adsorberse otra. Por otro lado, en el caso de la adsorción química o quimisorción, las moléculas de gas se mantienen unidas a la superficie formando un enlace químico fuerte por lo que se trata de una interacción más fuerte que la fisisorción. Las entalpías de quimisorción son mucho mayores que las de fisisorción y del orden de las que se liberan en la formación de enlaces químicos, es decir, semejante a una reacción química. Dado que implica la formación de un enlace entre adsorbato y el adsorbente, el proceso se detiene tras la formación de una monocapa sobre la superficie.

Durante el desarrollo de esta Tesis Doctoral, se han realizado ensayos de fisisorción y quimisorción de los catalizadores empleados. Ambos tipos de técnicas se han llevado a cabo en el mismo equipo, en concreto en un Micromeritics ASAP 2020, que dispone de la posibilidad de realizar ambos análisis (**Figura 3.1**).

Figura 3.1. Equipos utilizados para la fisisorción de nitrógeno (A) y para la quimisorción de H_2 y CO (B). Micromeritics ASAP 2020

Fisorción de nitrógeno

La técnica de fisisorción de gases es la más extendida para la determinación de áreas superficiales y distribución de tamaños de poros en sólidos. Esta técnica se basa en la adsorción generalmente de nitrógeno a 77 K. Las isotermas obtenidas (representación del volumen de nitrógeno fisisorbido en el sólido respecto a la presión relativa de nitrógeno) corresponden al proceso de adsorción y desorción del gas en el sólido, produciéndose histéresis cuando la isoterma de adsorción no coincide con la de desorción. Los sólidos se pueden clasificar en función del tipo de isotermas que presenten. Las isotermas de adsorción, mayoritariamente, se pueden agrupar en seis tipos diferentes (**Figura 3.2**):

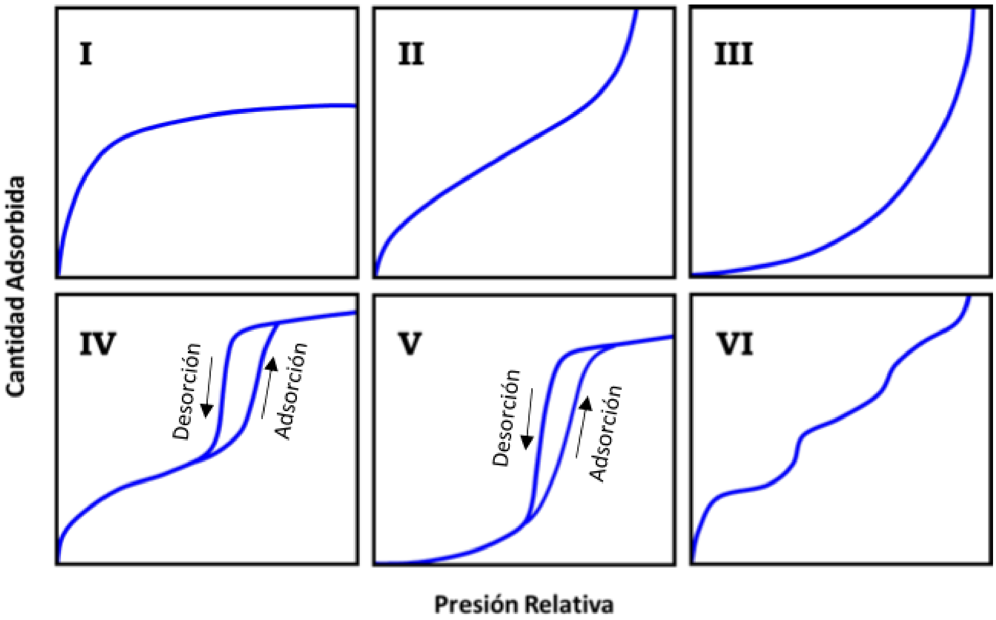

Figura 3.2. Isotermas de adsorción. Adaptada de Sing *et al.* [13]

- Isoterma de tipo I. denominado isoterma de Langmuir, corresponde a una adsorción en monocapa. La cantidad adsorbida aumenta con P hasta alcanzar un valor límite correspondiente al recubrimiento de la superficie por una monocapa. Es la isoterma característica de los sólidos microporosos.

- Isoterma de tipo II. es indicativo de una adsorción física en multicapa. El rápido ascenso inicial corresponde a la formación de la primera capa, que tiene en este caso una constante de formación mayor que para el resto de las capas. Al seguir aumentando la presión se forma la segunda capa de moléculas adsorbidas, seguida de otras más. Características de los materiales macroporosos.

- Isoterma de tipo III. corresponde también a una adsorción física en multicapas, pero donde la constante de equilibrio de formación de la primera capa es igual que para las siguientes, es decir, donde la interacción entre adsorbato y adsorbente es baja.

- Isoterma de tipo IV. La máxima extensión de la adsorción se produce antes de alcanzar la presión de saturación. Típica de materiales mesoporosos. Se produce un ciclo de histéresis debido a la condensación en los macroporos.

- Isoterma de tipo V. Se corresponde con una adsorción débil que presenta un ciclo de histéresis debido a la condensación. Es una variación de la isoterma tipo III.

- Isoterma de tipo VI. Es un tipo de adsorción en escalones donde cada escalón representa una capa fisisorbida. Este tipo de adsorción ocurre solo para solidos con una superficie no porosa muy uniforme, es poco frecuente.

Durante procedimiento experimental, se debe pesar el tubo que contiene la muestra y llevar a cabo a un proceso de desgasificación a vacío hasta 10 mm de Hg y a una temperatura que permita eliminar las impurezas de los poros del material (250 ºC durante 4h). A continuación, se pesa de nuevo el tubo de muestra y se especifica la masa empleada después de la desgasificación. La masa inicial debe garantizar un mínimo de 200 m^2 de superficie específica para asegurar la máxima sensibilidad y el funcionamiento óptimo del equipo. El análisis se lleva a cabo 77 K y aplica automáticamente las distintas presiones parciales de nitrógeno hasta alcanzar el equilibrio, que se corresponde con el momento en el que la presión en el interior del tubo portamuestras no varía. Es decir, el momento en el que, para dicha presión parcial, el adsorbente no admite más adsorbato en su superficie. Una vez finalizado el análisis, se emplea el rango de presiones de $0.05<P/P_0<0.35$ para determinar la superficie específica a través de la teoría de Brunauer, Emmet y Teller (BET) y aplica el modelo de Barret, Joyner y Halenda (BJH) a la curva de desorción de nitrógeno para obtener el volumen y el diámetro de mesoporos.

Quimisorción de hidrógeno y CO

La quimisorción es el término que se aplica a la interacción de superficies sólidas con gases cuando esta da lugar a la formación de enlaces químicos. Esta técnica se emplea para el cálculo de la dispersión metálica (**Ec 3.1**) y el tamaño de la cristalita en los catalizadores de metal reducido soportados, mediante adsorción específica de determinados gases. Durante el desarrollo de esta Tesis Doctoral se han empleado dos moléculas sonda para la realización de los experimentos de quimisorción H_2 y CO. Si bien la quimisorción con H_2 es la técnica más extendida, la quimisorción con CO es más adecuada para analizar Au y Pt.

$$\gamma(\%) = \frac{\frac{V_m}{V_{mol}}}{\frac{M_{\%}}{W_a}} \cdot F_s \cdot 100 \qquad \textbf{[3.1]}$$

donde "V_m" es el volumen de gas quimisorbido en cm_3/g; "V_{mol}" el volumen molar de dicho gas (en las mismas unidades); "F_s" el factor estequiométrico de la reacción de quimisorción; "M" el porcentaje de metal activo expresado en gramos de metal activo por cada gramo de muestra, y "W_a" el peso atómico del metal activo.

Esta técnica permite cuantificar la cantidad de H_2 o CO quimisorbida en cada átomo metálico. Con el objetivo de determinar este parámetro, se realiza un experimento para observar la cantidad de gas adsorbida a distintas presiones. Gracias a la formación de un enlace químico entre la molécula de adsorbato y un sitio activo en la superficie del adsorbente, el número de átomos activos (metálicos) se puede determinar simplemente midiendo la cantidad del gas adsorbido, si se conoce el factor estequiométrico (F_s) entre el gas y el metal en el proceso de adsorción (**Tabla 3.1**).

Tabla 3.1. Factores estequiométricos utilizados para determinar la dispersión metálica mediante quimisorción (F_s) [14,15]

Metal	Coeficiente $F_{S\ H_2}$	Metal	Coeficiente $F_{S\ CO}$
Pd	1	Pd	1
Pt	1	Pt	1
Au	0.2-0.9	Au	1
Ru	2	Ru	2
Rh	2	Rh	2

Dependiendo de la naturaleza del metal y los gases, y de las condiciones de operación, pueden coexistir especies de enlaces fuertes y débiles en la superficie del metal, y la quimisorción puede ser en parte reversible. La cantidad de hidrógeno quimisorbido reversiblemente se determina entonces mediante mediciones de readsorción, después de la evacuación del gas a la misma temperatura. Se realizan dos isotermas que representan la adsorción total y reversible, y la adsorción irreversible viene dada por la diferencia, tal y como se observa en la **Figura 3.3**.

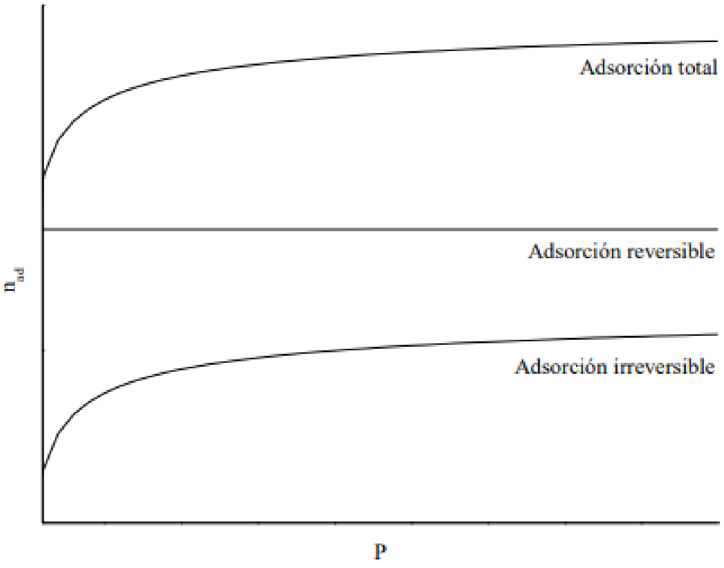

Figura 3.3. Determinación del volumen de la monocapa. Isotermas de adsorción total, reversible e irreversible

A partir de la dispersión metálica también es posible calcular el tamaño de cristalita (**Ec.3.2**). Para ello se considera una morfología esférica o semiesférica de las partículas metálicas. "A_{sm}" representa el área activa por gramo de metal puro y "ρ" la densidad del metal.

$$d = \frac{6}{A_{sm} \cdot \rho \cdot \gamma} \cdot 100 \qquad \textbf{[3.2]}$$

3.3.2. Técnicas de reacción o desorción a temperatura programada

Las técnicas a temperatura programada se emplean para determinar propiedades fisicoquímicas de los materiales. Principalmente, se ha utilizado para analizar la reducibilidad de los metales nobles empleados en este trabajo (y, con ello, determinar la temperatura a la que debe realizarse la reducción de los mismos), y para determinar la concentración y fortaleza de los centros activos ácido, base y redox. Para realizar estos análisis, se han utilizado tres variantes:

➢ Desorción de NH_3/CO_2 a temperatura programada (TPD): Estos ensayos se utilizan para caracterizar centros ácidos o básicos de los catalizadores. Se llevan a cabo mediante adsorción de NH_3 o CO_2 a temperatura ambiente, y el estudio de su desorción en función de la temperatura (monitorizado mediante espectrómetro de masas). Con este tipo de análisis se obtiene información sobre la acidez (desorción de NH_3) y basicidad (desorción del CO_2). En ambos casos, un calibrado previo permite cuantificar la totalidad de los centros, mientras que la deconvolución de las curvas obtenidas permite la clasificación de los centros por dureza en función de la temperatura de desorción. Para la realización de estos ensayos se realiza una previa limpieza de la superficie con helio para eliminar la humedad adsorbida en el material (200ºC, 1 h). Tras esta etapa, una vez alcanzada la temperatura ambiente, se satura la muestra con el gas sonda deseado durante 20 min. El posible exceso de gas se elimina de forma natural con un tiempo de estabilización de la señal mientras se mantiene el flujo de He y la temperatura ambiente (tiempo aproximado 2 h, asegurando en cada análisis haber alcanzado la línea base en la señal). Finalmente, la desorción de la molécula sonda se monitoriza con un programa de temperatura que alcanza los 900ºC con una rampa de 5ºC·min^{-1}. A pesar de estas condiciones generales, sólo se consideran las señales obtenidas hasta la temperatura de preparación de los materiales, para asegurar que no se consideran posibles degradaciones.

➢ Reducción a temperatura programada (TPR): Este tipo de ensayos se emplean para la caracterización de catalizadores que contengan un metal susceptible de ser reducido. En este caso, se monitoriza el consumo de H_2 que conlleva dicha reducción, siendo también relevante la temperatura a la cual ocurre dicha reacción (indicativo de la mayor o menor tendencia a reducirse/oxidarse). Tras limpiar la superficie del material durante 1 h a 200ºC en flujo de He, se recupera la temperatura ambiente y, con una rampa de 5ºC·min^{-1} se monitoriza la señal de H_2 hasta alcanzar los 500ºC (temperatura máxima de reducción de los materiales considerados en este estudio).

➢ Oxidación a temperatura programada (TPO): Se utiliza para la caracterización de los depósitos carbonosos adsorbidos sobre las superficies catalíticas tras las diferentes reacciones. El programa es análogo al realizado para los TPR, pero sustituyendo el H_2 por O_2 y monitorizando las señales de CO y CO_2 que se producirían por la combustión de dichos depósitos. Igualmente, la temperatura a la que ocurren estas oxidaciones indica la fortaleza relativa de los depósitos carbonosos.

Para llevar a cabo este tipo de ensayos, se ha empleado un Autochem 2910 de Micromeritics de la Universidad de Oviedo como el que se muestra en la **Figura 3.4** que permite realizar análisis de materiales sólidos a temperatura programada en un rango de temperaturas de -20º a 1000 ºC. Puede trabajar con 5 gases diferentes: He, CO_2, NH_3/He, H_2/Ar y O_2/He. Está equipado con un espectrómetro de masas (modelo Pfeiffer Omnistar Vacuum GSD 301) que permite seguir la señal de los diferentes gases empleados.

Figura 3.4. Equipo utilizado para la adsorción a temperatura programada. Autochem 2910 de Micromeritics

3.3.3. Difracción de rayos X (DRX)

La difracción de rayos X es una técnica analítica versátil y no destructiva que se utiliza para analizar propiedades físicas, como la composición de fases, la estructura cristalina de los catalizadores.

La técnica se basa en el fenómeno de difracción, es decir, se refiere al fenómeno de dispersión de ondas cuando pasan a través de una rendija o apertura estrecha, mientras que la extensión de la dispersión depende del tamaño de la rendija. Cuando los rayos X pasan a través de una estructura cristalina, son difractados por las diversas capas atómicas o moleculares dentro de ese cristal. Estos rayos difractados sufren interferencias constructivas o destructivas. Las interferencias constructivas constituyen el fundamento de la técnica y son aquellas que tienen lugar cuando se suman los efectos de dos ondas "en fase", es decir, cuando la longitud de onda de los rayos X utilizados es del mismo orden de magnitud de la distancia entre los átomos en una red cristalina se generan picos que dan lugar a un patrón de difracción que se puede analizar de varias maneras; la más popular es la aplicación ley de Bragg (**Ec. 3.3**).

$$n \cdot \lambda = 2 \cdot d \cdot sen\theta \qquad \textbf{[3.3]}$$

donde “n” es un número entero; “λ”, la longitud de onda de la radiación incidente; “θ”, el ángulo de difracción; y “d”, la distancia entre planos de átomos del cristal.

Además, La aproximación de Scherrer (**Ec. 3.4**) se emplea para la estimación del tamaño promedio de cristal cuando la red cristalina no tiene deformación y la muestra está compuesta mayoritariamente de pequeños cristales.

$$\beta = \frac{K \cdot \lambda}{L \cdot \cos\theta} \qquad \textbf{[3.4]}$$

donde: “L” es el tamaño medio de los cristales, “λ” es la longitud de onda, “θ” es el ángulo de Bragg, “β” es la anchura a media altura del pico (en radianes, FWHM) y K es la constante de Scherrer que depende de la forma del cristal y del método utilizado para calcular el tamaño (0.9).

En un difractómetro de rayos X, las diferentes fases cristalinas muestran diferentes patrones de difracción. La identificación de fases se puede realizar mediante la comparación de los patrones de difracción obtenidos de muestras desconocidas con los patrones de las bases de datos de referencia. Para la medición de los espectros se ha utilizado el difractómetro Philips PW1710 de los Servicios Científico-Técnicos de la Universidad de Oviedo (**Figura 3.5**). Se emplea como radiación incidente la line K-α de cobre (λ=1.54 Å) con un voltaje y una corriente del tubo de 45kV y 40mA, en un intervalo de 2θ comprendido entre 5.01 y 115°, con una velocidad de barrido de 2°min^{-1}.

Figura 3.5. Equipo empleado para llevar a cabo los análisis de difracción de rayos X para polvo cristalino. Philips PW1710

Esta técnica se ha utilizado para determinar las fases cristalinas o parcialmente amorfas existentes en los diferentes materiales, así como para calcular el tamaño de cristalita metálica en el caso de los catalizadores de metal soportado.

3.3.4. Análisis elemental

El análisis elemental se puede utilizar para determinar la cantidad de carbono, hidrogeno, nitrógeno, azufre y oxígeno de los diferentes materiales mediante el empleo de la oxidación instantánea y completa de muestras a través de la combustión en un horno a 1200°C y posterior reducción, convirtiendo cada sustancia orgánica e inorgánica en un producto de combustión (CO_2, H_2O, N_2O y SO_2). Posteriormente, el análisis de dichos gases se realiza empleando una columna de cromatografía para separarlos y un detector de conductividad térmica (TCD). El contenido de cala elemento en la muestra tiene una relación directa con la concentración de cada uno de estos gases.

La determinación del contenido en carbono, hidrógeno, nitrógeno y azufre de la celulosa y del serrín, frescos y tras los pretratamientos, se ha llevado a cabo empleando un analizador elemental C, H, N, S Elemental Vario EL disponible en los Servicios Científico-Técnicos de la Universidad de Oviedo.

3.3.5. Espectrometría de masas con plasma acoplado inductivamente (ICP-MS)

La espectrometría de masas con plasma acoplado inductivamente (ICP-MS, por sus siglas en inglés) es una técnica de análisis multielemental que permite determinar y cuantificar la mayoría de los elementos de la tabla periódica a nivel de traza que tengan un potencial de ionización menor que el potencial de ionización del argón. Se basa en el acoplamiento de un método para generar iones (plasma acoplado inductivamente) y un método para separar y detectar los iones (espectrómetro de masas). Esta técnica se ha utilizado para determinar la composición elemental de los diferentes catalizadores.

La muestra, en forma líquida, es transportada por medio de una bomba peristáltica hasta el sistema nebulizador donde es transformada en aerosol gracias a la acción de gas argón. Dicho aerosol es conducido a la zona de ionización que consiste en un plasma generado al someter un flujo de gas argón a la acción de un campo magnético oscilante inducido por una corriente de alta frecuencia. En el interior del plasma se pueden llegar a alcanzar temperaturas de hasta 8000 K. En estas condiciones, los átomos presentes en la muestra son ionizados. Los iones pasan al interior del filtro cuadrupolar a través de una interfase de vacío creciente, allí son separados según su relación carga/masa. Cada una de las masas sintonizadas llegan al detector donde se evalúa su abundancia en la muestra. Para los análisis de ICP-MS realizados se ha empleado el espectrómetro de masas de cuadrupolo tipo ICP-MS con celda de colisión (modelo HP 7500c de Agilent) disponible en los Servicios Científico Técnicos de la Universidad de Oviedo.

3.3.6. Análisis termogravimétrico

Los análisis termogravimétricos consisten en un grupo de técnicas que monitorizan los cambios en la masa de una muestra sólida con el tiempo mientras se somete a variaciones de temperatura, lo que puede relacionarse con cambios tanto físicos como químicos del material. Una característica fundamental de esta técnica es que permite la cuantificación de la ganancia o pérdida de masa de la muestra debido a procesos de, por ejemplo, descomposición, reducción, adsorción o desorción. En este caso, los ensayos termogravimétricos se han realizado siempre en N_2 con el objetivo de caracterizar las celulosas microcristalinas y pretratadas, el serrín (para establecer la temperatura en la que pierden el agua completamente y conocer la temperatura máxima a la que puede llevarse a cabo las reacciones sin descomponer el material térmicamente) y las sales de ácido furoico (para determinar la estabilidad y, con ello, la temperatura máxima para las reacciones de carboxilación).

El dispositivo experimental (**Figura 3.6**) consiste en una termobalanza conectada a un recipiente que contiene la muestra (crisol de platino) dentro de un horno y a un controlador de temperatura perteneciente a la casa comercial TA Instruments (modelo TGA 55). La configuración del horno, la colocación de la muestra y los puntos de entrada y salida de gas minimizan el ruido en la señal. El programa de temperatura empleado puede incluir etapas de calentamiento, enfriamiento, periodos isotérmicos o una combinación. En el caso del

Figura 3.6. Equipo utilizado para los ensayos termogravimétricos (TGA 55)

desarrollo de esta Tesis Doctoral, se ha utilizado un programa de temperatura que consta de una rampa de calentamiento de 5°C·min^{-1} desde 25°C hasta 900°C con un flujo de nitrógeno.

3.3.7. Espectroscopía infrarroja de reflexión difusa por transformada de Fourier (DRIFT)

La espectroscopía infrarroja de reflexión difusa (DRIFT) implica la captura y análisis de la radiación difusa reflejada en todas las direcciones por la muestra objeto de estudio cuando se le aplica un haz de radiación infrarroja. Al incidir el haz infrarrojo en la muestra, puede ser reflejado por su superficie o transmitido a través de ella. La energía transmitida puede encontrarse con otra partícula, donde puede ser reflejada nuevamente o transmitida hacia otra partícula diferente. Este proceso de transmisión y reflectancia puede repetirse múltiples veces en una misma muestra, lo que aumenta significativamente el recorrido del haz incidente. La reflexión difusa ocurre en todas las direcciones del espacio y se recopila utilizando un sistema de espejos orientados hacia el detector correspondiente. Los espejos concentradores, dirigen la radiación reflejada hacia el detector, capturando exclusivamente la radiación difusa. La intensidad de la reflexión puede expresarse, mediante la transformación empírica de Kubelka-Munk. Los picos o bandas observados a diferentes longitudes de onda se relacionan con las vibraciones de ciertos enlaces químicos presentes en la muestra cuando se expone a radiación infrarroja.

La asignación de estas bandas de absorbancia a cada tipo de enlace puede lograrse mediante referencia bibliográfica o análisis de estándares conocidos. Esta técnica, por tanto, facilita el estudio de la modificación o ruptura de enlaces existentes en el material, así como la formación de nuevos enlaces tras tratamientos o reacciones químicas. Además, la incorporación de un accesorio conocido como cámara catalítica permite el flujo controlado de gases sobre la muestra y una precisa regulación mediante una bomba de vacio. Además, dispone de un controlador de temperatura lo que permite el estudio de enlaces rotos o generados durante una reacción química o proceso de adsorción a temperaturas específicas. Para llevar a cabo estas mediciones, se emplea un espectrómetro Agilent Technologies Cary 600 Series FTIR Spectrometer perteneciente al Instituto Fritz-Haber de la sociedad alemana Max Planck de Berlín (**Figura 3.7**), equipado con un detector MCT/A, capaz de capturar el espectro infrarrojo en el rango de 700-4000 cm^{-1}. El equipo está configurado con una resolución de 2 cm^{-1} y realiza 256 escaneos consecutivos para obtener cada espectro.

Antes de la adsorción de CO, las muestras se secaron a 150°C en vacío. La adsorción de CO se llevó a cabo isotérmicamente a temperatura ambiente, con una adición gradual de CO en el rango de presión de 0,025 a 18 mbar, seguido de una evacuación escalonada. Mediante espectroscopía DRIFT, se ha evaluado posibles causas de desactivación del Au en reacciones de oxidación.

Figura 3.7. Equipo utilizado para la espectroscopía infrarroja de reflexión difusa por transformada de Fourier (DRIFT), Agilent Technologies Cary 600 Series FTIR Spectrometer

3.3.8. Espectroscopía Raman

La espectroscopía Raman es una técnica de dispersión de luz, mediante la cual una molécula dispersa la luz incidente desde una fuente de luz láser de alta intensidad. La mayor parte de la luz dispersada tiene la misma longitud de onda (o color) que la fuente del láser y no proporciona información útil; esto se denomina Dispersión de Rayleigh. Sin embargo, una pequeña cantidad de luz (normalmente $1 \cdot 10^{-7}$ %) se dispersa en diferentes longitudes de onda (o colores), que dependen de la estructura química del analito; esto se denomina dispersión Raman.

El procedimiento de medida es el siguiente: un haz de luz monocromático, de frecuencia νo, incide sobre la muestra, dispersándose de manera elástica (dispersión Rayleigh) en su mayor parte, pero existiendo una cantidad de luz que ha sido dispersada inelásticamente, y por tanto presenta un cambio en su frecuencia. Estos cambios en la frecuencia son característicos de la naturaleza química y del estado físico de la muestra, y por tanto son los datos que permiten identificar distintos compuestos y características moleculares. Microscópicamente, este efecto se puede describir como una excitación de la nube electrónica de la molécula debido a la interacción con el fotón incidente. Este provoca que la excitación de la molécula a un estado excitado virtual luego emite otro fotón con el objetivo de regresar al estado fundamental. Sin embargo, si el choque ha sido inelástico y se ha perdido o ganado energía, la molécula no volverá exactamente al mismo estado, sino que se encontrará en un estado rotacional o vibracional distinto del inicial. La diferencia de energía entre estos estados es lo que modifica la frecuencia del fotón emitido. Según la frecuencia de los fotones dispersados, se pueden distinguir los siguientes casos (**Figura 3.8**).

- Dispersión Rayleigh. Cuando el choque es elástico, la frecuencia del fotón incidente y emitido es la misma, y por tanto no hay ninguna variación energética. Este proceso no proporciona información espectroscópica.

- Dispersión Raman-Stokes. Si el choque es inelástico, y la frecuencia del fotón emitido es menor, quiere decir que ha transferido energía a la molécula, la cual se encontrará ahora en un estado vibracional o rotacional superior al inicial.

- Dispersión Raman Anti-Stokes. También para choques inelásticos, pero con frecuencias mayores del fotón. En este caso, la molécula no se encontraba en el estado fundamental, y al proporcionar energía al fotón, decae al estado de mínima energía.

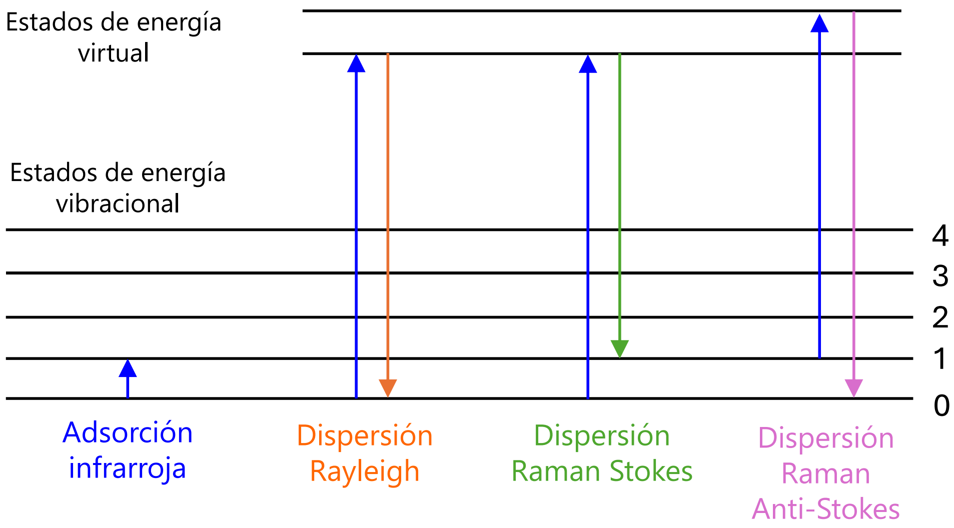

Figura 3.8. Diagrama de nivel de energía mostrando los estados implicados en la señal de Raman

Con esta técnica se puede analizar la composición química de diferentes materiales inorgánicos sin destruir las muestras y sin preparación especial. Los ensayos se realizaron en un microscopio WITec alpha300 R perteneciente al Instituto Fritz-Haber de la sociedad alemana Max Planck de Berlín, equipado con un espectrómetro UHTS300S VIS, un objetivo Zeiss EC Epiplan 10x / 0.25 y láseres WITec de 488 y 633 nm. Cada espectro se registró con una potencia de láser de 4 mW, un tiempo de integración de 0,5 s y 100 acumulaciones. Esta técnica se emplea para identificar posibles depósitos carbonos en la superficie de los catalizadores tras las diferentes reacciones estudiadas en esta Tesis Doctoral.

3.3.9. Microscopía electrónica

La microscopía electrónica analizar los materiales a escalas muy pequeñas que van más allá de lo que la microscopía óptica tradicional puede alcanzar. Mientras que la microscopía óptica utiliza luz visible para magnificar y visualizar muestras, la microscopía electrónica emplea haces de electrones para lograr una resolución mucho mayor. Esta técnica nos permite observar estructuras a nivel molecular y atómico.

La microscopía electrónica se divide principalmente en dos formas: microscopía electrónica de transmisión (TEM) y microscopía electrónica de barrido (SEM).

Microscopía electrónica de barrido

El microscopio electrónico de barrido (SEM, *Scanning Electron Microscope*) es un instrumento muy versátil, permite la observación y caracterización superficial de materiales orgánicos e inorgánicos, dando información morfológica y de composición química rápida, eficiente y simultáneamente del material analizado. Su versatilidad está dada en su alta resolución (de 20 a 50 Å) y apariencia tridimensional de las imágenes.

Estos microscopios trabajan con un haz de electrones para generar la imagen y en condiciones de alto vacío (10-6 torr), las partes esenciales del microscopio son: columna de electrones, consola de controles y sistema de adquisición de imágenes. En la parte superior de la columna se encuentra el emisor de electrones, que genera un haz de electrones, éste es conducido y dirigido por lentes electromagnéticas, el sistema de deflexión mueve el haz en forma de "*zig zag*" para hacer un barrido superficial del material, produciendo señales por la interacción del haz con el espécimen. Estas señales (rayos secundarios, rayos retro-dispersados y rayos X entre otros) son colectadas por detectores y cada uno de ellos nos brindan información específica, los rayos secundarios producen imágenes SEI (*Secundary Electron Image*) de morfología superficial de la muestra, los electrones retrodispersados producen imágenes con diferente brillantez en función de la composición química y topografía de la superficie BEI (*Backscattered Electron Image*) y los Rayos X, EDS (*Energy Dispersive Spectrometer*) obtiene información cualitativa de composición química de la muestra de manera rápida y eficiente, realizando un análisis semi-cuantitativo de los elementos detectados.

Figura 3.9. Microscopio electrónico de barrido FEI/Philips SXL30S FEG

Los análisis SEM realizados se han realizado en un microscopio electrónico de barrido modelo FEI/Philips SXL30S FEG disponible en los Servicios Científico-Técnicos de la Universidad de Oviedo. (**Figura 3.9**). Se requieren dos condiciones para analizar muestras en un SEM: que se encuentren libres de humedad y sean conductivas. Las muestras no conductoras necesitan un recubrimiento metálico para su observación, por ello se recubren con una capa de oro cuando se quiere realizar análisis químico por EDS. Durante el desarrollo de esta Tesis Doctoral, se caracteriza mediante análisis SEM la superficie de la celulosa microcristalina y del serrín, tanto fresco como después de los pretratamientos.

Microscopía electrónica de transmisión

Las aplicaciones de esta técnica son numerosas, entre ellas destaca el análisis de materiales nanoestructurados. Los análisis TEM realizados, se han llevado a cabo en un microscopio modelo TALOS F200X perteneciente al Instituto Fritz-Haber de la sociedad alemana Max Planck de Berlín y en un microscopio modelo JEOL-JEM 2100F perteneciente a los Servicios Científico-Técnicos de la Universidad de Oviedo (**Figura 3.10**).

Figura 3.10. Microscopios electrónicos de transmisión utilizados durante el desarrollo de la Tesis Doctoral. A la izquierda TALOS F200X, a la derecha JEOL-JEM 2100F

Durante el desarrollo de esta Tesis Doctoral se ha empleado para caracterizar la morfología de los diferentes tipos catalizadores bifuncionales empleados. Realizando micrografías TEM podemos distinguir la morfología del soporte de la morfología de las partículas soportadas y nos permite medir el tamaño de las partículas metálicas presentes, así como las dispersiones metálicas de las mismas en cada material.

En este tipo de microscopios, al tratarse de una muestra en polvo esta debe soportarse sobre una gradilla impregnada con nanofibras de carbono o con una membrana de silicona que permita la adhesión de la muestra. En ocasiones si la integración entre la gradilla y la muestra no es óptima, se debe preparar una suspensión del material, sonicarla varios minutos y finalmente añadir una gota en la gradilla para evitar que el material se desprenda en el interior del microscopio.

Posteriormente, se introduce la muestra en el microscopio y se irradia con un haz de electrones de densidad de corriente uniforme. Los electrones interactúan fuertemente con los átomos de la muestra mediante dispersión elástica e inelástica. Por lo tanto, la muestra debe ser muy delgada, típicamente del orden de 5 a 100 nm. Un sistema de lentes condensadoras de tres o cuatro etapas permite la variación de la apertura de iluminación y el área de la muestra iluminada. Para obtener la imagen, la distribución de intensidad electrónica detrás de la muestra se visualiza con un sistema de lentes, compuesto de tres a ocho lentes en una cámara que permite aumentar la imagen hasta un millón de veces.

3.4. EQUIPO Y PROCEDIMIENTOS EXPERIMENTALES PARA LOS ESTUDIOS EN REACCIÓN

En este apartado de la presente Tesis Doctoral, se detalla el dispositivo experimental y el procedimiento utilizado para todos los estudios catalíticos en discontinuo (hidrólisis, oxidación y carboxilación).

3.4.1. Pretratamientos de celulosa y serrín de pino

En las reacciones de hidrólisis se emplean como reactivos celulosa microcristalina (MCC) y serrín de pino. Estos reactivos se someten a pretratamientos con el fin de debilitar su estructura para facilitar su conversión y, en el caso del serrín de pino, para eliminar la lignina.

Pretratamientos de la celulosa microcristalina

Se llevan a cabo pretratamientos ácidos (HCl, HNO_3) y oxidantes (H_2O_2) de la celulosa para reducir su grado de cristalinidad [16, 17]. Los reactivos empleados se adquieren en Sigma Aldrich con una pureza del 49% de HCl, el 68% de HNO_3 y del 30% de H_2O_2. Estos pretratamientos, se realizan a temperatura ambiente, consisten en atacar 10 g de celulosa microcristalina con disoluciones de 250 mL de HCl, HNO_3 y H_2O_2 de diferente concentración (1, 5, 10 y 68% en peso en el caso de los ácidos; 5 y 10% en peso en el caso del peróxido de hidrógeno) durante 6 horas. Trascurrido este tiempo, las muestras de celulosa pretratada se filtran para retirar el líquido remanente y se lavan con agua destilada hasta pH neutro para garantizar la ausencia de ácido o peróxido de hidrógeno en la muestra filtrada ya que estos compuestos pueden interferir en el posterior proceso de hidrólisis.

Pretratamientos de la biomasa lignocelulósica

Durante el desarrollo de esta Tesis Doctoral, se estudia la influencia de dos tipos de pretratamientos para reducir el contenido de lignina de la biomasa lignocelulósica: el pretratamiento oxidativo y el pretratamiento reductivo. El pretratamiento oxidativo se realiza de acuerdo con el procedimiento propuesto en la literatura por *Yu et al.* [18]. Se basa en utilizar como reactivos clorito de sodio ($NaClO_2$, Sigma Aldrich, ≥99%) y ácido acético (Sigma Aldrich, ≥99%) en relación masa/volumen 3:1. Inicialmente, se introducen 15 gramos de serrín de pino natural junto con 600 ml de agua destilada en un matraz de bola equipado con un condensador y un baño de agua termostatizado. Una vez que se alcanza la temperatura deseada (80 °C), se añaden 7.5 g de ácido acético y cada 30 minutos durante un total de 4h se añaden 22.5 g de clorito de sodio. Una vez finalizado el proceso, el serrín deslignificado se extrae y se lava con agua destilada hasta que el filtrado es de color transparente y finalmente se lava 3 veces más. Por último, el serrín deslignificado se seca en una estufa a 110 °C y se tamiza para obtener un tamaño de partícula de 200 µm.

Por otro lado, el pretratamiento reductivo se realiza de acuerdo con el procedimiento propuesto por *Van den Bosch et al.* [19]. En este caso, el pretratamiento se realiza en un reactor discontinuo de tanque agitado (Autoclave Engineers EZE Seal) en el que se introducen 10 gramos de serrín de pino natural junto con un catalizador comercial 5% Ru/C y 200 ml de metanol. Posteriormente, se purga la atmosfera del reactor con N_2 para eliminar el

O_2 del interior, se presuriza con H_2 hasta 25 bar a temperatura ambiente y se calienta hasta 150 °C. La reacción transcurre durante 6h con una agitación de 700 rpm. Finalmente, se recupera el sólido de la reacción filtrándolo, se lava con agua destilada, se seca en una estufa a 110 °C y se tamiza a 200 µm.

3.4.2. Reacciones de hidrólisis y oxidación

Para llevar a cabo las reacciones de hidrólisis de biomasa y oxidación de aldehídos se emplea el reactor ilustrado en la **Figura 3.11**. Está fabricado por Autoclave Engineers, es el modelo Eze Seal y consta de una vasija de acero inoxidable (SS316L) de 500 mL de capacidad. Además, tiene una vasija adicional interna de titanio para poder emplear catalizadores ácidos a pH bajo, como en el caso de la hidrólisis, evitando así posibles efectos de corrosión y proporcionando, mediante el empleo de titanio, una buena conductividad térmica. Presenta un sistema de calefacción por encamisado compuesto por una manta calefactora eléctrica de cerámica de 550W de potencia y la posibilidad de incorporar un serpentín de refrigeración interna. Permite la regulación de la temperatura mediante un sistema compuesto por dos controladores PID unidos a dos termopares tipo K, uno de ellos situado en el interior del reactor por lo que permite medir la temperatura real de la reacción; mientras que el segundo permite regular la temperatura de la manta calefactora mediante la variación de la potencia suministrada a la misma. La temperatura máxima de trabajo está limitada a 250°C. La agitación viene proporcionada por un agitador magnético de turbina controlado a través de un tacómetro que permite medir la velocidad de giro. El intervalo de agitación está comprendido entre 100 y 1000 rpm.

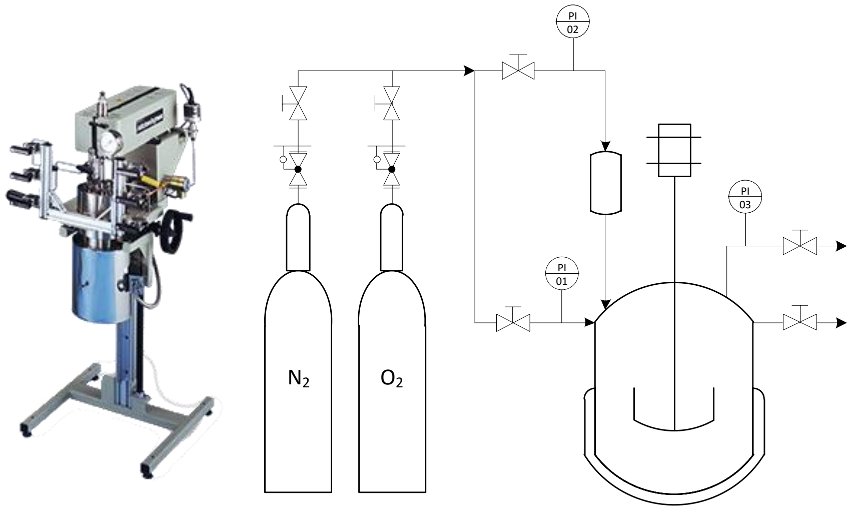

Figura 3.11. Dispositivo experimental y diagrama de flujo de Autoclave Engineers

El equipo permanece cerrado gracias a un sistema de cremallera, que, junto con una junta tórica, proporcionan estanqueidad para poder trabajar en presiones de hasta 100 bar. Dispone de un sistema de seguridad para evitar sobrepresiones compuesto por una válvula de alivio y un disco de ruptura. Por otro lado, el sistema de cierre de cremallera no permite abrir el reactor si está presurizado. Para poder extraer contenido de dentro del reactor mientras se encuentra presurizado, el dispositivo dispone de una salida de toma de muestra para recoger muestras. Esta tubería dispone de un filtro metálico que evita la pérdida de reactivo o catalizador durante la toma de muestra. Por otro lado, al reactor se le ha acoplado un sistema de alimentación adicional en su parte superior con el objetivo de poder inyectar el catalizador o el agente oxidante empleado una vez que el reactor ha alcanzado la temperatura de operación permitiendo establecer así perfectamente el tiempo de inicio de reacción.

Para llevar a cabo las reacciones se introducen los reactivos junto con el disolvente en el reactor discontinuo, se cierra el reactor empleando un sistema de manivela y se coloca la cremallera para garantizar la estanqueidad y la imposibilidad de abrir el reactor durante la reacción. A continuación, se elimina el aire del interior del reactor desplazándolo con nitrógeno u oxígeno en función de la reacción estudiada y se aumenta la presión hasta la presión de operación detallada en cada caso en el capítulo correspondiente de esta Tesis Doctoral. Se comprueba que la presión se mantiene estable y se activa la agitación y la manta calefactora. Una vez que se alcanza la temperatura de operación, con ayuda del dispositivo de alimentación adicional se agregan los catalizadores. En el caso de la hidrólisis de celulosa o biomasa lignocelulósica, a través del embudo de alimentación se añade la zeolita β y el HCl. Cuando se llevan a cabo reacciones de oxidación de FFL, el peróxido se introduce de forma análoga.

En las reacciones de hidrólisis, se emplea como reactivo una suspensión acuosa del 25% de celulosa (sin tratar o pretratada según los experimentos), y un 4% de zeolita β. En las reacciones de hidrólisis de serrín, se emplea un 1.5% de serrín en suspensión en cada ensayo. La reacción transcurre a 10 bar de N_2. La concentración de ácido, así como la temperatura, dependen del experimento y se especifican en el Capítulo 4 de esta Tesis Doctoral.

Para las reacciones de oxidación de furfural con peróxido de hidrógeno, se emplea como reactivo 250ml de una disolución acuosa al 0.5M de furfural y 1.5M de H_2O_2. En las reacciones de oxidación con O_2, se alimenta el reactor con una disolución acuosa 0.5 M de FFL el pH de la disolución inicial es 4.8 y se modifica empleando una disolución tampón $KHCO_3$ para ajustarlo a pH 8. En el caso de oxidación de HMF, se emplea como reactivo una disolución acuosa de HMF y NaOH (Sigma Aldrich, 99%) con diferentes concentraciones (de 0.1 a 0.01 M) y relaciones relativas (de 4:1 a 1:1) en función del experimento. En los estudios de oxidación de mezclas, se introduce en el autoclave una solución acuosa de HMF y FFL a la concentración inicial deseada y NaOH. En todas las reacciones de oxidación introduce una carga de catalizador de un 0.2%. Las presiones en cada caso se indican en la sección de resultados (Capítulo 4).

3.4.3. Reacciones de carboxilación

En las reacciones de carboxilación se emplea un reactor análogo, pero de menor volumen (50 ml, Parr 4590) y se plantean experimentos en ausencia de disolvente en los cuales se introducen 0.05 moles de la sal correspondiente, furoato de cesio (F-Cs) o difuroato de cobre ($Cu(F)_2$), y 0.05 moles de carbonato de cesio en el reactor previamente calentado (150 ºC). A continuación, se cierra el reactor, se presuriza con CO_2 y se lleva con ayuda de una manta calefactora a la temperatura deseada. Cuando se emplean disolventes se introducen en el reactor 30ml de una disolución de F-Cs o $Cu(F)_2$ y Cs_2CO_3 en relación 1:1 y posteriormente se presuriza y se calienta hasta 170 ºC.

3.5. TÉCNICAS DE ANÁLISIS

Para la cuantificación de los productos de reacción de las muestras obtenidas del reactor de forma periódica se han empleado diferentes técnicas de cromatografía. Esta técnica se basa en el principio de la retención selectiva, que consiste en el distinto comportamiento de los componentes de una mezcla sobre un soporte específico alojado en una columna de cromatografía. Cuanto más fuertemente se adsorbe un soluto, más lentamente atraviesa la columna y por lo tanto mayor será su tiempo de retención.

Debido a la naturaleza de los procesos estudiados y al hecho de trabajar empleando agua como disolvente, para el análisis cualitativo de las muestras se han empleado dos tipos de cromatografía: cromatografía de gases (GC) y cromatografía de líquidos (HPLC).

3.5.1. Análisis mediante cromatografía de gases

En este tipo de cromatografía la muestra se volatiliza y se inyecta en la columna de fluyendo a través de esta con un flujo conocido de gas portador, generalmente helio. En función de la interacción de los diferentes reactivos y productos los componentes se separan a lo largo de la columna y finalmente llegan al detector que genera una señal en función de la concentración del producto químico que se puede relacionar con un calibrado para obtener el valor exacto de concentración. En este trabajo se ha utilizado en concreto un detector de espectrometría de masas (MS). En concreto, durante el desarrollo de esta Tesis Doctoral, se empleó un GC-MS Shimadzu, modelo GC-MS QP2010 Plus Instrument, equipado con una columna capilar tipo TRB-5MS de 30 metros de longitud como el que se muestra en la **Figura 3.12**.

Figura 3.12. Cromatógrafo de gases empleado para identificación de compuestos. GC-MS QP2010 Plus Instrument.

Para obtener un espectro de masas, las moléculas gaseosas o las especies desorbidas de fases condensadas se ionizan, los iones se aceleran en un campo eléctrico y a continuación, se separan según su relación masa/carga (m/z). Cada ion que llega al detector pasa por un multiplicador de electrones que mediante una serie de dinodos desencadena una cascada de electrones antes de llegar al ánodo, donde se mide la corriente dando lugar al espectro de masas donde se representa la abundancia iónica de cada componente en función de la relación m/z. Un pico se puede identificar comparando su espectro con los de una librería de espectros guardados en el ordenador. El espectro de masas es extremadamente sensible. La espectrometría de masas requiere un alto vacío, para evitar las colisiones moleculares durante la separación de iones. Mediante una rampa de temperatura se consigue que eluyan todos los compuestos evitando así que algunos queden retenidos en el interior de la columna, y una separación de picos más o menos uniforme. Para el análisis se empleó un volumen de inyección de 1µL de muestra, una columna de polaridad media: CP-Sil 5CB de 15 metros de longitud y 0,15 mm de espesor. Los detalles del método se muestran a continuación, en las **Tablas 3.2-4**.

Tabla 3.2. Parámetros empleados en el método de análisis en GC.

Inyección	Temperatura de inyección (°C)	250
	Presión (bar)	0.99
	Flujo total (mL·min^{-1})	43.9
Columna	Flujo en columna (mL·min^{-1})	1.35
	Ratio de Split	31.4
	Gas portador	Helio
Detector	Tipo	FID
	Temperatura (°C)	250
	Make up (N_2/aire, mL·min^{-1})	30
	Flujo de H_2 (mL·min^{-1})	40
	Flujo de aire (mL·min^{-1})	400

Tabla 3.3. Rampa de temperaturas empleado en el análisis mediante GC-MS de las muestras de hidrólisis.

Rampa (ºC·min^{-1})	Temperatura (ºC)	Tiempo (min)
-	35	2
0.5	37	0
20	82	0
10	190	5
10	220	15
25	260	3
	Tiempo total	46.65

Tabla 3.4. Rampa de temperaturas empleado en el análisis mediante GC-MS de las muestras de oxidación.

Rampa (ºC·min^{-1})	Temperatura (ºC)	Tiempo (min)
-	33	2
0.5	37	0
10	44	0
12	62	0
4	100	5
30	250	2
	Tiempo total	28.70

Una vez obtenidos los correspondientes valores de concentración a partir de las áreas de cada pico en los cromatogramas de cada uno de los reactivos y productos, se aplica la metodología detallada en cada uno de los capítulos de resultados de esta Tesis Doctoral para el cálculo de selectividades, rendimientos, conversiones y balances al carbono.

3.5.2. Análisis mediante cromatografía de líquidos

La cromatografía de líquidos de alta eficacia (HPLC) utiliza una presión elevada para forzar al disolvente a que pase por una columna que contiene partículas muy finas, consiguiendo así separaciones de gran resolución. Los equipos típicos de HPLC constan de un sistema de suministro de disolvente, una válvula de inyección de muestra, una columna de alta presión, un detector y un ordenador para controlar el equipo y visualizar los resultados además de un horno para controlar la temperatura de la columna.

Para los análisis llevados a cabo, se ha empleado un detector de índice de refracción (RID) ya que responde casi a cualquier soluto, permitiendo la identificación simultánea de azúcares, aldehídos y ácidos. Consta de dos compartimentos de 5 a 10 mL, a través de uno pasa disolvente puro y a través del otro la muestra. Para eliminar la radiación infrarroja (que calentaría la muestra), se hace pasar luz visible colimada (paralela) a través de la celda, con disolvente puro en los dos compartimentos, y se dirige a la fotocélula mediante una placa de deflexión. Cuando a la celda entra un soluto de diferente índice de refracción, el haz se desvía y la señal dada por la fotocélula varía.

Los detectores de índice de refracción no sirven para llevar a cabo una elución con gradientes, porque es imposible ajustar exactamente la muestra y la referencia mientras varía la composición del disolvente.

Figura 3.13. Cromatógrafo de líquidos empleado para la cuantificación de productos y reactivos Agilent 1200

En este caso, el equipo empleado ha sido un cromatógrafo de líquidos de alta eficacia HLP Agilent-1200 como el que se muestra en la **Figura 3.13**, equipado con un desgasificador para eliminar posibles burbujas presentes en la fase móvil, una bomba cuaternaria de pistones, un sistema de inyección automática a través de la cual se introducen 20µL de muestra en el seno de la fase móvil, una columna situada en el interior de un horno que permite controlar la temperatura a la cual ocurre la elución y un detector de índice de refracción (RID), el cual que responde casi a cualquier soluto, permitiendo la identificación simultánea de azúcares, aldehídos y ácidos.

El detector, consta de dos compartimentos de 5 a 10 mL, a través de uno pasa disolvente puro y a través del otro la muestra. Para eliminar la radiación infrarroja (que calentaría la muestra), se hace pasar luz visible colimada (paralela) a través de la celda, con disolvente puro en los dos compartimentos, y se dirige a la fotocélula mediante una placa de deflexión. Cuando a la celda entra un soluto de diferente índice de refracción, el haz se desvía y la señal dada por la fotocélula varía. Los detectores de índice de refracción no sirven para llevar a cabo una elución con gradientes, porque es imposible ajustar exactamente la muestra y la referencia mientras varía la composición del disolvente. Además, consta de un detector adicional de absorción a diferentes longitudes de onda (DAD), este tipo de detector utiliza una rejilla para dispersar la luz en una matriz de fotodiodos después de que la luz ha pasado a través de la celda de flujo. Por lo tanto, la absorción se produce simultáneamente en todas las longitudes de onda, proporcionando un espectro de absorción completo del analito.

El método analítico empleado es análogo al de numerosos estudios que analizan derivados de biomasa, FFL o HMF [20]. En concreto, se emplea una disolución acuosa 0.005 M de H_2SO_4 como fase móvil. Se inyectan 20 µL de muestra en la columna Hiplex-H (7.7 x 300 mm, 8 µm) cuya temperatura se encuentra a 50 ºC siendo ésta, la misma temperatura utilizada en el detector. Las muestras fueron filtradas mediante filtros de jeringa de 0.22 µm y se les aplica un factor de dilución 1:2 o 1:4 en función de la reacción estudiada. Una vez que se han obtenido los cromatogramas con las áreas correspondientes, es necesario realizar los calibrados correspondientes para calcular la concentración tanto de los reactivos como de los productos. Cuando los datos de concentración son conocidos, se pueden calcular distintos parámetros como selectividades, conversiones, rendimientos y balances al carbono, entre otros. El procedimiento de cálculo de cada uno de estos parámetros depende en gran medida de la reacción estudiada por lo que se detalla en cada uno de los capítulos de resultados que componen esta Tesis Doctoral.

3.6. MODELIZACIÓN CINÉTICA

Para garantizar que las reacciones estudiadas se desarrollaran bajo un control cinético intrínseco, se seleccionaron cuidadosamente las condiciones de reacción. En primer lugar, se utilizó una distribución de tamaño de partícula del catalizador muy pequeña, en el rango de 50–80 µm. Este tamaño reducido de las partículas asegura que las limitaciones difusionales internas sean mínimas, permitiendo que la reacción esté dominada por la cinética de la superficie activa del catalizador.

Además, se empleó una alta velocidad de agitación de 700 rpm durante los experimentos. Esta velocidad fue seleccionada después de realizar pruebas comparativas empleando un modelo de ensayo catalítico para cada reacción a diferentes velocidades de agitación (600 y 1400 rpm). No se observaron diferencias significativas en la conversión ni en la selectividad de los productos al variar la velocidad de agitación, con diferencias menores al 3%. Esto sugiere que, a 700 rpm, se logra una agitación suficientemente vigorosa para evitar limitaciones difusionales externas y asegurar que la reacción se desarrolle bajo un control cinético intrínseco. Con estas consideraciones se asegura que los datos experimentales obtenidos reflejan de manera precisa la cinética intrínseca del proceso catalítico, permitiendo una modelización matemática confiable.

Para llevar a cabo la modelización cinética del proceso, se empleó MATLAB, una plataforma de programación y cálculo numérico ampliamente utilizada en diversas disciplinas científicas e ingenieriles. MATLAB, acrónimo de "MATrix LABoratory", es un entorno de programación de alto nivel que facilita la manipulación de matrices, la visualización de datos, la implementación de algoritmos y la creación de modelos matemáticos complejos. Su versatilidad y capacidad para resolver ecuaciones diferenciales y optimizar parámetros lo hacen especialmente adecuado para estos estudios.

Los modelos cinéticos se presentan como un sistema de ecuaciones diferenciales ordinarias (ODEs) que describen matemáticamente los diferentes mecanismos propuestos. Para este propósito, se empleó la función "ode45", que es un integrador basado en el método de Runge-Kutta de orden variable, ideal para la resolución de ODEs de primer orden no lineales. Todos los datos experimentales obtenidos fueron considerados en estos cálculos para garantizar que los resultados obtenidos reflejen fielmente el comportamiento de todos los catalizadores evaluados en los experimentos. Este enfoque permitió una representación precisa y global de los fenómenos cinéticos, obteniéndose en todos los casos coeficientes de regresión superiores a 0.9.

El ajuste de los parámetros desconocidos del modelo se realizó utilizando el método de mínimos cuadrados. Para ello, se empleó la función "lsqcurvefit" de MATLAB, que facilita el ajuste de curvas no lineales a los datos experimentales. Este ajuste se realizó utilizando el algoritmo de Levenberg-Marquardt, lo que permitió obtener una descripción matemática detallada y ajustada del mecanismo de reacción propuesto.

3.7. REFERENCIAS

[1] R.E. Patet, M. Koehle, R.F. Lobo, S. Caratzoulas, D.G. Vlachos, General Acid-Type Catalysis in the Dehydrative Aromatization of Furans to Aromatics in H-[Al]-BEA, H-[Fe]-BEA, H-[Ga]-BEA, and H-[B]-BEA Zeolites, The Journal of Physical Chemistry C **2017** (121) 13666-13679. https://doi.org/10.1021/acs.jpcc.7b02344

[2] T. Xie, S. Yue, T. Su, M. Song, W. Xu, Y. Xiao, Z. Yang, C. Len, D. Zhao, High selective oxidation of 5-hydroxymethyl furfural to 5-hydroxymethyl-2-furan carboxylic acid using Ag-TiO2, Molecular Catalysis **2022** (525) 112353. https://doi.org/10.1016/j.mcat.2022.112353

[3] A. Lolli, R. Amadori, C. Lucarelli, M.G. Cutrufello, E. Rombi, F. Cavani, S. Albonetti, Hard-template preparation of Au/CeO2 mesostructured catalysts and their activity for the selective oxidation of 5-hydroxymethylfurfural to 2,5-furandicarboxylic acid, Microporous and Mesoporous Materials **2016** (226) 466-475. https://doi.org/10.1016/j.micromeso.2016.02.014

[4] R. López-Asensio, J.A. Cecilia-Buenestado, C. Herrera-Delgado, M.Á. Larrubia-Vargas, C. García-Sancho, P.J. Maireles-Torres, R. Moreno-Tost, Mixed Oxides Derived from Hydrotalcites Mg/Al Active in the Catalytic Transfer Hydrogenation of Furfural to Furfuryl Alcohol, Catalysts **2023** (13) 45. https://doi.org/10.3390/catal13010045

[5] C.M. Pichler, M.G. Al-Shaal, D. Gu, H. Joshi, W. Ciptonugroho, F. Schüth, Ruthenium Supported on High-Surface-Area Zirconia as an Efficient Catalyst for the Base-Free Oxidation of 5-Hydroxymethylfurfural to 2,5-Furandicarboxylic Acid, ChemSusChem **2018** (11) 2083-2090. https://doi.org/10.1002/cssc.201800448

[6] C. Ampelli, G. Centi, C. Genovese, G. Papanikolaou, R. Pizzi, S. Perathoner, R.J. van Putten, K.J.P. Schouten, A.C. Gluhoi, J.C. van der Waal, A Comparative Catalyst Evaluation for the Selective Oxidative Esterification of Furfural, Topics in Catalysis **2016** (59) 1659-1667. https://doi.org/10.1007/s11244-016-0675-y

[7] T. Pirmohamed, J.M. Dowding, S. Singh, B. Wasserman, E. Heckert, A.S. Karakoti, J.E.S. King, S. Seal, W.T. Self, Nanoceria exhibit redox state-dependent catalase mimetic activity, Chemical Communications **2010** (46) 2736-2738. http://doi.org/10.1039/B922024K

[8] J. Quesada, R. Arreola-Sánchez, L. Faba, E. Díaz, V.M. Rentería-Tapia, S. Ordóñez, Effect of Au nanoparticles on the activity of TiO2 for ethanol upgrading reactions, Applied Catalysis A: General **2018** (551) 23-33. https://doi.org/10.1016/j.apcata.2017.12.004

[9] S. Eaimsumang, S. Wongkasemjit, S. Pongstabodee, S.M. Smith, S. Ratanawilai, N. Chollacoop, A. Luengnaruemitchai, Effect of synthesis time on morphology of CeO2 nanoparticles and Au/CeO2 and their activity in oxidative steam reforming of methanol, Journal of Rare Earths **2019** (37) 819-828. https://doi.org/10.1016/j.jre.2018.11.010

[10] O.V. Larina, K.V. Valihura, P.I. Kyriienko, N.V. Vlasenko, D.Y. Balakin, I. Khalakhan, T. Čendak, S.O. Soloviev, S.M. Orlyk, Successive vapour phase Guerbet condensation of ethanol and 1-butanol over Mg-Al oxide catalysts in a flow reactor, Applied Catalysis A: General **2019** (588) 117265. https://doi.org/10.1016/j.apcata.2019.117265

[11] M.A. Aramenďia, V. Borau, C. Jiménez, A. Marinas, J.M. Marinas, J.R. Ruiz, F.J. Urbano, Magnesium-containing mixed oxides as basic catalysts: base characterization by carbon dioxide TPD–MS and test reactions, Journal of Molecular Catalysis A: Chemical **2004** (218) 81-90. https://doi.org/10.1016/j.molcata.2004.04.006

[12] R. Zanella, S. Giorgio, C.-H. Shin, C.R. Henry, C. Louis, Characterization and reactivity in CO oxidation of gold nanoparticles supported on TiO2 prepared by deposition-precipitation with NaOH and urea, Journal of Catalysis **2004** (222) 357-367. https://doi.org/10.1016/j.jcat.2003.11.005

[13] K.S.W. Sing, Reporting physisorption data for gas/solid systems with special reference to the determination of surface area and porosity (Recommendations 1984), Pure and Applied Chemistry **1985** (57) 603-619. https://doi.org/10.1351/pac198557040603

[14] M. Králik, Adsorption, chemisorption, and catalysis. Chemical Papers 2014 (68) 1625-1638. https://doi.org/10.2478/s11696-014-0624-9

[15] L.O. Paz-Borbon, R.L. Johnston, G. Barcaro, A. Fortunelli, Chemisorption of CO and H on Pd, Pt and Au nanoclusters: a DFT approach. The European Physical Journal D 2009 (52) 131-134. https://doi.org/10.1140/epjd/e2009-00041-9

[16] S. Van de Vyver, J. Geboers, P.A. Jacobs, B.F. Sels, Recent Advances in the Catalytic Conversion of Cellulose, ChemCatChem **2011** (3) 82-94. https://doi.org/10.1002/cctc.201000302

[17] S.J.S. JingJing, Z.H.Z. HongXiang, W.L.W. LiJun, L.X.L. XinLiang, N.S.N. ShuangXi, X.J.X. JianHua, Optimization of microwave-hydrogen peroxide pretreatment of cellulose, BioResources **2016** (11) 7416–7430. https://doi.org/10.15376/biores.11.3.7416-7430

[18] Z. Yu, H. Jameel, H.-m. Chang, S. Park, The effect of delignification of forest biomass on enzymatic hydrolysis, Bioresource Technology **2011** (102) 9083-9089. https://doi.org/10.1016/j.biortech.2011.07.001

[19] S. Van den Bosch, W. Schutyser, R. Vanholme, T. Driessen, S.F. Koelewijn, T. Renders, B. De Meester, W.J.J. Huijgen, W. Dehaen, C.M. Courtin, B. Lagrain, W. Boerjan, B.F. Sels, Reductive lignocellulose fractionation into soluble lignin-derived phenolic monomers and dimers and processable carbohydrate pulps, Energy & Environmental Science **2015** (8) 1748-1763. http://doi.org/10.1039/C5EE00204D

[20] A. Toftgaard Pedersen, R. Ringborg, T. Grotkjær, S. Pedersen, J.M. Woodley, Synthesis of 5-hydroxymethylfurfural (HMF) by acid catalyzed dehydration of glucose–fructose mixtures, Chemical Engineering Journal **2015** (273) 455-464. https://doi.org/10.1016/j.cej.2015.03.094

4. RESULTS AND DISCUSSION

This PhD is focused on developing the full process to obtain FDCA from lignocellulosic biomass, according to the different steps outlined in **Figure 4.1**.

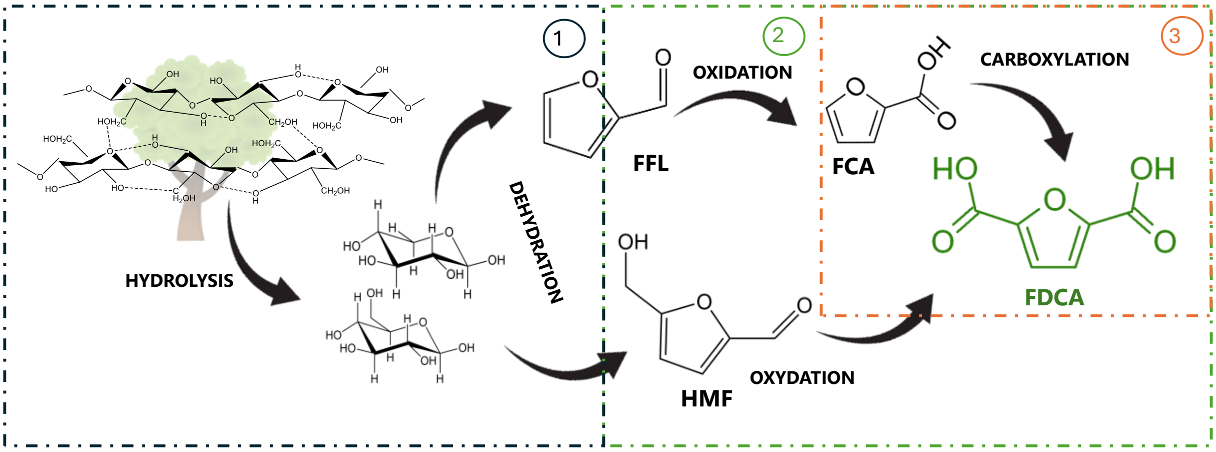

Figure 4.1. Pathway for the transformation of biomass into FDCA numbering the stages studied in the present PhD

The conversion of lignocellulosic biomass into FDCA requires a first step of hydrolysis to obtain carbohydrates by breaking the complex structure of this natural polymer. Previous pretreatments of this raw material to remove the lignin fraction is crucial to increase the efficiency of this step. The sugars are subsequently dehydrated to produce furfural (FFL) and 5-hydroxymethylfurfural (HMF). Using acid catalysts, both hydrolysis and dehydration are performed simultaneously. The oxidation of these intermediates leads to the formation of furoic acid (FCA) and FDCA, respectively. The conversion of FCA to FDCA requires an additional carboxylation step to introduce the necessary carboxyl groups.

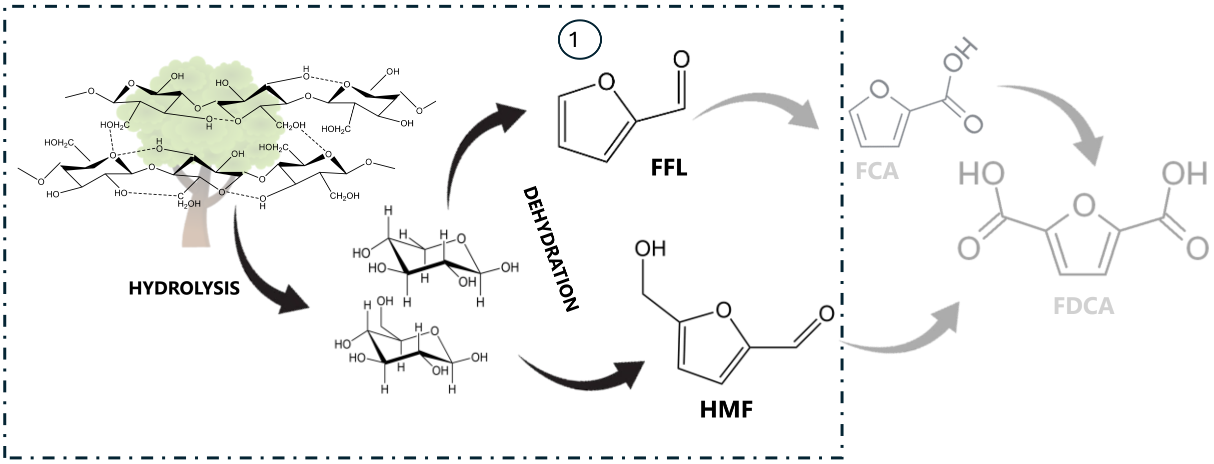

4.1. PRODUCTION OF 5-HYDROXYMETHYLFURFURAL BY PRETREATED CELLULOSES HYDROLYSIS

Based on the conclusions of the previous literature, this work evaluates the cellulose hydrolysis using a bi-catalytic system, HCl and β-zeolite, to guarantee the Lewis and Bronsted acidity required to maximize the 5-hydroxymethylfurfural (HMF) productivity reducing the severity of the process. This zeolite has been chosen based on a previous work where the activity of different zeolites for glucose dehydration has been studied [1]. Three chemical pretreatments are considered: HCl, which introduces acidity; H_2O_2, with oxidizing activity; and HNO_3, which combines both effects. The influence on conversion and product distribution was studied as a function of the chemical dosage.

Results were described in terms of conversion, carbon balance closure and selectivity. The cellulose conversion is calculated in terms of liquid-phase carbon yield, i.e., the theoretical cellulose required to obtain all compounds detected in the liquid phase (cellobiose and maltose, glucose, HMF, formic and levulinic acid), according to Equation (4.1):

$$x_C = \frac{[V \cdot \Sigma\,(n_i \cdot C_i)]_{aq}}{0.4421 \cdot \frac{m_{cellulose}}{M_{cellulose}}} \qquad [4.1]$$

where x_C is the liquid-phase carbon conversion, V is the total reaction volume, C_i the molar concentration of each compound detected in liquid phase, n_i the number of carbons in the molecule of compound *i*, $m_{cellulose}$ the mass of cellulose introduced in the reactor (5.83 g), $M_{cellulose}$ the molar mass of cellulose (162 g/mol), and 0.4421 corresponds to the atomic percentage of carbon in this cellulose, according to results obtained by ICP analysis of the raw material (44.21% C, 6.2% H, 49.59% O).

Carbon balance closure (C.B.) and selectivity were calculated as follows:

$$C.B.(\%) = \frac{\sum_{i=1}^{n} m_{C_i} + m_{C_t}}{m_{C_{t=0}}} \cdot 100 \qquad \textbf{[4.2]}$$

where $\sum_{i=1}^{n} m_{C_i}$ is the sum of the carbon mass present in all the reaction products; $m_{C_{t=0}}$ is the mass of carbon present in the cellulose initially introduced into the reactor; and m_{C_t} is the carbon mass of the cellulose collected by filtering and drying after the reaction.

$$S_i\,(\%) = \frac{n_i}{\sum_{j=1\ldots i}^{n} n_i} \cdot 100 \qquad \textbf{[4.3]}$$

where n_i is the moles of carbon that contains the reaction product *i* and $\sum_{j=1\ldots i}^{n} n_i$ is the sum of the moles of carbon corresponding to reaction products.

4.1.1. Hydrolysis of the non-pretreated cellulose

The initial experiments evaluate the influence of HCl on cellulose hydrolysis in the presence of β-zeolite to identify the optimum concentration of this homogeneous catalyst considering the equilibrium between activity, selectivity, and process sustainability. By sustainability criteria, a maximum value of 0.4% w/w (400 mg/L) was established to prevent corrosive effects in the equipment and to guarantee that the wastewater produced could be assimilated to a municipal wastewater stream, being far from the maximum allowed by the normative (2000 mg/L in the Spanish laws). It is expected that these low concentrations also minimize levulinic acid production (promoted by strong acidity). All reactions were performed in the presence of β zeolite to promote the HMF formation by the glucose isomerization route. This study is the first one reporting the co-utilization of homogeneous and heterogeneous acids for treating polymeric biomaterials. Results are analyzed in **Figure 4.2**.

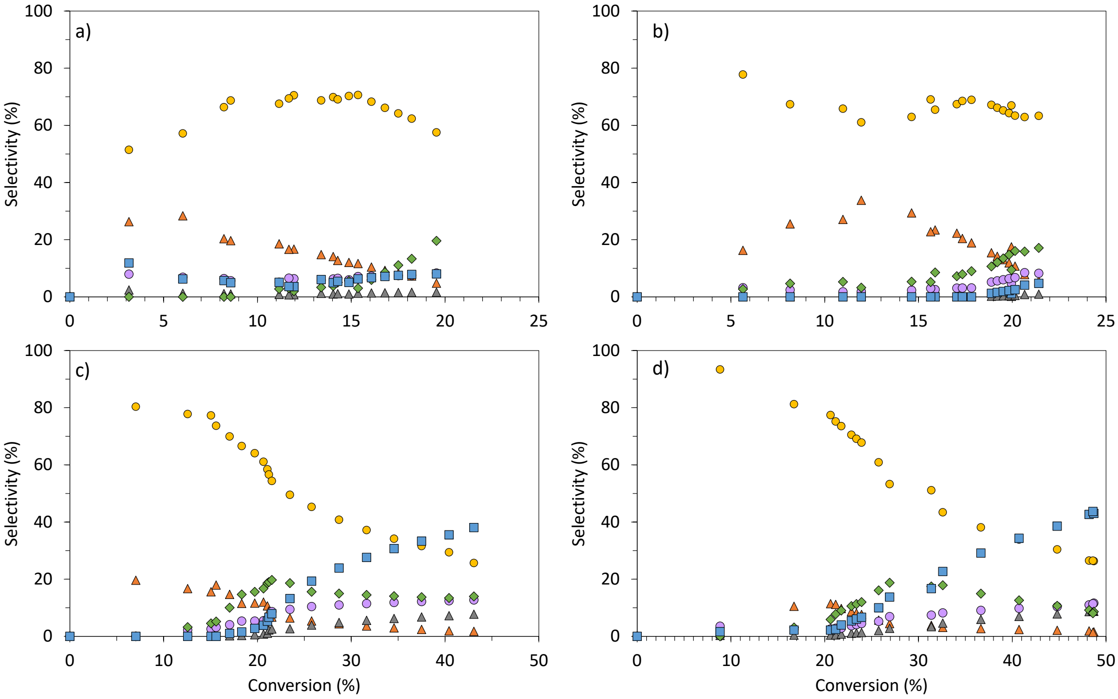

Figure 4.2. Selectivity *vs.* conversion plots obtained for the cellulose hydrolysis at 140 ºC using 8% β-zeolite as a function of the HCl concentration: (a) absence of HCl; (b) 0.005%; (c) 0.02%; (d) 0.04%. Symbols: (●) dimers; (▲) glucose; (◆) HMF; (●) AHG; (■) levulinic acid

The results shown in Fig. 4.2 are in good agreement with the general hydrolytic mechanism. Thus, dimers (mainly cellobiose but traces of maltose are also detected) are the first products obtained in the reaction, with very high selectivities at low cellulose conversion. The presence of heavier oligomers cannot be discarded but they cannot be analyzed because of their insoluble character (only the liquid phase is analyzed). For those reactions with low acidity, the initial selectivity of dimers is not 100% (close to 80%) because of the presence of glucose, even at very low conversions. This fact suggests the existence of terminal anhydroglucose units weakly linked to the general polymeric structure. These terminal units are easily hydrolyzed, resulting in an initial mixture containing oligomers but also glucose, as previously reported in the literature [2]. When using 0.02 and, mainly, 0.04%w/w, the high acidity increases the hydrolytic rate, and the relative weight of this glucose decreases because of the higher concentration of cellobiose.

As the reaction progresses, the decreasing selectivity of these dimers observed (more pronounced at higher acidity) is compatible with their hydrolysis into monomeric units. This behavior suggests that the hydrolysis at these diluted acidic conditions is limited, making total conversion not possible to reach. In fact, cellulose conversion never exceeds 50%, although results with 0.04% demonstrate the advance of the reaction to subsequent steps once reached this threshold. According to the literature, glucose suffers dimerization in an acidic medium, establishing an equilibrium with cellobiose [3, 4]. Analyzing the results in concentration units (see **Figure 4.3**), this contribution cannot be discarded.

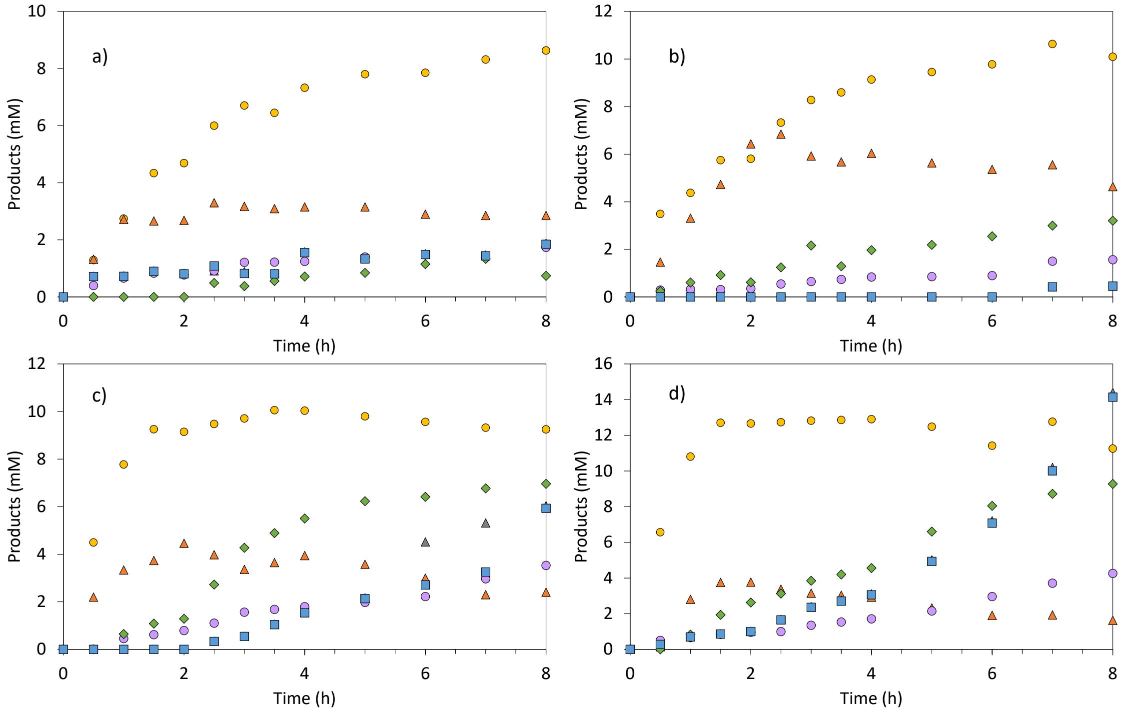

Figure 4.3. Products evolution obtained for the cellulose hydrolysis at 140 °C using 8% β-zeolite as a function of the HCl concentration: (a) absence of HCl; (b) 0.005 %; (c) 0.02 %; and (d) 0.04 %. Symbols: (●) dimers; (▲) glucose; (◆) HMF; (●) AHG; (■) levulinic acid

Glucose selectivity decreases with the advance of the reaction because of the simultaneous appearance of two different compounds: HMF and anhydroglucose (AHG). Both compounds are obtained by glucose dehydration, being catalyzed by the same acidic sites. In the presence of β zeolite, HMF prevails over AHG because the Lewis acidity of the zeolite promotes the previous glucose isomerization into fructose, a requirement to promote the pathway to HMF, according to the literature [5, 6]. However, fructose is not included in Fig. 4.2 since its selectivity is always lower than 1% (it dehydrates rapidly).

AHG is a final product, with a soft but continuous increasing trend. On the other hand, HMF can suffer rehydration, mainly under strong acidity, obtaining levulinic and formic acids. Both compounds are equimolar produced, their differences in selectivity being explained by the equation used (in carbon basis). These compounds are very relevant when cellulose conversion exceeds 30%.

This analysis was done considering theoretical cellulose conversion since its solid character makes its sampling impossible with the actual reaction system. To evaluate the carbon balance and determine the representativeness of these results, the reactions were repeated, reducing the time to 8 h (time that is expected to be the optimum one to maximize the HMF selectivity). The temporal profiles show (Fig 4.3) a discrepancy lower than 5% between both repetitions. **Figure 4.4** compares the results obtained after 8 h, in this case considering the conversion as the difference in weight between the initially introduced solid and the one recovered after the reaction. The recovered solids maintain their white color, discarding the presence of adsorbed humins, polymers obtained from glucose derivatives under high temperature and/or acidity [7, 8].

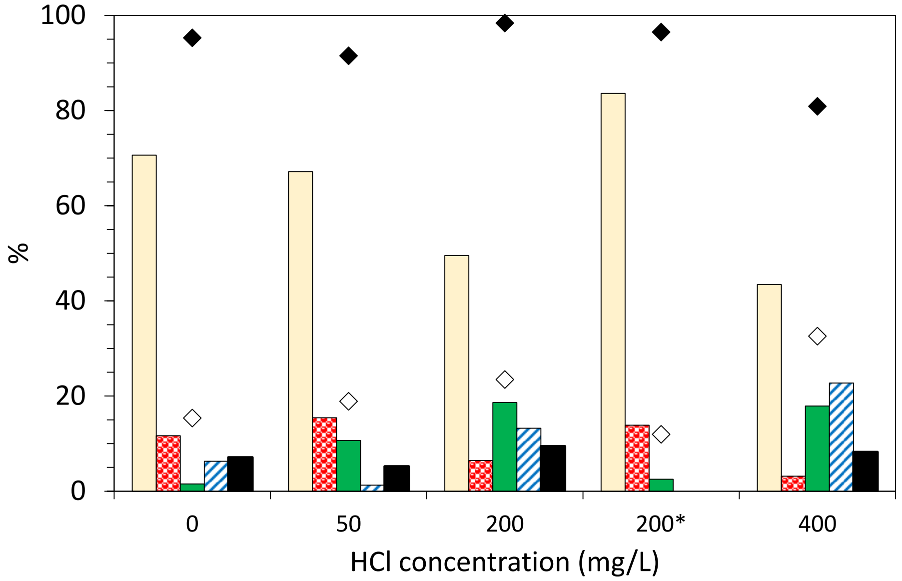

Figure 4.4. Cellulose conversion (◇), carbon balance (◆) and products selectivity obtained in the cellulose hydrolysis at 140 ºC using 8% of zeolite as a function of the amount of HCl. Bars corresponding to dimer (yellow), glucose (red bubbles), HMF (green), levulinic acid (blue lines) and anhydroglucose (black). (*) Experiment in the absence of zeolite

The reaction performed in the absence of HCl mainly produces the dimer (9 mM), the compound that represents 70.6% of the products detected. Glucose is also obtained, being 11.7% selectivity. In the absence of any catalyst, the dehydration is almost negligible, HMF being less than 3% of the total products. The high carbon balance (95.3%) indicates the representativeness of these data, suggesting that the production of soluble humins or other undetected liquid compounds is not very relevant.

The positive action of HCl is observed, leading to a linear dependence of cellulose conversion on acid concentration, from 15.4% in the absence of HCl to 32.6% when working with 0.04% of this acid (results after 8 h). The concentration of glucose dimer (cellobiose) remains almost constant despite the amount of HCl present, reaching final values (9-10 mM). These values are far from the maximum solubility of this compound (1g/mL) discarding the saturation of the sample. Acidity also promotes the HMF formation and the selectivity toward this compound rises to 10.7, 16.4, and 17.9%, with 0.005, 0.02, and 0.04% of HCl, respectively. At 0.02, and 0.04% of HCl, the rehydration of this compound is significantly promoted, levulinic and formic acid being the majority compounds detected (31.3 and 40.6 mM, selectivities of 13.6 and 22.7%, respectively). The good carbon balances obtained when working at 0.005 and 0.02% of HCl (91.5 and 98.4%) demonstrate a high control of the reaction. On the contrary, the significant depletion observed at 0.04% (80.9%) suggests that a relevant amount of cellulose is transformed into soluble humins. In global terms, 0.02% of HCl (pH 2.03) is suggested as the optimum acidity to enhance the HMF production.

As introduced before, fructose is only detected in traces. To identify if this fact is due to a null activity of the zeolite (i.e., all the HMF is produced directly by glucose dehydration) or if the fructose dehydration is so fast that fructose instantaneously disappears, a particular experiment with 0.02% of HCl but in the absence of zeolite is performed (see Fig. 4.4). Results after 8h demonstrate the relevance of these Lewis sites. When no zeolite is included, the HMF selectivity decreases by more than 84% (from 16.4 to 2.5%). Moreover, conversion is reduced by half in absence of zeolite, and the final mixture is enriched in dimers (83.6%), indicating the greater difficulty of breaking these structures and allowing the reaction to progress toward the final products. These effects are assumed to be due to the presence of Bronsted sites in the zeolite (proton form). Thus, solid cellulose particles migrate to the surface of the zeolite, which donates protons. The solid protonated cellulose on the surface of cellulose particles can degrade since part of it can dissolve and react with water. The corresponding chemisorption of oligomers justifies the improvement in glucose production, whereas the increase in HMF is justified by the previously mentioned role of Lewis sites. This experiment also corroborates the dimerization equilibrium between glucose and cellobiose since comparing the results at the same cellulose conversion, the total yield to products obtained without the zeolite is significantly lower than with it. As dehydration steps consume glucose, this equilibrium is shifted.

To sum up, both catalysts (HCl and zeolite) contribute to all the steps of the hydrolysis of cellulose. Increasing the acidity is discarded as a valid option to promote HMF production since the impact on the levulinic acid formation is more relevant, with the subsequent decrease in the HMF selectivity. Thus, increasing the HMF concentration and selectivity requires evaluating other options, such as modifying the temperature, considering cellulose pretreatments to increase the hydrolysis capacity, or working with biphasic systems that could selectively extract the HMF to prevent its decomposition into levulinic and formic acid.

4.1.2. Influence of the severity of the reaction conditions

According to the literature, temperatures lower than 200-220 ºC limit the depolymerization of cellulose only to its amorphous content [9]. However, the presence of levulinic acid is relevant at 140 ºC and higher temperatures are assumed to increase its production. Thus, higher temperatures are not considered in this work, trying to balance the thermal activation by the co-presence of two catalysts (HCl and β zeolite). Two lower temperatures were studied (120 and 130 ºC) considering that these conditions could minimize the HMF rehydration [3], increasing the selectivity by reducing its degradation into levulinic and formic acid. The main results after 8h are summarized in **Figure 4.5.**

As expected, cellulose conversion decreases when reducing the temperature (from 23.1 to 14.9%, from 140 to 120 ºC). Higher temperatures promote all the steps, decreasing the dimer selectivity (from 60.4 to 50.9) and increasing the final products, levulinic and formic acids (from 6.6 to 13.6%). As to HMF, its selectivity is maximum at 130 ºC (19.6%) but differences are not relevant enough to balance the differences in conversion. Thus, the maximum amount of HMF (18.6% of selectivity) is obtained at 140 ºC.

The temporal evolution of all the compounds (see Fig. 4.6) is congruent with the intermediate character of the target compound (HMF). Thus, larger reaction times increase the cellulose conversion (20.5, 28.3 and 43.1% of cellulose conversion after 24h with 200 mg/L of HCl at 120, 130 and 140 ºC, respectively) but the HMF concentration slightly increases (from 4.5 to 5.0 mM, from 5.3 to 6.8 mM, and from 6mM to 9.6 mM, after 8 and 24 h at the temperatures considered in this study) because of the promotion of further steps.

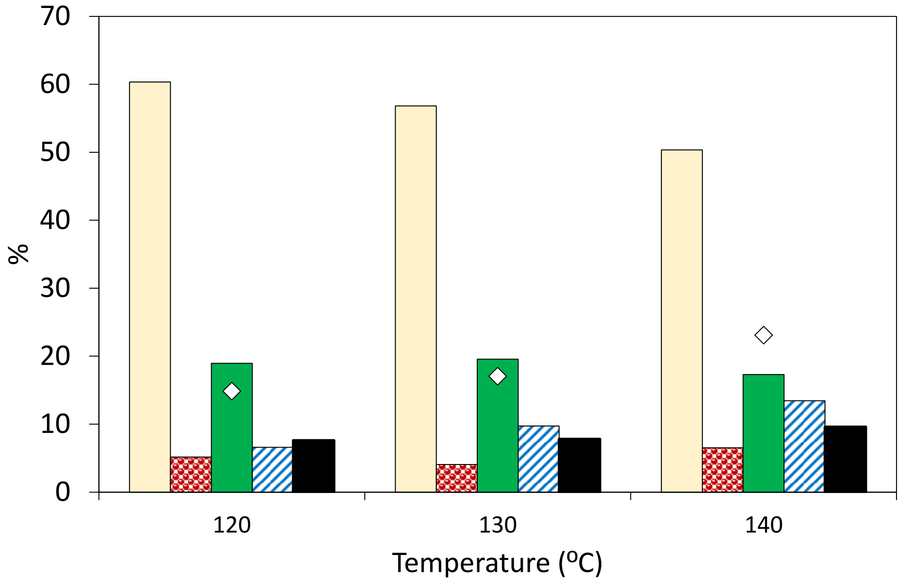

Figure 4.5. Cellulose conversion (◇) and products selectivity obtained in the cellulose hydrolysis using 8% of β-zeolite and 0.02% of HCl as a function of the temperature. Bars corresponding to dimer (yellow), glucose (red bubbles), HMF (green), levulinic acid (blue lines) and anhydroglucose (black)

Consequently, maximizing the HMF selectivity requires an equilibrium between temperature, acidity, and time. The combined severity factor (CSF) concept was used to integrate the effects of these three conditions [10]:

$$CSF = \log\left(t \cdot \exp\left(\frac{T}{14.75}\right)\right) - pH \qquad \textbf{[4.4]}$$

where t is the reaction time of hydrolysis in minutes, T is the reaction temperature in Celsius, and pH is the acidity of the aqueous solution measures before the reaction (4.92, 2.76, 2.03 and 1.76, for 0, 0.005, 0.02, and 0.04% of HCl, respectively).

Figure 4.6 displays the effect of variations in conditions (CSF) on the HMF and levulinic acid concentration. In the case of HMF, the results show a cloud of data points where the results with 0.005 and 0.02% of HCl overlap. In other words, the concentration of HMF increases as the severity of the process increases, regardless of whether this increase was achieved by increasing reaction time, temperature, or HCl concentration.

The results obtained with the highest HCl concentration (0.04%) show a different profile, characterized by lower concentrations at low CSF values and a very narrow area of higher concentrations (never exceeding those obtained with 0.02%). This instability rules out the use of these conditions.

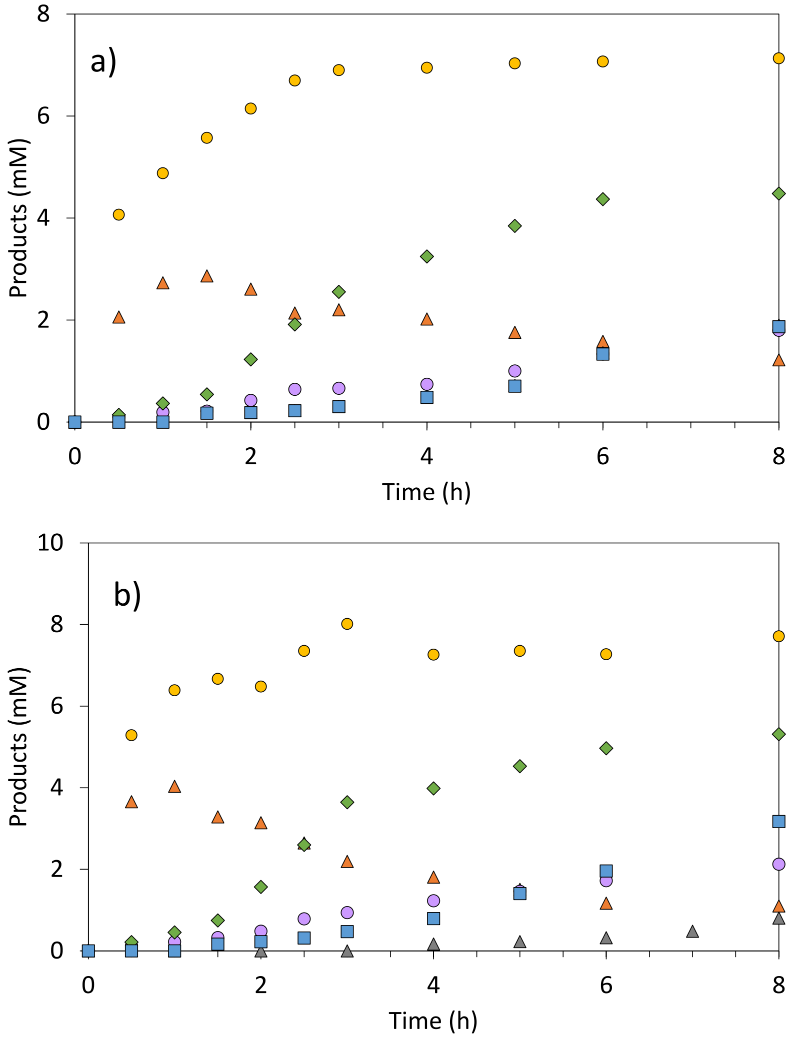

Figure 4.6. Products evolution obtained for the cellulose hydrolysis using 8% β-zeolite and 0.02 % of HCl as a function of the temperature: (a) 120 ºC; (b) 130 ºC. Symbols: (●) dimers; (▲) glucose; (◆) HMF; (●) AHG; (■) levulinic acid

The evolution of levulinic acid demonstrates increasing trends with CSF, requiring a minimum CSF of 4 to start observing it, and an exponential increase for values greater than this value. However, unlike what was observed with HMF, the results are scattered depending on the acid concentration. Thus, when working with 0.04%, higher levulinic acid values are obtained at lower CSF values.

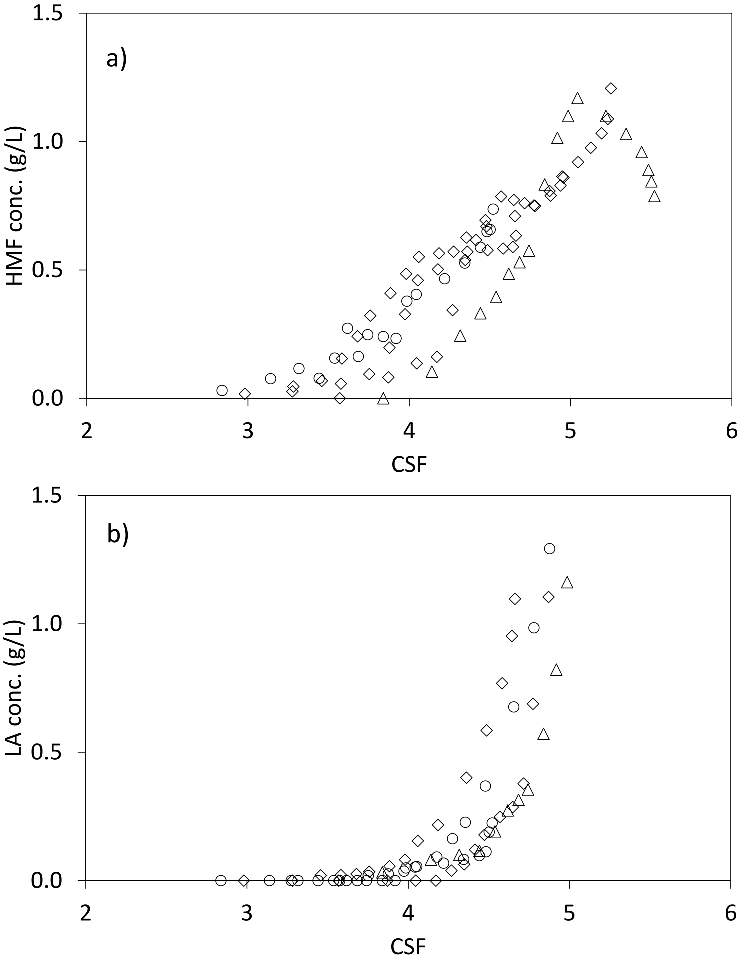

Figure 4.7. Effects of CSF on concentration of (a) HMF, and (b) levulinic acid. Data obtained with 0.005% of HCl (○);0.02% of HCl (◇);0.04% of HCl (△)

In conclusion, the maximum HMF selectivity (18.6%) obtained in this parametric study is higher than most of the typical values proposed in the literature for similar systems (10% at 150 °C [11], 15.5% at 220 °C [12]), suggesting a good activity of the catalytic system considered. Higher selectivities (up to 33%) have recently been proposed for a similar aqueous-phase system, using modified zeolites as heterogeneous catalysts [13]. Although this result is very relevant, a direct comparison with this work is not possible because of the different crystallinity degree of the raw material used, from 33-55% in the case of the bibliography, >82% in this case.

On the other hand, this study also demonstrates an HMF final yield (4.3%) conditioned by the low cellulose reactivity (23% conversion). This yield is congruent with previous literature, with values in the range of 2-7% [11, 12], suggesting the need for other strategies to increase the reactivity of cellulose.

4.1.3. Improving hydrolysis behavior by chemical liquid-phase pre-treatments.

The production of HMF by cellulose hydrolysis under dilute acid conditions is limited by the refractory character of the cellulose. Its almost complete crystallinity restricts the access of the catalyst to surface irregularities. A previous pretreatment could reduce the crystallinity of this biomass, increasing the number of potential active sites in the cellulose fiber for starting hydrolysis reactions and, subsequently, increasing the HMF production.

Three different chemical pretreatments were considered in this work, using a mineral acid (HCl), an oxidant (H_2O_2), and a chemical with both properties (HNO_3). In the three cases, the influence of the dosage in the pretreatment was studied. All the pretreatments were carried out at room temperature (20-25 ºC) to limit the activity of these acids to reduce the crystallinity of the cellulose, making its surface more accessible during the reaction but without promoting its hydrolysis or any degradation of the bulk structure that could produce liquid compounds during the pretreatment. Thus, pretreated cellulose could be recovered by filtration and the acid solution could be reused, minimizing the environmental and economic impact of using these chemicals. **Figure 4.8** shows the results obtained after 24 h hydrolysis.

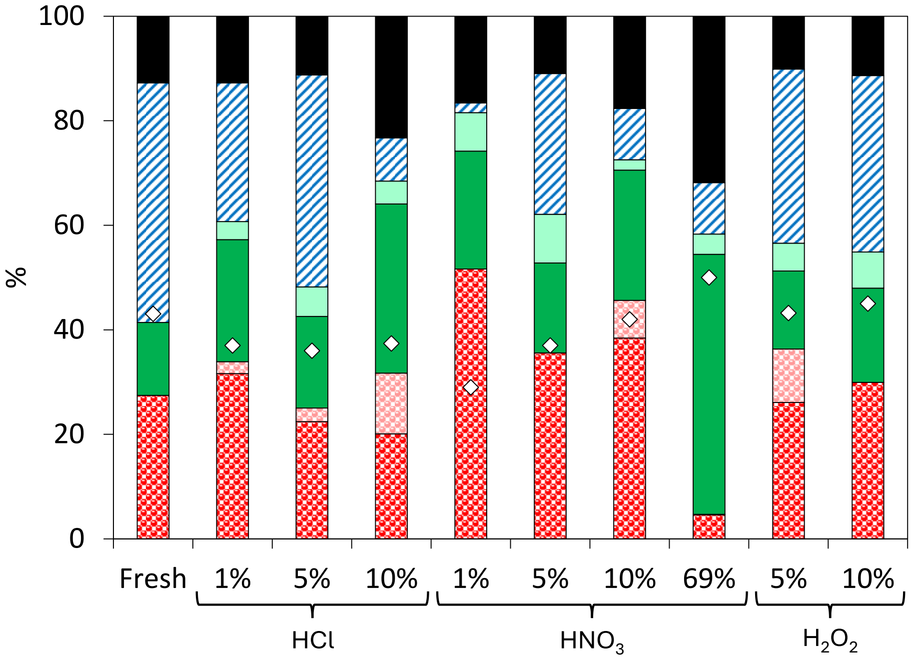

Figure 4.8. Results after 24h of cellulose hydrolysis at 140 ºC using 8% of β-zeolite and 0.02% of HCl as a function of the cellulose pretreatment used. Diamonds correspond to cellulose conversion, selectivities are shown in bars: C6 sugars (red bubbles), C5 sugar (pink bubbles), HMF (green), furfural (light green), acids (blue bars), AHG (black)

Despite the intermediate character of HMF, this reaction time corresponds to the maximum selectivity towards this compound of all the pretreated samples. The complete temporal profiles are included in **Figures 4.9-11**.

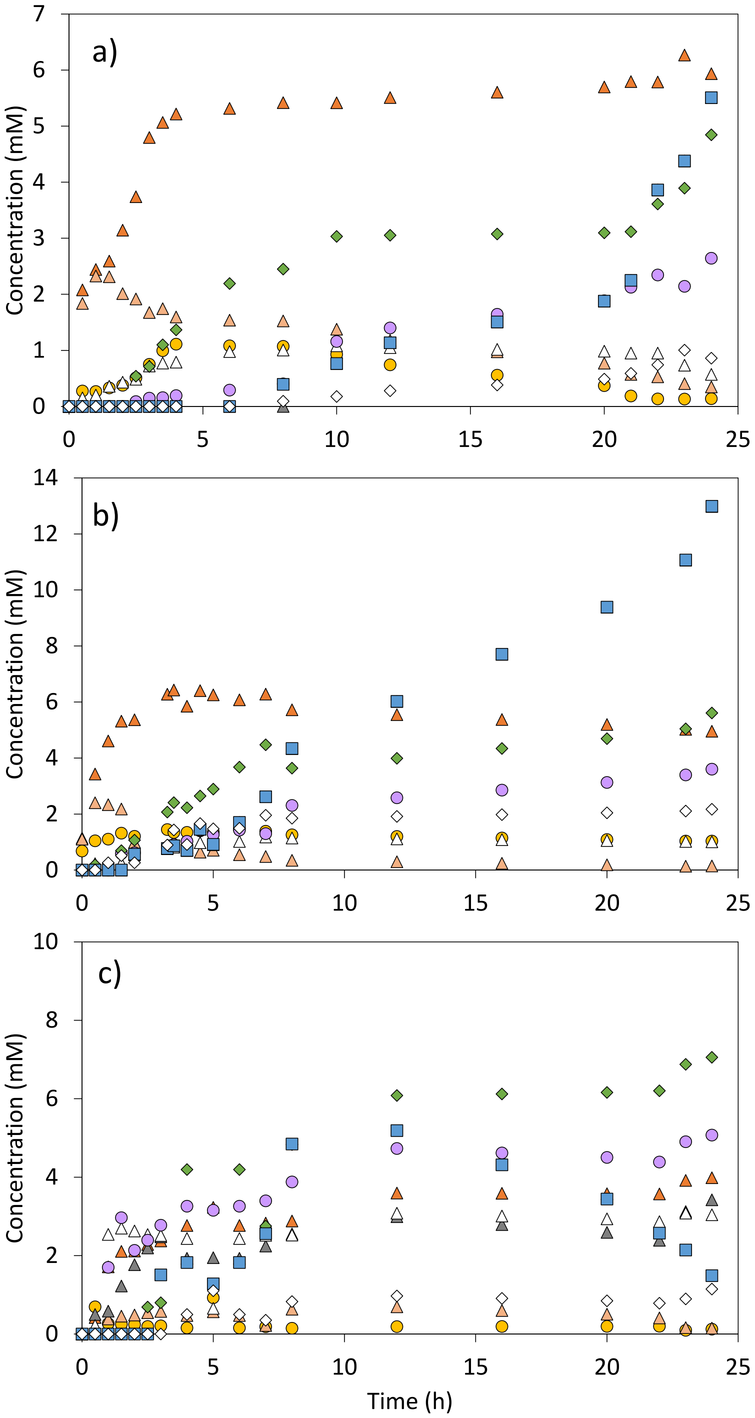

Figure 4.9. Products evolution obtained for the cellulose hydrolysis at 140 ºC using 8% β-zeolite and 0.02 % of HCl using acidic pretreatment: (a) 1% HCl; (b) 5% HCl, and (c) 10% HCl. Symbols: (●) dimers; (▲) glucose; (▲) fructose; (△) arabinose; (◆) HMF; (◇) furfural; (●) AHG; (■) levulinic acid

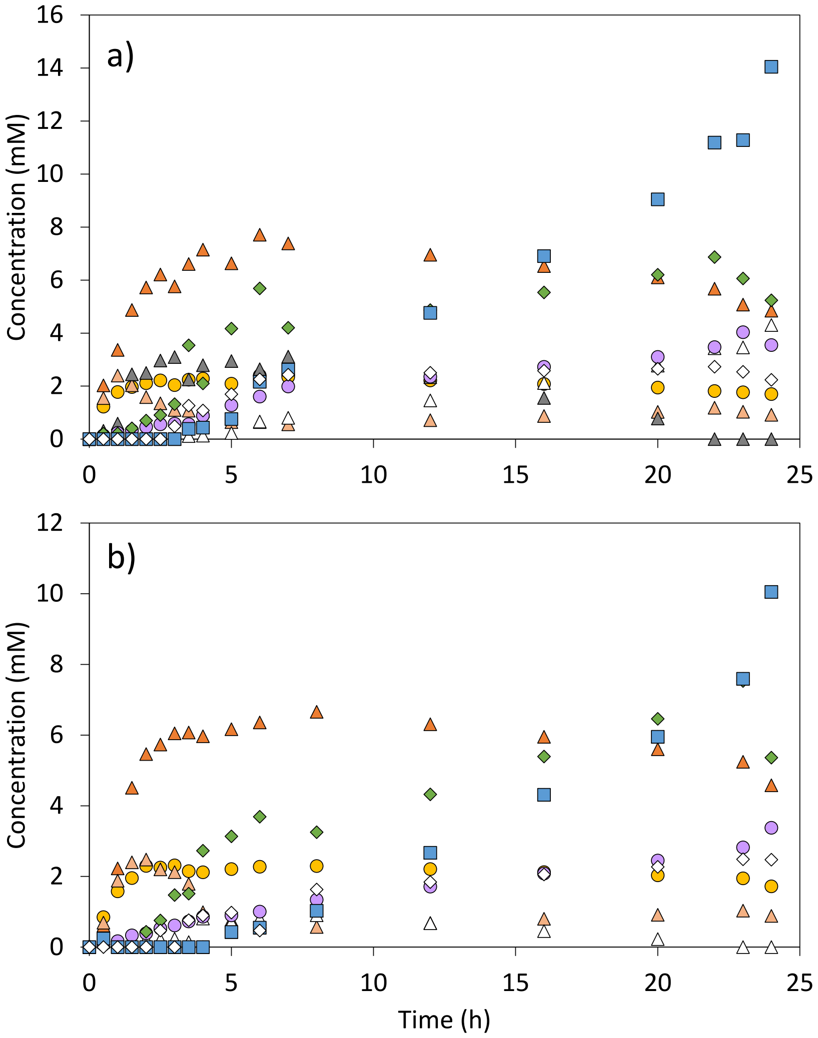

Figure 4.10. Products evolution obtained for the cellulose hydrolysis at 140 ºC using 8% β-zeolite and 0.02 % of HCl using oxidizing pretreatment: (a) 5% H_2O_2; (b) 10% H_2O_2. Symbols: (●) dimers; (▲) glucose; (▲) fructose; (△) arabinose; (◆) HMF; (◇) furfural; (●) AHG; (■) levulinic acid

In terms of conversion, pretreatments with HCl do not offer any improvement, obtaining very similar values in the three case studies (36-37.5%). These conversions are lower than the one obtained with the fresh cellulose (43%). This fact suggests that the potential surface degradation produced by this pretreatment does not lead to more accessible terminal glucose, but rather, a portion of the original terminal glucose (amorphous region) is dissolved during the pretreatment, removing the active sites of the fiber for starting hydrolysis reaction.

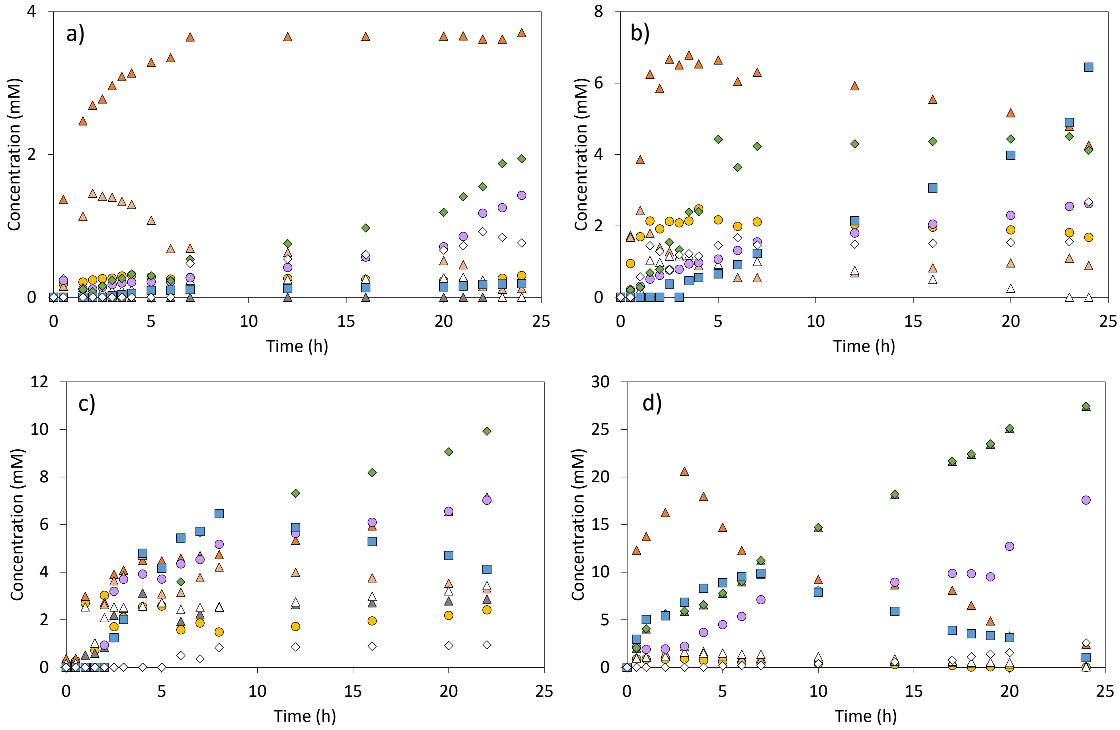

Figure 4.11. Products evolution obtained for the cellulose hydrolysis at 140 °C using 8% β-zeolite and 0.02 % of HCl using acidic-oxidizing pretreatment: (a) 1% HNO_3; (b) 5% HNO_3; (c) 10% HNO_3; (d) 69% HNO_3. Symbols: (●) dimers; (▲) glucose; (▲) fructose; (△) arabinose; (◆) HMF; (◇) furfural; (●) AHG; (■) levulinic acid

To support this hypothesis, fresh and pretreated celluloses were characterized by different techniques, trying to identify the main effect of each pretreatment on the cellulose structure. **Figure 4.12** shows the diffractograms of all the samples, including the theoretical main diffraction peaks of the three polymorphs of cellulose, according to the molecular orientation and hydrogen-bonding network: cellulose I, cellulose II, and cellulose III. The analysis of these XRD results is shown in **Table 4.1**.

Native cellulose shows the typical XRD patterns of cellulose I (the expected polymorph of cotton cellulose), with diffraction peaks at 2θ = 14.5°, 16.5°, and 22.5° attributed to the planes of $(1\,1\,\bar{0})$, $(1\,1\,0)$ y $(2\,0\,0)$, respectively [14]. This cellulose has a crystallinity index of 82.5% and, according to Scherrer's equation, a crystallite size of 7.3 nm. The region around 2θ=21° could be initially attributed to the plane $(2\,0\,0)$ of cellulose type III. However, the lack of signals at 11.7° and 17° (planes $(1\,1\,\bar{0})$ and $(1\,1\,0)$ of this polymorph) discards this hypothesis suggesting a contribution of a no well-ordered polymeric region. The typical rod-like structure of crystalline cellulose is observed by SEM (**Figure 4.13**). The purity of this material is corroborated by the results after treating this sample with NaOH; the sample has a non-cellulosic material percentage of less than 2%.

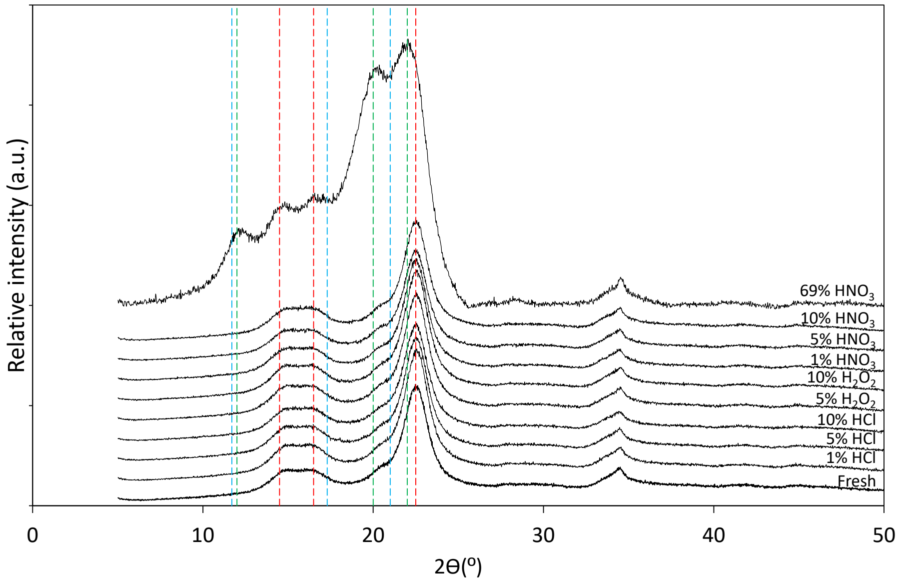

Figure 4.12. XRD patterns for different pretreated celluloses. XRD peaks of cellulose type I being identified by red lines; type II in green; type III in blue

Table 4.1. Crystallinity index (CrI), average crystallite size and non-cellulosic phase concentration of fresh and pretreated celluloses

Sample	CrI	Crystallite size (nm)	Non-cellulosic phase (%)
Fresh cellulose	82.1	7.3	1.8
1% HCl	82.4	9.2	3.6
5% HCl	82.4	9.5	13.4
10% HCl	82.5	9.9	24.2
5% H_2O_2	82.9	7.9	48.6
10% H_2O_2	83.2	9.2	49.1
1% HNO_3	82.8	9.3	38.3
5% HNO_3	83.1	9.5	38.8
10% HNO_3	83.2	10.0	39.9
69% HNO_3	37.8	7.8	41.9

Cellulose type I remains the predominant polymorph in samples pretreated with HCl, with no significant differences observed in comparison to the untreated cellulose. In fact, SEM micrographs do not reveal any significant difference (see Figure. 4.13). The effects of the pretreatments become evident through an increase in the crystallite size (from 7 to 9-10 nm) with a minimal rise in the crystallinity index. Both effects are congruent with the solubilization of the weakest parts of the surface (amorphous regions). The limited amount of weak β-glucosidic bonds on the parent surface (those susceptible to attack at these soft conditions) explains the low sensitivity of these results to the amount of HCl used.

The progressive increase in the percentage of non-cellulosic material, from 1.8 to 24.2%, explains the product distribution obtained, with an increasing selectivity in C_5 derivatives, both sugars (arabinose) and aldehyde (furfural), as the HCl concentration increases. It is suggested that the acidic pretreatment interacts with the terminal glucose of cellulose, altering their structure in such a way that, under reaction conditions (140 ºC, copresence of a heterogeneous catalyst), these terminal units suffer not only hydrolysis but also decarbonylation, leading to arabinose and its aldehyde (total selectivity of 16% with 10% HCl). The presence of these molecules, although not the most common situation, has already been referenced in the literature under oxidative conditions [15]. The hydrolysis and dehydration rates of C5 sugars are slower than the corresponding ones of glucose [16], justifying the lower conversions obtained. Moreover, furfural is significantly more stable than HMF, also explaining the lower relevance of acids in the reaction mixture. As to the target compound, the selectivity to HMF increases as the HCl concentration does, reaching a maximum of 32.3%, a value almost three times higher than the one obtained in the absence of any pretreatment.

Regarding the oxidizing pretreatment (H_2O_2), the conversion obtained with 5% of H_2O_2 is the same as with the fresh sample (43%). A slight increase is obtained when using 10% of H_2O_2, reaching a final conversion of 45%. Analyzing the products, the presence of C5 sugars and aldehydes is also relevant (similar selectivities than when using HCl), but the percentage of HMF only increases from 14 to 18%.

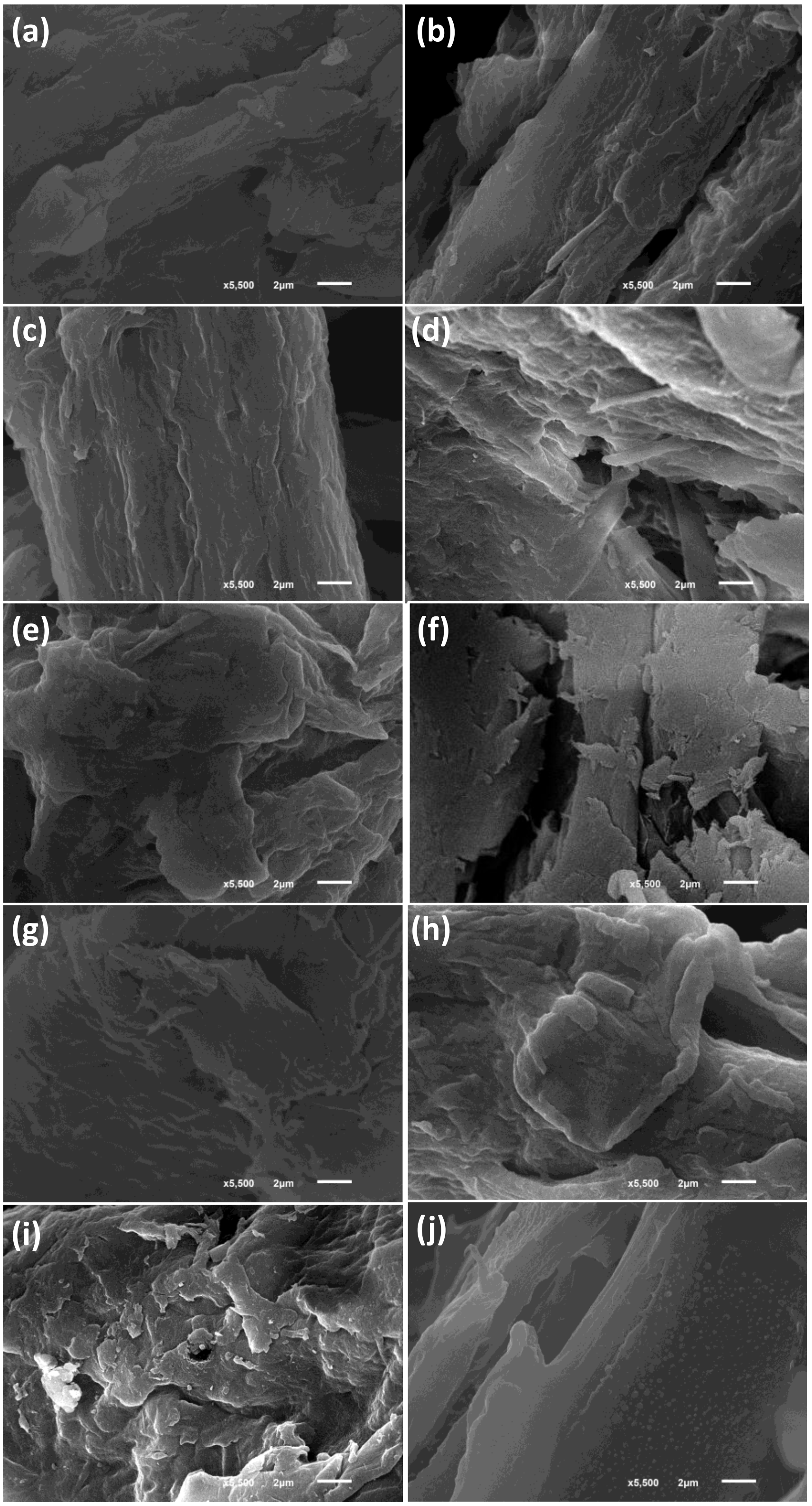

Figure 4.13. SEM micrographs of (a) raw microcrystalline cellulose; (b) 1% HCl; (c) 5% HCl; (d) 10% HCl; (e) 5% H_2O_2; (f) 10% H_2O_2; (g) 1% HNO_3; (h) 5% HNO_3; (i) 10% HNO_3; (j) 69% HNO_3

XRD diffractograms of these samples discard a deep change in the surface crystallography (Figure 4.12), cellulose type I being the main polymorph observed. With this chemical, the effects on the crystallinity index and the crystallite size are more evident than with HCl. The high percentage of "amorphous phase" (>45% in both cases) is not congruent with the conversion reached or the product distribution, suggesting that this pretreatment partially damages the cellulose surface, obtaining a solid that cannot lead sugars by acidic hydrolysis. Based on this fact, higher H_2O_2 concentrations were not tested.

Results with HNO_3 (acidic and oxidizing activity) demonstrate a high influence of concentration, obtaining lower conversions when using 1% (29%) and higher conversions (50%) when using a high-concentrated acid. This evolution is the result of two opposite effects: the acidic behavior of HNO_3 promotes the hydrolysis and solubilization of terminal oligomers during the pretreatment, limiting the potential conversion, whereas its oxidation activity (stronger than in the case of H_2O_2) partially degrades the cellulose surface increasing the terminal units available for the reaction. Increasing concentration remarks this positive effect because the number of sugars available for solubilization during pretreatment is limited, while the capacity to degrade the surface through the oxidative action increases. Based on this analysis, oxidative pretreatment is more effective than the acidic one.

The morphology and crystalline structure of samples treated with 1, 5, and 10% of HNO_3 are very similar and the cellulose I polymorph is the predominant one in the three cases. 1% of nitric acid is enough to produce the main differences, both in the crystallinity index and the crystalline size, whereas almost null differences were observed when increasing the nitric acid concentration. In agreement with XRD results, a continuous but soft increase in the amount of non-cellulosic percentage is observed, highlighting that more than 95% is obtained with only 1% of HNO_3. This analysis does not allow us to determine the specific amorphous character of this fraction. Conversion results suggest that this fraction is easier to hydrolyze after being treated with high HNO_3 concentration.

Pretreatment with 69% of HNO_3 demonstrates to be significantly more effective in deeply modifying the cellulose surface. Diffraction peaks of cellulose type I and type II ($2\theta=12^{\circ}$, 20°, and 22°[14]) coexist in this sample. The probable explanation for this result is that the crystalline regions swelled during the attack with HNO_3, leading to a rearrangement of the cellulose crystalline structure. This effect has been previously observed when cellulose is treated with strong mineral acids [17]. Cellulose type II is more stable than cellulose type I, justifying the low effect on conversion of this relevant change.

The degradation produced by this pretreatment is very effective in terms of selectivity, reaching 50% of HMF. Furfural is also obtained, reaching a final selectivity of 4%. The low sugar selectivity (<5%) demonstrates that, despite this pretreatment having limited effectiveness in increasing the availability of hydrolysable sugars, it does reduce the stability of glucosidic bonds, favoring the progression of the reaction toward the dehydration stage.

Selectivity results are comparable to those proposed in the literature, even when using more severe pretreatment conditions [18]. The selective extraction of HMF in an organic solvent could be an interesting option for increasing its selectivity. The purification of the stream is out of the scope of this work, but we have deeply studied this approach in a previous study using glucose as a reactant and the main conclusions could be extrapolated to this system [2]. On the contrary, the maximum yield obtained in this study (18%) is slightly lower than the optimum values reported in the literature (up to 60% for aqueous reactions), as discussed in the review previously indicated. However, the direct comparison is unrealistic due to the different conditions under which they are conducted. Those employed in this study, both for pretreatment and reaction, including temperatures, acid concentrations, and catalyst amounts, are significantly milder than those suggested in previous studies, resulting in a more sustainable process.

4.1.4. Reusability tests

The solid after 24 h of reaction time (using cellulose pretreated with 69% of HNO_3) was recovered by filtration and resuspended in a fresh HCl solution for a new hydrolytic batch. This solid includes zeolite as well as non-reacted cellulose, and the lack of any reaction (conversion lower than 1%) and, more relevant, the absence of glucose is congruent with the recalcitrant character of cellulose since the first step of hydrolysis does not need the catalytic activity of the zeolite. Thus, extending the reaction over 24 h is not a good approach to increase HMF productivity.

This result does not give clear information about possible zeolite deactivation since the role of this catalyst is mainly relevant for glucose isomerization. To study the zeolite stability, a new cycle feeding the recovered solid (mixture of used zeolite and recalcitrant cellulose) into a new cellulose suspension (using pretreated cellulose as fresh reactant) was performed. In this batch, the recalcitrant cellulose is considered as an inert solid and new pretreated-cellulose (69% HNO_3) and HCl is introduced to guarantee the initial conditions. Results after 24 h are plotted in **Figure 4.14**. As observed, the final mixture is enriched in reductive sugars, with a total selectivity of 76.3% (28.6% of arabinose, 23.6% of fructose and 24.1% glucose). A quite relevant HMF selectivity is also observed (14.2%). The presence of fructose indicates that the zeolite is still partially active (glucose isomerization is catalyzed by Lewis acidity). The lower conversion reached in this second cycle (22.8 % vs. 50%) as well as the lack of total fructose dehydration corroborates the initial hypothesis that Bronsted acid sites of the zeolite collaborate with HCl catalyzing the cellulose hydrolysis and the dehydration steps and these sites are at least partially deactivated after the first cycle. A possible reason for this deactivation could be the adsorption of cellulose oligomers or humins precursors, both aspects being discarded according to the good carbon balance obtained at these mild conditions (98.4%, see Fig. 4.4).

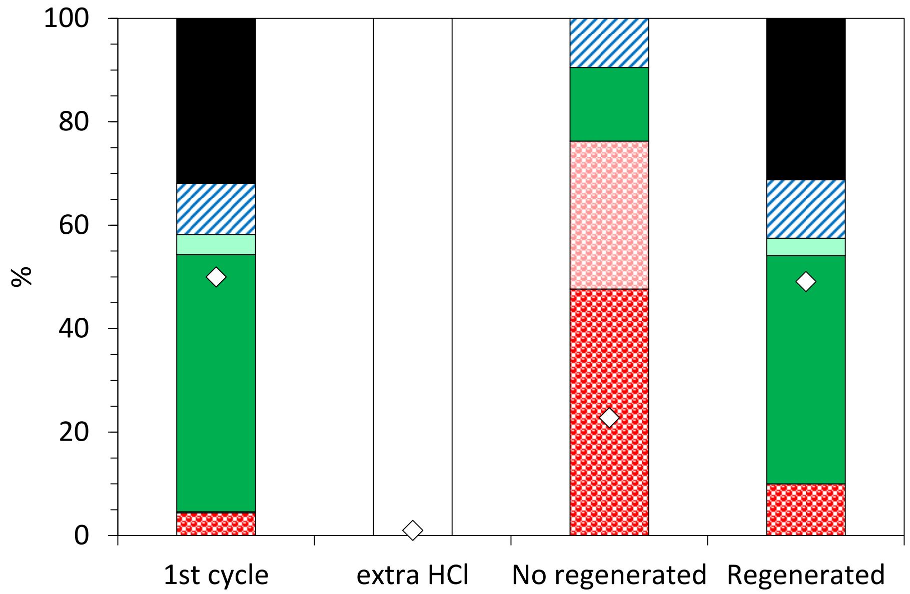

Figure 4.14. Stability tests of pretreated cellulose (69% HNO_3) hydrolysis at 140 ºC using 8% of β-zeolite and 0.02% of HCl. Results obtained after 24 h. Diamonds correspond to cellulose conversion, selectivities are shown in bars: C6 sugars (red bubbles), C5 sugar (pink bubbles), HMF (green), furfural (light green), acids (blue bars), AHG (black)

An alternative explanation of these results is related to the method used to get the catalyst after the first reaction, suggesting that the remaining cellulose could be stuck on the zeolite surface, blocking the access to the active sites. To check this hypothesis, the solid recovered after the first cycle was calcined in furnace (550 ºC, 8h) to remove the cellulose. The zeolite after the thermal treatment was introduced in a new cycle with pretreated cellulose, the results after 24 h being summarized in Fig. 4.14. As observed, zeolite recovers its initial activity, obtaining very similar conversion (49.1%) and a product distribution enriched in HMF (44.1%) and AHG (32.2%). These results reinforce the interesting results obtained in the cellulose hydrolysis at soft conditions using a pretreatment based on HNO_3.

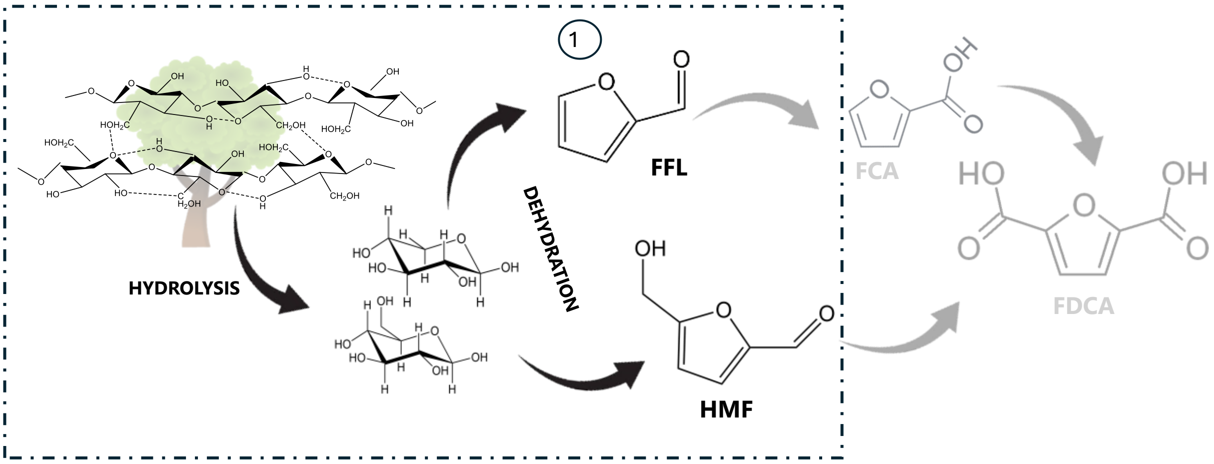

4.2. PRODUCTION OF 5-HYDROXYMETHYLFURFURAL AND FURFURAL BY PINE SAWDUST HYDROLYSIS

This work analyses the effects of the oxidative and reductive delignification pretreatments in the subsequent hydrolysis of pine sawdust, considered as a model biomass. The hydrolysis is studied using HCl as catalyst, considering the influence of temperature and acid concentration. The aim of this work is to identify the optimum conditions to enhance the production of different platform molecules, levulinic acid (LA) and 5-hydroxymethylfurfural (HMF) being the most relevant ones. Despite the HMF is faster produced after the isomerization of glucose into fructose by the presence of a Lewis acid [3, 19], a mineral acid is proposed as catalyst considering that temperature and time could balance the kinetic without introducing a solid catalyst that could significantly reduce the kinetic of the first step of the reaction, due to the low efficiency of the solid-solid interactions [20].

The sawdust conversion is calculated in terms of liquid-phase carbon yield, a concept involving the theoretical sawdust required to obtain all compounds detected in the liquid phase, extensively used in biomass conversion [1, 21, 22]. The direct use of the conversion calculated from solid weight measurement before and after the reaction is discarded since the temporal evolution cannot be analyzed based on this parameter, and the accurateness is limited by the presence of humins or other insoluble products (mainly the trimers). The liquid-phase carbon yield is calculated according to Equation (4.5):

$$\varphi_S = \frac{V \cdot \sum(n_i \cdot C_i) \cdot MW_C}{\%C \cdot m_{sawdust}} \cdot 100 \qquad \textbf{[4.5]}$$

where "V" is the volume of the solution; "C_i", the molar concentration of each compound detected in each liquid phase; "n_i", the number of carbon atoms in the molecule of "i" compound; "$m_{sawdust}$" is the mass of cellulose introduced in the reactor at the initial point; "MW_C" is the molar mass of carbon; and "%C" corresponds to the mass percentage of carbon in this sawdust, according to the elemental analysis.

The selectivity to any individual product quantified in the liquid phase is indicated in carbon basis, according to Equation [4.6]:

$$S_i\ (\%) = \frac{n_i \cdot C_i}{\sum_{j=1 \ldots i}^{n} n_i \cdot C_i} \cdot 100 \qquad \textbf{[4.6]}$$

being $n_i \cdot C_i$ the moles of carbon that contains the reaction product *i* and $\sum_{j=1 \ldots i}^{n} n_i \cdot C_i$ the sum of the moles of carbon corresponding to reaction products.

With the aim of guaranteeing the reproducibility of these analyses, each reaction was carried out at least twice. Considering the heterogeneity and complexity of this raw material, results were validated if the standard deviation between two experiments is lower than 7 %. In case of a higher discrepancy, a third experiment allowed defining the good results. As consequence, all the values shown in this work correspond to the average of two experiments.

4.2.1. Sawdust characterization before and after delignification

The amount of cellulose, hemicellulose and lignin was determined before and after the delignification pretreatments, the results being summarized in **Table 4.2.** Each analysis was carried out twice obtaining deviations lower than 3%. Results shown in Table 4.2 are the average values obtained with both analyses.

Data obtained for natural sawdust are in good agreement with typical composition of softwood, with percentages from 25 to 35 % of the three main polymers and less cellulose than hardwood [23]. From a macroscopic point of view, the oxidative pretreatment seems to be quite efficient, since the original brown color of the pine sawdust disappears, obtaining a white material. This evolution is a clear consequence of the lignin removal [24], and it is not totally observed in the case of the reductive pretreatment. However, the use of carbonaceous support could alter this appreciation.

Table 4.2. Sawdust characterization, in terms of fractionation and elemental analysis, before and after delignification pretreatment. Result expressed in dry basis.

	Natural Sawdust	Oxidative delignification	Reductive delignification
Extractives (%)	6.9	-	-
Cellulose (%)	24.9	58.1	38.5
Hemicellulose (%)	31.5	35.2	57.1
Lignin (%)	36.6	6.7	4.4
C (%)	46.9	40.7	42.6
O (%)	43.6	52.0	49.1
H (%)	6.2	6.3	5.5
N (%)	2.2	0.4	0.7
S (%)	1.1	0.6	2.1

Considering the quantitative analysis, the lignin content decreases considerably after both pretreatments, with the subsequent increase in the relative percentage of cellulose or hemicellulose. Thus, 81.5 % of lignin is removed in case of the oxidative delignification, whereas this value increases up to more than 88 % with the reductive method. These values are in good agreement with previous literature applied to other raw materials, suggesting that the reductive pretreatment is more effective than the oxidative one [25, 26]. Despite the similar delignification efficiency, significant differences between both methods related to the effects on the hydrocarbon structure are observed. It can be concluded that the reductive method mainly affects the lignin fraction, since the decrease in the proportion of this fraction directly correlates with the increase in the cellulose and hemicellulose ones (theoretical values corresponding to this delignification ratio: 42.2 % of cellulose and 53.4 % of hemicellulose), with slight differences (less than 4 %) in favor of hemicellulose. This fact indicates that only a small fraction of cellulose is partially degraded, obtaining a less crystalline structure with similar behavior as the hemicellulose. On the other hand, when the oxidative method is used, the expected percentages of cellulose and hemicellulose if only lignin was removed would be 41 and 52 %, respectively. Considering the high discrepancy with respect to the values obtained, a partial degradation of hemicellulose is produced. It removes a relevant fraction of external functional groups, obtaining a high ordered polymer, with a structure closer to cellulose than to the initial hemicellulose one. This conformation evolution could affect sawdust behavior in hydrolysis conditions, making it not possible to determine if this is a positive or a negative effect before being tested in the reaction. According to these results, the reductive pretreatment is less aggressive with the hemicellulosic structure of the sawdust, obtaining a more selective delignification than with the oxidative one.

This hypothesis is corroborated by elemental analysis, whose results are also summarized in Table 4.2. Regarding to the fresh material, values are similar to those proposed in the literature for other softwoods [27]. Results related to delignified samples are congruent with the removal of lignin, with a decrease in N and C, and a slight increase in the oxygen percentage (present in high amount in sugar structures). The decrease in the C/H ratio is also congruent with the removal of aromatic rings, typical structures of lignin fractions, and the prevalence of saturated compounds. The more marked changes observed with the oxidative method are in good agreement with its more aggressive character. This fact suggests that samples after reductive pretreatment have lost the lignin fixed structure, but the total decomposition is not achieved, with some S and N remaining in the solid sample.

4.2.2. Hydrolysis of fresh sawdust

The acidic hydrolysis of fresh sawdust (without any pretreatment) was carried out using HCl as catalyst, in the range 200 – 1000 ppm, to identify the optimum conditions, and to determine the effect the pH in these reactions. The mineral acid has been reported as an active catalyst for the hydrolysis of biomass polymers [28-30], but it could also enhance the subsequent steps of sugar dehydrations and degradations, obtaining acids and humins [1, 4, 31]. Thus, a balance between positive and negative effects requires a well-defined concentration, different for each type of wood, trying to enhance the production of desired platform molecules. A blank experiment was done to discard hydrothermal hydrolysis, despite being not expected considering the temperatures of the non-catalytic hydrolysis reported in the literature [32, 33]. The evolution of the liquid-phase carbon yield with time is analyzed in **Figure 4.15a**. Values plotted in this figure correspond to the average ones after two repetitions, obtaining standard deviations lower than 7 % in all cases, as observed by the small error bars. Then, in some cases, it cannot be appreciated.

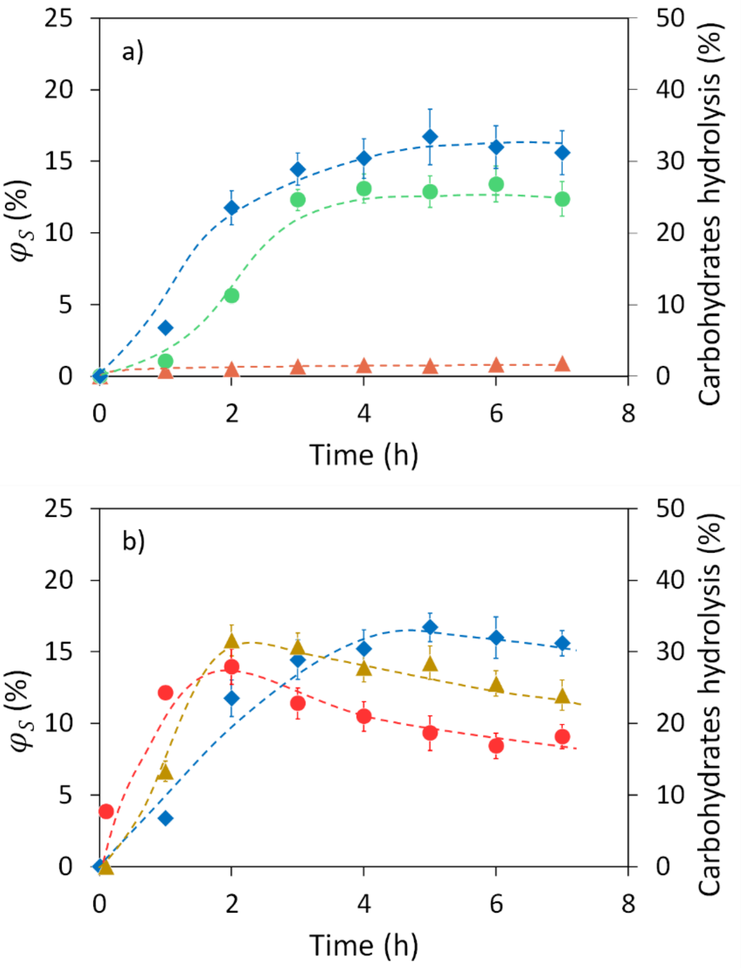

Figure 4.15. Temporal evolution of the liquid-phase carbon yield obtained in the hydrolysis of fresh sawdust as function of: (a) the acid concentration and (b) the reaction temperature. Data analyzed considering the total amount of sawdust (left axes) and only the potential sugars, cellulose, and hemicellulose (right axes). Results corresponding to (▲) 200 ppm of HCl, 140 °C; (●) 600 ppm of HCl, 140 °C; (◆) 1000 ppm of HCl, 140 °C; (▲) 1000 ppm of HCl,180 °C, (●) 1000 ppm of HCl, 220 °C

Results obtained with 200 ppm indicate an almost negligible degradation activity at these conditions, reaching constant yield in less than two hours (0.9 %). Considering the total amount of carbohydrates present in sawdust (cellulose and hemicellulose), this liquid-phase carbon yield represents 1.8 % of the maximum theoretical grade of hydrolysis. A clear evolution is observed when increasing the acidity up to 600 ppm, with a maximum carbon yield obtained after 4 h of reaction (12.5 %). This value corresponds to the hydrolysis of 24.6 % of the total sugar fractions in this sawdust. Once the maximum is reached, it keeps constant with the time, without observing any evolution when the reaction is extended up to 24 h. This result suggests that conditions are not severe enough to degrade the recalcitrant structure of biomass polymers. This hypothesis is congruent with results obtained with 1000 ppm of HCl, observing a faster hydrolysis that only reaches a maximum of 15.6 % (equivalent to 31.4 % of the sugar polymers). This value, obtained after 5 h, is not stable, followed by a continuous decrease for products detected, up to 9.8 % after 24 h. Considering the irreversible character of this reaction, the decreasing trend suggests that, at these conditions, different side reactions involving solid products (humins production) take place. According to the literature, humins are formed by cross-polymerization reactions between HMF, furfural (FFL) and sugars during the acid catalyzed hydrothermal hydrolysis [34, 35]. The fact that this is only observed in the most severe conditions suggests a different product distribution, which is analyzed in **Figure 4.16**.

This figure analyses the results in terms of carbon selectivities. The compounds considered for this analysis represent a carbon balance closure higher than 60 % in all cases, the value being higher as the acidity decreases (70.4, 75.4 and 60.5 %, for 200, 600 and 1000 ppm of HCl, respectively). Seven compounds derived from the typical route of acid-catalyzed biomass hydrolysis are detected: dimers (corresponding mainly, but not only, to cellobiose), three reduced sugars (glucose, arabinose and xylose), HMF (cyclic aldehyde derived from hexose), FFL (cyclic aldehyde derived from pentoses), levulinic and formic acids. These last two products are obtained by the rehydration of HMF in equimolar amounts. Considering that there is not any other reaction that consumes any of these acids, the same concentrations of both acids are obtained, so only levulinic acid is shown in the graphs (to prevent repeated information). An almost perfect carbon balance closure is obtained (higher than 90 % in all cases) if this analysis is completed with light alcohols detected at significant extent. These alcohols are identified as terminal units of sugar polymers, this location justifying the high amount obtained. However, as these compounds do not interfere in the main reaction scheme, they are not included in the following analyses.

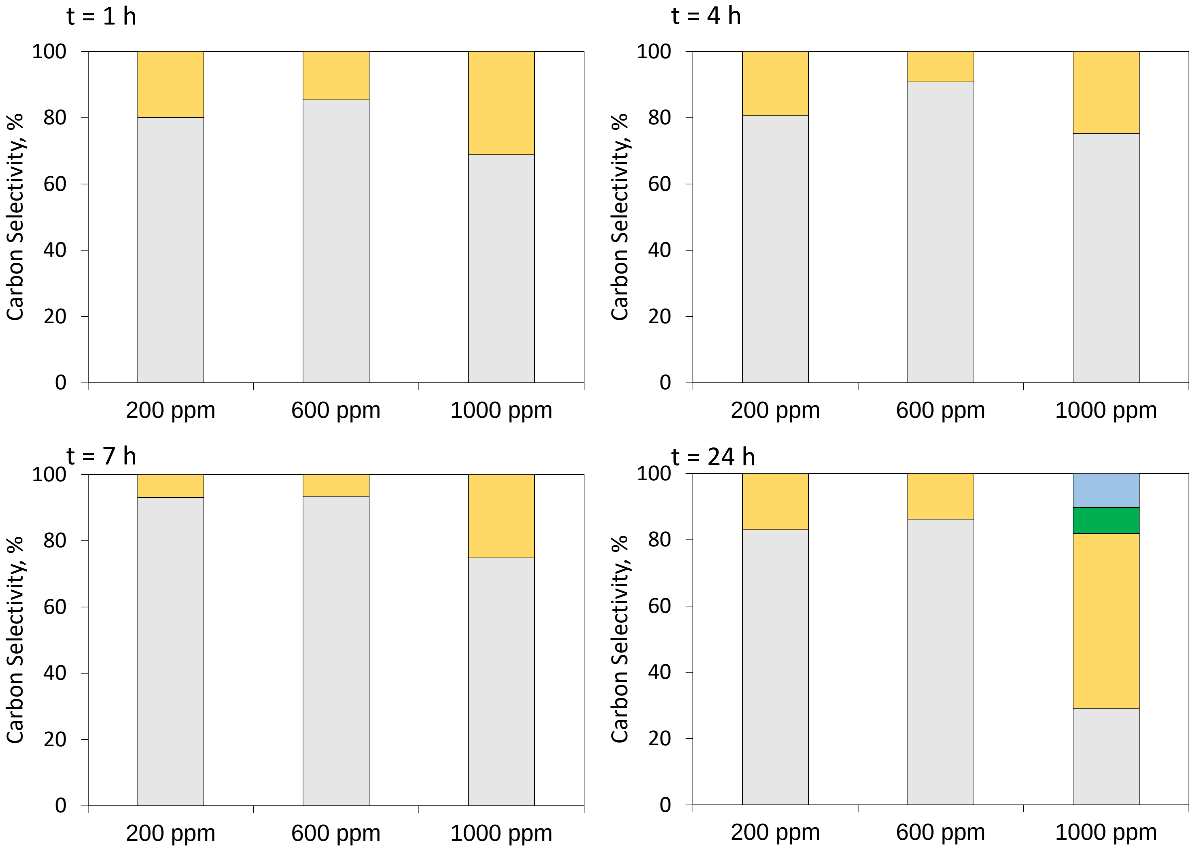

Figure 4.16. Comparative distribution of products selectivities obtained with fresh sawdust as function of the acidity. Data corresponding to dimers (grey); TRS (yellow); HMF (green); FFL (blue)

As anticipated by the soft conditions (low temperature and low acidity), dimers are the main product obtained during the first 7 h, despite the HCl concentration used. The absence of glucose and the detection of arabinose and xylose during the first 2 h is congruent with the recalcitrant structure of cellulose and the presence of pentoses in the external structure of hemicellulose (weakest bonds, the most easily hydrolyzed ones). With 200 and 600 ppm of HCl, the relative relevance of these pentoses decreases as the incomplete hydrolysis of cellulose increases, observing low amount of glucose and suggesting that most of the dimers correspond to cellobiose (experimentally tested). Thus, stable selectivities around 7 % of total reduced sugars (TRS) are obtained during the first 7 h. A slight improvement with the time is observed, with an increase up to 17 and 13.7 % of TRS, with 200 and 600 ppm. However, considering the low hydrolysis degree, these values only correspond to 68 and 277 ppm of TRS, respectively. As anticipated, no aldehydes or acids are observed under these conditions. The evolution with 1000 ppm is considerably different, with a relevant formation of TRS (24 % after 7 h, 52.8 % after 24 h, corresponding with 686 and

1020 ppm, respectively). Aldehydes formation is clearly observed after 24 h, with 8 % of HMF and 10.2 % of FFL, whereas levulinic acid is not detected in these experiments. The presence of aldehydes in the liquid phase is congruent with the promotion of humins and the decrease in the carbon balance.

According to these results, increasing the reaction temperature working with 1000 ppm of HCl is suggested as the following approach, trying to balance the promotion of the desired steps with the avoidance of side reactions. The influence of temperature was studied in the range 140-220 ºC, obtaining the evolution of the liquid-phase carbon yield observed in **Figure 4.15b.**

Experimental results follow the anticipated trend considering the positive effect of temperature in the kinetics and the relevance of side reactions obtained when working at 140 ºC. Thus, there is a first increase in the liquid-phase carbon yield, reaching a maximum value of around 16 %, despite the temperature. This result indicates the maximum hydrolysis efficiency at these conditions, corresponding with 34 % of the potential amount of sugars. This result suggests that temperature is not the key parameter for this variable. However, it is worth noticing that this first step requires less time as the temperature increases, i.e., 4-5 h, 2 h and around 1.5-2 h at 140, 180 and 220 ºC, respectively. After these maximums, the relevance of side reactions is clearly observed, being promoted by the temperature. In good agreement, final carbon balance closures after 24 h decrease from 59 % to 54 and 33 %, as the temperature increases.

These results only consider the solubilization of sugar fractions, the analysis of selectivities being required to determine the optimum conditions for recovering each platform molecule. The simultaneous comparison after different reaction times is plotted in **Figure 4.17**.

A clear influence of reaction temperature is observed, being all the products observed from the first hour when the temperature is higher than 140 ºC. Xylose is the main product detected at intermediate temperatures and short times, whereas a fast dehydration is observed at 220 ºC, aldehydes and acids prevailing over the TRS. A similar amount of arabinose obtained at 180 and 220 ºC, not only in selectivity but also in concentration. This result suggests that FFL is mainly produced by the dehydration of xylose, pentose for which the differences are more marked. The glucose dehydration to produce HMF is observed at 180 and 220 °C, with selectivities of 5.6 and 14.5 %, respectively, in less than 1 h. According to the previous literature, Lewis acidity is defined as a key factor to promote the HMF via glucose isomerization, since the fructose dehydration is thermodynamically favored [28]. The role of temperature in this step is more relevant when the catalyst is a Brønsted acid (such as the HCl), because of the higher activation energy of the direct glucose dehydration [29].

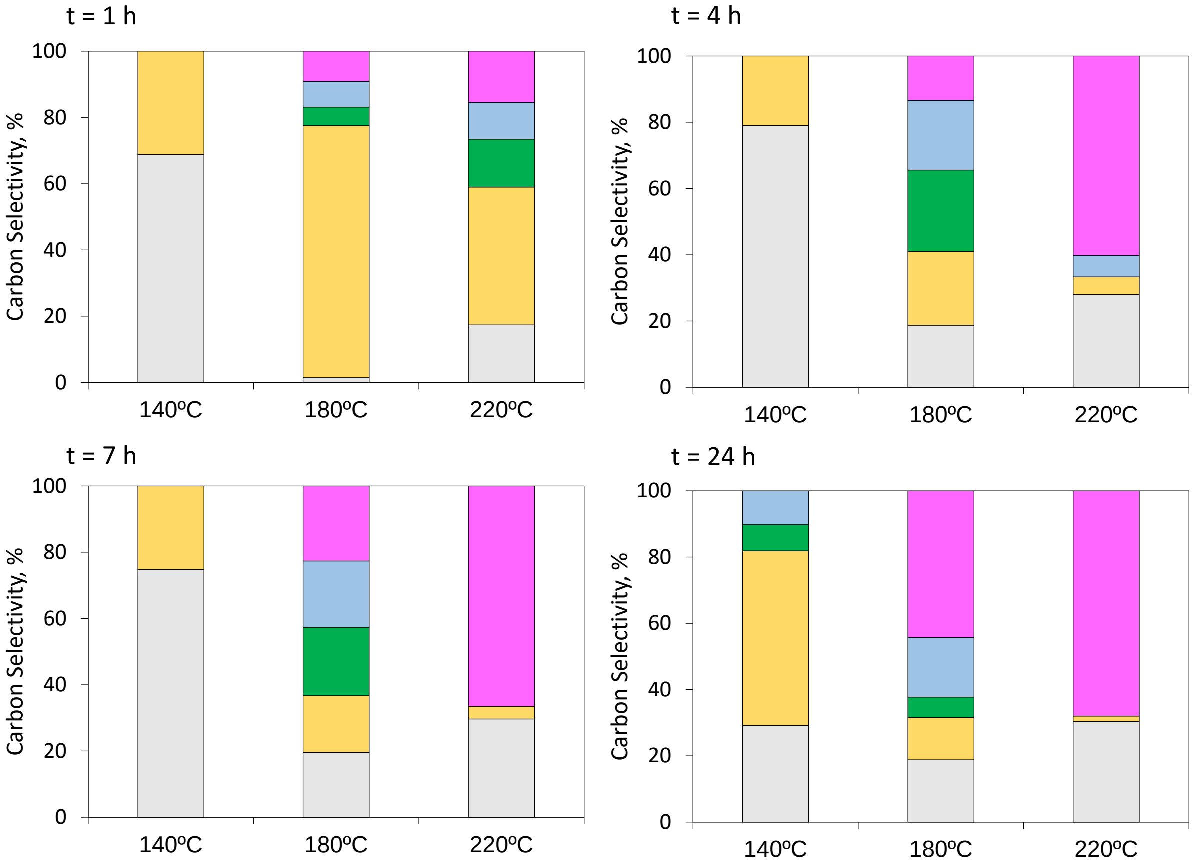

Figure 4.17. Comparative distribution of products selectivities obtained with the fresh sawdust as function of the reaction temperature. Data corresponding to dimers (grey); TRS (yellow); HMF (green); FFL (blue); and levulinic acid (purple)

At larger reaction times, side reactions determine the observed product distribution. On the one hand, the almost total rehydration of HMF into levulinic and formic acid is clearly observed at 220 °C, with the disappearance of this aldehyde and a relevant increase of levulinic acid selectivity (60, 66 and 68 % after 4, 7 and 24 h). This effect is less marked at 180 °C. On the other hand, the FFL total amount reaches a maximum of 330 ppm at 180 °C after 4 h (selectivity of 21 %), with a soft decrease to 250 ppm after 24 h (equivalent to 18 % of selectivity). However, this effect is much more relevant at 220 ºC, reaching the maximum FFL concentration (270 ppm) after only 2 h, with a total disappearance of this compound in less than 5 h, due to the promotion of humins.

According to these results, there is not a clear range of conditions to maximize the productivity and selectivity of almost any compound. This fact seems to be determined by the low rate of the first step of the process: the sugar solubilization to produce TRS. Thus, all the concentrations are quite low, and the reaction conditions required to promote this step are so strong that the subsequent steps occur too fast. In this context, the lignin pretreatment could play a relevant role since a feasible degradation of the recalcitrant structure of sugar polymers could reduce the severity requirements to enhance the hydrolysis. Then, the temperature and reaction time would have a key role in maximizing the productivity and selectivity of the platform molecules.

4.2.3. Influence of the oxidative and reductive pretreatments

To identify the effect of both pretreatments, the comparative analysis of liquid-phase carbon yield obtained is shown in **Figure 4.18** (Fig. 4.18a and 4.18b). In these plots, values over and below the diagonal line indicate higher or lower values once the pretreatments are applied with respect to the reaction with fresh sawdust, always comparing data at same conditions (temperature and acidity) and time on reaction. The discrepancies between results of each pair of experiments were lower than 8 % in all the cases, 2-3 % being the typical errors obtained. The error bars are included in the temporal profiles of concentration evolutions.

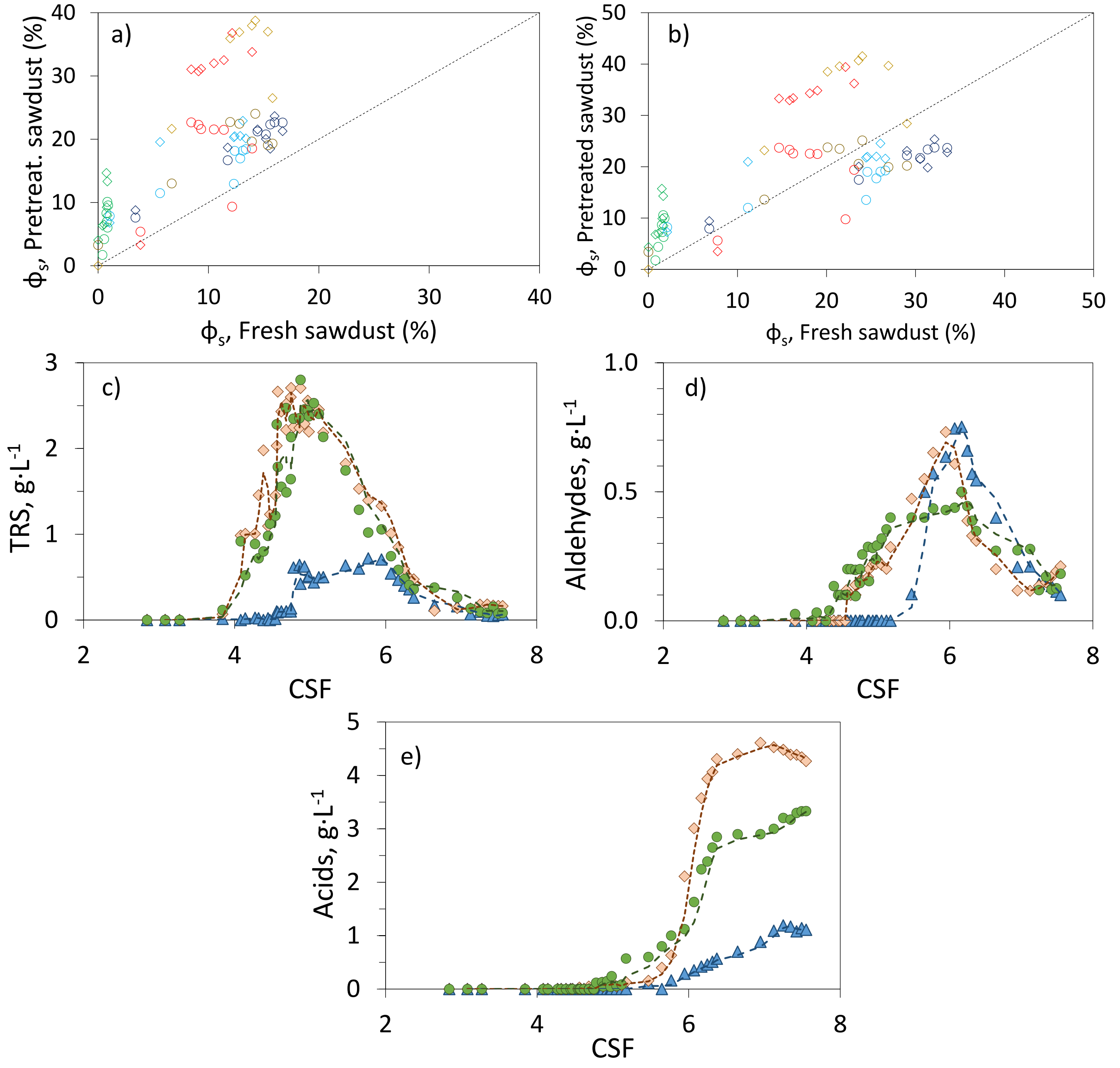

Figure 4.18. Comparative analysis of liquid-phase carbon yields obtained with the pretreated (circles for the reductive delignification, diamonds for the oxidative one) and fresh sawdust considering (a) the total amount of sawdust; and (b) cellulose and hemicellulose. Results corresponding to: 200 ppm of HCl and 140 ºC (green), 600 ppm of HCl and 140 ºC (light blue), 1000 ppm of HCl and 140 ºC (dark blue), 1000 ppm of HCl and 180 ºC (gold), 1000 ppm of HCl and 220 ºC (red). Evolution of (c) TRS, (d) aldehydes, and (e) acids as function of the CSF factor. Data correspond to (▲) fresh sawdust; delignified sawdust using (◆) oxidative and (●) reductive pretreatments

The comparison considering the total amount of sawdust treated (Fig. 4.18a) indicates that both pretreatments have a positive effect in the liquid-phase carbon yield, duplicating the values at almost all the conditions, reaching maxima close to 40 % when the oxidative pretreatment is applied, at 180 and 220 ºC. In addition, the humins production slows down, in good agreement with the increase of the carbon yield increases observed for the pretreated samples. For example, at 220 ºC, a decreasing trend is observed after 2 h of reaction, this time being increased up to 5 and 7 h, after the reductive and oxidative pretreatment, respectively. However, if same values are analyzed considering only the potential maximum amount of sugars (Fig. 4.18b), these values are quite different, since they are strongly affected by the almost total absence of lignin in the pretreated samples. In this case, the differences between reductive and oxidative pretreatments are more evident, with a clear prevalence of the oxidative one, when working at with 1000 ppm of HCl and 180 or 220 ºC. Softer conditions (600 ppm and 140 ºC) do not imply any improvement with respect to the hydrolysis of fresh sawdust. Despite the low values obtained when working with 200 ppm of HCl, around 10 % of liquid-phase carbon yield is reached with both pretreatments whereas no reaction is observed with the fresh material. Two main conclusions of these results can be drawn: i) pretreatments do not modify the potential amount of sugar polymers (increase or reduction) that can be hydrolyzed at these conditions; ii) these pretreatments seem to debilitate the glycosidic bonds, reducing the severity to obtain a similar hydrolytic efficiency. A deeper study of these pretreatments requires the analysis of the products distribution, these data being shown in **Figure 4.19**.

Reactions carried out with 200 ppm of HCl mainly produce dimers and TRS, the dimer concentration being always higher with the oxidative pretreatment than with the reductive one. Thus, in the case of the oxidative pretreatment, dimers correspond to 90 % of the total liquid products during the first 4 h of reaction, decreasing only to 75 % after 7 h. On the contrary, an initial 41 % of dimer is obtained with the reductive pretreatment, with less than 6 % observed after 7 h, when more than 89 % of the total selectivity corresponds to TRS and small traces of aldehydes can be observed (1.5 of HMF and 3.7 % of FFL). Thus, these conditions are identified as the optimum ones to selectively obtain these sugar monomers, the mixture being always enriched in xylose (75 and 80 % when working with the oxidative and reductive treated sawdust). In concentration values, working with 200 ppm, 1.55 g/L of TRS is obtained when working with the treated sample (reductive pretreatment), this value being more than 3 times higher than the value obtained with the oxidative pretreated sample, and 140 times higher than the corresponding one obtained with the fresh sample.

A logical evolution with the acidity, temperature and reaction time is obtained, despite the samples analyzed, with an increase in the degradation process as all these parameters increase. In general, reactions with the oxidized samples suggest a more sensitivity to the reaction parameters, making it difficult to control the reaction in the intermediate steps. Thus, levulinic and formic acid are the main compounds identified in the samples at 220 ºC after only 1 h of reaction, 79 % of selectivity, whereas the corresponding value obtained with the samples pretreated with Ru/C is lower than 10 %.

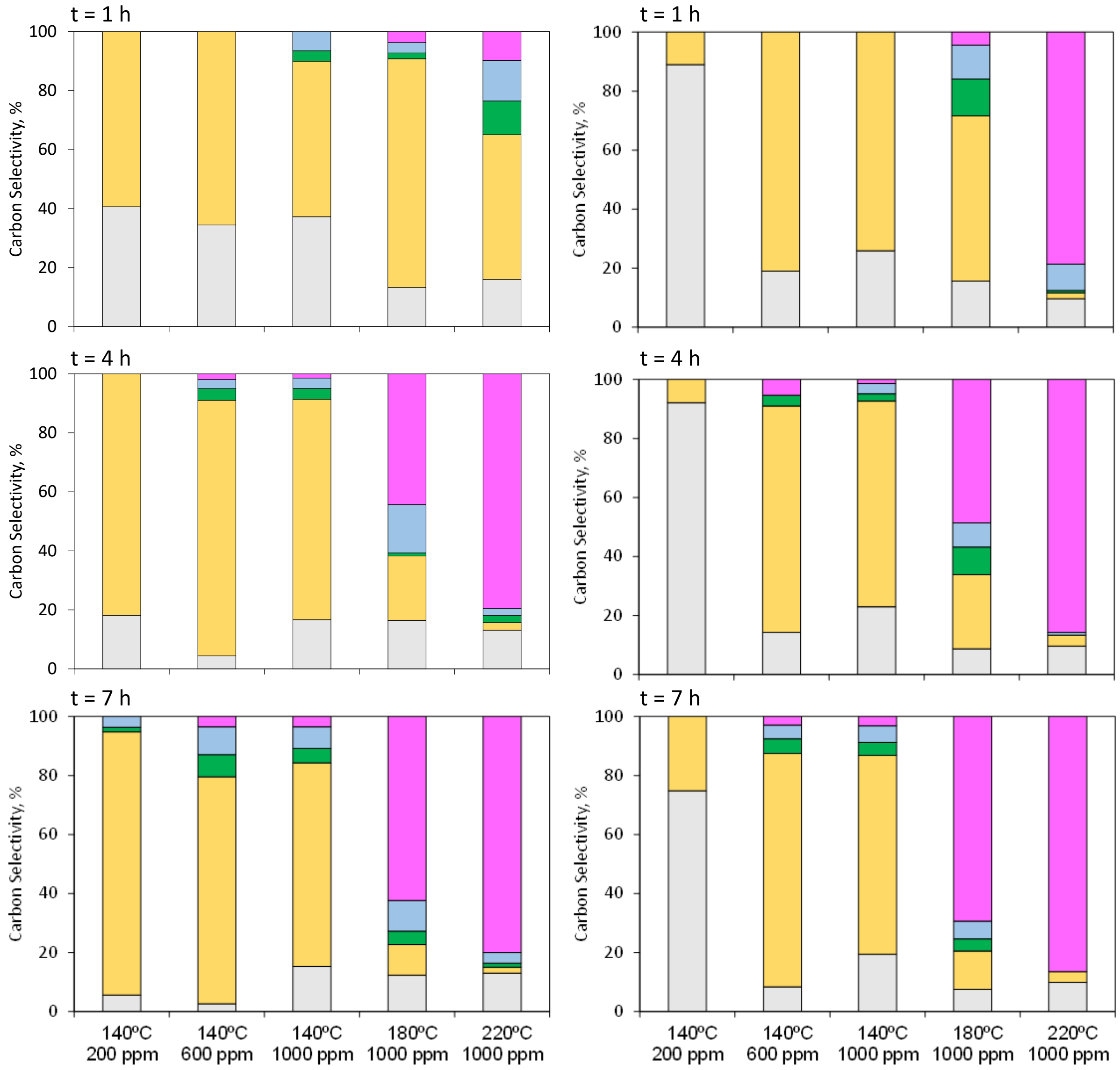

Figure 4.19. Comparative distribution of products selectivities obtained with the hydrolysis of pretreated sawdust as function of the reaction time. Left graphs related to reductive pretreatment; right graphs related to the oxidative one. Data corresponding to dimers (grey); TRS (yellow); HMF (green); FFL (blue); and levulinic acid (purple)

These results conclude that the oxidative pretreatment is the optimum one to maximize the production of these platform molecules, obtaining almost a total degradation of all the sugars in less than 7 h (selectivity to levulinic acid higher than 86 %). This selectivity cannot be reached without a previous pretreatment, even increasing the reaction time up to 24 h. In concentration terms, this selectivity corresponds to 3.2 g/L of levulinic acid produced with the oxidative pretreatment. With the reductive pretreatment, this amount is limited to 2.4 g/L, these two values being significantly higher than the one obtained during the hydrolysis of the fresh sample (0.8 g/L).

Concerning the aldehydes (HMF and FFL), a selective production of these intermediates is not possible, since HMF is faster degraded to levulinic acid, and a high selectivity of FFL is limited by the undesired oligomerization. In any case, the pretreatments also imply an improvement at this point, the reductive process being the optimum to enhance the selectivity of FFL (19 % after 3 h of reaction at 180 ºC with 1000 ppm of HCl, this selectivity being reduced to 16 % at 4 h). The maximum value obtained with sawdust after the oxidative process is limited to 11 %. Seeing both aldehydes together, 35.4 % of both compounds are obtained in less than 1 h of reaction at 220 ºC with the reductive pretreatment. This selectivity corresponds with the maximum concentration observed for these compounds (1.2 g/L). This concentration is 1.8 times higher than the maximum one obtained with the fresh sawdust, 0.68 g/L after 4 h at 180 ºC with 1000 ppm of HCl. A similar selectivity than with the reductive process (34 %) is obtained with oxidative pretreatment, even at softer conditions (180 ºC, 4 h). However, considering the total conversion, this selectivity only corresponds with 0.75 g/L, this value being only half of the concentration reached after the oxidative pretreatment.

To globally identify the impacts of delignification processes in sawdust hydrolysis, and considering the simultaneous effect of acidity, temperature and reaction time, the evolutions of different intermediates and final products are compared considering the combined severity factor (CSF). This parameter has been previously proposed in the literature to unify the role of all the variables involved in one coefficient, according to Eq. 4.4 [36, 37].

In this case,"t" is the reaction time of hydrolysis in minutes, "T" is the reaction temperature in Celsius, "T_{Ref}" is the reference temperature, most often 0 ºC, and pH is the acidity of the aqueous solution measured before reaction. These values correspond to 2.1, 1.8 and 1.6, for reactions with 200, 600 and 1000 ppm of HCl, respectively. The concentrations of total reduced sugars (TRS), aldehydes and acids as function of the CSF values are plotted in **Figure 4.18** (parts c to e).

The soft trends obtained for all the compounds studied corroborate the utility of this parameter, showing distributions with clear maxima, which indicates a common evolution as function of the acidity, temperature, and reaction time for all the platform molecules. A similar effect of both pretreatments in the TRS productivity is observed (Fig. 4.18c), with a maximum clearly concentrated in CSF values 4.5 – 5 and a fast decrease in the concentration at both, lower and higher CSF values. In these two cases, the maximum concentration is close to 3 g·L^{-1}. More severe conditions are required in the hydrolysis of fresh sawdust, with and more extensive optimum CSF range from 5 to 6. Even at the optimum conditions, the total amount of sugars obtained is significantly lower than with the pretreated sawdust (maximum 0.75 g·L^{-1}).

As to the aldehydes (HMF and FFL), the maximum obtained with the fresh sawdust is concentrated in a very narrow range (5.8 -6.4), without observing HMF nor FFL with CSF values under 5. The concentration at these optimum conditions, 0.8 g·L^{-1}, is also the optimum obtained with the oxidative pretreatment, the most relevant difference being the presence of aldehydes even at CSF values lower than 5. The most extended range is observed for sawdust after the reductive pretreatment, obtaining aldehydes almost at all the conditions tested. However, this sawdust follows a flat evolution in the range 5 – 6.5, being not possible to identify clear optimum conditions, and with a maximum concentration lower than 0.5 g·L^{-1}.

In concentration terms, acids (levulinic and formic acid considered together) are the compounds most affected by the pretreatment used. However, the general trends are the same, and CSF values higher than 6.5 are required in all the cases to obtain these compounds in significant amounts. The clearest difference is then the slope of this increasing trend, the oxidative pretreatment being the most efficient one to increase acid yields.

According to this analysis, the oxidative delignification method is considered the best one to clearly identify different optimum conditions, in terms of productivity and selectivity, for each platform molecule. On the contrary, these optimum values partially overlapping with the reductive pretreated and fresh sawdust.

4.2.4. Kinetic study

To sum up, relevant influences are observed as a function of the pretreatment carried out. These higher reaction progresses can be analyzed in kinetic terms, proposing a kinetic model to describe the solubilization of hexoses and pentoses present in sawdust as well as their degradation to HMF, FFL and levulinic and formic acids. For this model, the quantity of sugar polymers is obtained as the difference between the initial amount (experimentally determined) and the sum of all compounds detected in liquid phase. The evolution of all the compounds (grouped by families) with the time could be assimilated to a sequence of irreversible first-order steps in series configuration, see Eq. [4.7]:

$$C_P \overset{k_1}{\rightarrow} C_D \overset{k_2}{\rightarrow} C_M \overset{k_3}{\rightarrow} C_{ald.} \overset{k_4}{\rightarrow} C_{ac.} \qquad \textbf{[4.7]}$$

where: C_P is the sum of hemicellulose and cellulose in the sawdust; C_D and C_M are the dimer and monomer (hexoses and pentoses) concentrations detected in the liquid phase, respectively; C_{adl}, the sum of HMF and FFL; and $C_{ac.}$ the amount of formic and levulinic acid. All concentrations are expressed in g/L.

To guarantee the absence of any limitation because of the amount of HCl, only the set of reactions obtained with 1000 ppm of this catalyst were considered for the adjustment. This decision is justified by the negligible pH evolution observed in these experiments during the 8 h analyzed. Considering the possible humins formation, as well as the subsequent alteration in the theoretical amount of polymers, a fifth rate was evaluated, being responsible for aldehyde oligomerization to obtain these solid deposits. Experimental data were fitted to this kinetic model using MATLAB code ("ode45"). The fitting of the unknown parameters was accomplished by the least-square method using the "lsqcurvefit" function and the Levenberg-Marquardt algorithm, obtaining the kinetic rates summarized in **Table 4.3**.

The comparison of these data requires corroborating the reliability of these values. An ANOVA analysis confirms that temperature is a significant model terms that influences the kinetic of the hydrolysis, for fresh and pretreated samples, with p-values lower than 0.5 in all the cases (0.028, 0.022 and 0.016 for fresh samples and sawdust after oxidative and reductive pretreatments, respectively). The sawdust pretreatments also produce a relevant influence in the kinetic, mainly at 220 ºC, when the p value is 0.036. This influence is not so significant at lower temperatures, with p-values a bit higher: 0.17 and 0.11, for 140 and 180 ºC, respectively. These values are too high to conclude a clear influence of these pretreatments at low temperatures at this level of confidence (95 %). The p-values decrease up to less than 0.07 if only the first steps of the reaction are considered (sugar solubilization), in good agreement with the suggested hypothesis of a main effect of these pretreatments making easier the cellulose and hemicellulose hydrolysis, whereas the subsequent steps of the process are mainly conditioned by the acidity of the medium.

Table 4.3. Kinetic model parameters for the hydrolysis of sawdust catalysed by 1000 ppm of HCl.

Raw Material	Temp. (ºC)	k_1 (s^{-1})	k_2 (s^{-1})	k_3 (s^{-1})	k_4 (s^{-1})	k_5 (s^{-1})
Fresh sawdust	140	$4.0 \cdot 10^{-5}$	$1.3 \cdot 10^{-4}$	$1.2 \cdot 10^{-5}$	$2.5 \cdot 10^{-7}$	$7.0 \cdot 10^{-5}$
	180	$7.7 \cdot 10^{-5}$	$8.5 \cdot 10^{-4}$	$4.2 \cdot 10^{-4}$	$1.7 \cdot 10^{-4}$	$2.3 \cdot 10^{-4}$
	220	$2.4 \cdot 10^{-4}$	$1.7 \cdot 10^{-3}$	$3.3 \cdot 10^{-3}$	$2.1 \cdot 10^{-3}$	$3.2 \cdot 10^{-4}$
	Ea (kJ·mol^{-1})	33.7	54.1	120.0	193.3	31.9
	r^2	0.93	0.95	0.99	0.96	0.93
Delignified by oxidative method	140	$4.3 \cdot 10^{-5}$	$1.1 \cdot 10^{-3}$	$2 \cdot 10^{-4}$	$3.5 \cdot 10^{-5}$	0
	180	$8.6 \cdot 10^{-5}$	$2.4 \cdot 10^{-3}$	$3.6 \cdot 10^{-4}$	$6.4 \cdot 10^{-4}$	$3.7 \cdot 10^{-6}$
	220	$1.6 \cdot 10^{-4}$	$1.1 \cdot 10^{-2}$	$9.1 \cdot 10^{-3}$	$7.7 \cdot 10^{-3}$	$3.1 \cdot 10^{-4}$
	Ea (kJ·mol^{-1})	27.8	49.1	78.9	113.9	205.1
	r^2	0.999	0.95	0.83	0.999	0.999
Delignified by reductive method	140	1.1310^{-5}	$5.2 \cdot 10^{-4}$	$1.7 \cdot 10^{-4}$	$3.4 \cdot 10^{-5}$	$4.7 \cdot 10^{-8}$
	180	$2.9 \cdot 10^{-5}$	$7.6 \cdot 10^{-4}$	$3.5 \cdot 10^{-4}$	$5.3 \cdot 10^{-4}$	$7.0 \cdot 10^{-5}$
	220	$3.9 \cdot 10^{-5}$	$1.0 \cdot 10^{-3}$	$1.5 \cdot 10^{-3}$	$1.7 \cdot 10^{-3}$	$5.8 \cdot 10^{-4}$
	Ea (kJ·mol^{-1})	29.0	14.0	45.9	84.1	202.0
	r^2	0.93	0.997	0.95	0.97	0.94

The good fit of this model with experimental values is shown in **Figure 4.20**, including the reactions at 220 ºC as examples. The good regression coefficients of kinetic rates as function of the temperature indicates an optimum adjustment of experimental data according to Arrhenius model. This model, previously proposed in the literature [31, 38, 39] represents a first approach to the kinetic since a deeper analysis would require individual steps for the hydrolysis of each sugar polymer, as well as particular steps of degradation of each monomer. However, the common existence of glucose in both polymers, cellulose and hemicellulose, prevents this possibility.

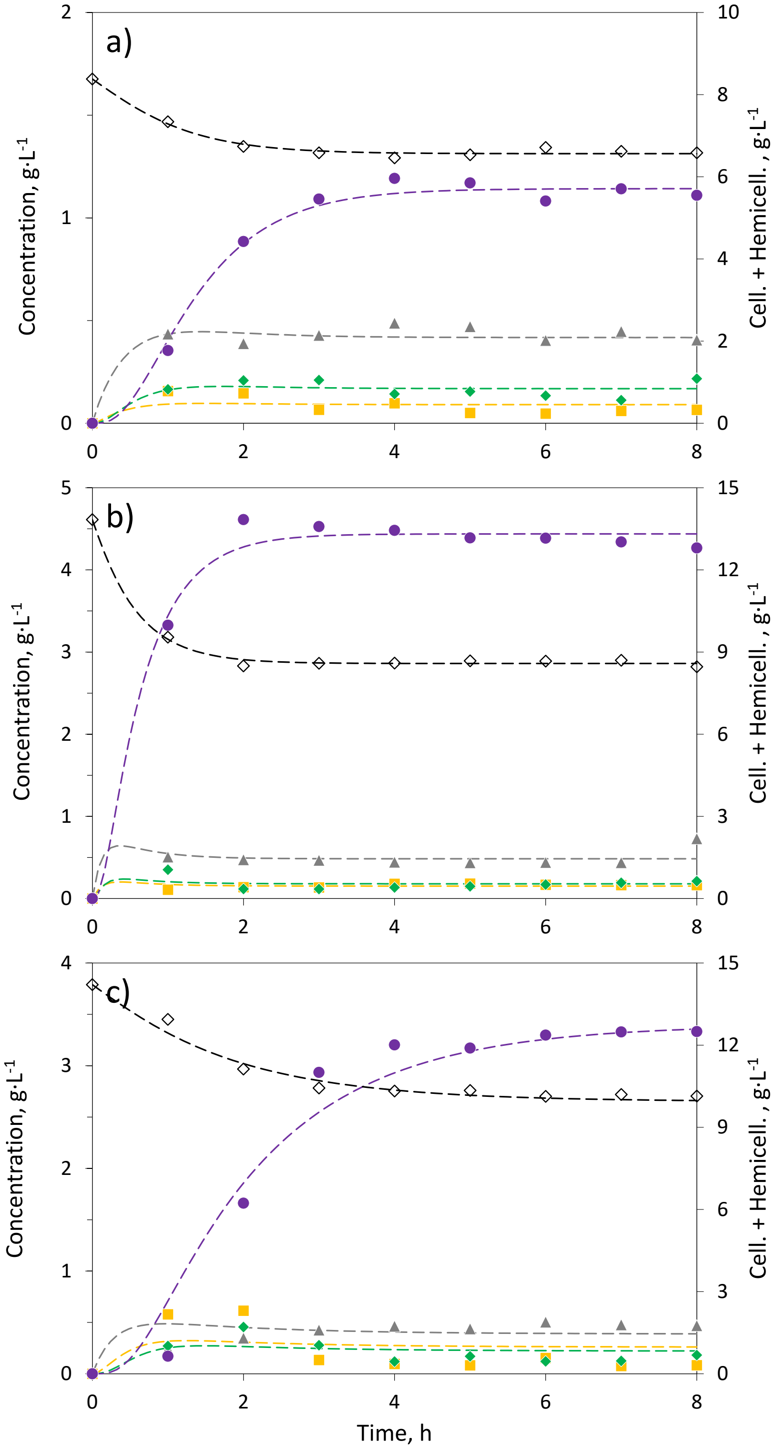

Figure 4.20. Kinetic adjustment of experimental data according to the kinetic model proposed. Results corresponding to hydrolysis at 220 ºC with 1000 ppm of HCl of the (a) fresh sawdust; (b) pretreated sawdust by oxidative method; and (c) pretreated sawdust by reductive method. Symbols: (◇) sugar polymer; (■) dimers; (▲) TRS; (◆) aldehydes; (●) acids

Despite this general character, the influence of delignification pretreatments is clearly observed, with significant decreases in the activation energy of all the kinetic rates of the hydrolysis pathway. On the contrary, significant increases in the activation energy of undesired reaction is observed after both pretreatments, being more evident in the case of the oxidation one. All these results are congruent with the initial assumption, considering that removing lignin has a positive effect increasing the accessibility to the sugar polymers, promoting their solubility and the subsequent steps. In addition, removing lignin as well as the external functional groups of hemicellulose (more evident in the case of oxidative pretreatment) significantly decreases the humins formation, preventing the oligomerization of aldehydes involved in the reaction.

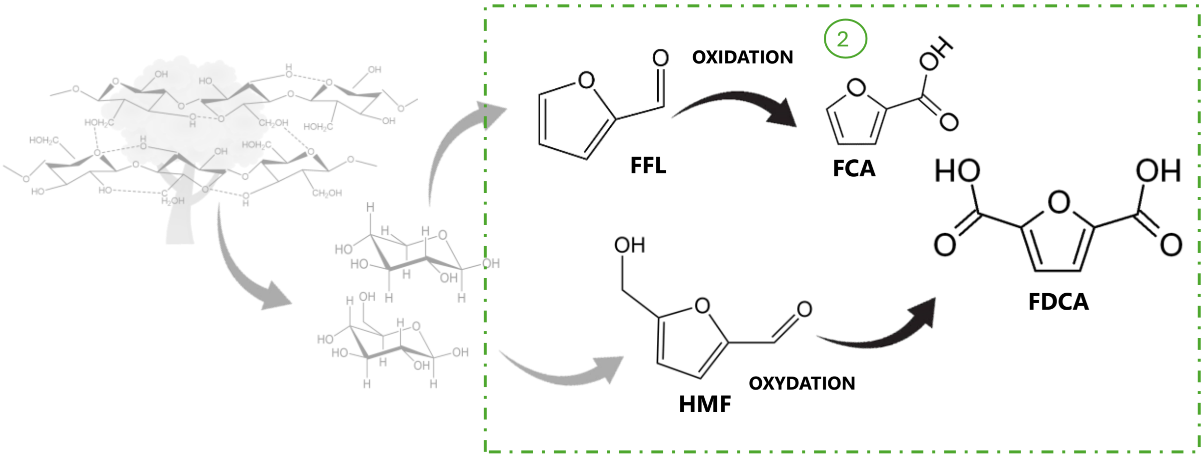

4.3. FUROIC ACID PRODUCTION BY CATALYTIC OXIDATION OF FURFURAL WITH H_2O_2

The partial oxidation of FFL using hydrogen peroxide is evaluated focusing on a catalyst screening and on the optimization of reaction parameters to increase FCA selectivity limiting other by-products formation such as maleic acid, and 2-hydroxyfuran. Experiments were conducted in a batch reactor using different catalytic supports like MgAl, MgZr, CeO_2, and TiO_2, with the incorporation of metals such as Au, Pd, and Pt. These materials have different redox, acidic, and basic properties, offering a range of behaviors in oxidation reactions. The evolution of the different involved compounds (organics and H_2O_2) is present in terms of conversion, selectivity, yield, and carbon balance closure, according to the following expressions:

$$x_{FFL}\ (\%) = \frac{C_{FFL,0} - C_{FFL,t}}{C_{FFL,0}} \cdot 100 \qquad [4.8]$$

$$x_{H_2O_2}\ (\%) = \frac{C_{H_2O_2,0} - C_{H_2O_2,t}}{C_{H_2O_2,0}} \cdot 100 \qquad [4.9]$$

$$Selectivity\ (\%) = \frac{n_i \cdot C_i}{\sum(n_i \cdot C_i)} \cdot 100 \qquad [4.10]$$

$$Yield\ (\%) = = \frac{n_i \cdot C_i}{5 \cdot C_{FFL,0}} \cdot 100 \qquad [4.11]$$

$$C.B.(\%) = \frac{\sum(n_i \cdot C_i)}{5 \cdot C_{FFL}} \cdot 100 \qquad [4.12]$$

4.3.1. Reaction pathway in absence of heterogeneous catalysts

According to literature [40], compounds with five but also four carbon atoms are expected to be obtained during the furfural oxidation, releasing formic acid that acts as a homogeneous catalyst. Considering the high oxidation capacity of H_2O_2, a contribution of the autocatalytic process is not discarded, with the subsequent formic acid production that triggers the homogeneous catalytic mechanism. Thus, a correct study of the heterogeneous catalytic mechanism requires a preliminary analysis of these concomitant effects.

An initial experiment in the absence of heterogeneous catalysts was carried out at 50 ºC, with a 3/1 H_2O_2/furfural molar ratio, to study the influence of autocatalytic and homogeneous catalytic mechanisms. The evolution of reactants and products concentration is plotted in **Figure 4.21**. A continuous H_2O_2 conversion is observed, more markedly during the first 2h, reaching 55% of conversion after 8 h. A similar furfural conversion is observed (58%), but the temporal profile indicates a faster reaction rate after 2h. This profile is congruent with the presence of catalytic steps activated by an intermediate.

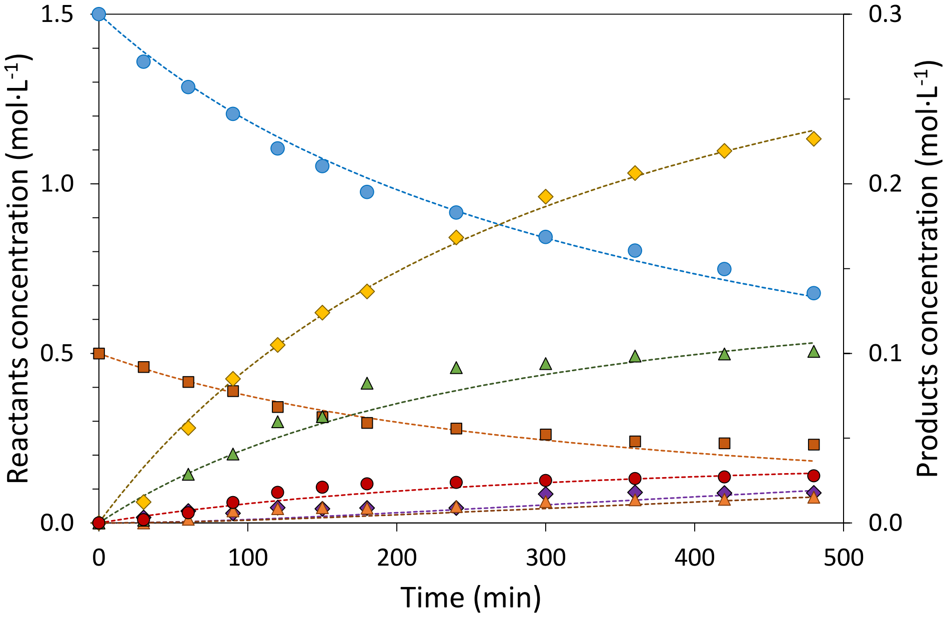

Figure 4.21. Furfural oxidation with H_2O at 50 ºC in absence of a catalyst. Symbols: H_2O_2 (●); furfural (■); formic acid (◆); 2-hydroxyfuran (▲); furoic acid (●); maleic acid (◆); and 2(5H) furanone (▲). *Broken lines correspond to the kinetic model predictions*

The product distribution is congruent with previous literature, despite the diverging values because of the different temperatures used [41]. Formic acid (FA) is the main reaction product, with a clear increasing trend, yielding more than 0.2 mol·L^{-1} after 6 h. 2-Hydroxyfuran is also relevant (HF, 0.12 mol·L^{-1}), showing a typical profile of a primary compound, with an almost flat concentration after 4 h justified by its decomposition. The same trend is detected for furoic acid (FCA), although FCA is obtained with significantly lower concentrations (max. value of 0.03 mol·L^{-1}). The stable phase of HF and FCA corresponds with an increase in minority products, 2(5H)-furanone (FN) and maleic acid (MA), suggesting that these compounds are obtained by the oxidation of one or both precursors (HF and FCA). Consequently, their formation is equilibrated with their decomposition. The final concentrations of FN and MA, 0.018 and 0.015 mol·L^{-1}, are too low to support a strong discussion about the mechanistic route to their formation.

The final carbon balance in the liquid phase is 85.4%, suggesting a significant carbon loss in the gas phase. The presence of any other condensate product in the liquid phase or humins was discarded considering the lack of any unknown signal on the HPLC chromatograms. Moreover, solids were not recovered after the reaction. This loss is then compatible with CO_2 released because of the total oxidation of the different compounds. A separate analysis of the gas phase by a mass-spectrometer identifies CO_2 as the only carbon-containing molecule of the gas sample.

These results suggest that formic acid (FA) is a common product obtained by all the routes that produce C4 compounds from furfural (C5). In fact, there is a good correspondence between FA concentration and the difference between the furfural converted and the furoic acid obtained (once the carbon balance closure is considered). Based on this premise, FA is excluded from the selectivity analysis (see Figure 4.22), only considering the C4-C5 compounds. Thus, in carbon basis (Eq. 4.12), the reaction in absence of catalyst produces 60% of HF and similar selectivity of FCA (20.5%) and the mixture of FN and MA (9 and 10.5%). In global terms, these results indicate that the 2-hydroxyfuran route (Baeyer-Villiger mechanism, henceforth, B-V) prevails, the compounds of this pathway being 80% of the total mixture. It is expected that introducing a heterogeneous catalyst could modify the ratio between the two main routes of furfural partial oxidation and, subsequently, the relative distribution of products.

4.3.2. Influence of the catalytic support

Once the relevance of the homogeneous reaction pathways was determined, the activity of the bulk supports was compared. The main characterization results in terms of morphology, acidity, and basicity of the supports considered are summarized in **Table 4.4**. Data shown in this table are obtained by the analysis of N_2 physisorption isotherms, NH_3 and CO_2 spectra included in **Figures 4.22-24**).

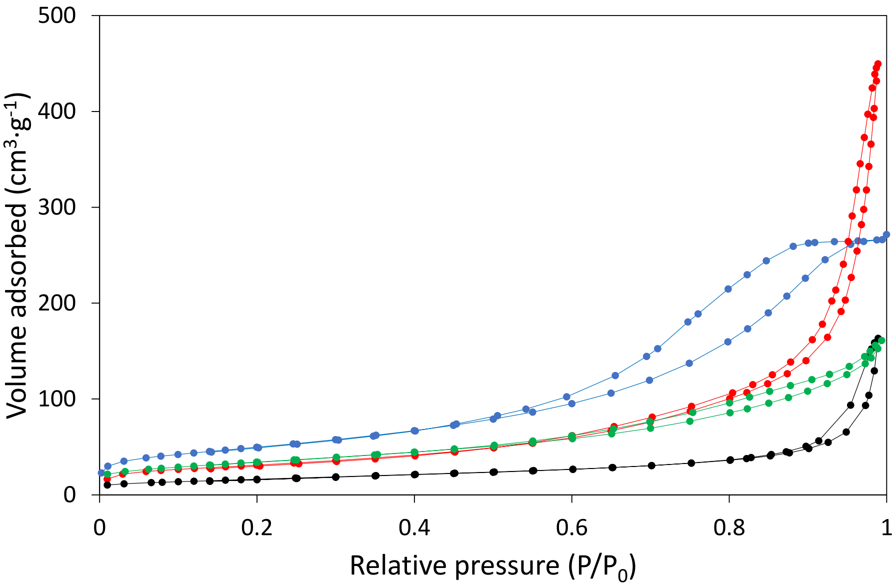

Figure 4.22. N_2 physisorption isotherms of MgAl (blue), MgZr (red), TiO_2 (black), and CeO_2 (green)

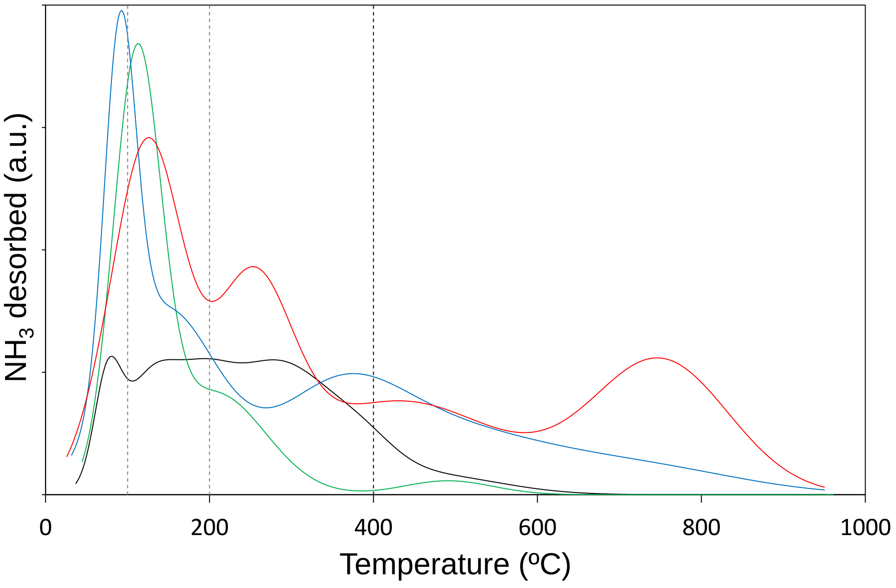

Figure 4.23. NH_3-TPD desorption profiles of MgAl (blue), MgZr (red), TiO_2 (black), and CeO_2 (green)

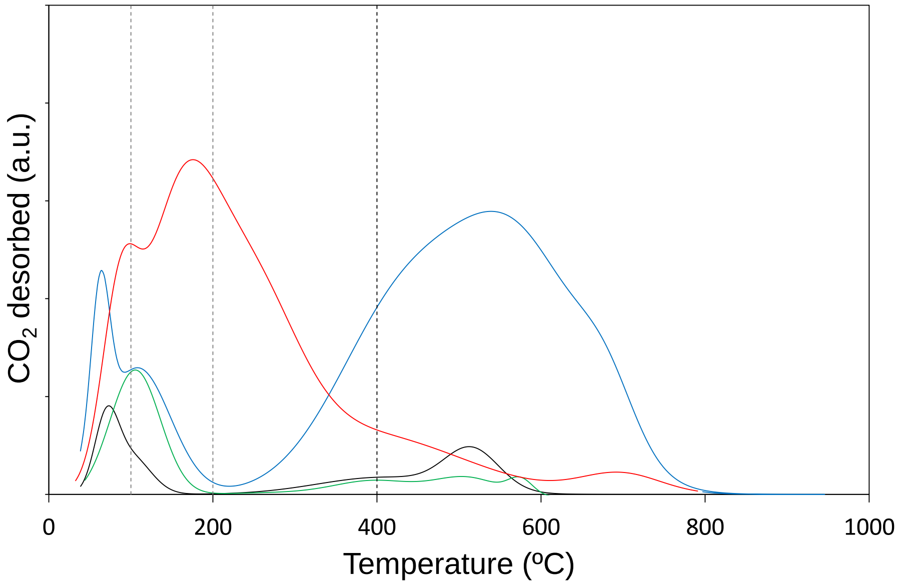

Figure 4.24 CO_2-TPD desorption profiles of MgAl (blue), MgZr (red), TiO_2 (black), and CeO_2 (green)

Table 4.4: Main morphological and chemical properties of the different supports used in this work.

	MgAl	MgZr	TiO_2	CeO_2
N_2 physisorption				
Surface area ($m^2 \cdot g^{-1}$)	179	111	59	123
Pore volume ($cm^3 \cdot g^{-1}$)	0.4	0.7	0.3	0.3
Pore diameter (nm)	7	18	19	8
Acidity (µmol $NH_3 \cdot g^{-1}$)				
Physisorbed (<100 ºC)	109.6	16.3	17.4	0
Weak (100 – 200 ºC)	181.5	227.0	67.3	45.7
Medium (200 - 400 ºC)	78.5	147.4	127.7	177.3
Strong (>400 ºC)	161.2	183.7	18.6	9.2
Total	***530.7***	***574.4***	***231.1***	***232.2***
Basicity (µmol $CO_2 \cdot g^{-1}$)				
Physisorbed (<100 ºC)	14.2	17.9	15.6	22.5
Weak (100 – 200 ºC)	40.1	50.3	0	0
Medium (200 - 400 ºC)	0	97.2	11.3	9.5
Strong (>400 ºC)	268.5	0	11.0	6.1
Total	***322.7***	***165.3***	***37.9***	***38.2***

All the catalysts are mesoporous materials with surface areas from 60 (TiO_2) to 180 $m^2 \cdot g^{-1}$ (MgAl) and pore diameters significantly higher than the kinetic diameter of all the molecules involved in the process.

Figure 4.25 illustrates, in terms of selectivity *vs.* conversion, the experimental data obtained with the four metal oxides tested, keeping the temperature (50 ºC) and the initial H_2O_2/furfural ratio (3) of the homogeneous experiments described in the previous section. Results obtained with MgAl match those obtained in the absence of a catalyst, whereas the other three supports present relevant differences, including the formation of other intermediates, such as 5-hydroxy-2(5H)-furanone (HFN), β-formylacrylic acid (BFA), and malic acid (MAL). The presence of these compounds suggests that some steps of the global mechanism require a heterogeneous catalyst to be feasible.

Obtained results can be turned by the reactivity of the hydrogen peroxide. Relevant differences between materials were found, from a slight increase with MgAl and MgZr (64 and 70% at the final reaction time) to an almost total decomposition in the case of CeO_2 (93.7%), with an intermediate behaviour for the TiO_2.

Furfural conversions are lower than the one reached without a catalyst, detecting values from 33% (MgZr) to 46.7% (MgAl), with an opposite trend than the one observed for H_2O_2 conversion. These results indicate that H_2O_2 is involved in all the steps where furfural is. Thus, the fast decrease of H_2O_2 concentration leads to a reduction in the rates of these reactions, with the subsequent reduction in the furfural conversion. This conclusion is supported by the literature. López Granados and co-workers demonstrate that the larger the H_2O_2 concentration, the faster the furfural conversion rate [42], and several authors propose using different oxides as catalysts for hydrogen peroxide decomposition [43, 44].

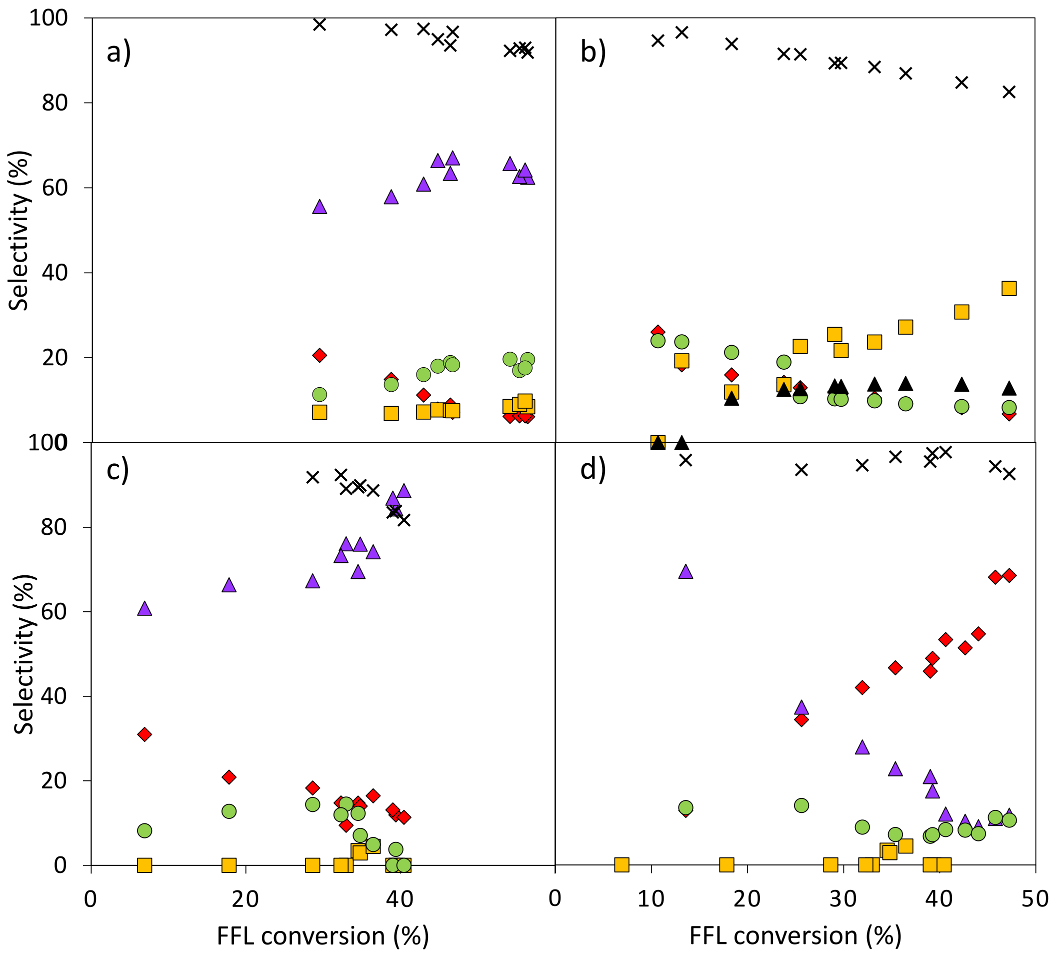

Figure 4.25. Conversion - selectivity plots for furfural oxidation using H_2O_2 at 50 ºC over (a) MgAl, (b) MgZr, (c) CeO_2, and (d) TiO_2. Data correspond to carbon balance (✱), and selectivities to MA (◆), FN (■), HF (▲), FCA (●), and HFN (▲)

According to the previous discussion, the H_2O_2 conversion and, subsequently, the furfural one is improved by the redox properties of Ce [45], Ti [46], and Zr [47]. However, the comparison between the blank and experiments with MgZr suggests that the role of acidic/basic properties of the catalysts in the product distribution and the reaction control cannot be discarded.

With MgAl, the distribution of the main products is quite similar than in absence of any catalyst, obtaining a final sample enriched in HF (66.6%) with 18.3% of FCA and 17% of the sum of FN, MA and HFN (catalytic route not observed with the blank). The high carbon balance (93%) and the constant concentration of FCA suggests a positive role of strong basic sites preventing CO_2 formation and stabilizing the resulting organic acids.

In the case of MgZr, the higher strength of the acid sites promotes B-V oxidation pathways [48], observing a significant decrease in the furoic acid selectivity (10.1%), as well as an increase in the formation of acyclic compounds (selectivity of 33.7% of BFA), and their total decomposition to CO_2, fostered by the absence of strong basic sites that could stabilize the organic acids.

With CeO_2, furoic acid is only observed in traces at the beginning of the reaction and FN, HFN, BFA or MAL are not detected. This material presents the highest production of 2-hydroxyfuran (HF), with almost constant selectivity during all the reaction (~90%). In addition to the redox activity of this catalyst, its marked medium-strength acidity (see data in Table 1), with the subsequent total H_2O_2 decomposition (only observed with this material) explains the promotion of this route. The carbon balance (83.2%) suggests that the decomposition of organic compounds is relevant. The maleic acid selectivity is not negligible (11.3%). These results are explained by the easy Ce^{3+}/Ce^{4+} redox transition, increasing the oxygen mobility and storage capacity, favoring total oxidations [49].

TiO_2 highlights by the fast decomposition of primary products, with maximum selectivities of 67.2% for HF (after 30 min), and 17.4% for FCA (after 1h). Due to their decomposition, maleic acid represents more than 66% of the total selectivity after 8 h, result that corresponds to 20.7% of the product yield. This material presents the best carbon balance (94.8%), discarding relevant decomposition to CO_2. The acidity and basicity properties of this material cannot explain these results, its redox capacity being proposed as the main responsible of it. In the case of TiO_2, oxidations are enhanced but not decompositions, suggesting a complex effect of support oxygen vacancies.

According to this support screening, the role of heterogeneous catalysts tuning the selectivity is very relevant, in such a way that CeO_2 is proposed for the selective production of hydroxyfuran (HF), whereas maleic acid (MA) formation is promoted with TiO_2. This analysis is not so conclusive concerning other reaction intermediates, such as furoic acid. For this compound, a maximum selectivity of 28% is obtained with MgZr, but this result corresponds to a low FFL conversion (9.2%, 1h) and the FCA yield is then almost negligible (1.2%). On the contrary, results with MgAl present a better balance between conversion and selectivity, reaching a maximum yield of 6.7% after 6 h. To sum up, the analysis of relevant reaction intermediates requires a balance between the catalytic activity and the reaction time to prevent the advance of the reaction to more oxidized compounds.

4.3.3. Kinetic study

With the temporal evolution of reactants and products obtained with and without catalysts and considering the literature [50-52], the mechanism shown in **Figure 4.26** is proposed.

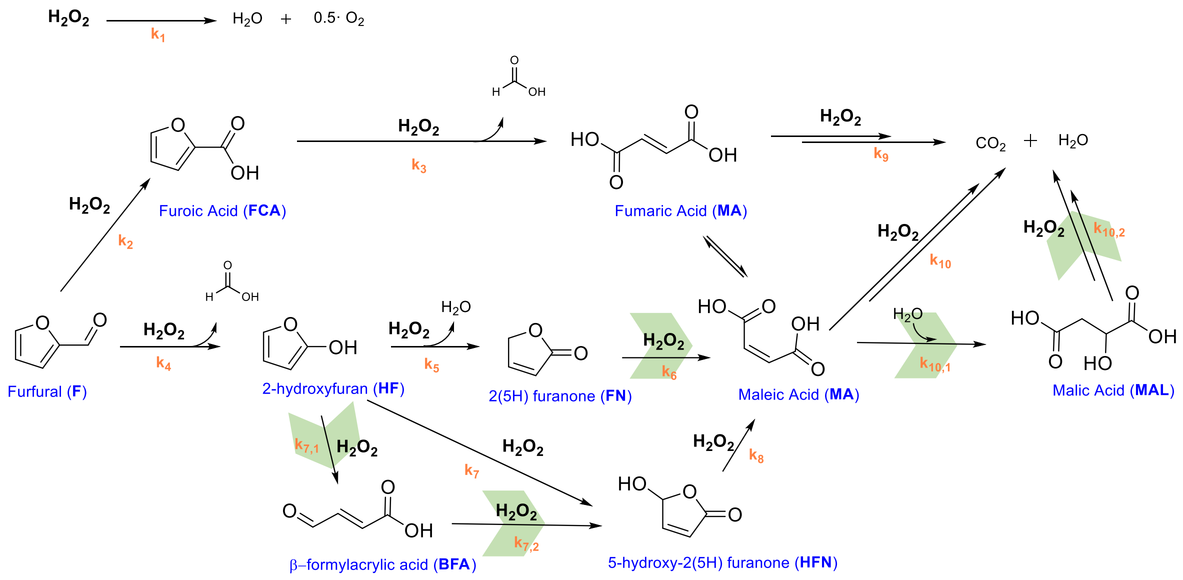

Figure 4.26. Scheme of reaction network of furfural oxidation using H_2O_2 as oxidizing agent. *Steps highlighted in green require a heterogeneous catalyst*

According to this mechanism, furfural is oxidized by two parallel pathways, obtaining furoic acid and 2-hydroxyfuran, respectively, as primary compounds. Through the second pathway (B-V), oxidation implies a partial decomposition, releasing formic acid. 2-hydroxyfuran is a reactive intermediate that undergoes dehydration, yielding 2(5H)-furanone. The co-presence of hydrogen peroxide and formic acid catalyzes the oxidation of furoic acid and 2(5H)-furanone into maleic and fumaric acid, two isomers in cis-trans rearrangement equilibrium. The low pH (2.8 after 8 h) and the oxidizing medium promotes the degradation of these compounds through consecutive oxidative decarboxylations, releasing CO_2 and water [53]. The absence of a direct correspondence between the products and the hydrogen peroxide conversion suggests an independent self-decomposition of this reactant.

Experimental results were fitted to the kinetic model obtained by applying the mass balances suggested by the reaction mechanism and considering the hypothesis of an ideal stirred batch reactor, according to Eq. (4.12) to (4.18). In these equations, fumaric and maleic acid are considered together. All the compounds are labeled as indicated in Figure 4.26 to simplify the mathematical expressions.

$$\frac{dC_H}{dt} = -k_1 \cdot H - k_2 \cdot FFL \cdot H - k_3 \cdot FCA \cdot H - k_4 \cdot FFL \cdot H - k_6 \cdot FN \cdot H - k_7 \cdot HF \cdot H - k_8 \cdot HFN \cdot H - k_9 \cdot MA \cdot H - k_{10} \cdot MA \cdot H \quad \textbf{[4.12]}$$

$$\frac{dC_{FFL}}{dt} = -k_2 \cdot FFL \cdot H - k_4 \cdot FFL \cdot H \quad \textbf{[4.13]}$$

$$\frac{dC_{FCA}}{dt} = k_2 \cdot FFL \cdot H - k_3 \cdot FCA \cdot H \quad \textbf{[4.14]}$$

$$\frac{dC_{FA}}{dt} = k_3 \cdot FCA \cdot H + k_4 \cdot FFL \cdot H - k_9 \cdot MA \cdot H \quad \textbf{[4.15]}$$

$$\frac{dC_{MA}}{dt} = k_3 \cdot FCA \cdot H + k_6 \cdot FN \cdot H + k_8 \cdot HFN \cdot H - k_{10} \cdot MA \cdot H \quad \textbf{[4.16]}$$

$$\frac{dC_{HF}}{dt} = k_4 \cdot FFL \cdot H - k_5 \cdot HF \cdot H - k_7 \cdot FN \cdot H \quad \textbf{[4.17]}$$

$$\frac{dC_{FN}}{dt} = k_5 \cdot HF \cdot H - k_6 \cdot FN \cdot H \quad \textbf{[4.18]}$$

The coexistence of homogeneous and heterogeneous reaction pathways is modeled considering each kinetic rate constant as the sum of two values: a constant one due to the homogeneous contribution (related to the activity of hydrogen peroxide and protons), and a variable one related to the solid catalyst. Due to the extended number of terms, this disaggregation ($k_i=k_{(i,hom)}+k_{(i,het)}$) is not specified in the equations. This methodology requires a previous analysis of the blank experiment to isolate the contribution of the homogeneous rates in those steps identified without a solid catalyst. This analysis also allows identifying those steps that require a solid catalyst to be promoted (identified with green shadow in Figure 4.26).

The low pH (<3) obtained in less than 2h allows considering the homogeneous catalysis is due to the presence of protons as constant. Based on these appreciations, the effect of the acidity is embedded in the common contribution (homogeneous terms) without including any extra term in the mass balances. Since no relevant differences between the acids that could release these protons were observed, the main contribution is attributed to formic acid because of its significantly higher concentration (more than 90% in some cases).

In contrast, experimental results demonstrate a marked influence of the hydrogen peroxide concentration on the different steps, as well as a different evolution of its concentration as a function of the catalyst used. Therefore, it is a relevant parameter in the mass balances for the heterogeneous catalysis, leading to an apparent second order kinetics for most of the steps, as well as a decomposition rate (k_1) with a homogeneous and a heterogeneous contribution, in the same way as for the organic compounds.

The kinetic rates of the main steps (k_1-k_4) are summarized in **Table 4.5**, whereas the values for secondary steps that could be affected by a higher inaccuracy (due to the lower concentrations to be fit) are included in **Table 4.6**. The kinetic rates reported for the different supports correspond only to the heterogeneous contribution. The real rates are obtained by the sum of both terms, but the discussion is more clearly based only on those terms affected by the solid catalysts.

The goodness of fit for the blank experiment is illustrated in Figure 4. 21, observing a great correspondence between experimental (dots) and fitted values (broken lines). These values represent a common homogeneous contribution for those experiments with a solid catalyst.

Table 4.5. Reaction rate constants based on the proposed reaction network. Units: k_1 (s^{-1}); $k_2 - k_4$ ($L \cdot mol^{-1} \cdot s^{-1}$). Except in the case of the blank experiment, values shown correspond to the heterogeneous contribution to each step, the total rate being obtained as the sum of the homogeneous rate (blank experiment) and each value.

	Blank	MgAl	MgZr	CeO_2	TiO_2
k_1	$1.8 \cdot 10^{-5}$	0	$3.2 \cdot 10^{-5}$	$2.2 \cdot 10^{-4}$	$9.3 \cdot 10^{-6}$
k_2	$1.0 \cdot 10^{-5}$	$2.1 \cdot 10^{-5}$	$1.4 \cdot 10^{-5}$	$1.1 \cdot 10^{-5}$	$1.8 \cdot 10^{-5}$
k_3	$5.2 \cdot 10^{-5}$	$3.9 \cdot 10^{-1}$	$3.9 \cdot 10^{-1}$	$6.4 \cdot 10^{-2}$	$1.1 \cdot 10^{-1}$
k_4	$1.9 \cdot 10^{-5}$	$3.4 \cdot 10^{-6}$	$3.4 \cdot 10^{-6}$	$2.8 \cdot 10^{-5}$	$9.9 \cdot 10^{-6}$
r^2	0.914	0.909	0.903	0.919	0.931

Table 4.6. Reaction rate constants based on the proposed reaction network (k_1 indicated in s^{-1}, the other constants in $L \cdot mol^{-1} \cdot s^{-1}$)

	Blank	MgAl	MgZr	CeO_2	TiO_2
k_1	$1.8 \cdot 10^{-5}$	-	$3.2 \cdot 10^{-5}$	$2.2 \cdot 10^{-4}$	$9.3 \cdot 10^{-6}$
k_2	$1.0 \cdot 10^{-5}$	$2.1 \cdot 10^{-5}$	$1.4 \cdot 10^{-5}$	$1.5 \cdot 10^{-5}$	$2.2 \cdot 10^{-5}$
k_3	$5.2 \cdot 10^{-5}$	$3.9 \cdot 10^{-1}$	$3.9 \cdot 10^{-1}$	$6.4 \cdot 10^{-2}$	$1.1 \cdot 10^{-1}$
k_4	$1.9 \cdot 10^{-5}$	$3.4 \cdot 10^{-6}$	$3.4 \cdot 10^{-6}$	$2.8 \cdot 10^{-5}$	$9.9 \cdot 10^{-6}$
k_5	$2.0 \cdot 10^{-5}$	-	$1.4 \cdot 10^{-4}$	-	$2.5 \cdot 10^{-5}$
k_6	-	-	-	$2.0 \cdot 10^{-9}$	-
k_7	$5.0 \cdot 10^{-6}$	-	$9.9 \cdot 10^{-5}$	-	$1.6 \cdot 10^{-8}$
$k_{7,1}$	-	$3.0 \cdot 10^{-6}$	$3.0 \cdot 10^{-4}$	-	$1.2 \cdot 10^{-4}$
$k_{7,2}$	-	$3.3 \cdot 10^{-4}$	$4.6 \cdot 10^{-5}$	$2.8 \cdot 10^{-4}$	$4.9 \cdot 10^{-5}$
k_8	$5.1 \cdot 10^{-6}$	-	-	$6.9 \cdot 10^{-3}$	-
k_9	-	$2.5 \cdot 10^{-5}$	$2.1 \cdot 10^{-4}$	$1.3 \cdot 10^{-7}$	$2.1 \cdot 10^{-5}$
k_{10}	-	-	$5.2 \cdot 10^{-1}$	-	$1.1 \cdot 10^{-8}$
$k_{10,1}$	-	$6.4 \cdot 10^{-4}$	$6.6 \cdot 10^{-7}$	$6.0 \cdot 10^{-4}$	$7.4 \cdot 10^{-5}$
$k_{10,2}$	-	$1.0 \cdot 10^{-2}$	-	$1.7 \cdot 10^{-2}$	$1.2 \cdot 10^{-3}$

As illustrated in Figure 4.26 when a solid catalyst is involved, the quantification of all the intermediates suggests that steps 7 and 10 of the original mechanism must be decomposed into two intermediate ones, justifying the detection of β-formylacrylic (BFA) and malic acid (MAL), compounds not detected without a catalyst. The detailed temporal profiles comparing experimental and fitted data obtained with the most promising supports (TiO_2 and MgAl) are included in **Figure 4.27**, whereas the corresponding ones with MgZr and CeO_2 are incorporated **Figure 4.28**.

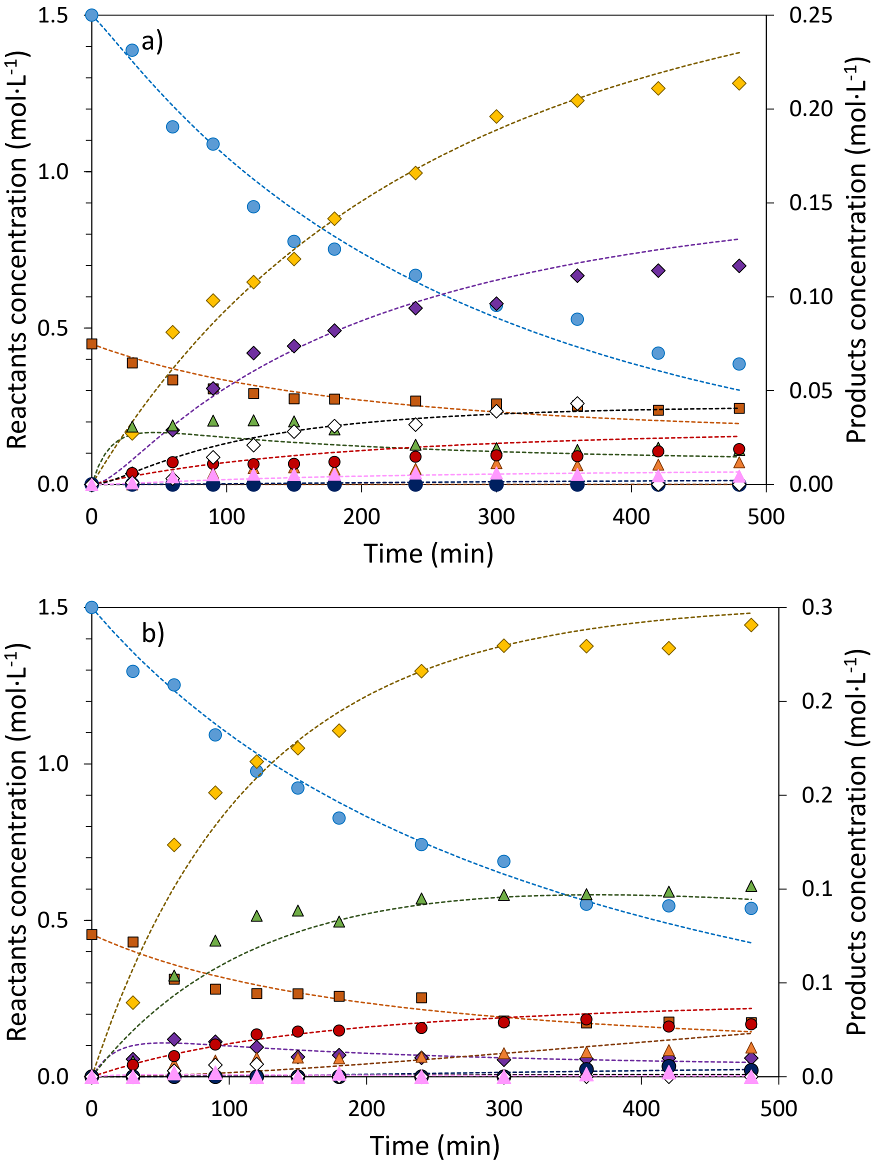

Figure 4.27. Furfural oxidation with H_2O_2 at 50 ºC in presence of (a) TiO_2 and (b) MgAl. Symbols: H_2O_2 (●); FFL (■); FA (◆); HF (▲); FCA (●); MA (◆); FN (▲); HFN (●); BFA (◇); MAL (▲). *Broken lines correspond to the kinetic model predictions*

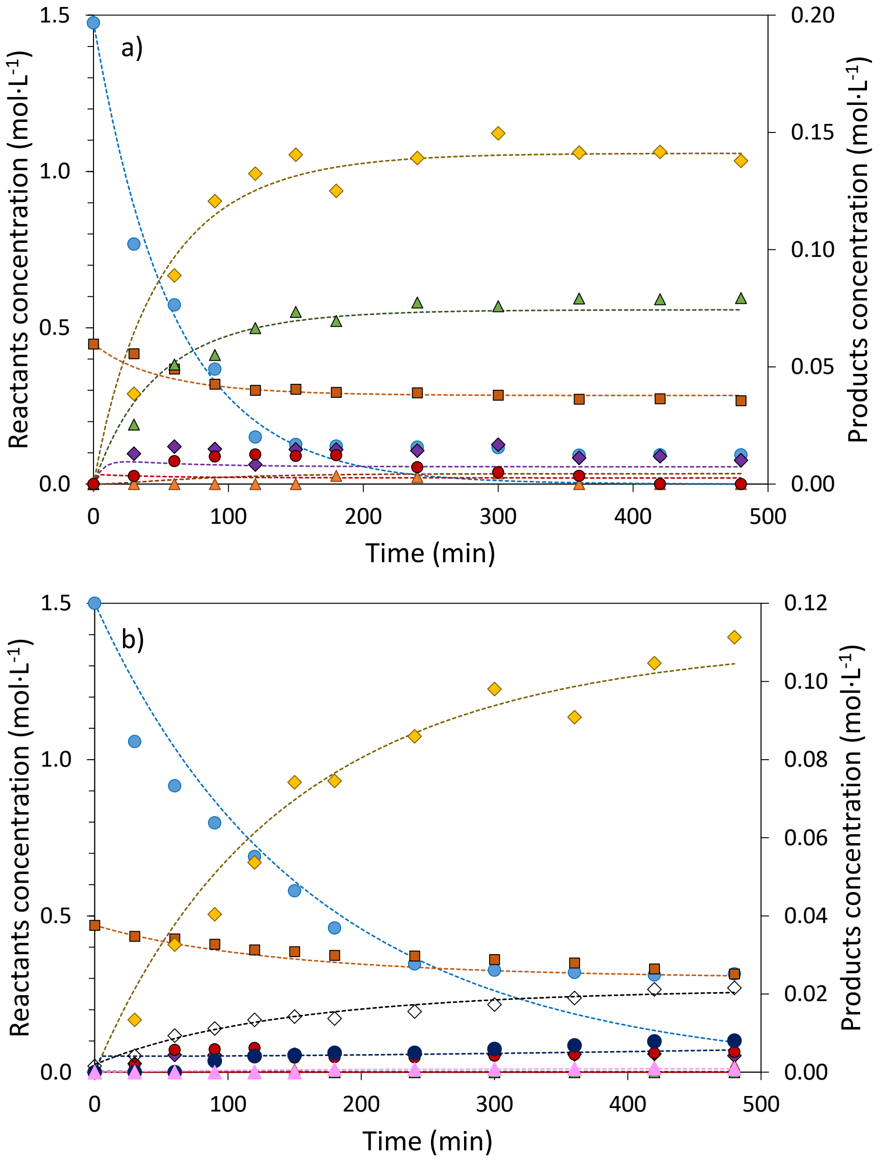

Figure 4.28. Furfural oxidation with H_2O at 50 ºC with (a) CeO_2, and (b) MgZr. Symbols: H_2O_2 (●); FFL (■); FA (◆); HF (▲); FCA (●); MA (◆); FN (▲); HFN (●); BFA (◇); MAL (▲). *Broken lines correspond to the kinetic model adjustment*

The complexity of the mechanism limits the analysis based on the characterization parameters. However, a clear correspondence between the main kinetic rates and the catalyst acidity is observed, as shown in **Figure 4.29**.

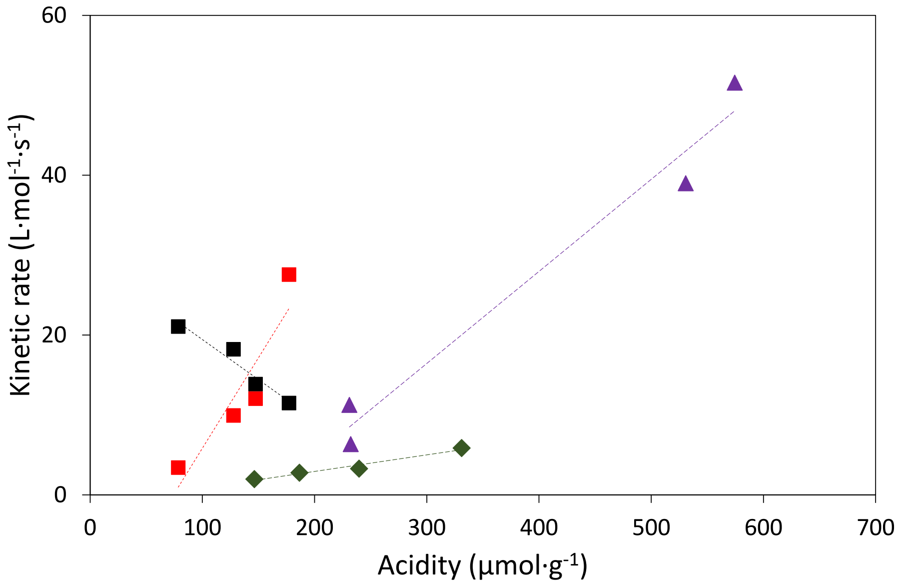

Figure 4.29. Evolution of the kinetic constants for furfural conversion considering both pathways, k_2 (■, x10^{-5}) and k_4 (🟥, x10^{-6}), as a function of the medium-strength acidity; HF oxidation, $k_5 + k_7 + k_{11}$ (◆, x10^{-4}) as a function of the medium-strength and strong acid sites, and the furoic acid oxidation, k_3 (▲, x10^{-2}) as a function of the total acidity of the oxides used as catalysts

As anticipated by the literature [54, 55] and corroborated with our experimental results, the lateral route of 2-hydroxyfuran formation (B-V mechanism) is promoted by the acidity (k_4), the medium-strength sites being the most relevant ones for this step. An opposite influence is observed for the furoic acid production, supporting the negative role of acidity to maximize its yield. In the same way, a positive effect of acidity is observed also for the following oxidizing steps, with a higher relevance of the strong acidic sites for the total decomposition of the two main products of the reaction, the 2-hydroxyfuran, and furoic acid, producing CO_2 as the final compound.

The parallel analysis considering the basicity of these materials is not conclusive. The lack of a clear correlation between oxidizing steps and basicity discards the prevalence of the Cannizaro disproportionation mechanism also proposed in the literature [56, 57]. In good agreement, furfuryl alcohol is not observed. Although a positive role of basicity is suggested by the experiments (increasing the acids stability and preventing their total decomposition into CO_2), the redox properties of some of these catalysts alter the H_2O_2 available to produce the furfural conversion, this fact prevailing over the basicity. These effects are more relevant for first intermediates, such as the furoic acid (FCA), compounds whose production is more sensitive to the weak equilibrium between activity, selectivity and stability.

4.3.4. Activity of bifunctional catalysts

Bifunctional catalysts were prepared with a theoretical 1% of Pt, Pd, or Au. These metals were chosen considering their high oxidation capacity demonstrated for similar systems [49], to analyze their influence tuning the selectivity of the reaction. The low metal loading leads to good metal dispersions, maximizing the activity of these metal particles and enabling a direct comparison with the bulk material. In good agreement, there is a complete correspondence between the surface structure of the bulk and the metal-modified catalysts, as observed by XRD (**Figure 4.30-31**). **Table 4.7** shows the main characterization results, in terms of morphology, metal loading and dispersion, and surface chemistry.

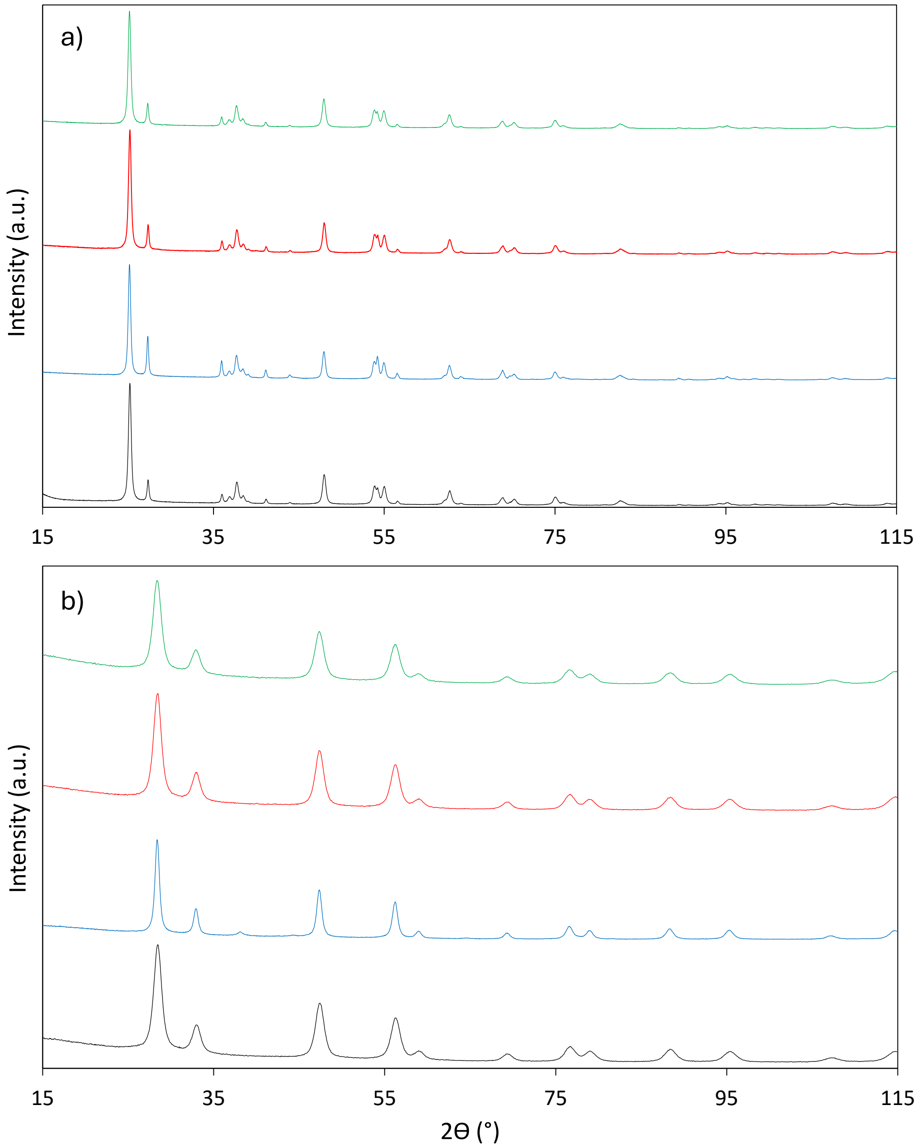

Figure 4.30. XRD diffractograms of (a)TiO_2 (black), Au/TiO_2 (blue), Pd/TiO_2 (red) and Pt/TiO_2 (green) and (b) CeO_2 (black), Au/CeO_2 (blue), Pd/CeO_2 (red) and Pt/CeO_2 (green)

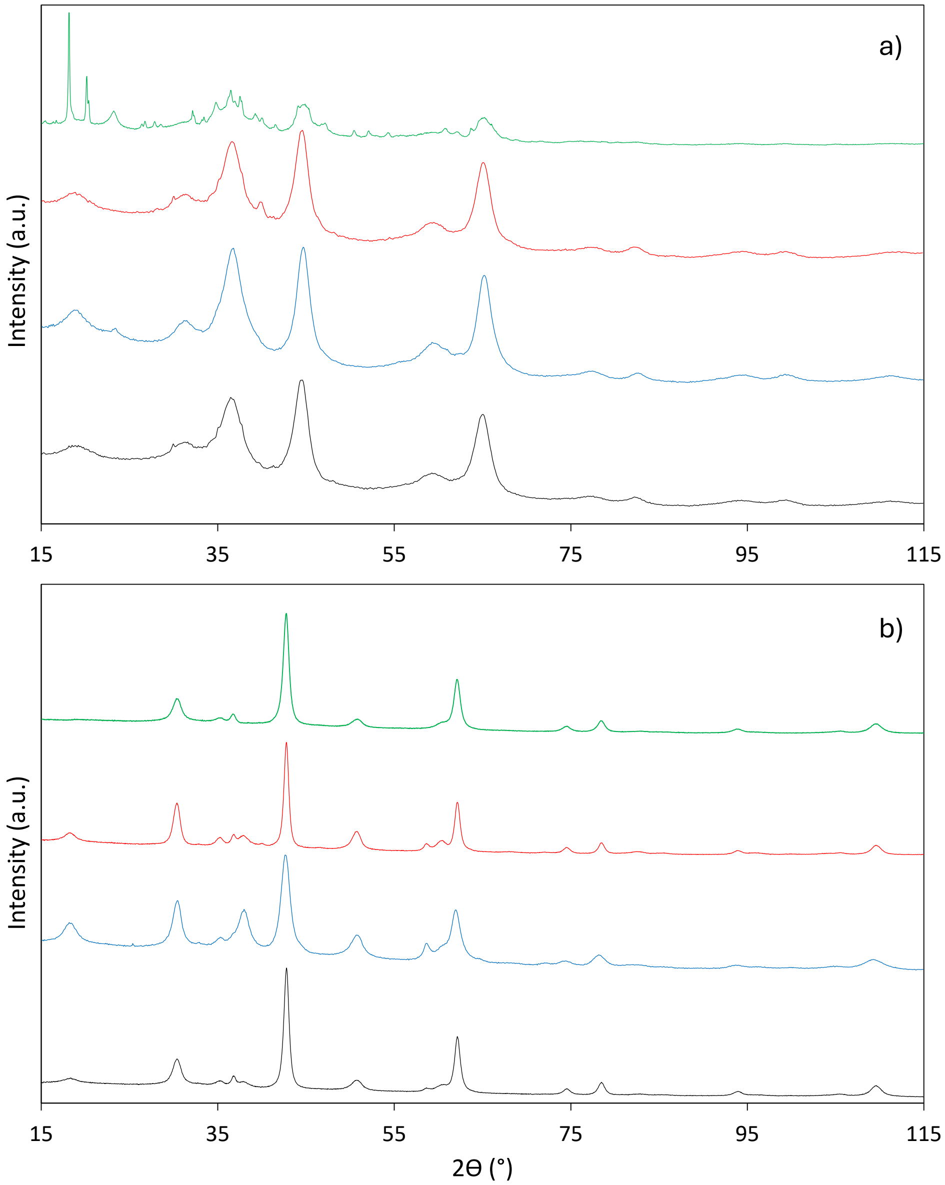

Figure 4.31. XRD diffractograms of (a) MgAl (black), Au/ MgAl (blue), Pd/ MgAl (red) and Pt/MgAl (green) and (b) MgZr (black), Au/ MgZr (blue), Pd/ MgZr (red) and Pt/MgZr (green).

Table 4.7. Main characterization properties of the different bifunctional oxides used in this work

	Pd/MgAl	Pt/MgAl	Au/MgAl	Pd/MgZr	Pt/MgZr	Au/MgZr	Pd/CeO_2	Pt/CeO_2	Au/CeO_2	Pd/TiO_2	Pt/TiO_2	Au/TiO_2
N_2 physisorption												
Surface area ($m^2 \cdot g^{-1}$)	151	165	196	82	128	78	118	114	115	66	54	63
Pore volume ($cm^3 \cdot g^{-1}$)	0.4	0.3	0.4	0.7	0.6	0.3	0.2	0.2	0.2	0.4	0.4	0.7
Pore diameter (nm)	8	12.1	5.6	23.1	17.7	11.9	4.8	4.4	4.7	21	24.4	35.9
ICP, Metal loading (%)	0.87	0.87	1.05	0.97	0.88	0.89	0.8	0.79	1.06	0.85	0.82	1.01
TEM												
Particle size (nm)	8.3	7.7	9.9	7.8	11.9	8.6	1.5	4.6	9.3	8.5	10.8	6.5
Dispersion (%)	14.1	21.6	15.9	16.5	15.4	14.7	49.4	36.4	13.8	13.1	11	24.2
Acidity (μmol $NH_3 \cdot g^{-1}$)												
Physisorbed (<100 ºC)	0	19.7	116.1	0	52.4	75.5	0	0	35.5	22.9	25.4	22.2
Weak (100 – 200 ºC)	0	58.9	158.1	119.8	116.7	191.7	201.3	231.1	36.2	81.4	78.3	52.9
Medium (200 - 400 ºC)	315	36.5	64.1	109.3	148	130	0	22.9	124.2	0	50.3	54.9
Strong (>400 ºC)	50.7	43.5	0	192.3	86.3	0	0	0	0	0	0	0
Total	**365.7**	**158.6**	**338.3**	**421.5**	**403.4**	**397.3**	**201.3**	**254**	**195.9**	**104.3**	**153.9**	**130**
Basicity (μmol $CO_2 \cdot g^{-1}$)												
Physisorbed (<100 ºC)	24.8	12.2	36.4	6.6	40.3	13.8	24.1	110.5	28.3	17.1	24.5	15
Weak (100 – 200 ºC)	0	58	80.3	37.5	78.3	33.1	0	0	8.1	0	0	0
Medium (200 - 400 ºC)	116.5	93.1	199.2	50.4	110.1	70.2	0.8	16.4	0	4.9	3.1	6.5
Strong (>400 ºC)	156.7	56.5	0	25.9	20.9	0	4.5	37.8	14.1	46.7	38.8	3.8
Total	**298.1**	**219.8**	**315.8**	**120.3**	**249.7**	**117.1**	**29.4**	**164.4**	**50.5**	**68.6**	**66.3**	**25.2**

Bifunctional catalysts keep the surface properties of the bulk materials, observing slight decreases in the surface area due to the non-porous surface of metal nanoparticles. The N_2 isotherms are included in **Figure 4.32**

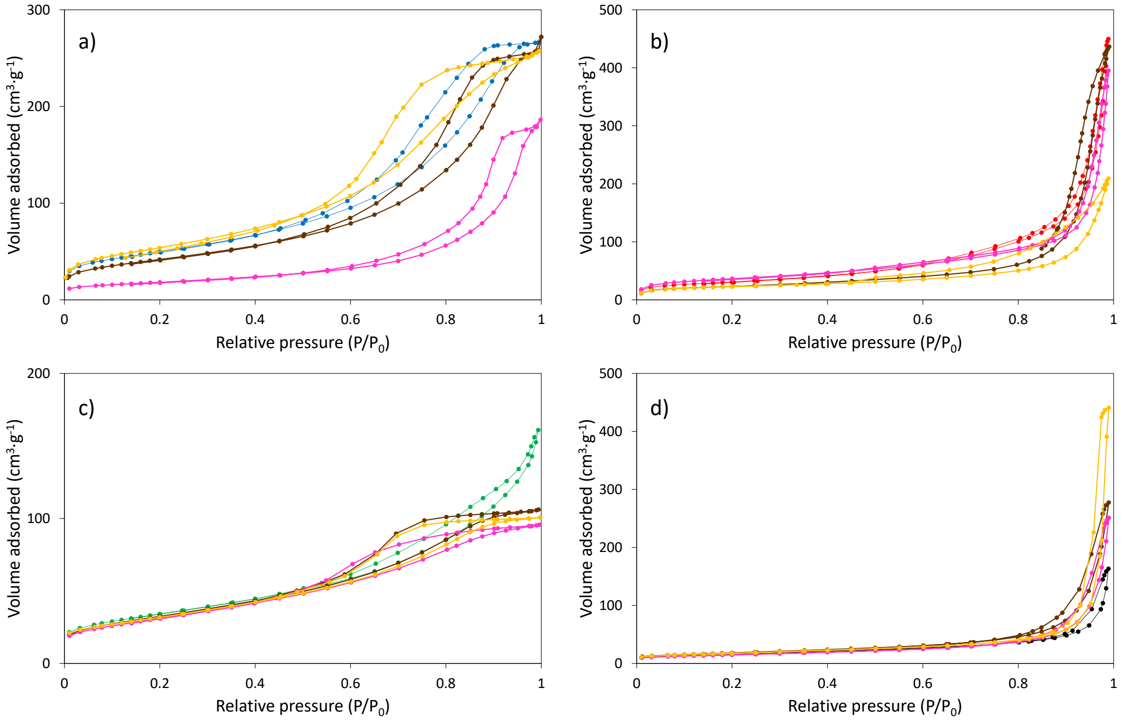

Figure 4.32. N_2 isotherms of catalysts based on (a) MgAl, (b) MgZr, (c) CeO_2, and (d) TiO_2. *See Fig. 4.22 to codes for the supports*. Au-based materials are indicated in yellow, Pd in brown, and Pt in pink

Considering the preparation methodology (dry impregnation except in the case of Au materials), these particles are located inside the pores. Consequently, there is a slight increase in the average size of the pores because the smallest ones can be completely blocked, increasing the relative weight of the biggest ones. This partial blockage is also congruent with the differences observed in surface chemistry. In most cases, the total concentration of the acid sites is lower than the one of the bulk materials, keeping the same relative weight in strength terms. The highest decrease is observed with Pt/MgAl (70.1% with respect to the total concentration of the parent material), being also very significative with Pd/TiO_2 (33.4%), Pd/TiO_2 (54.9%) and Au/TiO_2 (43.7%). For the other materials, the decrease is less relevant, in general lower than 20%. The effect on the basicity is not so clear. There is a relevant decrease in basicity with Au/TiO_2 and Pt/MgAl (~33%), whereas the basicity of other materials, such as Pt/TiO_2 and Pd/TiO_2 significantly increases. The TPD data are included in **Figure 4.33-34**.

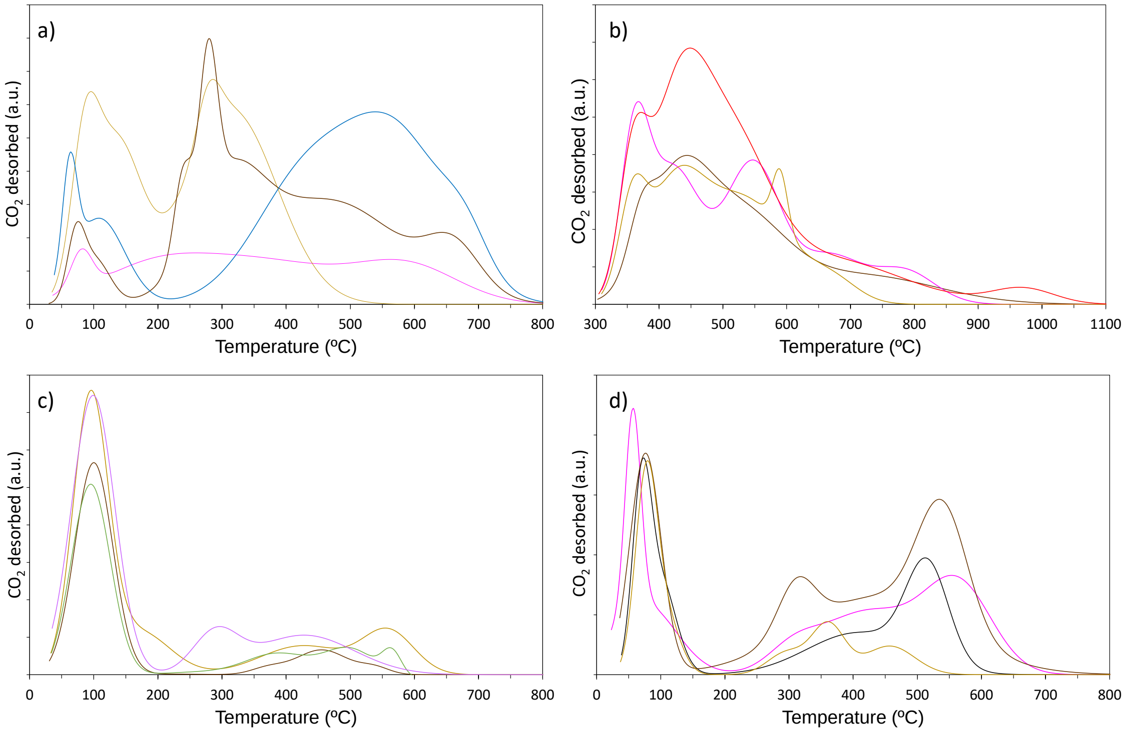

Figure 4.33. CO_2 desorbed during the TPD-CO_2 of catalysts based on (a) MgAl, (b) MgZr, (c) CeO_2, and (d) TiO_2. *See Fig. 4.21 to codes for the supports*. Au-based materials are indicated in yellow, Pd in brown, and Pt in pink.

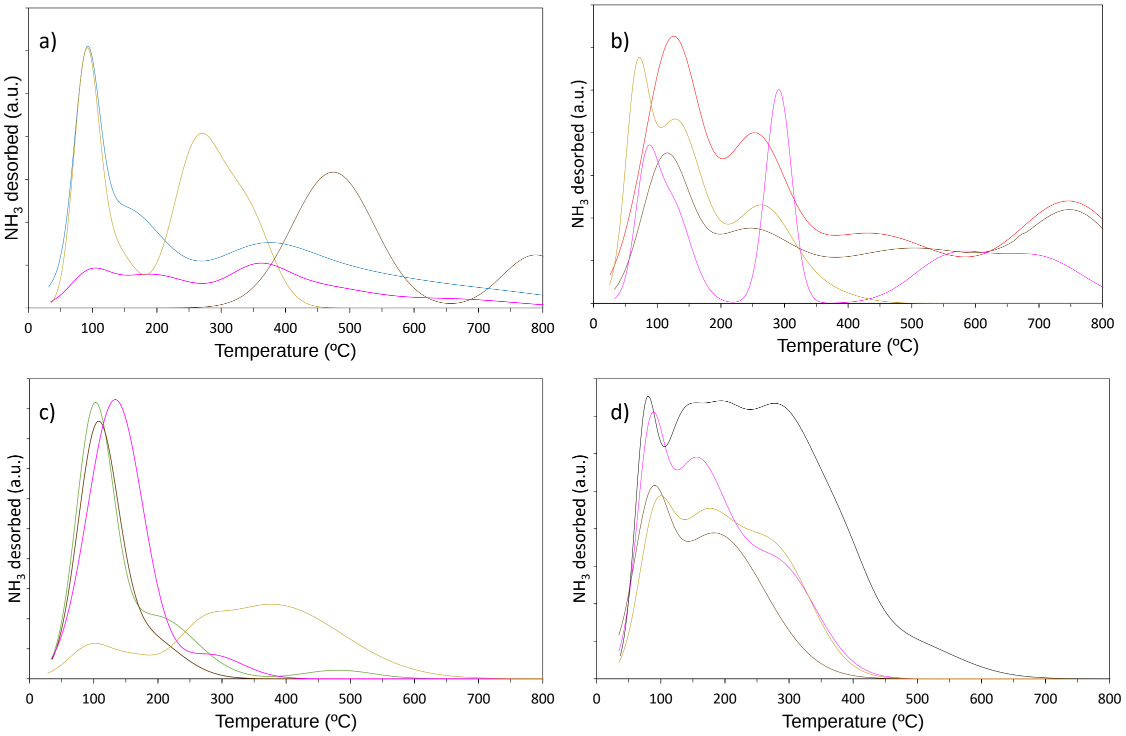

Figure 4.34. NH_3 desorbed during the TPD- NH_3 of catalysts based on (a) MgAl, (b) MgZr, (c) CeO_2, and (d) TiO_2. *See Fig. S1 to codes for the supports*. Au-based materials are indicated in yellow, Pd in brown, and Pt in pink

The dispersion values indicated in these tables correspond to TEM results. The CO chemisorption analyses were also carried out, obtaining discrepancies lower than 5% in most cases (see **Table 4.8**). However, these results were not included in these tables since this technique could not be efficiently applied to Au-catalysts. TEM results demonstrate the presence of reduced metal particles in the range of 5.5-7.5 nm, with slightly lower values for Pt/CeO_2 and Pd/CeO_2 (4.6 and 1.5 nm). These values were obtained after measuring more than 100 particles from micrographs such as those shown in **Figure 4.35-38**. In agreement with these similar particle sizes, most of these materials have a similar metal dispersion, from 18 to 30 %, reaching values up to 45 % for those catalysts with the smallest particle size.

Table 4.8. CO chemisorption results of the different bifunctional oxides used in this work

	Pd/MgAl	Pt/MgAl	Au/MgAl	Pd/MgZr	Pt/MgZr	Au/MgZr	Pd/CeO$_2$	Pt/CeO$_2$	Au/CeO$_2$	Pd/TiO$_2$	Pt/TiO$_2$	Au/TiO$_2$
CO chemisorption												
Particle size (nm)	10.5	6.5	9.9	10.2	9.7	13.4	2.4	0.8	-	8.9	7.9	-
Dispersion (%)	15.3	20.5	15.9	11.4	16.5	8.9	45.9	49.2	-	12.7	14	-
Adsorbed CO (cm^3/g SPT)	0.17	0.21	0.19	0.13	0.20	0.10	0.35	0.44	-	0.14	0.16	-

Table 4.10. Selectivities distribution and carbon balance obtained with the different bifunctional catalysts used in this work

	Pd/MgAl	Pt/MgAl	Au/MgAl	Pd/MgZr	Pt/MgZr	Au/MgZr	Pd/CeO$_2$	Pt/CeO$_2$	Au/CeO$_2$	Pd/TiO$_2$	Pt/TiO$_2$	Au/TiO$_2$
FCA	37.4	34.8	37.1	37.1	0	23.8	13.8	0	20.9	23	14.8	39.1
FN	0	4	2.2	0	100	4	0	0	0	0	6.8	0
MA	5.9	3.9	17.9	7.7	0	18	7.1	0	5.6	76.5	9.8	0
MAL	18.8	10.1	0.3	27.5	0	1.9	21.4	78.5	0	0	7.7	38.1
HF	7	0	24.8	7.5	0	24.7	45.5	21.5	36.9	0	0	16.5
HFN	0	47.2	0	0	0	0	0	0	0	0	60.8	0
BFA	27.7	0	17.7	20.2	0	27.6	12.3	0	36.6	0	0	6.3
Carbon Balance (%)	90.5	95.5	85.6	93.5	80.4	97.8	93.9	73.8	93	87.2	91	86.3

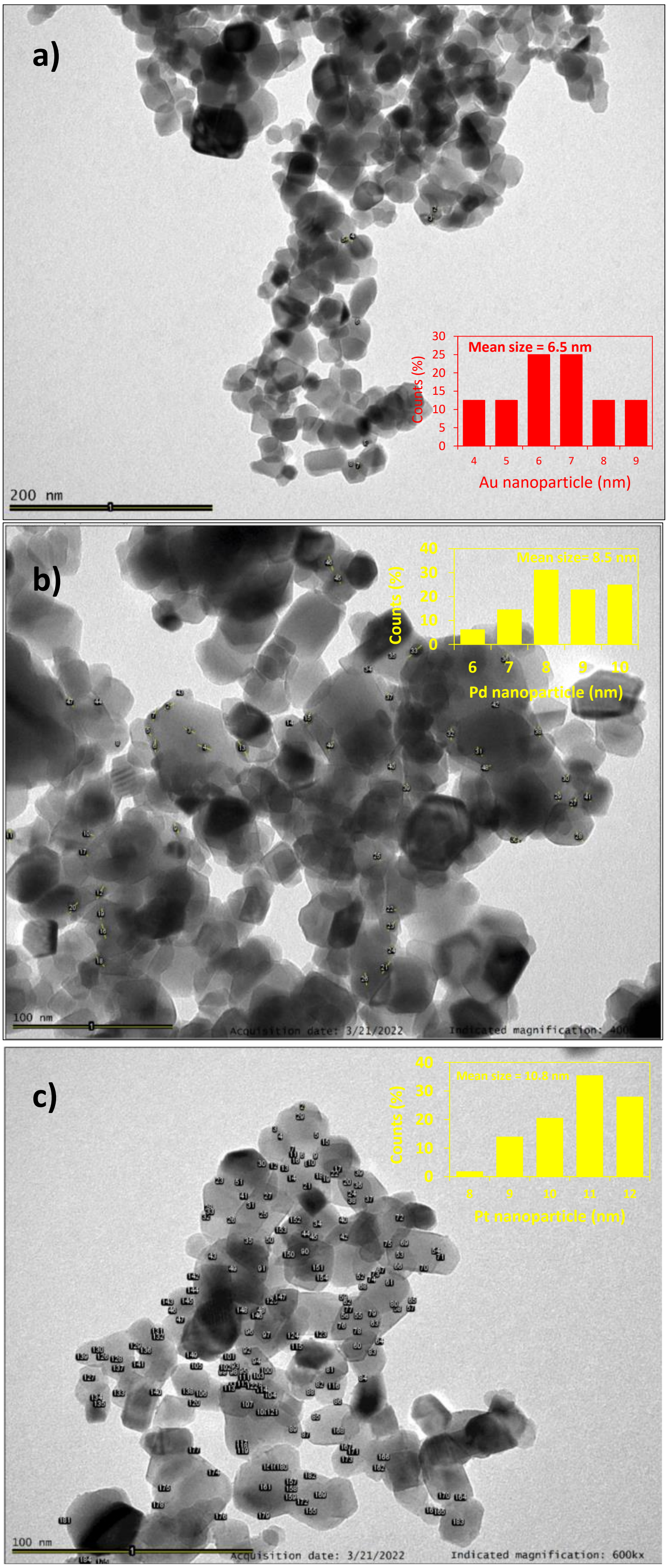

Figure 4.35. TEM micrographs and histograms of (a) Au/TiO_2, (b) Pd/TiO_2, and (c) Pt/TiO_2

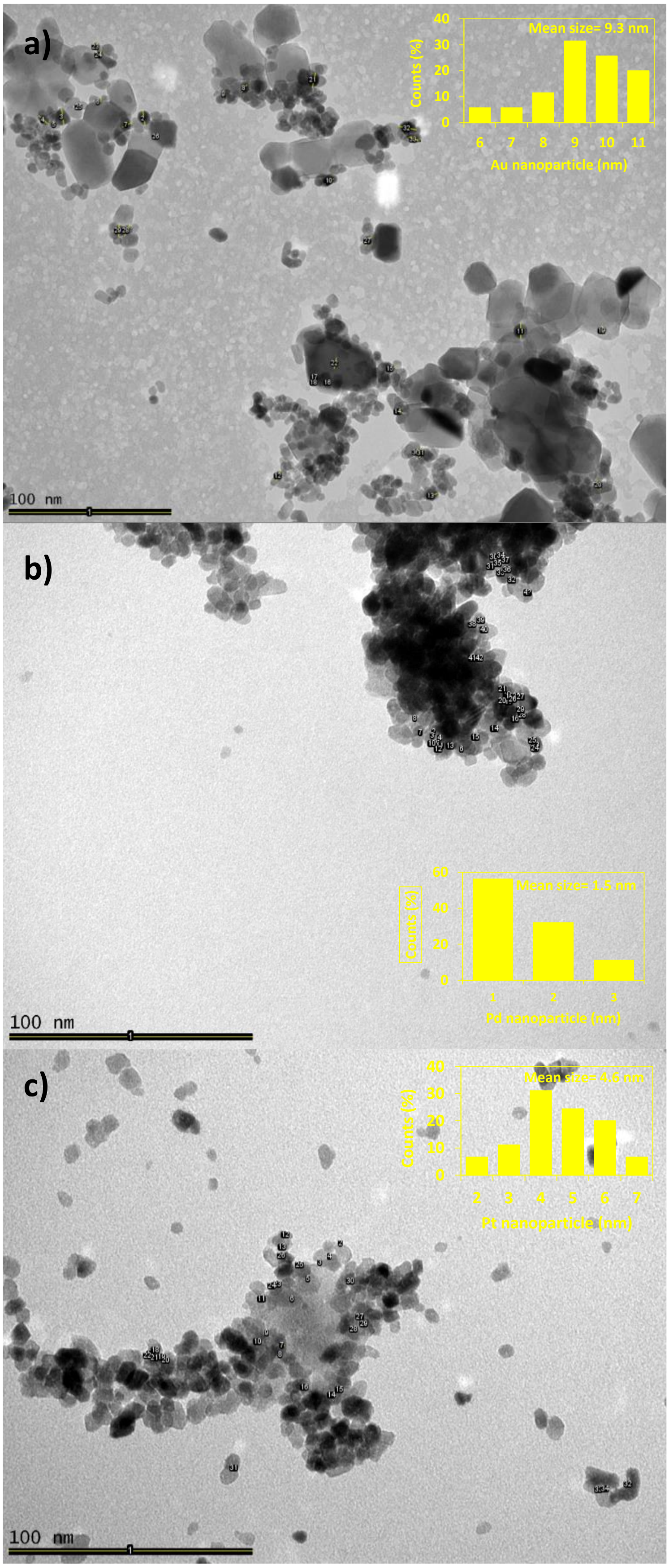

Figure 4.36. TEM micrographs and histograms of (a) Au/CeO_2, (b) Pd/CeO_2, and (c) Pt/CeO_2

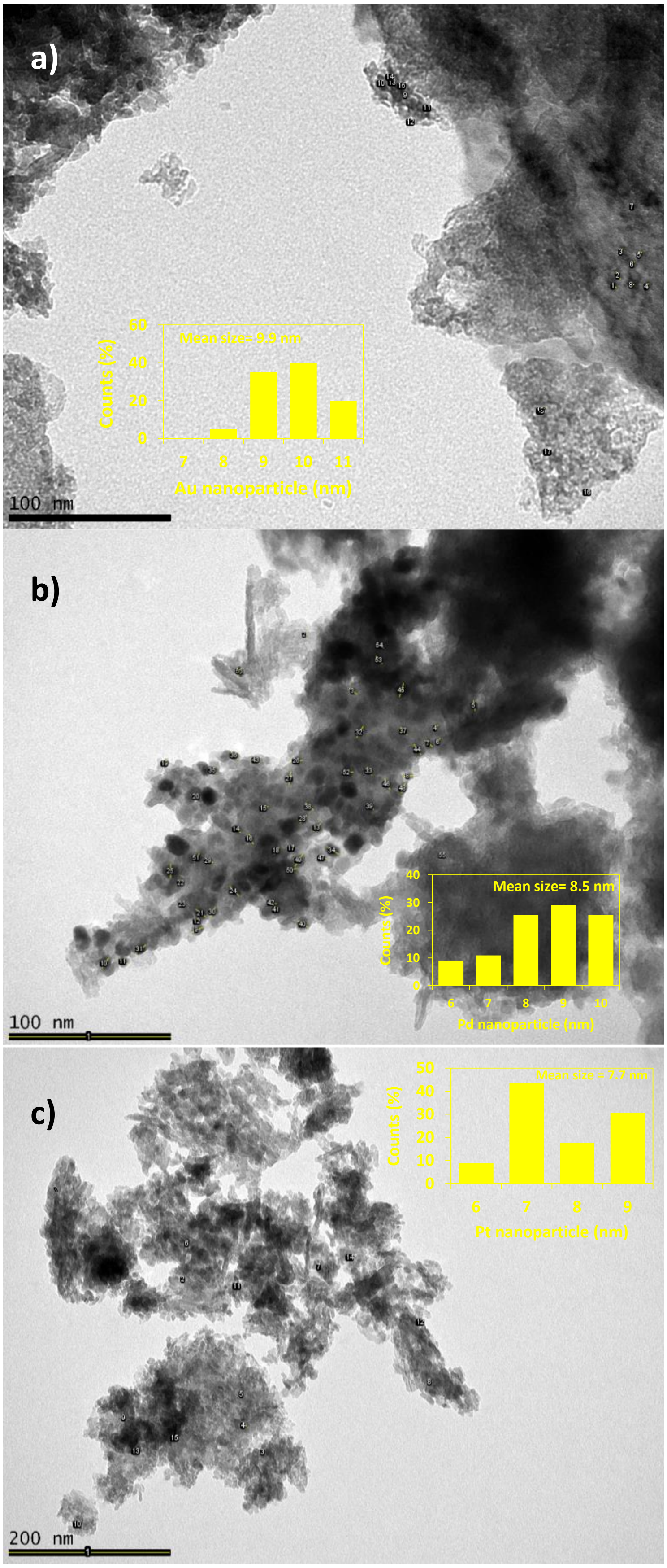

Figure 4.37. TEM micrographs and histograms of (a) Au/MgAl, (b) Pd/MgAl, and (c) Pt/MgAl

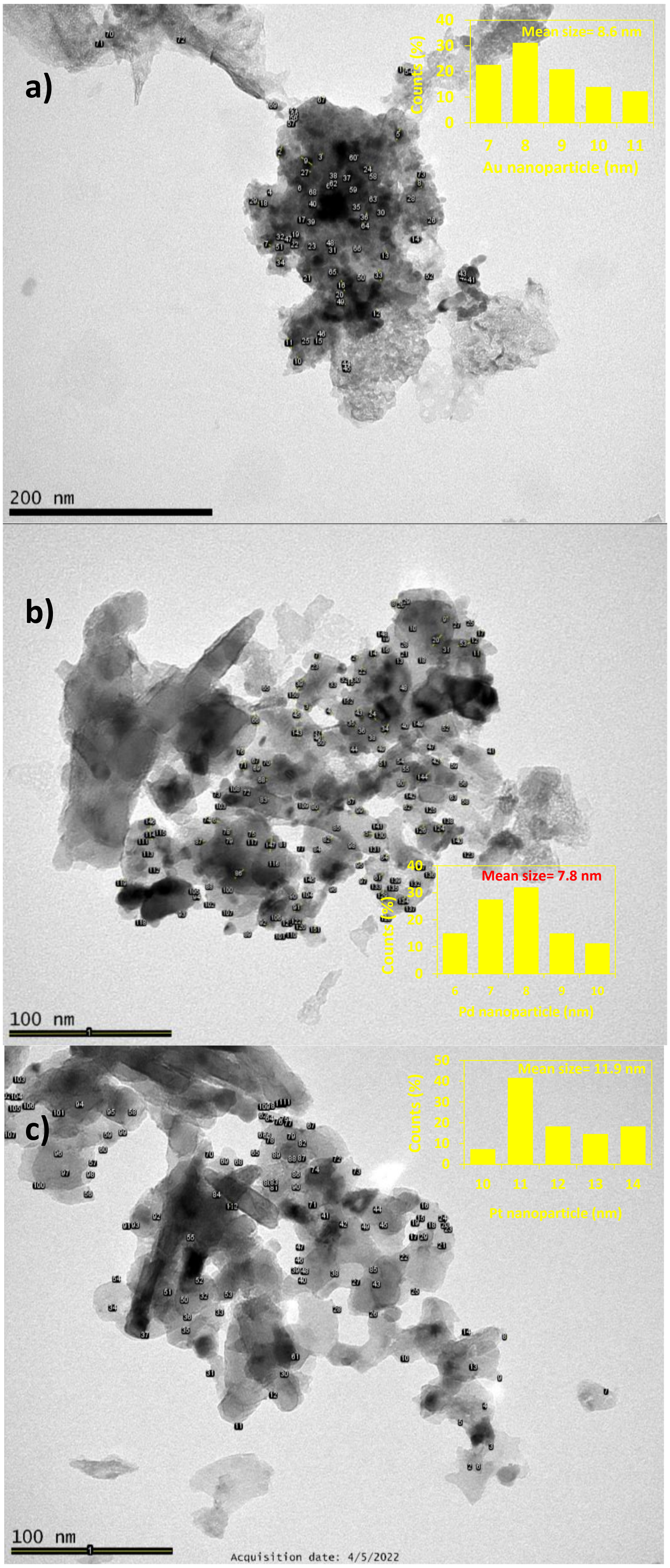

Figure 4.38. TEM micrographs and histograms of (a) Au/MgZr, (b) Pd/MgZr, and (c) Pt/MgZr

These dispersion results, as well as the own nature of these metals and their synergetic effect with the surface chemistry of the catalytic support, are assumed to be the most relevant parameters to discuss the catalytic activity of these bifunctional catalysts. TPR analyses of the spent catalysts discard that experimental results are affected by a total or partial oxidation of metal particles. As indicated in the introduction section, furoic acid (FCA), 2(5H)-furanone (FN), maleic and malic acids (MA and MAL, respectively) are the most interesting compounds obtained by furfural partial oxidation. 2(5H)-furanone (FN) is not significantly produced with almost none of the catalysts tested, except for Pt/MgZr, a catalyst that selectively produces this compound (100%).

Figure 4.39 shows the FCA selectivity-conversion plots for the different catalysts, whereas main results after 8h reaction time are summarized in **Table 4.9** (the detailed products distribution is included **Table 4.10**. As observed in Fig. 4.39, the presence of noble metals increases the maximum selectivity of FCA obtained with each support. Platinum is the only exception, its behaviour strongly depends on the support. Thus, using MgZr and CeO_2, FCA is not detected whereas, with the other two oxides (MgAl and TiO_2), the maximum selectivities (40.8 and 23.3%) are reached in less than 1h. In the case of Pt/MgAl, the corresponding FFL conversion is almost negligible (1.5%), whereas Pt/TiO_2 is significantly more active, with 18.9% of FFL conversion after this 0.5h.

Pt/MgAl shows the slowest kinetic (9.2% of FFL conversion after 8 h), but its selectivity and stability to FCA is quite high, with a remaining selectivity of 34.8%. Both results are congruent with the significant blockage of acidic sites produced by Pt nanoparticles, slowing down all the oxidizing reactions. On the contrary, Pt/TiO_2 is discarded because of the poor FCA stability observed.

Pd/MgAl is the catalyst that produces the maximum FCA selectivity (49.2% after 3 h of reaction, with a 11.2% of FFL conversion). The slow activity also observed with this material results in a quite stable FCA production (remaining selectivity after 8 h of 37.1%). Very similar results are reached with Pd/MgZr (37.1% of selectivity with 12% of FFL conversion). The FCA selectivities obtained when using supports with redox activity are significantly lower, both comparing the maximum values (22.3 and 23.3% with Pd/CeO_2 and Pt/TiO_2, respectively), and results after 8h.

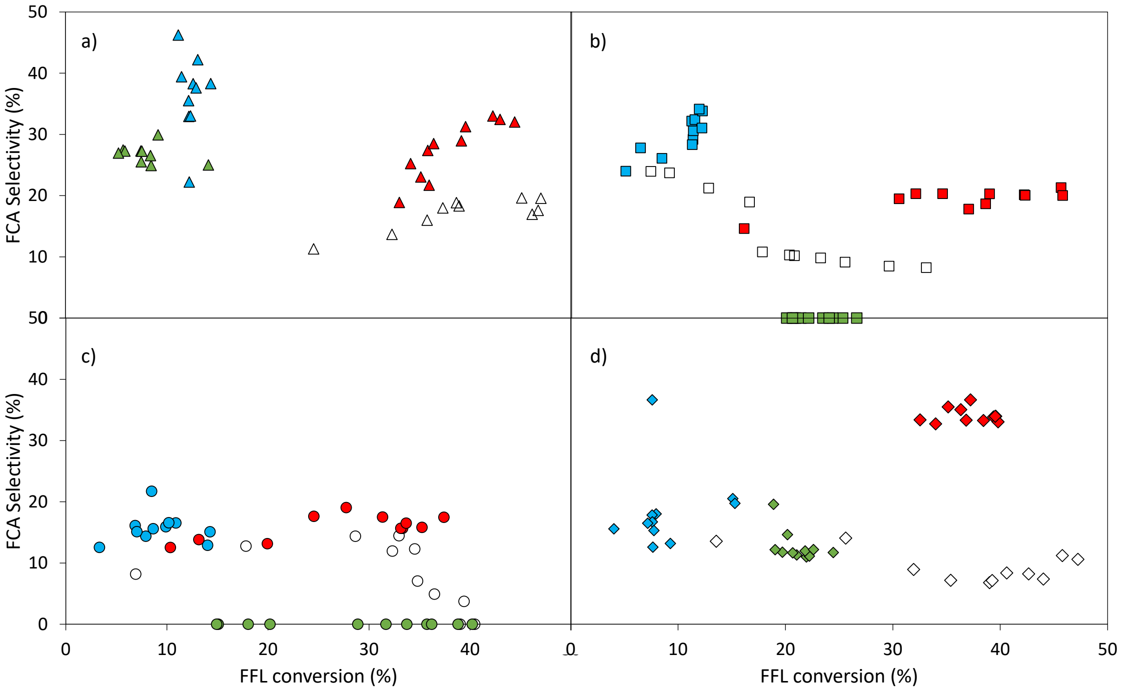

Figure 4.39 Conversion vs. FCA selectivity plots for furfural oxidation using H_2O_2 at 50 ºC over (a) MgAl-supported, (b) MgZr-supported, (c) CeO_2-supported, and (d) TiO_2-supported catalysts. Red dots correspond to Au-based catalysts, green dots to Pt-based catalysts, blue dots to Pd-based catalysts, and white dots to bulk supports

Both using Pt and Pd, almost total H_2O_2 conversion is reached in less than 3h (>99%), this fact strongly affecting the distribution of the products. These results could be different modifying the reactor configuration to allow a continuous addition of H_2O_2. Despite the high interest of this configuration (previously tested in the literature [40]), the continuous change in volume limits the use of temporal data to evaluate the kinetic of the systems as well as the influence of the catalyst in the H_2O_2 decomposition rate. These points will be deeply discussed below.

Concerning the Au-modified catalysts, the maximum FCA selectivities are quite high (38.1, 24.2, 22.7, and 42%, with Au/MgAl, Au/MgZr, Au/CeO_2, and Au/TiO_2, respectively). This metal offers the maximum stability of this production, and their final FFL conversion are the highest ones (from 37 to almost 50%), resulting in the maximum FCA yields obtained with all the screening of catalysts tested in this work (8.5, 7.5 and 7.1% with Au/MgAl, Au/MgZr, and Au/TiO_2). These yields could be significantly increased by modifying the reaction configuration since FFL conversion increases by increasing the catalytic loading or recycling the unconverted reactant. Thus, the relevance of these results is directly related to the high selectivity obtained. Concerning to H_2O_2, although obtained conversions are very high (86.6, 97.1, 81.1, and 97.3%, with Au/MgAl, Au/MgZr, Au/CeO_2, and Au/TiO_2 after 8h), a remaining amount of oxidant is present in most of the experiments. In the same way, final carbon balances are always higher than 86% (see Table 4.10), the lack of information because of total FFL decomposition into CO_2 being not very relevant. The similar trends obtained with all the Au-modified catalysts suggests a positive role of this metal that can be discussed independently of the properties of the support (it will be analysed below). Based on these results, Au/TiO_2 is defined as the optimum catalyst to produce FCA.

Table 4.9. Furfural conversion and selectivity distribution after 8 h of reaction at 50 ºC as a function of the catalyst used

	FFL Conv. (%)	Selectivity (%)			
		FCA	FN	MA	MAL
MgAl	49.2	1.8	66.6	0	0
Pd/MgAl	14.4	37.4	0	5.9	18.8
Pt/MgAl	9.2	34.8	4	3.9	10.1
Au/MgAl	49.2	37.1	2.2	17.9	0.3
MgZr	33.1	10.1	35.6	6.6	1.4
Pd/MgZr	12	37.1	0	7.7	27.5
Pt/MgZr	21.4	0	100	0	0
Au/MgZr	45.8	23.8	4	18	1.9
CeO_2	40.5	0	0	11.3	0
Pd/CeO_2	14	13.8	0	7.1	21.4
Pt/CeO_2	27.8	0	0	0	78.5
Au/CeO_2	37.4	20.9	0	5.6	0
TiO_2	45.8	13.6	6.9	66.2	2.6
Pd/TiO_2	15.3	23.0	0	76.5	0
Pt/TiO_2	22.6	14.8	6.8	9.8	7.7
Au/TiO_2	39.5	39.1	0	0	38.1

The presence of noble metals also modifies the selectivity to lineal carboxylic acids, as β-formyl-acrylic (BFA), maleic (MA) and malic (MAL) acids productions. The maximum selectivities with the corresponding FFL conversions are compared in **Figure 4.40**.

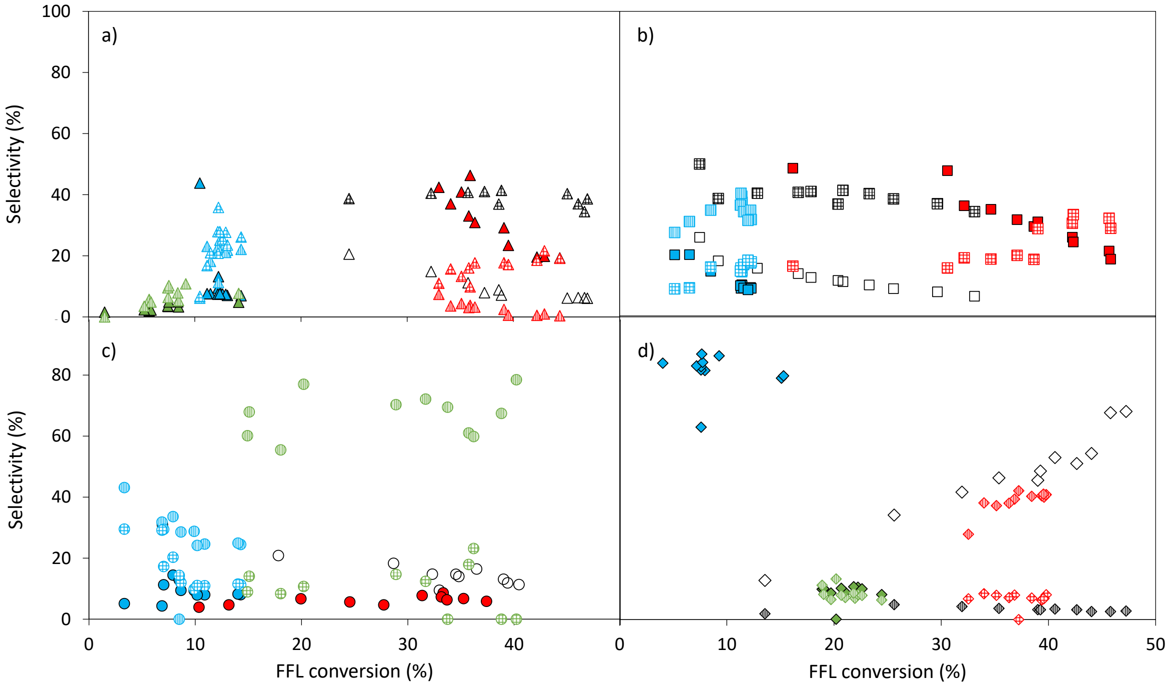

Figure 4.40. Conversion vs. selectivity plots for furfural oxidation using H_2O_2 at 50 ºC over (a) MgAl-supported, (b) MgZr-supported, (c) CeO_2-supported, and (d) TiO_2-supported catalysts. Red dots correspond to Au-based catalysts, green dots to Pt-based catalysts, blue dots to Pd-based catalysts, and white dots to bulk supports. Solid colors correspond to MA, vertically stripped symbols to MAL and squared symbols to BFA

Maleic acid (MA) is produced with almost total selectivity using Pd/TiO_2 (84.8%), value reached after 5h that corresponds to a very low FFL conversion (7.7%). The low basicity of this material suggests a low stabilization of previous intermediates, promoting their oxidation. In this case, the chemical properties seem to be more relevant than the own activity of the metal, observing the poor results obtained when using other supports.

The maximum selectivities obtained with Au/MgAl and Au/MgZr are also quite relevant (43.9 and 46.9%), but the stability of MA with these materials is very weak, suffering a fast disappearance, discarding the gold as a good metal to obtain this compound. Pt is also discarded, observing that this metal hinders the MA route. Maleic acid (MAL) is a very unstable product that suffers fast oxidation with almost all the catalyst. Pt/CeO_2 is the only exception, with a constant MAL production, reaching a final selectivity of 78.5% with almost 28% of FFL conversion. This result could be a synergetic effect of its low basicity (the lowest basicity of all the catalysts tested) and a particular interaction between Pt nanoparticles and the redox surface of CeO_2. The analysis about the non-carboxylic intermediates is included in **Figure 4.41**.

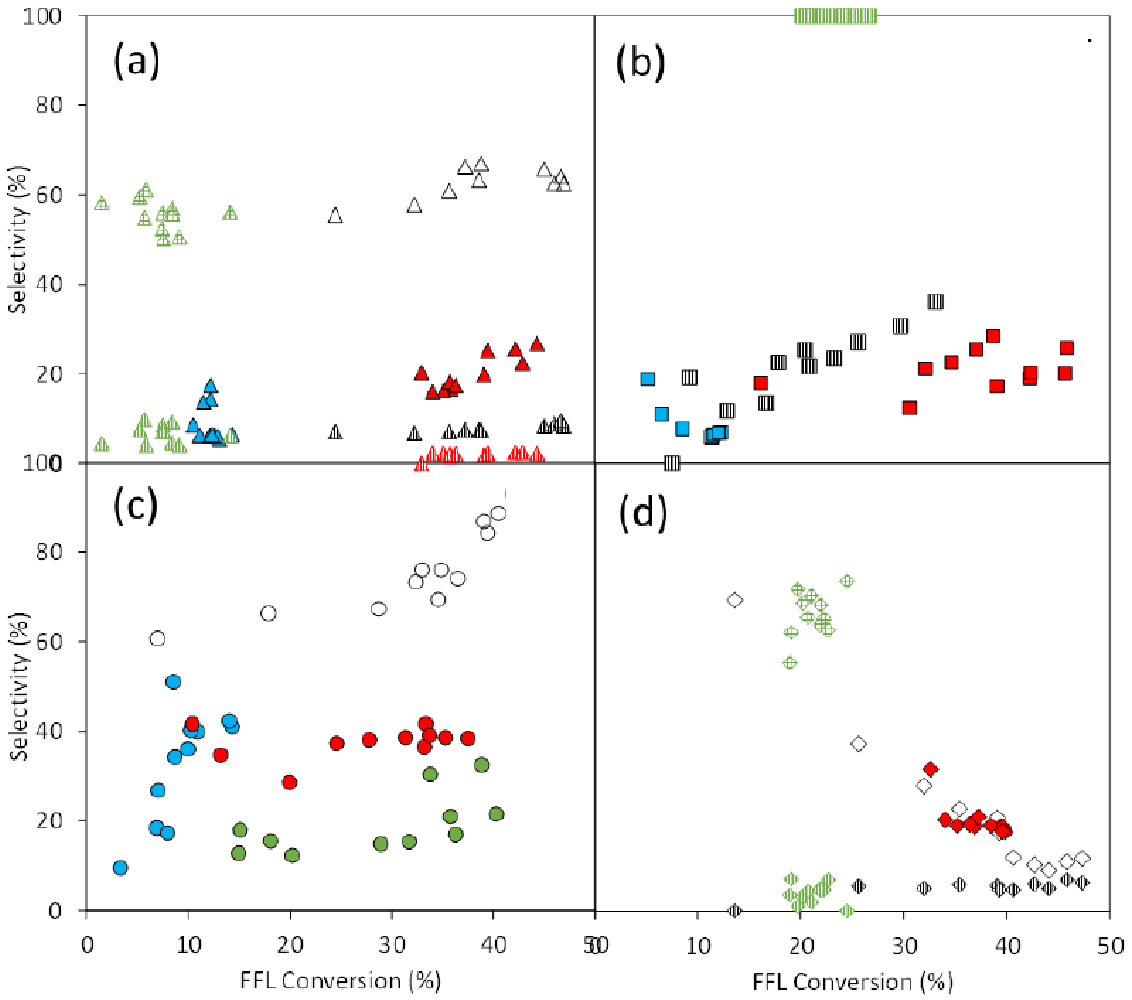

Figure 4.41. Conversion vs. selectivity plots for furfural oxidation using H_2O_2 at 50 ºC over (a) MgAl-supported, (b) MgZr-supported, (c) CeO_2-supported, and (d) TiO_2-supported catalysts. Red dots correspond to Au-based catalysts, green dots to Pt-based catalysts, blue dots to Pd-based catalysts, and white dots to bulk supports. Solid colors correspond to HF, vertically stripped symbols to FN and squared symbos to HFN. The formation patterns are less clear in good agreement with their more complex formation and depletion mechanism, being remarkable that TiO_2-based catalysts present a clearly decreasing trend (reactive intermediate), whereas for the other catalysts a more stable selectivity plateaus were observed, highlighting the total selectivity to FN observed for Pt/MgZr

4.3.5. Kinetic study of bifunctional catalysts

All the experimental data were fitted to the proposed kinetic model. The kinetic rates obtained for the heterogeneous contribution are summarized in **Table 4.11 and 12**. The correspondence between experimental and fitted values of the best catalysts is shown in **Figure 4.42**, whereas the other materials are included in **Figures 4.43-46**.

Table 4.11. Reaction rate constants based on the proposed reaction network (k_1 indicated in s^{-1}, the other constants in $L\cdot mol^{-1}\cdot s^{-1}$)

	Au/TiO_2	Pd/TiO_2	Pt/TiO_2	Au/CeO_2	Pd/CeO_2	Pt/CeO_2
k_1	$5.3\cdot10^{-4}$	$1.6\cdot10^{-3}$	$7.4\cdot10^{-5}$	-	-	$1.2\cdot10^{-4}$
k_2	$7.4\cdot10^{-4}$	$3.2\cdot10^{-5}$	$2.4\cdot10^{-5}$	$1.2\cdot10^{-5}$	$3.8\cdot10^{-5}$	$3.6\cdot10^{-5}$
k_3	$6.8\cdot10^{-4}$	$1.8\cdot10^{-2}$	$2\cdot10^{-3}$	$4.4\cdot10^{-4}$	$8.5\cdot10^{-4}$	$4.5\cdot10^{-4}$
k_4	-	$5.5\cdot10^{-5}$	-	-	$4.9\cdot10^{-5}$	-
k_5	-	$6.6\cdot10^{-4}$	-	-	-	-
k_6	$6.1\cdot10^{-4}$	$7.5\cdot10^{-2}$	$1.3\cdot10^{-3}$	$2.3\cdot10^{-4}$	$6.2\cdot10^{-1}$	-
k_7	$1.8\cdot10^{-6}$	$5.7\cdot10^{-1}$	$2.4\cdot10^{-2}$	-	$1.6\cdot10^{-1}$	-
$k_{7,1}$	$2.9\cdot10^{-4}$	$4.9\cdot10^{-3}$	-	-	$1.5\cdot10^{-3}$	$1.7\cdot10^{-4}$
$k_{7,2}$	$3.8\cdot10^{-4}$	$2.3\cdot10^{-4}$	$5.8\cdot10^{-1}$	-	$5.8\cdot10^{-3}$	$4.8\cdot10^{-5}$
k_8	$1.1\cdot10^{-3}$	$1.2\cdot10^{0}$	$6\cdot10^{-5}$	$9.7\cdot10^{-4}$	$5.8\cdot10^{-1}$	-
k_9	$2.5\cdot10^{-4}$	$1.2\cdot10^{-5}$	$2.3\cdot10^{-4}$	$3.1\cdot10^{-4}$	$2.8\cdot10^{-5}$	$3.7\cdot10^{-5}$
k_{10}	-	$1.8\cdot10^{-4}$	-	$4.5\cdot10^{-4}$	$1.7\cdot10^{-5}$	-
$k_{10,1}$	$9.8\cdot10^{-3}$	$1.5\cdot10^{-4}$	$4.5\cdot10^{-3}$	$1.9\cdot10^{-5}$	$1.8\cdot10^{-2}$	$4.7\cdot10^{-4}$
$k_{10,2}$	$3.1\cdot10^{-5}$	$2.1\cdot10^{-2}$	$4.2\cdot10^{-3}$	-	$8.1\cdot10^{-5}$	$5\cdot10^{-3}$
r^2	0.903	0.996	0.88	0.92	0.994	0.97

Table 4.12. Reaction rate constants based on the proposed reaction network (*Cont.*)

	Au/MgAl	Pd/MgAl	Pt/MgAl	Au/MgZr	Pd/MgZr	Pt/MgZr
k_1	$1.2\cdot10^{-4}$	$1.1\cdot10^{-3}$	$2.9\cdot10^{-4}$	$7\cdot10^{-5}$	$1.9\cdot10^{-3}$	$1.1\cdot10^{-3}$
k_2	$3.6\cdot10^{-5}$	$1.6\cdot10^{-5}$	$1.6\cdot10^{-5}$	$2.8\cdot10^{-5}$	$3.2\cdot10^{-5}$	$1.9\cdot10^{-5}$
k_3	$4.5\cdot10^{-4}$	$4.1\cdot10^{-4}$	$3.5\cdot10^{-4}$	$4.3\cdot10^{-4}$	$1.9\cdot10^{-3}$	$5.8\cdot10^{-2}$
k_4	-	$6\cdot10^{-5}$	$1.5\cdot10^{-5}$	-	$6.1\cdot10^{-5}$	$2.4\cdot10^{-5}$
k_5	-	$1.6\cdot10^{-5}$	$6\cdot10^{-4}$	-	-	$1.8\cdot10^{-3}$
k_6	-	$6.2\cdot10^{-2}$	$2.7\cdot10^{-3}$	-	$2.6\cdot10^{-2}$	-
k_7	-	$5.2\cdot10^{-2}$	$1.1\cdot10^{-3}$	-	$2.1\cdot10^{-1}$	$1.4\cdot10^{-3}$
$k_{7,1}$	$1.7\cdot10^{-4}$	$5.7\cdot10^{-3}$	$3.1\cdot10^{-5}$	$1.4\cdot10^{-4}$	$1.3\cdot10^{-2}$	$5\cdot10^{-3}$
$k_{7,2}$	$4.8\cdot10^{-5}$	$6.2\cdot10^{-3}$	$1.7\cdot10^{-6}$	$3\cdot10^{-6}$	$6.8\cdot10^{-3}$	$1.1\cdot10^{-2}$
k_8	-	$3.4\cdot10^{-1}$	-	-	$1.5\cdot10^{-1}$	$3.7\cdot10^{-2}$
k_9	$3.7\cdot10^{-5}$	$1.9\cdot10^{-3}$	$9.1\cdot10^{-4}$	$1.6\cdot10^{-5}$	$1.2\cdot10^{-4}$	$4.7\cdot10^{-2}$
k_{10}	-	$1.2\cdot10^{-2}$	$3\cdot10^{-3}$	-	$8.1\cdot10^{-3}$	$2.6\cdot10^{-1}$
$k_{10,1}$	$4.7\cdot10^{-4}$	$1.3\cdot10^{-5}$	$3.5\cdot10^{-5}$	$3\cdot10^{-4}$	$8.5\cdot10^{-3}$	$3.4\cdot10^{-2}$
$k_{10,2}$	$5\cdot10^{-3}$	$1.1\cdot10^{-3}$	$1.1\cdot10^{-5}$	$3.8\cdot10^{-3}$	$2.6\cdot10^{-5}$	$1.1\cdot10^{0}$
r^2	0.991	0.996	0.993	0.86	0.997	0.998

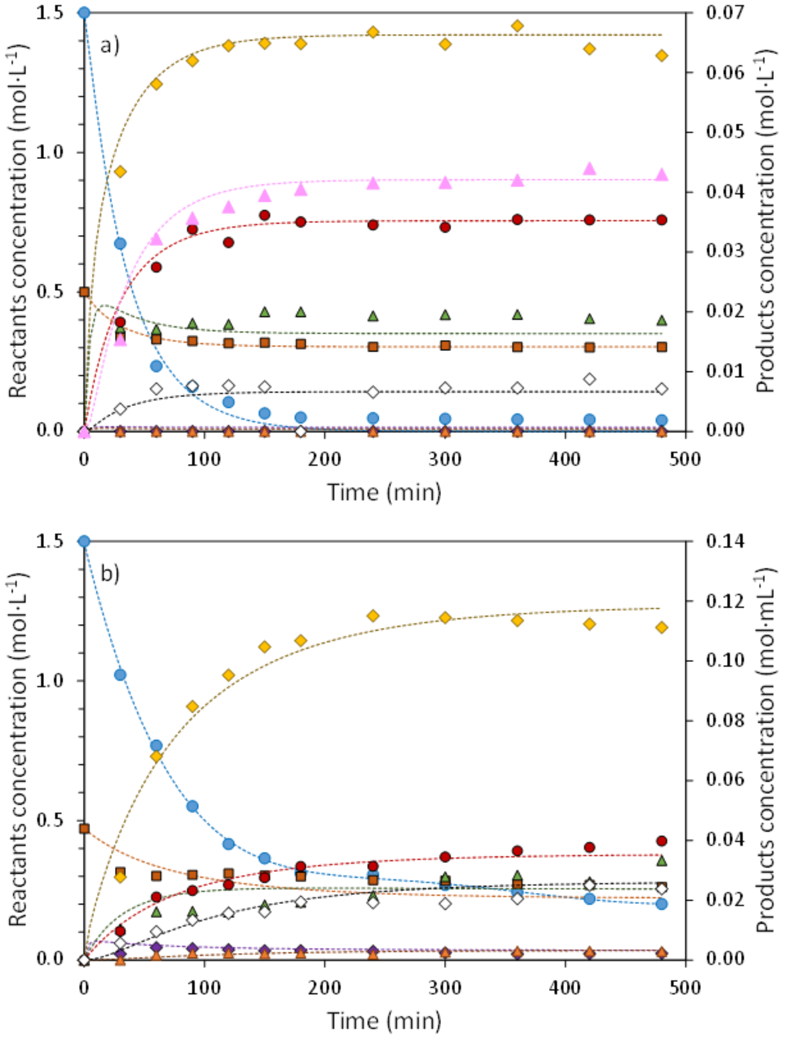

Figure 4.42. Furfural oxidation with H_2O_2 at 50 ºC in presence of (a) Au/TiO_2 and (b) Au/MgAl. Symbols: H_2O_2 (●); FFL (■); FA (◆); HF (▲); FCA (●); MA (◆); FN (▲); HFN (●); BFA (◇); MAL (▲). *Broken lines correspond to the kinetic model predictions*

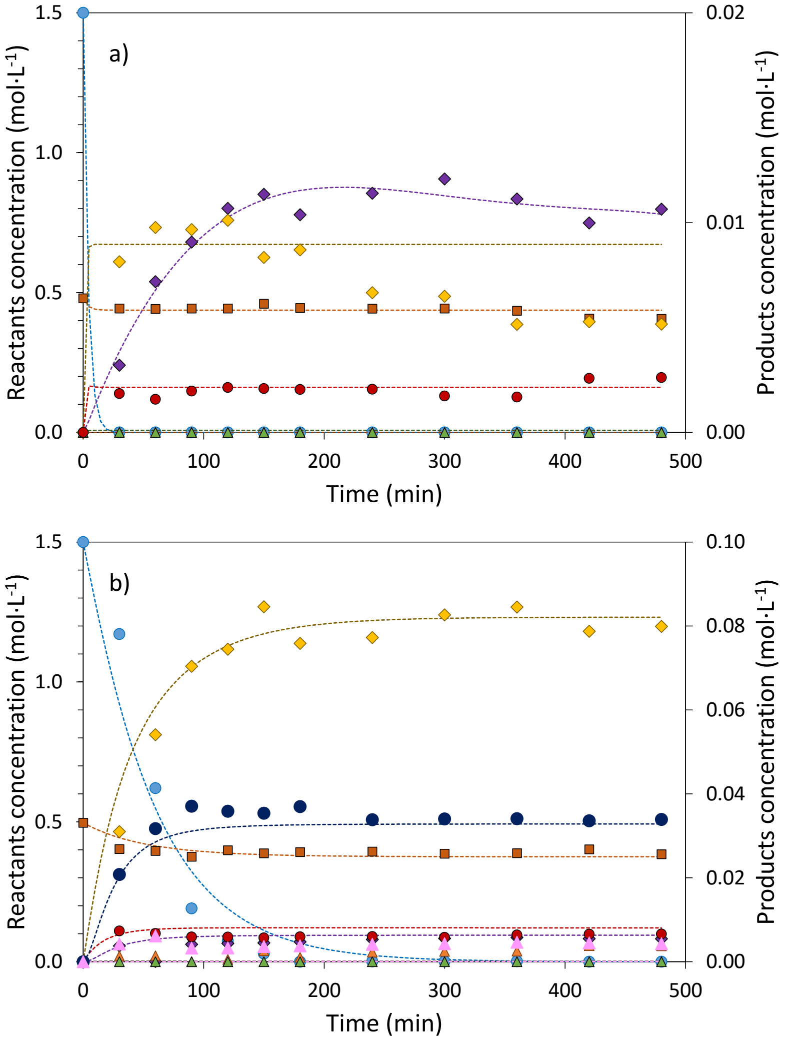

Figure 4.43. Furfural oxidation with H_2O at 50 ºC with a) Pd/TiO_2, b) Pt/TiO_2. Symbols: H_2O_2 (●); FFL (■); FA (◆); HF (▲); FCA (●); MA (◆); FN (▲); HFN (●); BFA (◇); MAL (▲). *Broken lines correspond to the kinetic model adjustment*

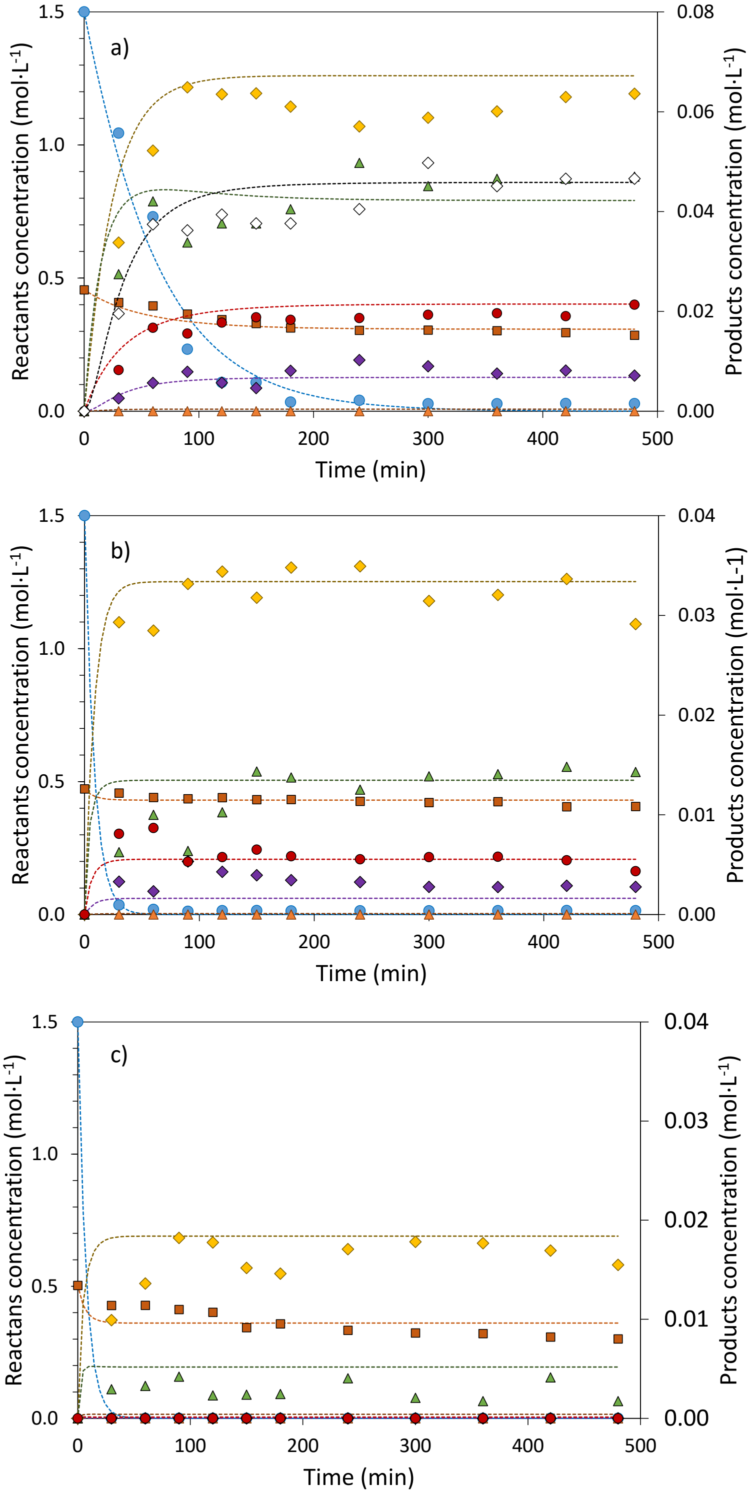

Figure 4.44. Furfural oxidation with H_2O at 50 ºC with a) Au/CeO_2, b) Pd/CeO_2, c) Pt/CeO_2. Symbols: H_2O_2 (●); FFL (■); FA (◆); HF (▲); FCA (●); MA (◆); FN (▲); HFN (●); BFA (◇); MAL (▲).*Broken lines correspond to the kinetic model adjustment*

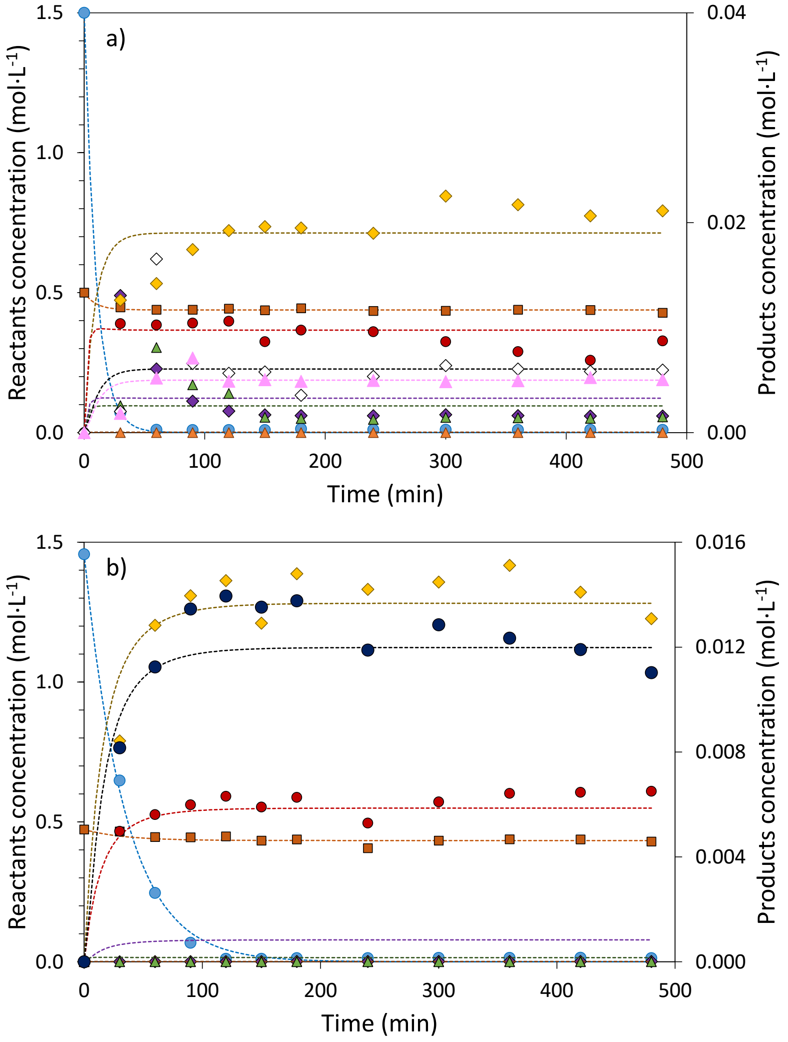

Figure 4.45. Furfural oxidation with H_2O at 50 ºC with a) Pd/MgAl, b) Pt/MgAl. Symbols: H_2O_2 (●); FFL (■); FA (◆); HF (▲); FCA (●); MA (◆); FN (▲); HFN (●); BFA (◇); MAL (▲). *Broken lines correspond to the kinetic model adjustment*

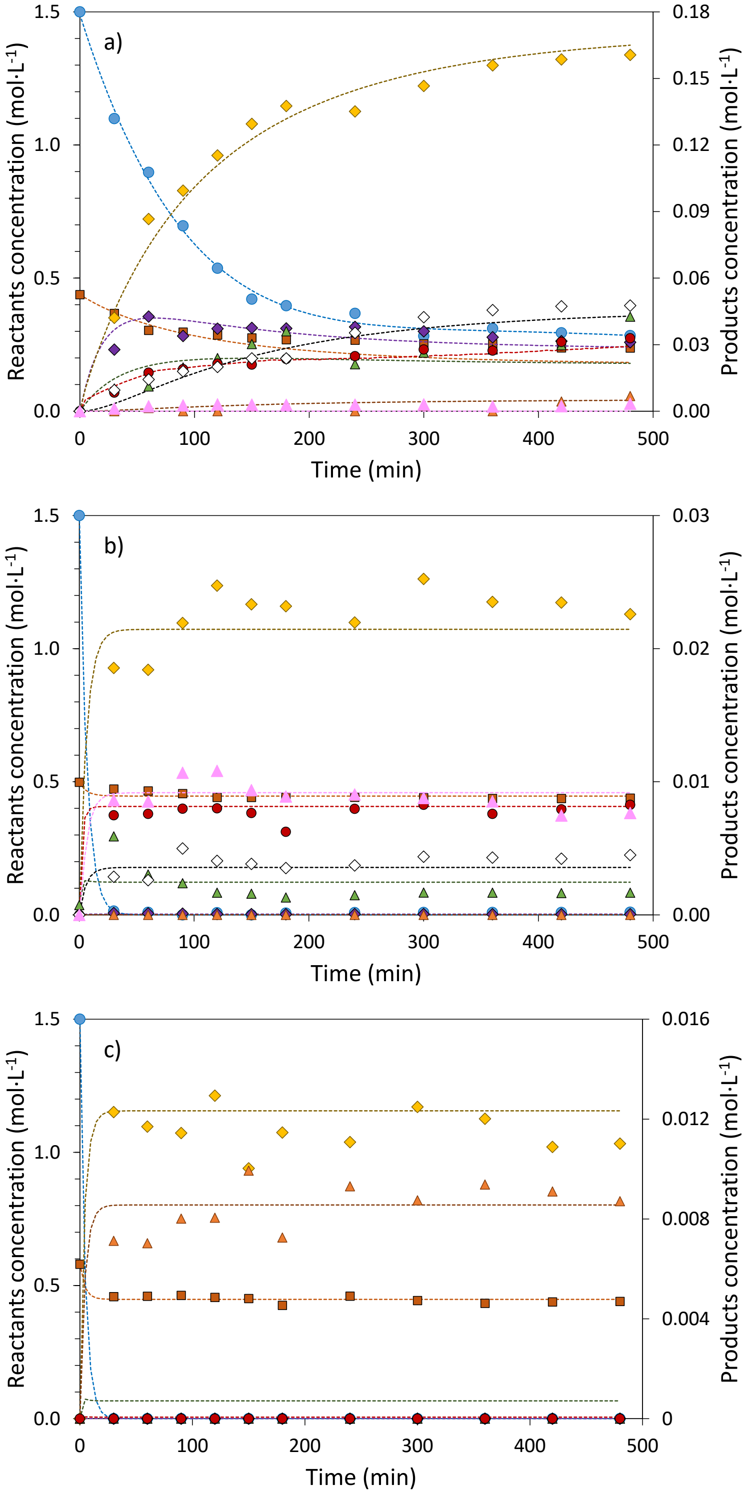

Figure 4.46. Furfural oxidation with H_2O at 50 ºC with a) Au/MgZr, b) Pd/MgZr, c) Pt/MgZr. Symbols: H_2O_2 (●); FFL (■); FA (◆); HF (▲); FCA (●); MA (◆); FN (▲); HFN (●); BFA (◇); MAL (▲).*Broken lines correspond to the kinetic model adjustment*

The main conclusions derived from the kinetic study are analyzed in **Figure 4.47**. Except in the case of using CeO_2, all the metal modified materials show higher k_1 values than the parent supports, in good agreement with the higher hydrogen peroxide conversions obtained. The lack of correspondence between the medium-strength acidity and these values suggests the prevalence of the metal activity in the H_2O_2 decomposition over the support one. The positive role of these metals in promoting hydrogen peroxide decomposition has been previously proposed in the literature [45, 58].

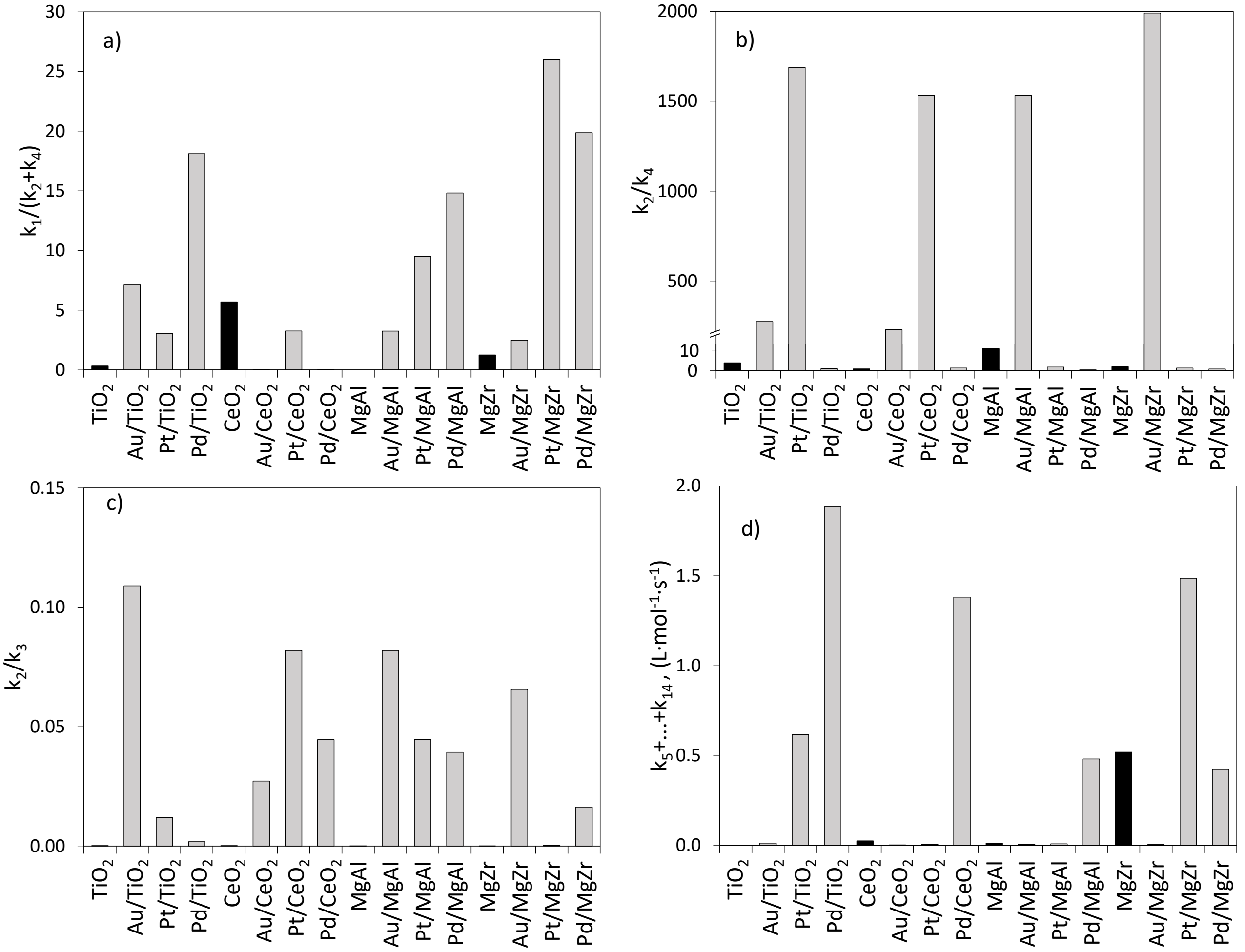

Figure 4.47. Analysis of the kinetic rates as a function of the metal-modified catalyst used

The increment in the H_2O_2 self-decomposition is more notorious than the increase in the rates of the two first steps of the main process, as illustrated in Fig. 4.47a. This effect is more relevant in those catalysts involving Pd and Pt, whereas this undesired effect is less significant when using Au-modified materials. The presence of metal nanoparticles also affects the dominant oxidizing route. A high prevalence for the furoic route is observed with

Pt and Au. In the case of Pt materials, this improvement requires support with redox properties, TiO_2 or CeO_2. On the contrary, the enhancement with Au is observed despite the type of support used, being more significant with mixed oxides (four orders of magnitude) because, with oxides, both steps are promoted, reducing the relative differences.

The effect of using bifunctional catalysts is extended to the undesired oxidations, the different steps that decompose the two primary compounds (FCA and HF), reducing the selectivity and the carbon balance. As observed in Fig. 4.47c, the relative weight of the FCA decomposition decreases, increasing the relative k_2/k_3 value. This effect is more relevant with Au materials, mainly Au/TiO_2 and Au/MgAl. As to the secondary steps, Au is the only metal that does not produce an increment in these rates (Fig. 4.47d). The sum of all these secondary kinetic rates is significantly higher with materials containing Pd and Pt, whereas these rates globally decrease with Au-modified catalysts to obtain values lower than those reached with the bulk materials.

These results suggest the coexistence of two different oxidizing mechanisms, the effect of metal nanoparticles (mainly Au) promoting the oxidation by a redox reaction, i.e., the furoic acid production by a selective interaction between furfural and hydrogen peroxide. On the other hand, those oxidation steps that follow a decomposition mechanism, releasing a formic acid molecule are not promoted by these bifunctional catalysts. This hypothesis suggests that the metal particles (mainly Au ones) enhance the simultaneous chemisorption of both reactants required. Thus, the decomposition of H_2O_2 occurs close to the active site where the furfural is adsorbed. On the contrary, the decomposition reactions are less selective and not as sensitive to this proximity as the furoic acid (FCA).

Au is identified as the best metal to maximize FCA production, and the metal dispersion is the most relevant parameter since this determines the frequency of the correct interactions between the active site and the reactants. This hypothesis is corroborated in **Figure 4.48**, where a clear correspondence between the principal kinetic rates and the metal dispersion is observed. Not only the desired step (k_2) is promoted by a high dispersion, but also the hydrogen peroxide decomposition (k_1), the furoic acid decomposition (k_3), and the undesired 2-hydroxyfuran formation (k_4). These last two steps are less influenced than k_1 and k_2, in agreement with the lower slope of their correlations. Thus, a medium metal dispersion must be considered, trying to reach a selective activation of the target route. Based on this premise, an intermediate dispersion (15-20%) is defined as the optimum one, a range involving Au/TiO_2 and Au/MgAl. A similar analysis with the other metals is not conclusive, no trends for the metal dispersion being observed. This fact reinforces the hypothesis of effective chemisorption required to promote the reaction (sensitive phenomenon).

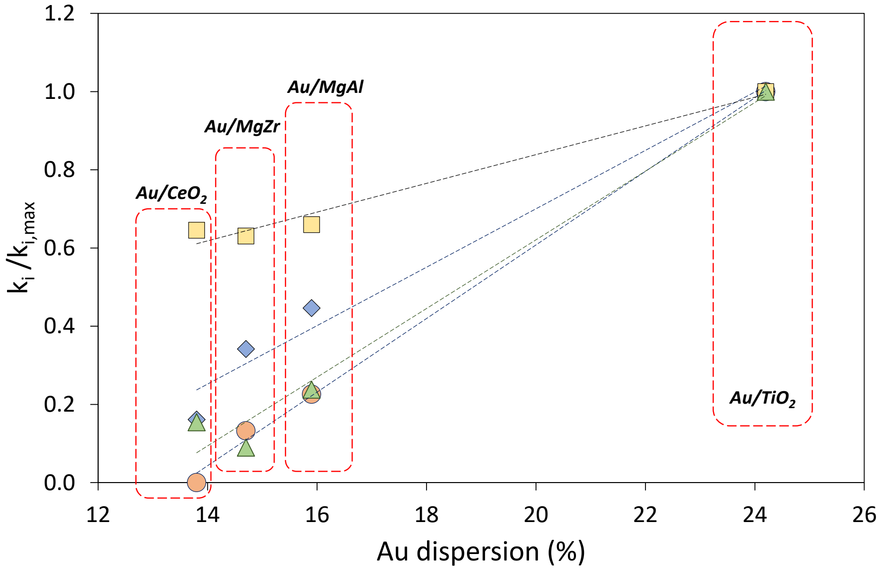

Figure 4.48: Normalized evolution of k_1 (●), k_2 (◆), k_3 (■), and k_4 (▲) kinetic rates as a function of the metal dispersion of Au-modified materials. *Values obtained with Au/TiO_2 are used as reference values*

4.3.6. Deactivation phenomena

Experimental results demonstrate that Au/TiO_2 is the most promising catalysts for the furfural partial oxidation to produce furoic acid, both in terms of activity and selectivity. However, the stability of this catalyst must be also evaluated since this aspect is also crucial to evaluate the technical viability of the oxidation process. This study involves not only reusability tests to evaluate the remaining activity after several cycles, but also a deep characterization of spent catalysts to identify the deactivation reasons, if applicable. By gaining insights into the factors that lead to reduced efficiency or complete catalyst failure, strategies can be developed to mitigate these effects, thereby enhancing the long-term viability and effectiveness of Au/TiO_2.

Reusability tests were performed by loading the reactor with a fresh furfural solution and the catalyst previously recovered by filtration (no regeneration process). **Figure 4.49** summarizes the main results obtained after five cycles of furfural oxidation at 50ºC, using H_2O_2 as the oxidizing agent.

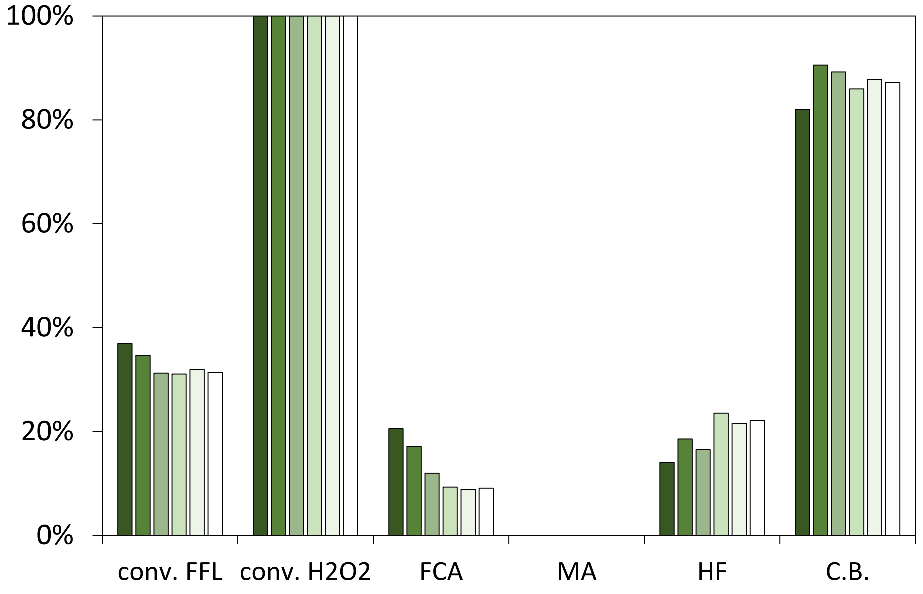

Figure 4.49. Reusability results obtained after six cycles (dark-intermediate-light colors) of 4 h of furfural oxidation at 50 ºC using H_2O_2 as oxidizing agent and Au/TiO_2 as a catalyst. Legend: Product distribution in terms of selectivity

Au/TiO_2 shows a soft but clear deactivation during the first three cycles. Thus, furfural conversion after 4 h decreases from 36.9% (1st cycle) to 31.2% (3rd cycle). This deactivation also affects the products distribution, observing a significant reduction in FCA selectivity (from 20.5% to 12%), obtaining the corresponding increase in HF (from 14.1% to 18.6%). After these three cycles, experimental results suggest a stable behavior, both in conversion and FCA selectivity. The slight increase in carbon balance (from 82.25 in the first cycle to 86.3% after the sixth one) indicates that the relevance of furfural total oxidation is reduced. These results suggest that Au/TiO_2 suffers a stabilization phase with a partial loss of activity, after which the activity and selectivity remains stable.

Previous literature indicates three possible routes of catalyst deactivation when using a biomass-based molecule: structural damage by the water (used as solvent), fouling by coke, and sintering of active metal particles. A deep characterization of recovered materials was performed to identify the relevance of any of these deactivation routes. To guarantee a comprehensive analysis of these results, fresh and spent TiO_2 was also characterized. The comparison between results obtained with both materials will be helpful to identify the role of Au nanoparticles in this deactivation.

Regarding support hydrolysis or collapse, the surface area and pore volume of each material were measured by nitrogen physisorption. Results are summarized in **Table 4.13**.

Table 4.13. Results obtained by nitrogen physisorption analysis of catalysts after the first cycle

Catalyst	BET Surface Area (m^2/g)	Pore volume (cm^3/g)
TiO_2	49.7	0.83
Spent TiO_2	43.0	0.49
1%wt Au-TiO_2	51.5	0.55
Spent 1%wt Au-TiO_2	43.0	0.45

The BET surface area of both TiO_2 and 1% wt Au-TiO_2 remains relatively stable after the reaction, showing a slight decrease from 49.7 m^2/g to 43.0 m^2/g for TiO_2 and from 51.5 m^2/g to 43.0 m^2/g for Au-loaded TiO_2. This modest reduction suggests that the structural integrity of the catalysts is largely preserved during the reaction, with minimal surface area loss. However, more significant changes are observed in the pore volume of the catalysts. The fresh TiO_2 exhibits a pore volume of 0.83 cm^3/g, which decreases by approximately 50% to 0.49 cm^3/g after the reaction. Similarly, the pore volume of the 1% wt Au-TiO_2 catalyst reduces from 0.55 cm^3/g in the fresh catalyst to 0.45 cm^3/g in the spent catalyst. This reduction in pore volume can be attributed to the exposure of TiO_2 to water during the reaction process. Fresh TiO_2, which has not previously encountered water, may form large agglomerates that are detected as pores in the physisorption analysis. Upon exposure to water, these agglomerates likely disintegrate, leading to a reduction in the measured pore volume.

To gain further insights into the morphological changes in the catalysts, X-ray diffraction (XRD) analyses were conducted on both fresh and spent materials. The results, illustrated in **Figure 4.50**, indicate that there are no significant changes in the crystalline structure of Au/TiO_2 and TiO_2 before and after the reaction. Both fresh and spent catalysts display reflections corresponding to the anatase and rutile phases of the TiO_2 support [59, 60], with no new phases or significant peak shifts observed.

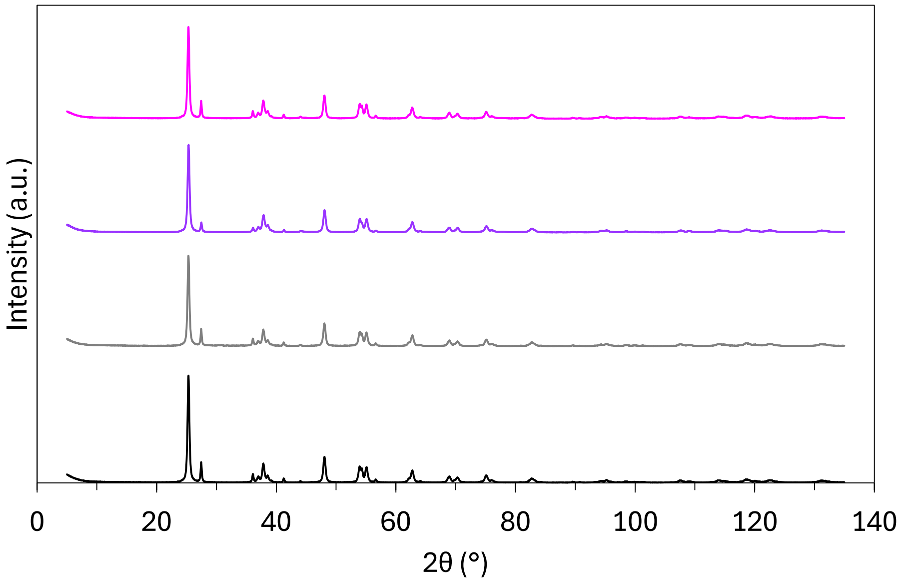

Figure 4.50. XRD diffractograms for fresh and spent TiO_2 and Au/TiO_2. Legend: Black and grey lines represent fresh and spent TiO_2 and purple and pink lines represent fresh and spent Au/TiO_2, respectively

Regarding carbon deposition, the Raman analysis of the TiO_2 catalyst provides insightful information about the surface composition after the reaction. The Raman spectra show no significant shifts or peaks between 1500 and 2500 cm^{-1}, which are typically associated with carbonaceous species, such as graphitic carbon or amorphous carbon deposits [59]. This absence of Raman shifts in this region strongly indicates that no significant organic molecules or carbon deposits are present on the surface of the TiO_2 after the catalytic reaction. The only observable features in the Raman spectra are the characteristic shifts related to the anatase phase of TiO_2, confirming that the TiO_2 support remains largely unaltered in terms of its structural and chemical properties.

These Raman findings are further corroborated by the thermogravimetric analysis coupled with mass spectrometry (TG-MS), which was employed to detect any potential carbon dioxide (CO_2) release upon heating the spent catalyst. The TG-MS results showed no evidence of CO_2 evolution, further supporting the conclusion that carbon deposition did not occur during the reaction. This is a significant observation, as carbon deposition is a common cause of catalyst deactivation in many oxidation reactions, often leading to pore blockage, reduced active site availability, and overall catalyst performance degradation.

The consistency between the Raman and TG-MS analyses provides strong evidence that the TiO_2 catalyst remains free from carbon contamination after the reaction process. This absence of carbon deposition is crucial for maintaining the long-term activity and selectivity of the catalyst, as it suggests that the reaction conditions and catalyst formulation effectively minimize the risk of fouling by carbonaceous species. Consequently, the durability of the TiO_2-supported catalyst in oxidative reactions is enhanced, potentially allowing for extended catalyst lifetimes and more efficient catalytic cycles. **Figure 4.51** visually presents the Raman analysis results, highlighting the stability of the anatase phase and the lack of carbon-related features.

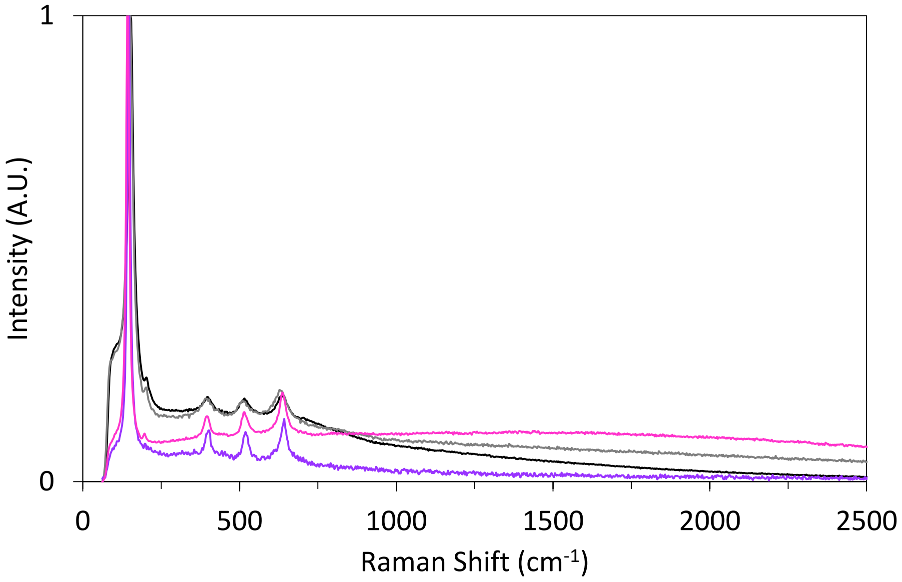

Figure 4.51. Raman spectra of (black) fresh TiO_2, (grey) spent TiO_2, (purple) fresh Au/TiO_2, and (pink) spent Au/TiO_2

The vibrational bands within the 962–400 cm^{-1} range are indicative of the bending modes associated with Ti-O-Ti and Ti-O bonds, which are key to identifying the specific crystalline phases of TiO_2. In the anatase phase, a prominent vibrational band appears at 534 cm^{-1}, serving as a distinct marker for this phase, characterized by symmetric bending of Ti-O-Ti bonds [59, 61]. This band is crucial for recognizing the anatase structure, which is noted for its high photocatalytic activity. In contrast, the rutile phase exhibits strong vibrational bands at 663 cm^{-1}, 750 cm^{-1}, and 422 cm^{-1}. These bands correspond to the unique lattice vibrations of the rutile structure, which is more compact and thermodynamically stable than anatase. The 663 cm^{-1} band is particularly associated with Ti-O bond stretching, while the bands at 750 cm^{-1} and 422 cm^{-1} represent other characteristic modes of the rutile phase [61].

Infrared spectroscopy measurements of CO adsorption were conducted to gain deeper insights into the mechanisms of catalyst deactivation. This technique provides detailed information on the interactions between carbon monoxide and the catalytic material, enabling the identification of changes in the electronic and structural properties of the active sites. Specifically, infrared spectroscopy can reveal alterations in CO adsorption patterns that are indicative of deactivation processes, such as the formation of unwanted surface species or modifications in the geometry of active sites.

The data obtained from these measurements are summarized in **Figure 4.52**, which highlights the key differences observed between the Au-TiO_2 catalyst in its fresh state and after it has been used under reaction conditions. This figure offers a comparative view that facilitates the identification of significant changes in catalyst activity and stability, as well as the potential mechanisms responsible for its deactivation.

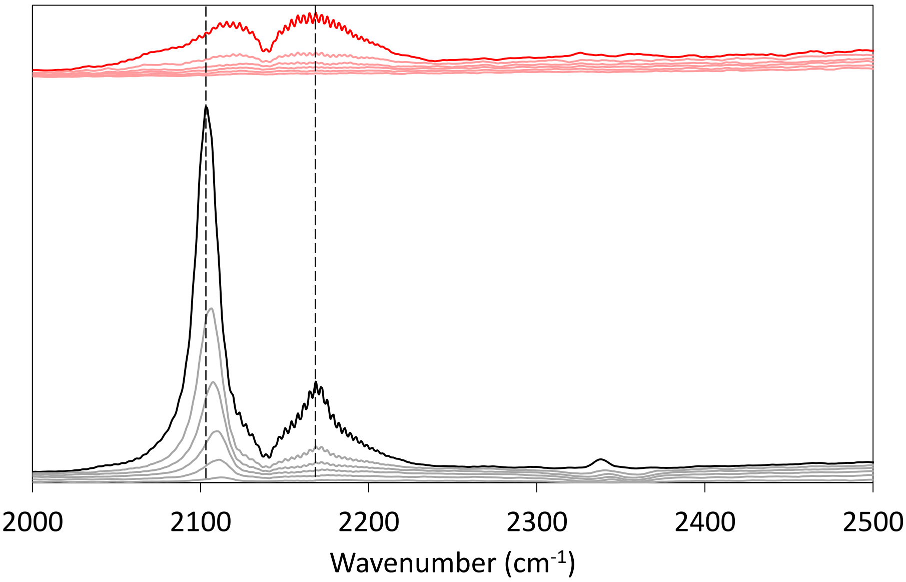

Figure 4.52. Sequence of DRIFT spectra representing the adsorbed CO species of Au/TiO_2. Legend: Spent material (red lines), fresh material (black lines)

A strong adsorption at 2103–2105 cm^{-1} was observed on the fresh sample, which can be attributed to CO adsorbed on metallic Au (CO–Au^0), and the CO-Ti^{4+} adsorption is observed at 2170 cm^{-1} [62, 63]. Comparing analysis before and after the reaction, peaks shift and reduce the intensity. The lower CO coverage on the spent catalyst under present adsorption conditions is attributed to a lower CO adsorption energy in the presence of TiO_2 bulk defects generated during the reaction, which is at least partly responsible also for the lower oxidation activity of these catalysts [64]. Another possible hypothesis is that Au nanoparticles change the electron structure due to interaction with radicals generated from H_2O_2 producing a "fouling" on the particles.

Regarding the phenomenon of sintering, comprehensive ex-situ TEM measurements were conducted to meticulously observe and analyze the particle shape and particle size distribution of the catalyst before and after subjecting it to the oxidation reaction. This approach provides valuable insights into how the physical characteristics of the catalyst particles evolve due to the reaction conditions. Specifically, the ex-situ TEM technique allows for high-resolution imaging, enabling the examination of particle morphology and size with precision. **Figure 4.53** presents a series of representative TEM images that capture the detailed structural changes occurring in the catalyst particles.

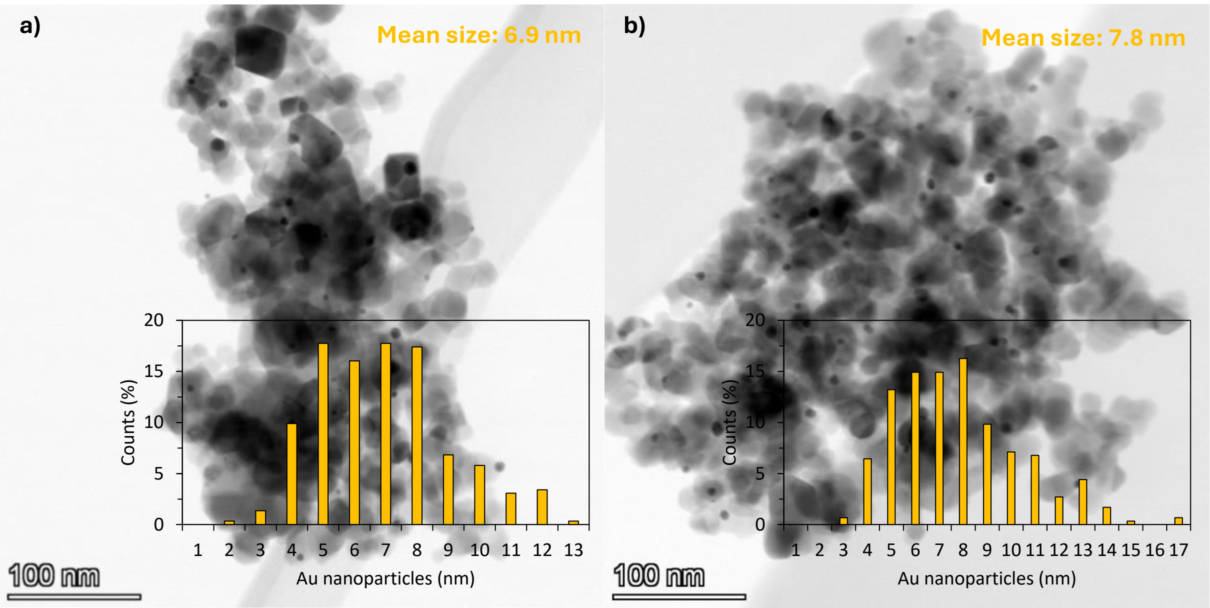

Figure 4.53. Au particle size distributions and representative high-resolution TEM images of the Au/TiO_2 catalyst. Legend: (a) Fresh catalyst, (b) spent catalyst

Alongside these images, the figure also includes the corresponding particle size distribution data, which quantitatively illustrates the shifts in particle size as a result of the oxidation process. This comprehensive analysis helps in understanding the extent of sintering and its impact on the catalytic performance, highlighting any significant changes in particle aggregation or growth that could affect the overall efficiency and stability of the catalyst. After the oxidation reaction, there is a growth in the size of the particles, going from an average size of 6.9 nm to 7.8 nm. These results have been obtained after counting more than 300 particles in each case. Although the change in particle size is relatively small, Au is one of the noble metals most sensitive to particle size distribution and therefore this change can cause deactivation in the catalyst, resulting in a decrease in FCA selectivity. To validate and confirm the findings obtained from earlier analyses, *quasi-in-situ* reactions were conducted within a TEM reactor. This advanced experimental approach allows for real-time observation of catalyst particles under reaction conditions, providing a more accurate representation of their behavior and transformations during the reaction process. **Figure 4.54** provides a series of TEM images captured during these quasi-in-situ experiments. These images showcase the catalyst particles at various stages of the reaction, highlighting key observations such as changes in particle shape, aggregation, and other morphological transformations.

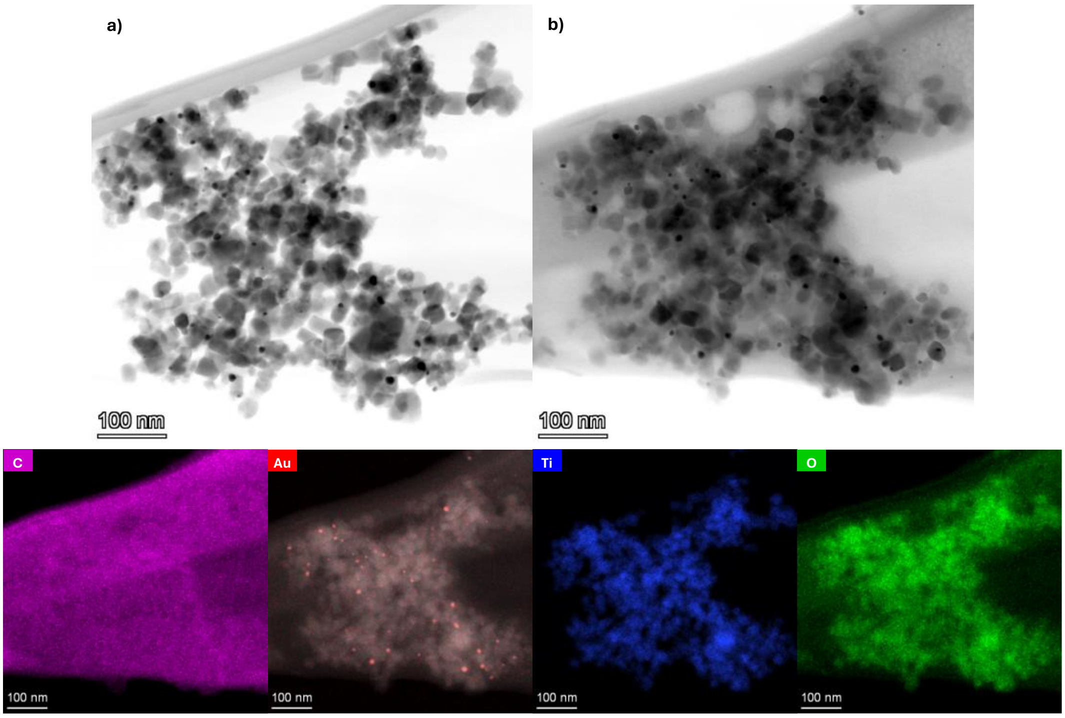

Figure 4.54. Au particle size distributions and representative high-resolution *quasi-in-situ* TEM images of the Au/TiO_2 catalyst and EDS analysis after reaction. Legend: (a) Fresh catalyst, (b) spent catalyst

Before the oxidation reaction, particle size distribution obtained is the same as in *ex-situ* analysis. After the reaction, it is not possible to wash the catalyst, and it is observed how a layer of carbonaceous deposits forms on the fibers of the grid and it is present on the surface of the particles. This is due to the accumulation of reagent remains on the surface. In conclusion, it was observed that particle size distribution before and after the reaction is approximately the same, and deactivation cannot be attributed to this issue. However, it appears that gold nanoparticles may become saturated with radicals originating from H_2O_2, leading to a reduction in CO adsorption experiments. This phenomenon could potentially alter the interaction of furfural, resulting in decreased selectivity towards FCA.

Since the inhibiting factors or deactivation pathways are not fully understood, further characterization through ex-situ and quasi-in-situ TEM analysis, as well as CO adsorption studies using IR spectroscopy, focusing on the interaction between gold nanoparticles and the TiO_2 support, would be interesting. According to literature findings, TiO_2 may cover the gold nanoparticles under certain redox conditions, which could contribute to catalyst deactivation.

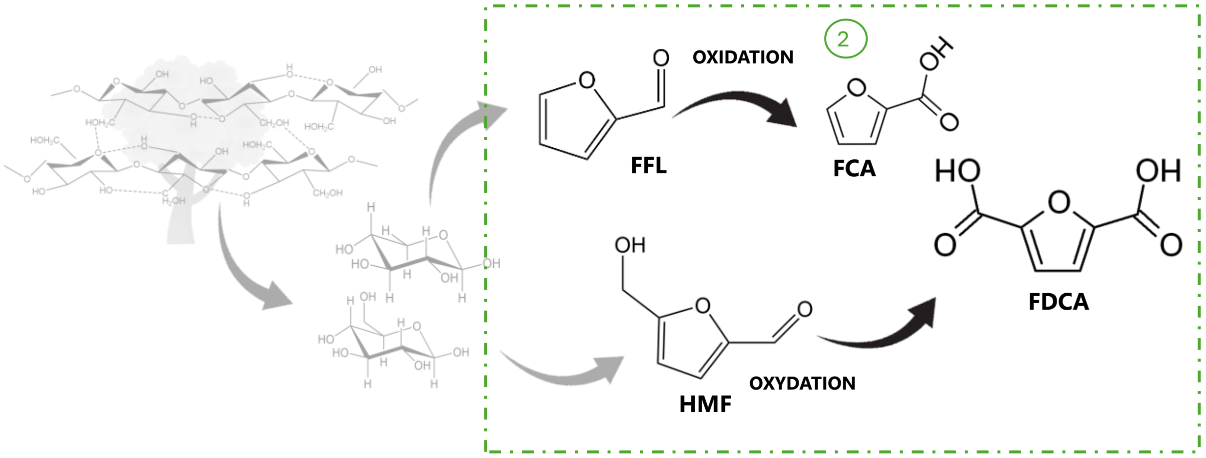

4.4. FUROIC ACID PRODUCTION BY CATALYTIC OXIDATION OF FURFURAL WITH O_2

This research proposes the furfural partial oxidation into furoic acid using bifunctional heterogeneous catalysts and substituting the strong basic conditions by a buffer solution. Au is selected as the active metal, considering two different supports, MgAl and TiO_2. When using MgAl, a positive influence is expected due to the basic properties that stabilize the reactants and intermediates [46, 65]. In contrast, the use of TiO_2 aims to enhance oxygen activation because oxygen can be adsorbed not only on the Au nanoparticles but also on this reducible support, leading to its dissociation at the interface [66]. The analysis focuses on the main reaction parameters to optimize the selectivity and productivity of the FCA, including catalyst, reaction time, pH, O_2 pressure and temperature. The stability is also assessed through multiple consecutive tests. The main novelty of this work is considering a buffer at pH 8 to perform the reaction at softer conditions with respect to the previous literature.

The analysis of the reaction evolution is presented in terms of conversion, yield, carbon balance closure, and selectivity, according to Eq. 4.8,11,12, and 19.

$$S_i\ (\%) = \frac{n_i \cdot C_i}{5 \cdot (C_{FFL,0} - C_{FFL,t})} \cdot 100 \qquad \textbf{[4.19]}$$

where "C_{FFL}" is the furfural concentration, "n_i" and "C_i" are the number of carbons and the molar concentration of each compound. All the reactions were analyzed twice and discrepancies between analyses were lower than 5%. Due to the complexity of most figures presented, error bars are not included to facilitate the legibility of the plots.

4.4.1. Catalyst screening

A blank reaction in the absence of any catalyst was performed at 80 ºC with 20 bar of O_2, using $KHCO_3$ to establish a constant pH (8), to evaluate the relevance of a possible autocatalytic mechanism. No products were detected after 8 h, observing a furfural conversion of 9.4 %, a value that directly corresponds to the carbon unbalance (91.5 %), suggesting a high relevance of furfural oligomerization. In good agreement with this hypothesis, the initial yellow solution is significantly darker after 8h, as well as the aspect of the solid catalyst. This undesired effect has been previously observed in the literature[67, 68].

The same results were obtained when using different supports (TiO_2, CeO_2 and MgAl), with total correspondence between conversions of 10.5, 10.2, and 9.8%, and carbon balance closure of 89.5, 89.7, and 90.1%, for TiO_2, CeO_2, and MgAl, respectively. To sum up, these catalysts are not active for the furfural oxidation at these conditions whereas they promote furfural oligomerization. These results are in good agreement with the previous literature [46, 69, 70], highlighting the high furfural oligomerization trend and the need for a noble metal catalyst to activate the oxygen dissociation required for the oxidation steps. Despite the initial assumption of TiO_2 as an active support to activate the oxygen, these results demonstrate that this activity is only relevant in the metal-TiO_2 interface [66]. Once the need for metal nanoparticles is corroborated, a set of experiments using bifunctional catalysts with different noble metals supported on TiO_2 was performed. The main results after 2 h are summarized in **Figure 4.55**.

FCA or any other products of furfural oxidation are not detected when using Ru or Rh, despite observing furfural conversion with both catalysts. Based on these results, Ru and Rh are discarded for further studies, concluding that they are not active for the target oxidation. The furfural conversions obtained with these materials are mainly caused by adsorption and decomposition into humins, in the same way as when using parent supports.

On the other hand, Pd, Pt, and Au produce furoic acid, FCA selectivity being the highest when using Au (9.6% vs. 5.8 and 4.6% of Pt and Pd after 2 h, respectively). In all the cases, furoic acid is the only compound detected in the liquid phase. If the selectivity was expressed in terms of the relative distribution of detected products, Pd, Pt, and Au will produce 100% furoic acid. Similar selectivities are only reported when using a very complex catalyst (Au(-PVP)/Nb_2O_5-AC) and NaOH to guarantee a basic medium [56], or in a few works under free-base conditions [69, 71]. These results in free-base conditions are limited by a very relevant deactivation, a drawback prevented by this approach, as discussed below.

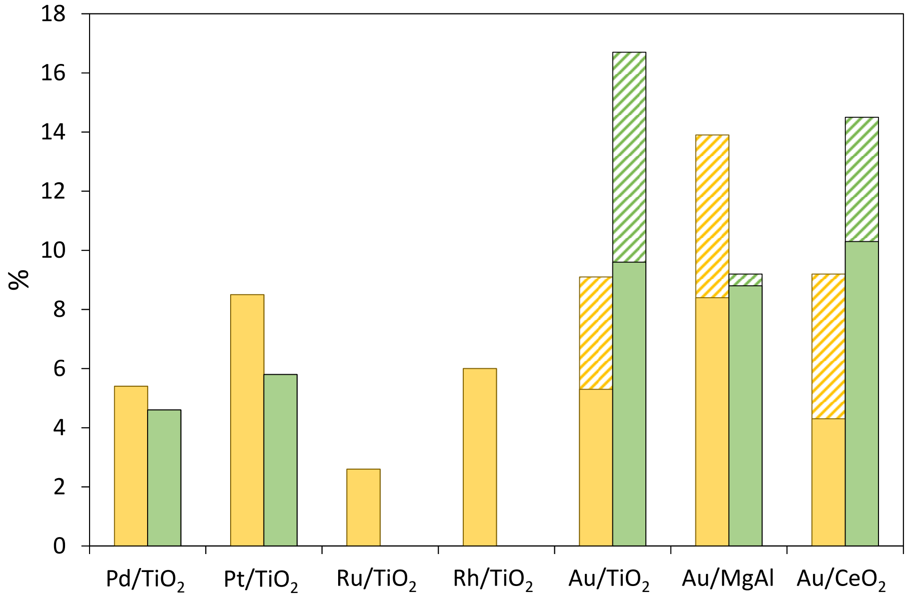

Figure 4.55. Furfural conversion (yellow) and FCA selectivity (green) obtained in the furfural oxidation at 80 ºC with 20 bar of O_2 as a function of the catalyst. Results after 2 h except those shown with diagonal bars that corresponds to 8 h reaction time

Although the analysis in terms of total selectivity (based on the furfural conversion and not only on the distribution of the liquid-phase products) could mask the goodness of these results in comparison to other published studies, but this parameter also allows identifying the relative weight of humins production. To our best knowledge, the only reference with high FCA selectivity that includes the carbon balance indicates values even lower than 10% [72], suggesting a humins production higher than in this approach.

Despite the highest conversion after 2h is obtained with Pt/TiO_2 (8.5%), the FCA selectivity is almost 40% lower than the one obtained with Au/TiO_2. Thus, Au/TiO_2 shows the best compromise between activity and FCA selectivity, reaching almost double selectivity than the one obtained with Pd/TiO_2, despite the same conversion. This result suggests that this catalyst minimizes humins production.

According to this screening, Au is selected as the most promising metal. Its activity is also analyzed using other supports, such as MgAl or CeO_2. The highest conversion after 2 h reaction time is obtained for Au/MgAl (8.4%). However, this catalyst presents low FCA selectivity (8.8%), with almost 93% of the converted furfural being transformed into degradation products (humins). Similar FCA selectivities are reached with Au/TiO_2 and Au/CeO_2 (9.6 and 10.3%, respectively), observing slightly higher conversion in the case of Au/TiO_2 (5.3% vs. 4.3%). Since no conclusive results were obtained by this screening, the activity of these materials was compared at longer reaction times (8 h).

The relative increase in the furfural conversion after 8h reaction time is quite similar in all the cases, obtaining almost double values (9.1, 13.9, and 9.2 %, for Au/TiO_2, Au/MgAl, and Au/CeO_2, respectively). As to the FCA production, Au/TiO_2 is highlighted as the most selective one (16.7%), followed by Au/CeO_2 (14.5%) and, finally, Au/MgAl (9.2%). With the two first catalysts, the carbon balance closure remains over 92%, whereas a lower value (88.6%) is reached with Au/MgAl, suggesting a higher relevance of humins formation since no other product was detected in the liquid phase.

According to the literature, the metal dispersion and, subsequently, the metal nanoparticle size are the key parameters to activate the oxygen [73]. Considering the characterization results summarized in **Table 4.14**, the best Au dispersion corresponds with Au/TiO_2, a result that could justify the highest FCA selectivity reached with this material (16.7 %, 100% if considering only the products in the liquid phase). However, there is not a good correlation between these two parameters, with significant discrepancies in terms of FCA selectivity despite the similar metal dispersion of Au/MgAl and Au/CeO_2. These results suggest that the catalyst performance cannot be explained in terms of structure sensitiveness, with surface reactivity playing a key role in the selectivity evolution. Thus, the high surface acidity of MgAl is suggested as the responsible for its high humins production. The relevant role of these active sites in humins formation has been demonstrated in the literature [34, 74, 75].

To maximize the FCA production and to evaluate the relative relevance of the different active sites, the influence of reaction conditions (O_2 pressure and temperature) has been studied, considering two catalyst with opposite properties: Au/TiO_2 (the highest metal dispersion and the lowest concentration of acidic and basic sites) because of its high FCA production, and Au/MgAl (the material with the highest concentration of acidic and basic sites) because of its high furfural conversion. If active sites related to the support are not of key relevance, working at higher pressures and temperatures could improve the results by a faster O_2 activation. On the other hand, the evaluation of these results when using Au/MgAl could be relevant to evaluate the different kinetics and mechanisms of humins formation and furfural oxidation.

Table 4.14. Summary of the main characterization properties of the different catalysts

	Surface Area ($m^2 \cdot g^{-1}$)	**Pore Volume** ($cm^3 \cdot g^{-1}$)	**Metal dispersion** (%)	**Acidity** ($\mu molNH_3 \cdot g^{-1}$)	**Basicity** ($\mu molCO_2 \cdot g^{-1}$)
Pd/TiO_2	66	0.4	13.1	104.3	68.6
Pt/TiO_2	54	0.4	11.0	153.9	66.3
Ru/TiO_2	48	0.4	21.0	186.2	19.3
Rh/TiO_2	55	0.3	42.7	175.1	26.3
Au/TiO_2	62	0.7	24.2	130.0	25.2
Au/MgAl	196	0.4	15.9	338.3	315.8
Au/CeO_2	115	0.2	13.8	195.9	50.5

4.4.2. Influence of the oxygen partial pressure

The influence of O_2 pressure was studied from 5 to 25 bar of O_2, keeping constant the temperature at 80 ºC. A different effect is observed when working with Au/TiO_2 or Au/MgAl, as shown in **Figure 4.56.**

Reaction conditions are chosen to guarantee that experimental results are not limited by oxygen availability. In reactions at 10, 15, 20, and 25 bar, the oxygen (from 0.34 to 0.85 M) is higher than the stoichiometric one (furfural requires 0.5 M of oxygen to be transformed into FCA). The fast stirring ensures a good mixture between the liquid and the gas phases, leading to the effective oxygen saturation of the liquid phase (concentrations in the liquid phase of 0.005, 0.008, 0.104, and 0.013 M, at 10, 15, 20, and 25 bar, respectively). As to the experiment at 5 bar, the O_2 concentration (0.17 M) is slightly lower than the stoichiometric one, but the conversion obtained is significantly lower than the maximum that could be obtained at these conditions. Thus, all the results can be explained based on the activity of the catalyst.

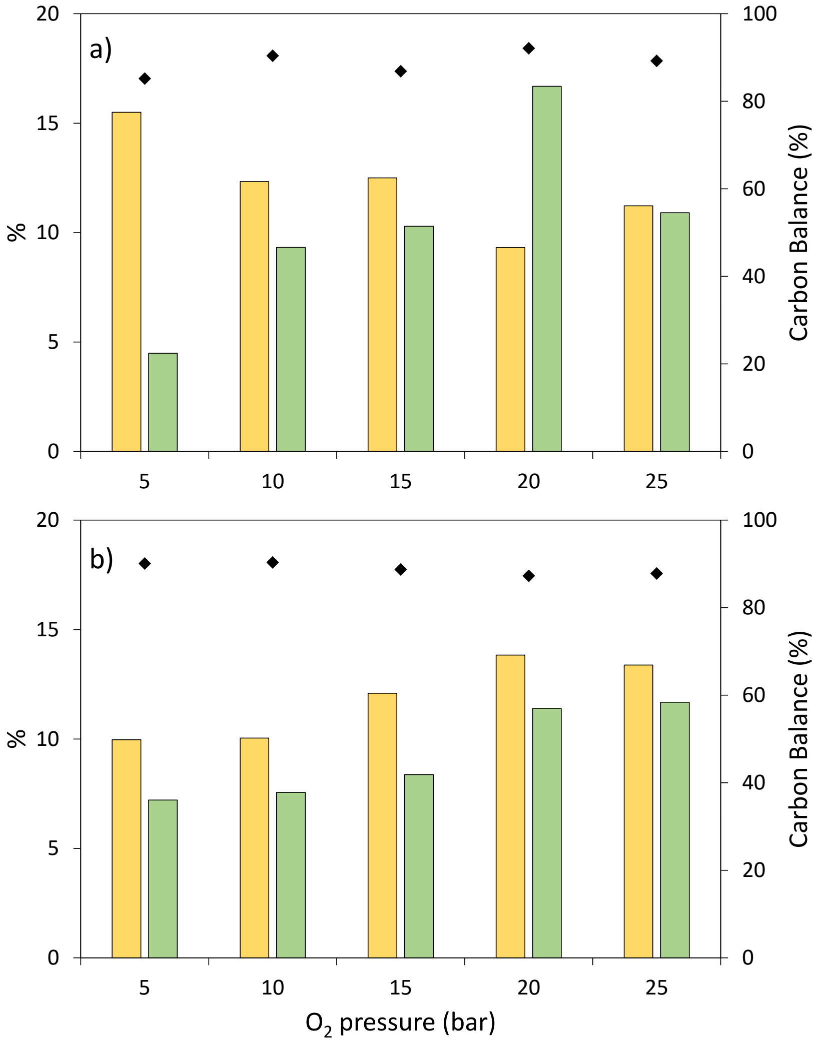

Figure 4.56. Furfural conversion (yellow), FCA selectivity (green) and carbon balance closure (◆, right axis) obtained after 8 h of furfural oxidation at 80 ºC as a function of the O_2 pressures using (a) Au/TiO_2 and, (b) Au/MgAl as catalyst

In both cases, very different behaviours are observed below and above 20 bar, although with different trends depending on the catalyst. When using Au/TiO_2, the highest conversion (15.5%) is obtained at the lowest pressure (5 bar), observing a clear decreasing trend with the pressure, reaching a minimum at 20 bar (9.3%). At 25 bar, a slight increase in conversion is observed (11.3%). As to the target product, its selectivity strongly increases from 5 to 20 bar (from 4.5 to 16.7%), with a relevant decrease (10.9%) at 25 bar. These results suggest a positive effect of the O_2 pressure on the control of the main reaction explained suggesting that the surface oxygen concentration can be limiting for this step. Thus, most of the furfural converted at low pressure is transformed into humins since the low surface oxygen concentration promotes those routes that do not require oxygen (mainly oligomerization to humins). Once the availability of the oxygen increases, humins production is hindered, increasing the selectivity for partial oxidation. The decrease in FCA selectivity observed at 25 bar is explained because the excess of O_2 and the subsequent promotion of secondary reactions degrade the FCA released in the reaction. The final product of these reactions is CO_2 (not analysed) but its intermediates in the oxidation process, maleic and formic acid, are, mainly at intermediate times (1.5% after 3.5 h). In good agreement, the maximum FCA selectivity is obtained after 3 h (11.4%), its degradation being more favourable than its production for longer times.

As for Au/MgAl, from 5 to 20 bar, there is a clear correspondence between the O_2 pressure, the furfural conversion (from 10 to 13.8%, values that correspond to activities from 12.5 to 17.3 mmol/g·h) and the FCA concentration (from 7.2 to 11.4%), suggesting that the surface concentration of oxygen is somewhat limiting the catalyst performance (opposite behavior than Au/TiO_2). At 25 bar, the FCA selectivity slightly increases (from 11.4 to 11.8%) but the furfural conversion decreases (from 13.8 to 13.4%), suggesting that the presence of oxygen is changing the properties of the metal sites or that there is a competitive adsorption between furfural and oxygen. With this catalyst, maleic and formic acid are not detected and the carbon balance obtained is only due to the presence of humins production, a process insensitive to pressure.

4.4.3. Influence of the temperature

To study the influence of temperature, furfural oxidation was studied in the range 80-150 ºC keeping 20 and 25 bar of O_2 pressure and using the $KHCO_3$ buffer to guarantee a constant pH of 8. The main results obtained with both catalysts are shown in **Figure 4.57**, comparing the furfural conversion, carbon balance closure, and product distribution in selectivity terms.

Furfural conversion strongly increases when increasing the temperature, at both pressures and catalysts tested. These increments are more relevant when working at 20 bar, reaching maximum values of 85 and 69.5%, for Au/TiO_2 and Au/MgAl, respectively. The corresponding maximum values at 25 bar are 45.4 and 41%, respectively.

These rising trends match with a decrease in the carbon balance, which is in both cases more relevant when working at 25 bar. Considering the low carbon balance at 120 ºC (62.6 and 41% for Au/TiO_2 and Au/MgAl, respectively), this pressure was not tested at 150 ºC. At the same temperature, when working at 20 bar, the carbon balance obtained were 83 and 74%, respectively. The carbon unbalance increase suggests that, at these conditions, a relevant fraction of the furfural converted is not transformed into the target compound (FCA). On the contrary, it undergoes oligomerization, producing insoluble humins not detected in the liquid phase.

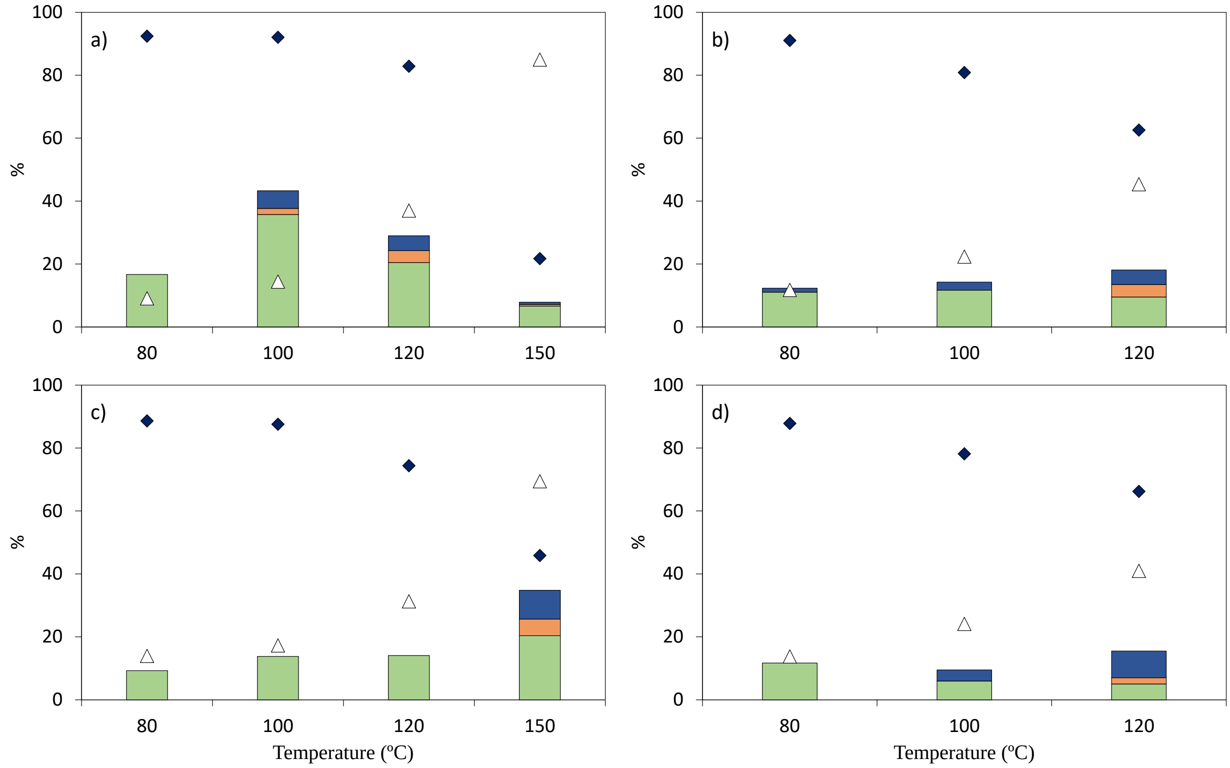

Figure 4.57. Furfural conversion (△), carbon balance (◆) and selectivity distribution (bars) obtained in the furfural oxidation at different temperatures (80-150 ºC) for Au/TiO_2 at (a) 20 and (b) 25 bar, and Au/MgAl at (c) 20 and (d) 25 bar. Legend: FCA (green), MA (orange), FA (blue)

The presence of these humins determines the selectivity distribution since, according to the selectivity equation (Eq. (4.19)), these undesired compounds are also considered for the calculus (parameter based on the total furfural disappearance). However, this is not the only aspect to explain the carbon balance depletion. The presence of FCA oxidation compounds, such as maleic and formic acid, involves the release of CO_2, a compound involved in the carbon balance that cannot be detected with our experimental system. Moreover, the temporal profiles of these compounds (discussed in the kinetic section) suggest that the severity of the reaction is high enough to lose control of the main reaction, producing the total oxidation of these organics into CO_2.

Looking at the effect of temperature and pressure on catalyst performance, the optimum conditions must be established by analysing the FCA selectivity and yield. In general, Au/TiO_2 presents higher oxidation activity than Au/MgAl, not only because of the higher conversion but also since maleic and formic acids are detected in relevant amounts in all the cases, except when working at 80 ºC and 20 bar. Thus, mild conditions are the optimum to maximize FCA production. In good agreement, the maximum selectivity is reached at 100 ºC and 20 bar (35.8%), observing a decrease in selectivity when increasing the temperature. This effect is not so well observed when working at 25 bar because the increase in conversion masks the global result. As to the production, the maximum FCA yield is obtained at 120 ºC and 20 bar (7.6%). In this case, the selectivity decrease is compensated with a conversion increase. Similar selectivities are obtained at 100 ºC and 150 ºC, with yields of 5.3%. As to the results obtained at 25 bar, the selectivity is always significantly lower, as well as the yield, reaching the maximum value at 120 ºC (4.3%).

The lower oxidation activity of Au/MgAl produces lower FCA selectivities (maximum value of 20.4 at 150 ºC and 20 bar of O_2 pressure) but this compound is the only one detected in the liquid phase (i.e. the selectivity in the liquid phase is 100% for FCA) except when working at 150 ºC or 25 bar. In yield terms, 120 ºC and 20 bar are the optimum conditions for this catalyst, reaching 4.4% of FCA yield. However, this value is more than 40% lower than the optimum with Au/TiO_2 (same conditions).

As conclusion of this reaction conditions screening, the oxygen activation (promoted by Au/TiO_2) is identified as the key aspect to perform the furfural oxidation whereas no relevant problems related to the stability of the adsorption of reaction intermediates (aspect in which the acidic/basic properties of Au/MgAl could be crucial) is not so important.

4.4.4. Kinetics studies

To elucidate the reaction mechanism, identify all the possible routes for the furfural transformation, and discern if the same mechanism explains the results obtained by the two catalysts, **Figure 4.58** illustrates the evolution of the selectivities with conversion for the most representative experiments (those in which a larger number of compounds are involved). At milder conditions, FCA is obtained with almost 100% selectivity in the liquid phase.

FCA, the target product, is an oxidation primary product, being the main reaction product at low conversions, and following a marked decreasing trend as the conversion increases. This conclusion is the same despite the catalyst and the reaction conditions. At low conversions, the FCA decrease coincides with the appearance of formic and maleic acid (FA and MA, respectively).

In the same way, the FCA profile reaches a flat evolution, more noticeable in the case of the reaction catalyzed with Au/TiO_2 at 120 ºC and 20 bar. According to these results, the furfural oxidation into FCA and the subsequent degradation into MA and FA is identified as the main route, being common for both catalysts tested.

Results obtained with Au/TiO_2 at 25 bar and 120 ºC demonstrate the presence of a parallel route, producing 2-hydroxy-2(5H)-furanone (henceforth, HFN) as a primary product. The well-marked selectivity decrease observed for HFN indicates that its degradation is a fast process. This second route is identified as relevant only for the most severe pressure and temperature conditions tested using Au/TiO_2, i.e., at 120 and 150 ºC and 20 bar, and at 100 and 120 ºC with 25 bar of O_2. The detailed profiles are included in **Figure 4.59-64**. On the contrary, this compound is not observed in any case when working with Au/MgAl.

It should be noted that FA selectivities are always higher than the MA ones, suggesting that FA is produced from more than one route. This fact is more evident in the case of using Au/MgAl. In this case, MA is only detected when the furfural conversion is higher than 65%, whereas FA is relevant from 20%. This observation suggests a third parallel route in which furfural is directly oxidized into formic acid, obtaining a very unstable intermediate that is only observed at trace levels at low conversions (2-hydroxyfuran, HF).

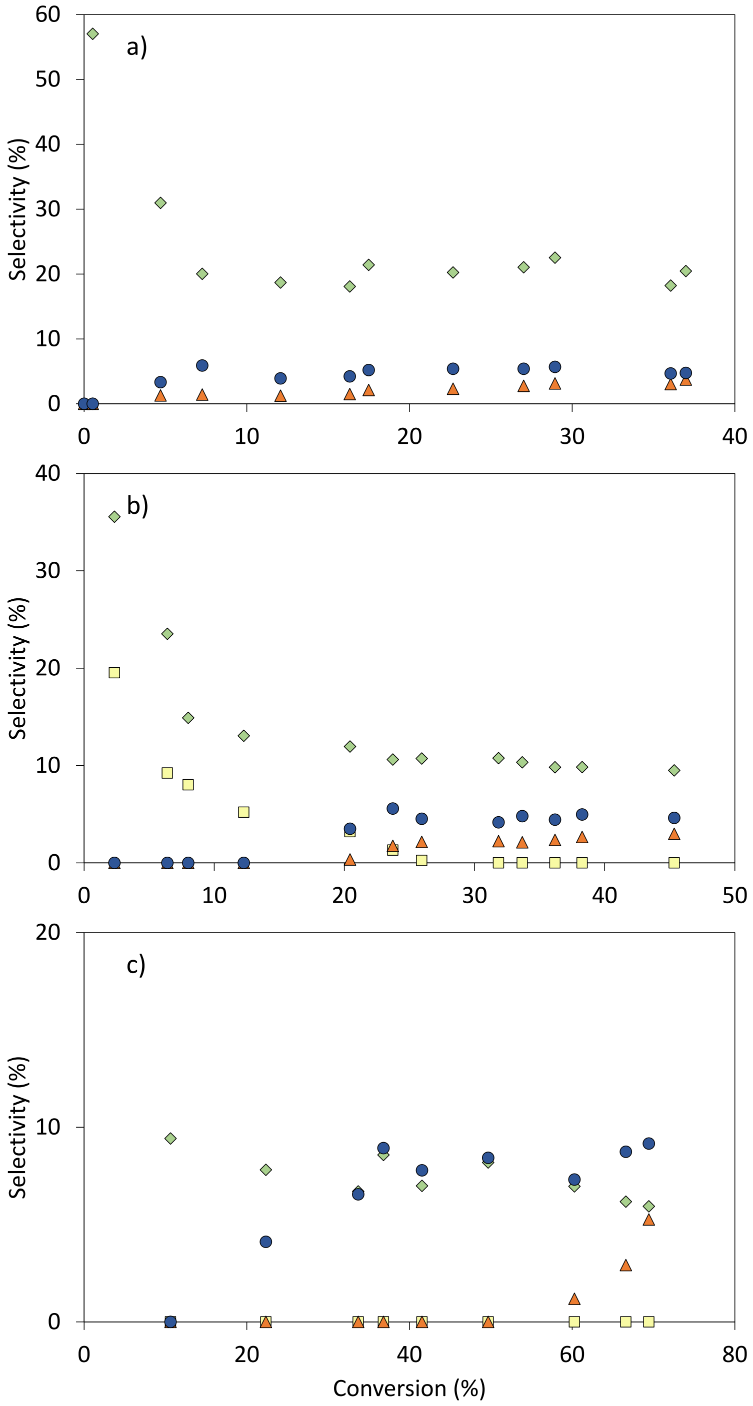

Figure 4.58. Selectivity evolution as a function of conversion. Data corresponding to: (a) Au/TiO_2 at 120 °C and 20 bar, (b) Au/TiO_2 at 120 °C and 25 bar, and (c) Au/MgAl at 150 °C and 20 bar. Symbols: FCA (◆), HFN (□), FA (●), MA (▲)

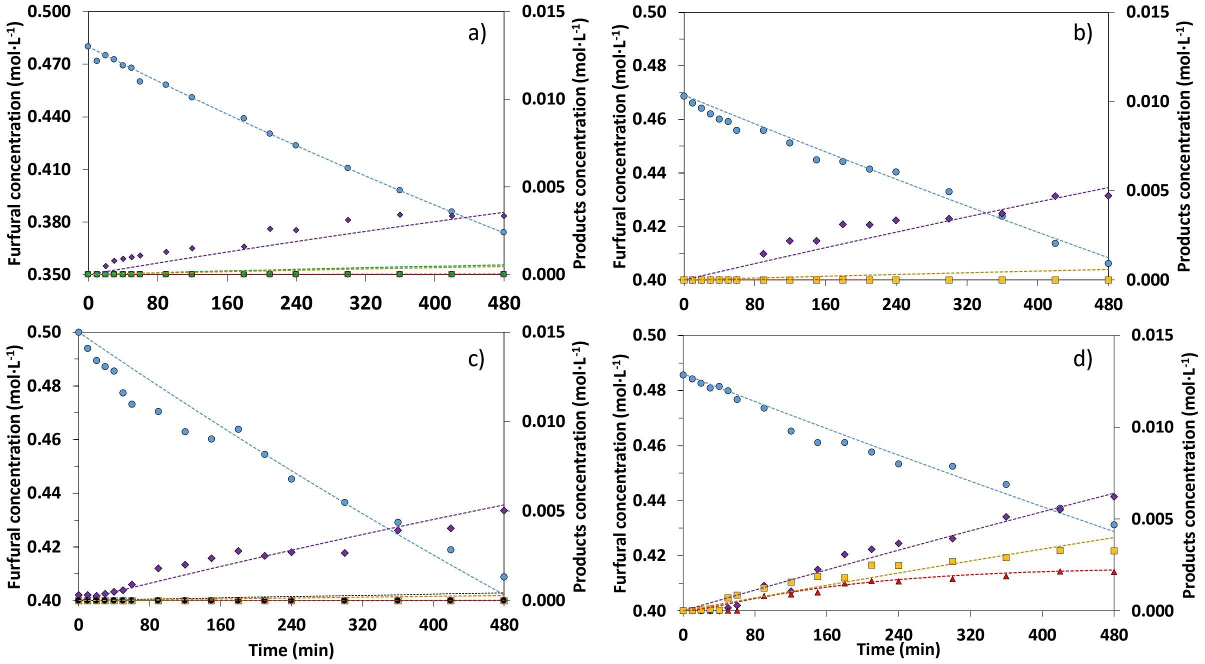

Figure 4.59. Furfural oxidation at 80 ºC in presence of Au/TiO$_2$ modifying pressure: (a) 5 bar, (b) 10 bar, (c) 15 bar, (d) 25 bar. Symbols: FFL (●); FCA (◆); FA (■); MA (▲). *Broken lines correspond to the kinetic model predictions*

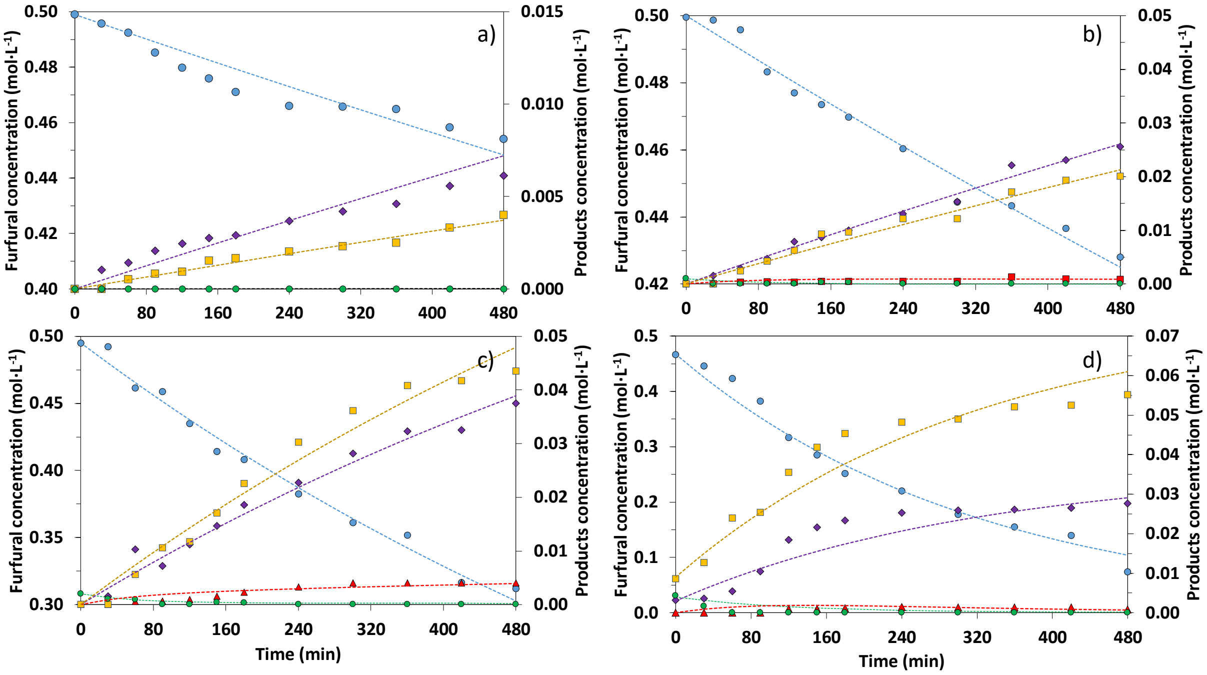

Figure 4.60. Furfural oxidation at 20 bar in presence of Au/TiO$_2$ modifying temperature: (a) 80 ºC, (b) 100 ºC, (c) 120 ºC, (d) 150 ºC. Symbols: FFL (●); FCA (◆); FA (■); MA (▲); HFN (●). *Broken lines correspond to the kinetic model predictions*

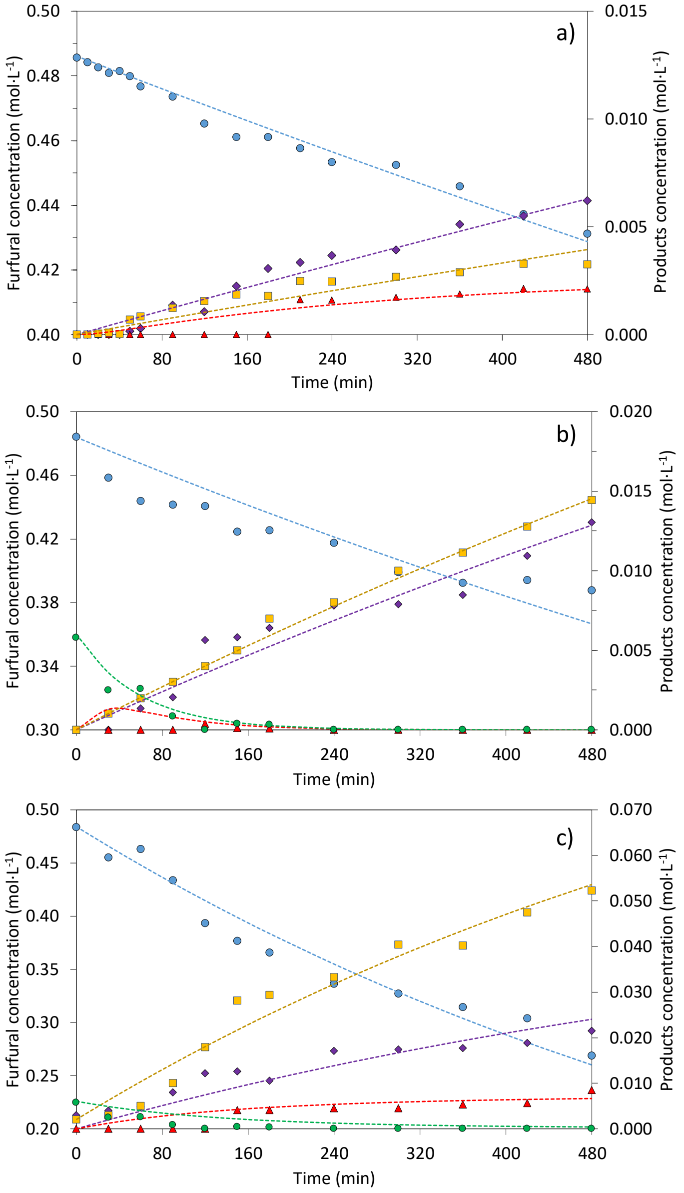

Figure 4.61. Furfural oxidation at 25 bar in presence of Au/TiO$_2$ modifying temperature: (a) 80 ºC, (b) 100 ºC, (c) 120 ºC. Symbols: FFL (●); FCA (◆); FA (■); MA (▲); HFN (●). *Broken lines correspond to the kinetic model predictions*

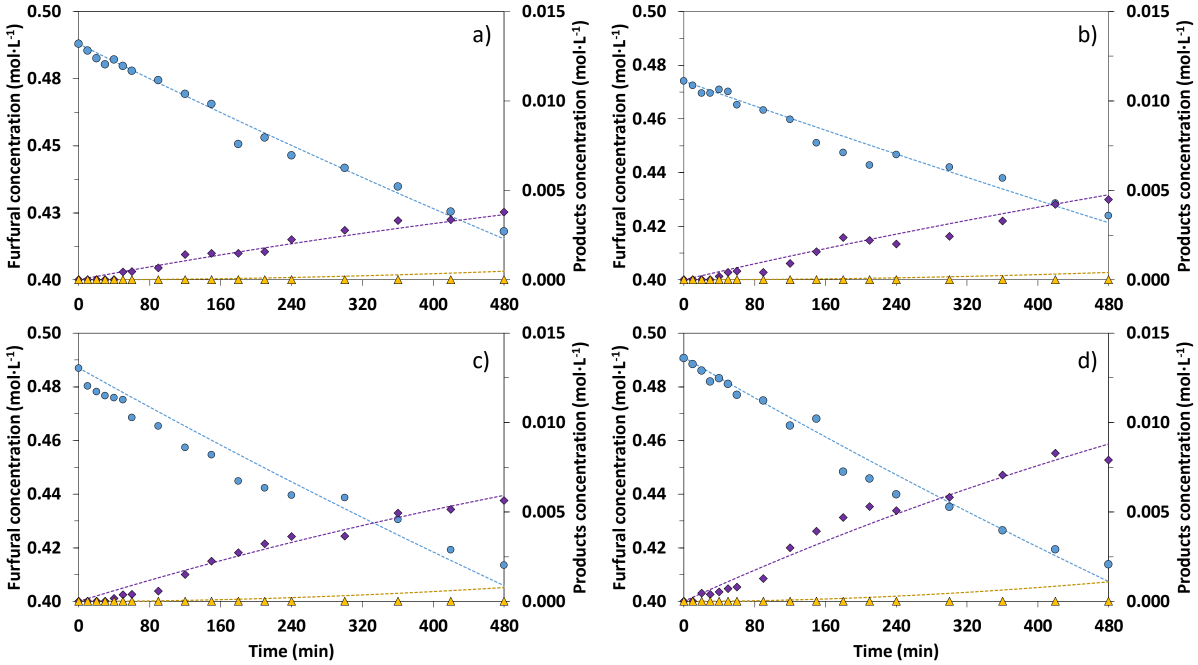

Figure 4.62. Furfural oxidation at 80 ºC in presence of Au/MgAl modifying pressure: (a) 5 bar, (b) 10 bar, (c) 15 bar, (d) 25 bar. Symbols: FFL (●); FCA (◆); FA (■); MA (▲). *Broken lines correspond to the kinetic model predictions*

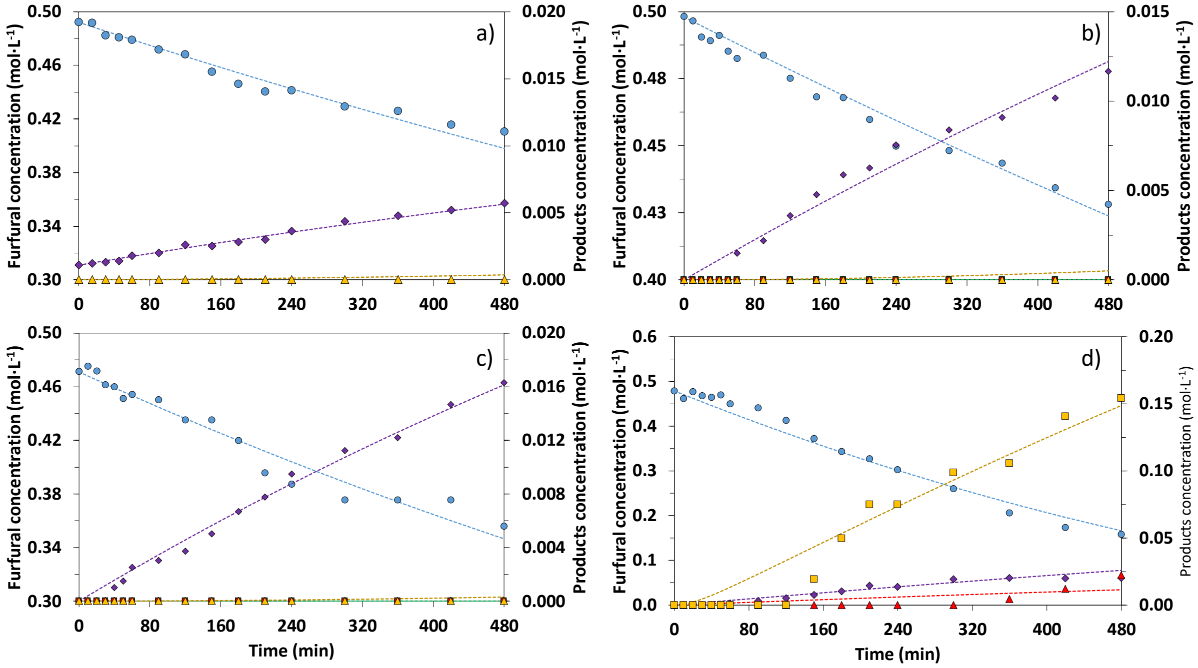

Figure 4.63. Furfural oxidation at 20 bar in presence of Au/MgAl modifying temperature: (a) 80 ºC, (b) 100 ºC, (c) 120 ºC, (d) 150 ºC. Symbols: FFL (●); FCA (◆); FA (■); MA (▲); HFN (●). *Broken lines correspond to the kinetic model predictions*

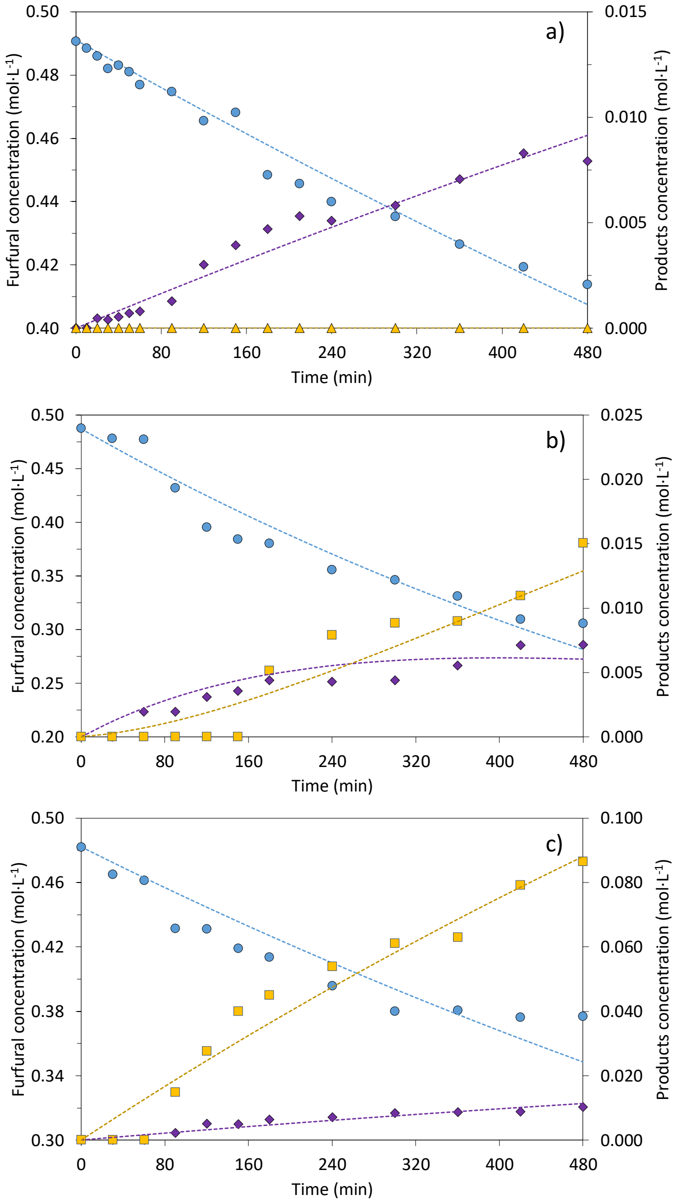

Figure 4.64. Furfural oxidation at 25 bar in presence of Au/MgAl modifying temperature: (a) 80 ºC, (b) 100 ºC, (c) 120 ºC. Symbols: FFL (●); FCA (◆); FA (■); MA (▲); HFN (●). *Broken lines correspond to the kinetic model predictions*

These conclusions allow defining the reaction mechanism illustrated in **Figure 4.65**, where compounds in grey color are required to complete the carbon balance, but they are not quantitatively detected at working conditions (only in traces at the most severe ones).

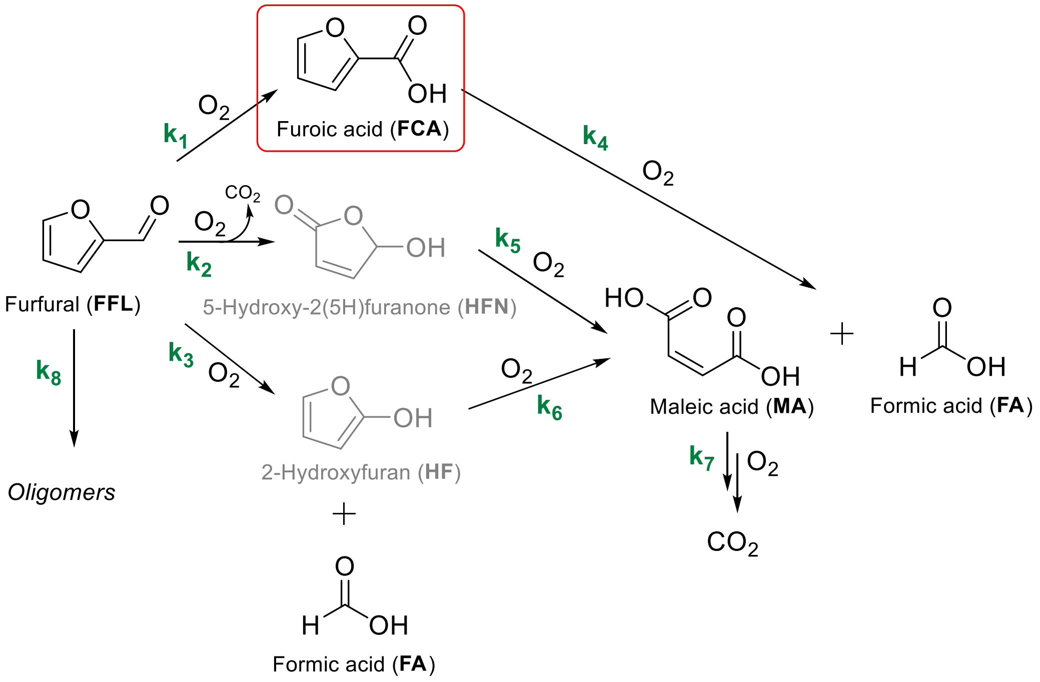

Figure 4.65. Scheme of the reaction mechanism of furfural oxidation using O_2 as oxidizing agent

Based on this mechanism, a preliminary fit of the experimental data considering all the steps were carried out for both materials and all the conditions. Experimental results were fitted to different kinetic models, the best results being obtained when considering an evolution type Langmuir-Hinshelwood for the main reactions, and a potential and independent behavior for the oligomerization and the total oxidation into CO_2. This model is congruent with the furfural and FCA adsorptions previously discussed, a hypothesis that could be extended to all the organics involved since they have the same functional groups. Considering that O_2 is continuously provided by gas-liquid interphase transport, the concentration of this reactant can be considered constant and embedded in the apparent kinetic rate values.

The temporal evolution of all the compounds obtained with both catalysts at the different conditions tested was fit to the proposed mechanism applying the corresponding mass balances, considering the reactor as an ideal stirred batch reactor. All the equations as well as the kinetic rates and the adsorption constants are presented in Equation 4.20-25 and **Tables 4.15-20**. In the same way, all the temporal profiles comparing the experimental points with the fitted data are also included in **Figure 4.59-64**.

$$\frac{dC_{FFL}}{dt} = \frac{-k_1 \cdot K_{ads,\ FFL} \cdot C_{FFL} - k_2 \cdot K_{ads,\ FFL} \cdot C_{FFL} - k_3 \cdot K_{ads,\ FFL} \cdot C_{FFL}}{1 + K_{ads,\ FFL} \cdot C_{FFL}} - k_8 \cdot C_{FFL} \qquad \mathbf{[4.20]}$$

$$\frac{dC_{FCA}}{dt} = \frac{k_1 \cdot K_{ads,\ FFL} \cdot C_{FFL}}{1 + K_{ads,\ FFL} \cdot C_{FFL}} - \frac{k_4 \cdot K_{ads,\ FCA} \cdot C_{FCA}}{1 + K_{ads,\ FCA} \cdot C_{FCA}} \qquad \mathbf{[4.21]}$$

$$\frac{dC_{MA}}{dt} = \frac{k_4 \cdot K_{ads,\ FCA} \cdot C_{FCA}}{1 + K_{ads,\ FCA} \cdot C_{FCA}} + \frac{k_5 \cdot K_{ads,\ HFN} \cdot C_{HFN}}{1 + K_{ads,\ HFN} \cdot C_{HFN}} + \frac{k_6 \cdot K_{ads,\ HF} \cdot C_{HF}}{1 + K_{ads,\ HF} \cdot C_{HF}} - k_7 \cdot C_{MA} \qquad \mathbf{[4.22]}$$

$$\frac{dC_{FA}}{dt} = \frac{k_3 \cdot K_{ads,\ FFL} \cdot C_{FFL}}{1 + K_{ads,\ FFL} \cdot C_{FFL}} + \frac{k_4 \cdot K_{ads,\ FCA} \cdot C_{FCA}}{1 + K_{ads,\ FCA} \cdot C_{FCA}} \qquad \mathbf{[4.23]}$$

$$\frac{dC_{HF}}{dt} = \frac{k_3 \cdot K_{ads,\ FFL} \cdot C_{FFL}}{1 + K_{ads,\ FFL} \cdot C_{FFL}} - \frac{k_6 \cdot K_{ads,\ HF} \cdot C_{HF}}{1 + K_{ads,\ HF} \cdot C_{HF}} \qquad \mathbf{[4.24]}$$

$$\frac{dC_{HFN}}{dt} = \frac{k_2 \cdot K_{ads,\ FFL} \cdot C_{FFL}}{1 + K_{ads,\ FFL} \cdot C_{FFL}} - \frac{k_5 \cdot K_{ads,\ HFN} \cdot C_{HFN}}{1 + K_{ads,\ HFN} \cdot C_{HFN}} \qquad \mathbf{[4.25]}$$

Table 4.15. Reaction rate constants based on the proposed reaction mechanism for Au/TiO_2 catalyst as function of different O_2 pressures. Units: k_1 – k_8, (h^{-1}) and $K_{ads,\ FFL}$; $K_{ads,\ HFN}$; $K_{ads,\ HF}$, and $K_{ads,\ O_2}$ ($L \cdot mol^{-1}$). Reaction conditions: 0.5 g Au/TiO_2, $C_{0(FFL)} = 0.5\ mol \cdot L^{-1}$, T = 80 ºC, 700rpm, 8h reaction.

P (bar)	**k_1**	**k_2**	**k_3**	**k_5**	**k_6**	**k_7**	**k_8**	**$K_{ads,\ FFL}$**	**$K_{ads,\ HFN}$**	**$K_{ads,\ HF}$**	**r^2**
5	0.435	0.072	0.057	0.110	0.109	0.150	0.030	0.002	0.110	0.109	0.999
10	0.458	0.068	0.053	0.111	0.110	0.150	0.015	0.003	0.111	0.110	0.988
15	0.586	0.070	0.054	0.109	0.109	0.150	0.025	0.003	0.109	0.109	0.998
20	0.556	0.001	0.286	0.225	1.180	0.149	0.010	0.003	0.225	1.180	0.999
25	0.402	0.002	0.252	0.210	2.774	0.147	0.013	0.004	0.210	2.774	0.999

Table 4.16. Reaction rate constants based on the proposed reaction mechanism for Au/TiO_2 catalyst as function of temperature. Units: k_1 – k_8, (h^{-1}) and $K_{ads, FFL}$; $K_{ads, HFN}$; $K_{ads, HF}$, and K_{ads, O_2} ($L \cdot mol^{-1}$). Reaction conditions: 0.5 g Au/TiO_2, $C_{0(FFL)}$ = 0.5 $mol \cdot L^{-1}$, 20 bar O_2, 700rpm, 8h reaction.

T (°C)	k_1	k_2	k_3	k_5	k_6	k_7	k_8	$K_{ads, FFL}$	$K_{ads, HFN}$	$K_{ads, HF}$	r^2
80	0.556	0.001	0.286	0.225	1.180	0.149	0.010	0.003	0.225	1.180	0.999
100	0.449	0.001	0.365	0.915	3.210	0.021	0.007	0.016	0.915	3.208	0.999
120	0.407	0.032	0.501	1.049	3.226	0.045	0.033	0.031	1.049	3.221	0.999
150	0.446	0.026	0.888	1.033	3.609	1.033	0.147	0.031	1.032	3.602	0.995

Table 4.17. Reaction rate constants based on the proposed reaction mechanism for Au/TiO_2 catalyst as function of temperature. Units: k_1 – k_8, (h^{-1}) and $K_{ads, FFL}$; $K_{ads, HFN}$; $K_{ads, HF}$, and K_{ads, O_2} ($L \cdot mol^{-1}$). Reaction conditions: 0.5 g Au/TiO_2, $C_{0(FFL)}$ = 0.5 $mol \cdot L^{-1}$, 25 bar O_2, 700rpm, 8h reaction.

T (°C)	k_1	k_2	k_3	k_5	k_6	k_7	k_8	$K_{ads, FFL}$	$K_{ads, HFN}$	$K_{ads, HF}$	r^2
80	0.402	0.002	0.252	0.210	2.774	0.147	0.013	0.004	0.210	2.774	0.999
100	0.512	0.012	0.578	1.016	2.222	2.505	0.027	0.007	1.014	2.221	0.998
120	0.324	0.014	0.694	0.688	2.259	0.000	0.051	0.026	0.663	2.254	0.997

Table 4.18. Reaction rate constants based on the proposed reaction mechanism for Au/MgAl catalyst as function of different O_2 pressures. Units: $k_1 - k_8$, (h^{-1}) and $K_{ads, FFL}$; $K_{ads, HFN}$; $K_{ads, HF}$; $K_{ads, FCA}$; and K_{ads, O_2} ($L \cdot mol^{-1}$). Reaction conditions: 0.5 g Au/MgAl, $C_{0(FFL)}$ = 0.5 mol·L^{-1}, T = 80 ºC, 700rpm, 8h reaction.

P (bar)	k_1	k_2	k_3	k_4	k_5	k_6	k_7	k_8	$K_{ads, FFL}$	$K_{ads, HFN}$	$K_{ads, HF}$	$K_{ads, FCA}$	r^2
5	0.061	0.000	0.000	0.139	0.000	0.000	0.300	0.019	0.019	0.000	0.000	0.219	0.997
10	0.065	0.000	0.000	0.131	0.000	0.000	0.100	0.016	0.022	0.000	0.000	0.130	0.999
15	0.071	0.000	0.000	0.134	0.000	0.000	0.100	0.021	0.040	0.000	0.000	0.216	0.998
20	0.069	0.000	0.000	0.113	0.000	0.000	0.100	0.025	0.020	0.000	0.000	0.113	0.999
25	0.075	0.000	0.000	0.117	0.000	0.000	0.100	0.017	0.047	0.000	0.000	0.084	0.998

Relevant conclusions can be drawn from this comprehensive study, allowing a significant simplification of this complex model. The values obtained for "k_2" (HFN formation step) are systematically lower than those values obtained for "k_1" (FCA formation step), being zero in most of the cases and more than two orders of magnitude lower than "k_1" in the other cases. Moreover, the "k_5" (HFN decomposition) values are significantly higher than the "k_2" ones. In the same way, "k_6" (HF decomposition) values are one or two orders of magnitude higher than "k_3" (HF formation). In fact, this last constant has null values for all the reactions carried out with Au/MgAl. With this context and considering the negligible concentration of HF and HFN intermediates, the production of maleic and formic acid can be assimilated to a primary step, being directly obtained from furfural, without distinguishing if the formation route is from HF or HFM. With this simplification, "$K_{ads,HFN}$" and "$K_{ads,HF}$" are also neglected in the simplified model.

The profiles of the FCA discard a relevant decomposition of this compound when using Au/TiO_2. In good agreement, negligible values for "k_4" and "$K_{ads,FCA}$" were obtained. However, to define a common mechanism for both catalysts, the FCA decomposition into MA and FA is considered. Based on the conclusions of this detailed study, the reaction mechanism can be simplified to the one shown in **Figure 4.66**, and the kinetic model can be expressed according to the following equations (Eq. 4.25-28), in which only the relevant kinetic steps and adsorption processes are considered.

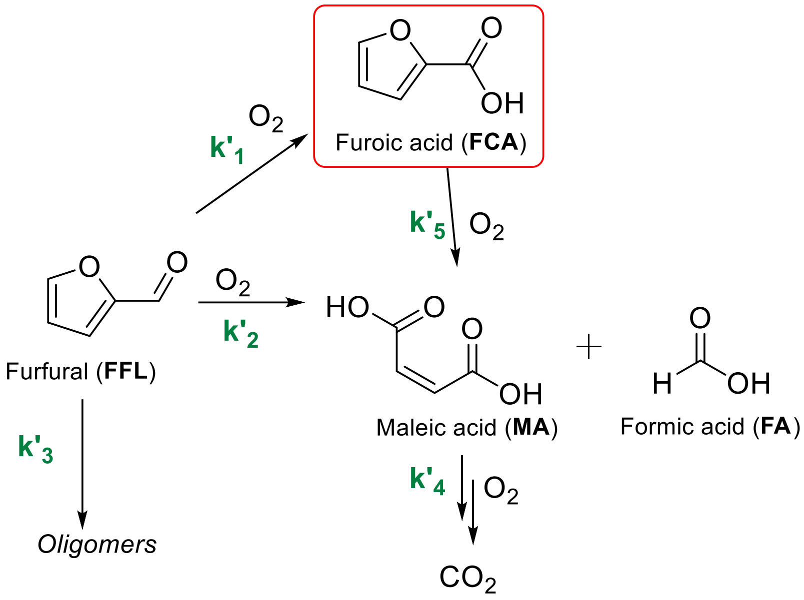

Figure 4.66. Scheme of the simplified reaction mechanism of furfural oxidation using O_2 as oxidizing agent according to the preliminary analysis of the complex mechanism

$$\frac{dC_{FFL}}{dt} = \frac{-k'_1 \cdot K_{ads,\ FFL} \cdot C_{FFL} - k'_2 \cdot K_{ads,\ FFL} \cdot C_{FFL}}{1 + K_{ads,\ FFL} \cdot C_{FFL}} - k'_3 \cdot C_{FFL} \qquad \textbf{[4.25]}$$

$$\frac{dC_{FCA}}{dt} = \frac{k'_1 \cdot K_{ads,\ FFL} \cdot C_{FFL}}{1 + K_{ads,\ FFL} \cdot C_{FFL}} - k'_5 \cdot C_{FCA} \qquad \textbf{[4.26]}$$

$$\frac{dC_{MA}}{dt} = \frac{k'_2 \cdot K_{ads,\ FFL} \cdot C_{FFL}}{1 + K_{ads,\ FFL} \cdot C_{FFL}} - k'_4 \cdot C_{MA} + k'_5 \cdot C_{FcA} \qquad \textbf{[4.27]}$$

$$\frac{dC_{FA}}{dt} = \frac{k'_2 \cdot K_{ads,\ FFL} \cdot C_{FFL}}{1 + K_{ads,\ FFL} \cdot C_{FFL}} \qquad \textbf{[4.28]}$$

After comparing different types of kinetics and analyzing the fit of all the reactions tested, some steps are considered with a Langmuir-Hinshelwood model, whereas other steps follow first-order behavior. For the adsorption processes, the best fit was obtained considering that both oxidation routes involving furfural require the adsorption of this reactant on the same type of active sites. In all the cases, apparent rates are considered, involving in these constants the oxygen concentration, since, as commented before, oxygen concentration will be constant throughout each entire experiment.

The kinetic constants obtained for Au/TiO_2 are summarized in **Table 4.19**. This model represents the temporal evolution of all the compounds obtained in reactions at the most severe conditions whereas, for all the reactions at 80 ºC (and most of those at 100 ºC), the presence of only one product (FCA) reduces the number of steps involved, with null values for k'_2, k'_4 y k'_5. The corresponding values for Au/MgAl are shown in **Table 4.20**, observing slightly higher values for almost all the kinetic rate constants.

Figures 4.67 and **68** show the good fit of experimental values to those predicted by the model for the most representative experiments, with Au/TiO_2 and Au/MgAl, respectively. The adjustment of each reaction is shown in **Figures 4.69-72**.

Table 4.19. Reaction rate constants based on the simplified reaction mechanism for Au/TiO_2 catalyst as function of different O_2 pressures and reaction temperatures.

P (bar)	**T (ºC)**	**k'_1** $(mol \cdot L^{-1} \cdot s^{-1})$	**k'_2** $(mol \cdot L^{-1} \cdot s^{-1})$	**k'_3** **(s^{-1})**	**k'_4** **(s^{-1})**	**k'_5** **(s^{-1})**	**$K_{ads, FFL}$** $(L \cdot mol^{-1})$	**r^2**
5	80	0.0017	-	$8.3 \cdot 10^{-6}$	-	-	0.00036	0.9999
10	80	0.0015	-	$5.5 \cdot 10^{-6}$	-	-	0.00034	0.9999
15	80	0.0017	-	$5.2 \cdot 10^{-6}$	-	-	0.00030	0.9995
20	80	0.0017	-	$4.3 \cdot 10^{-6}$	-	-	0.00029	0.9998
25	80	0.0017	-	$3.9 \cdot 10^{-6}$	-	-	0.00028	0.9999
20	100	0.0142	0.012	$7.4 \cdot 10^{-6}$	0.105	$8 \cdot 10^{-8}$	0.00015	0.9999
25	100	0.0110	0.010	$5.1 \cdot 10^{-6}$	0.141	$1.7 \cdot 10^{-6}$	0.00012	0.9984
20	120	0.0944	0.140	$1.4 \cdot 10^{-5}$	0.111	$1.2 \cdot 10^{-6}$	$4 \cdot 10^{-5}$	0.9996
25	120	0.0750	0.101	$8.9 \cdot 10^{-6}$	0.250	$2.2 \cdot 10^{-5}$	$4 \cdot 10^{-5}$	0.9977
20	150	0.2148	0.414	$3.8 \cdot 10^{-5}$	0.240	$5 \cdot 10^{-6}$	$2 \cdot 10^{-5}$	0.9942

Table 4.20. Reaction rate constants based on the simplified reaction mechanism for Au/MgAl catalyst as function of different O_2 pressures and reaction temperatures.

P (bar)	T (ºC)	k'_1 ($mol\cdot L^{-1}\cdot s^{-1}$)	k'_2 ($mol\cdot L^{-1}\cdot s^{-1}$)	k'_3 (s^{-1})	k'_4 (s^{-1})	k'_5 (s^{-1})	$K_{ads,\ FFL}$ ($L\cdot mol^{-1}$)	r^2
5	80	0.0051	-	$7.6\cdot10^{-6}$	-	-	$1.0\cdot10^{-5}$	0.9999
10	80	0.0073	-	$7.3\cdot10^{-6}$	-	-	$1.4\cdot10^{-5}$	0.9996
15	80	0.0082	-	$6.0\cdot10^{-6}$	-	-	$1.4\cdot10^{-5}$	0.9997
20	80	0.0090	-	$6.6\cdot10^{-6}$	-	-	$9.2\cdot10^{-6}$	0.9997
25	80	0.0011	-	$5.9\cdot10^{-6}$	-	-	$1.1\cdot10^{-5}$	0.9998
20	100	0.0012	-	$8.1\cdot10^{-6}$			$1.3\cdot10^{-5}$	0.9992
25	100	0.0039	0.0046	$1.7\cdot10^{-5}$	0.030	$3.4\cdot10^{-5}$	$1.5\cdot10^{-6}$	0.9979
20	120	0.0035	-	$9.3\cdot10^{-6}$	-	-	$1.5\cdot10^{-6}$	0.9953
25	120	0.0099	0.0764	$2.8\cdot10^{-5}$	0.076	$8.0\cdot10^{-5}$	$1.6\cdot10^{-6}$	0.9986
20	150	0.0156	0.0886	$1.6\cdot10^{-5}$	0.018	$5.3\cdot10^{-6}$	$0.8\cdot10^{-6}$	0.9998

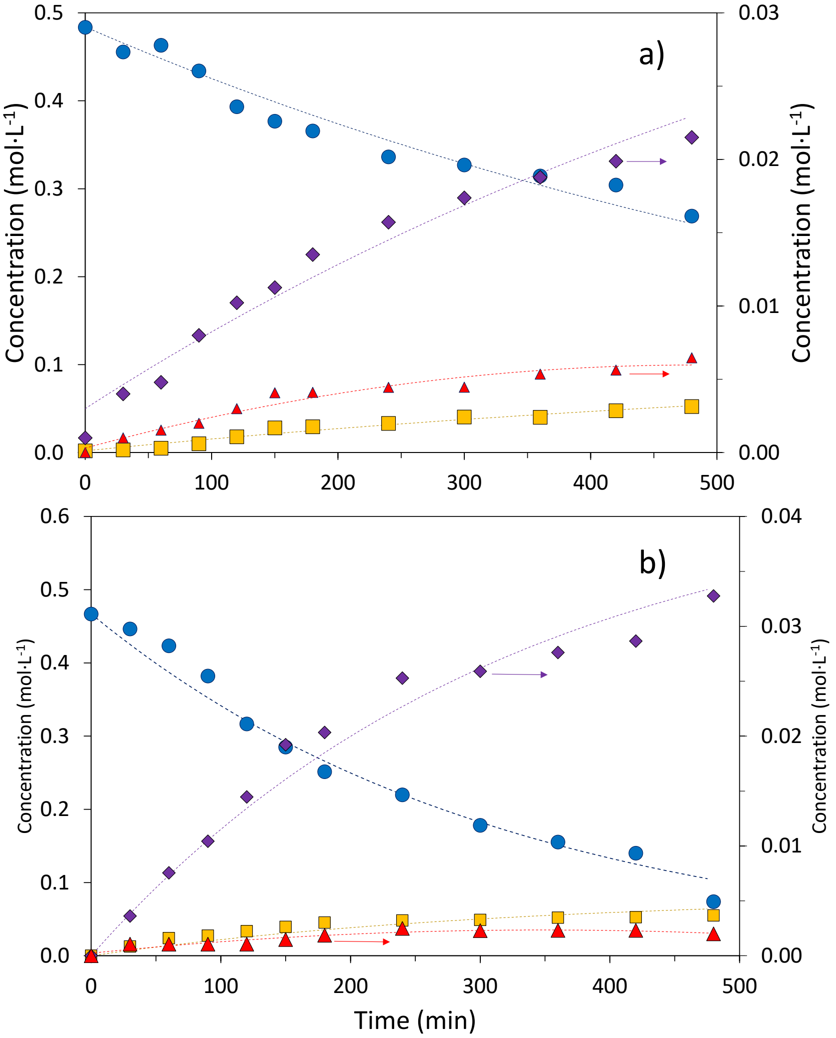

Figure 4.67. Comparison between experimental (symbols) and fit values (broken lines) obtained for the temporal evolution of all the compounds involved in the furfural oxidation catalyzed by Au/TiO$_2$ at (a) 120 ºC and 25 bar, and (b) 150 ºC and 20 bar. Symbols: FFL (●), FCA (◆), MA (▲), and FA (■)

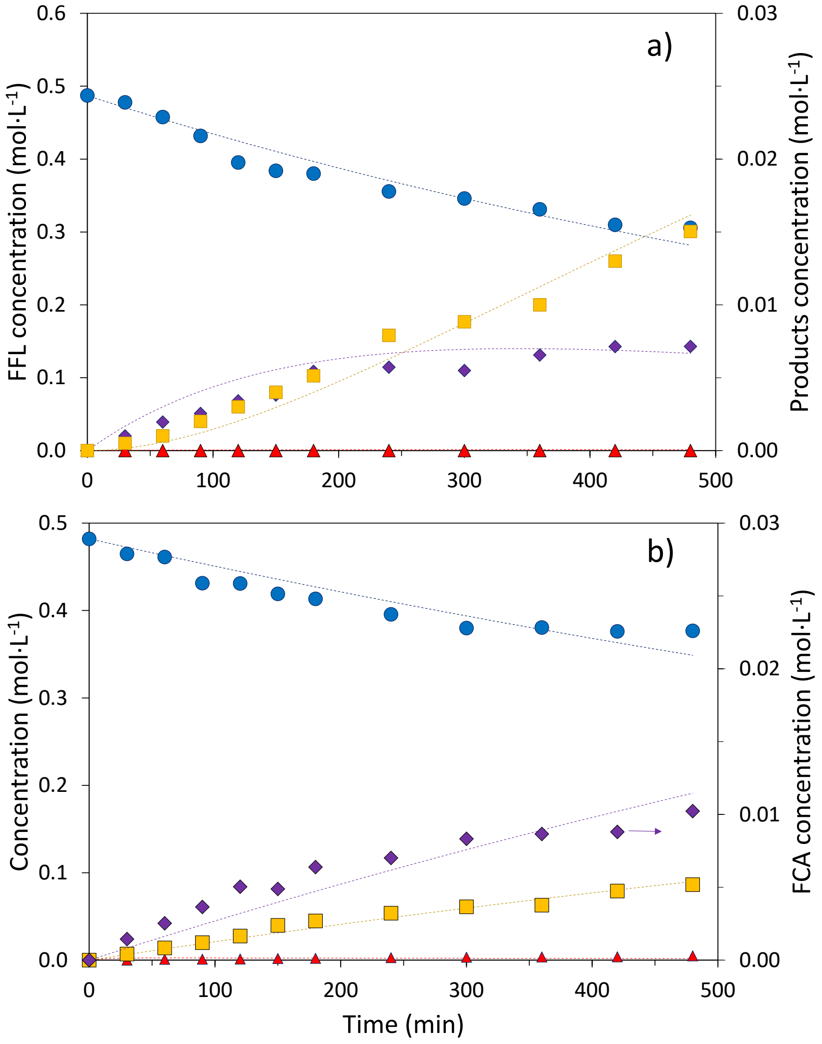

Figure 4.68. Comparison between experimental (symbols) and fit values (broken lines) obtained for the temporal evolution of all the compounds involved in the furfural oxidation catalyzed by Au/MgAl at (a) 100 ºC and 25 bar, and (b) 120 ºC and 25 bar. Symbols: FFL (●), FCA (◆), MA (▲), and FA (■)

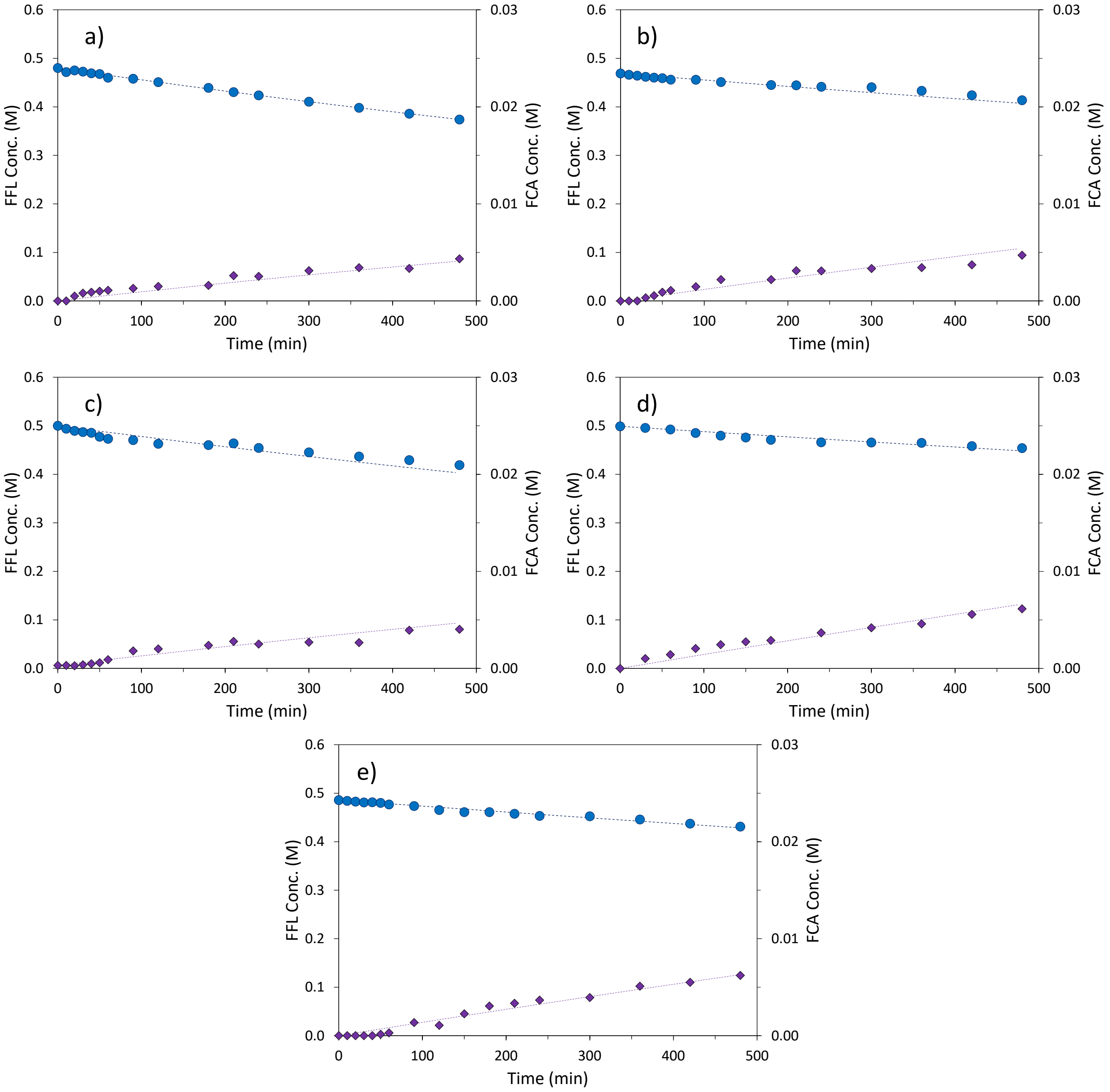

Figure 4.69. Comparison between experimental (symbols) and fit values (broken lines) obtained for the temporal evolution of the furfural oxidation catalyzed by Au/TiO_2 at 80 ºC as a function of the O_2 pressure: (a) 5 bar, (b) 10 bar, (c) 15 bar, (d) 20 bar, and (e) 25 bar. Symbols: FFL (●), FCA (◆)

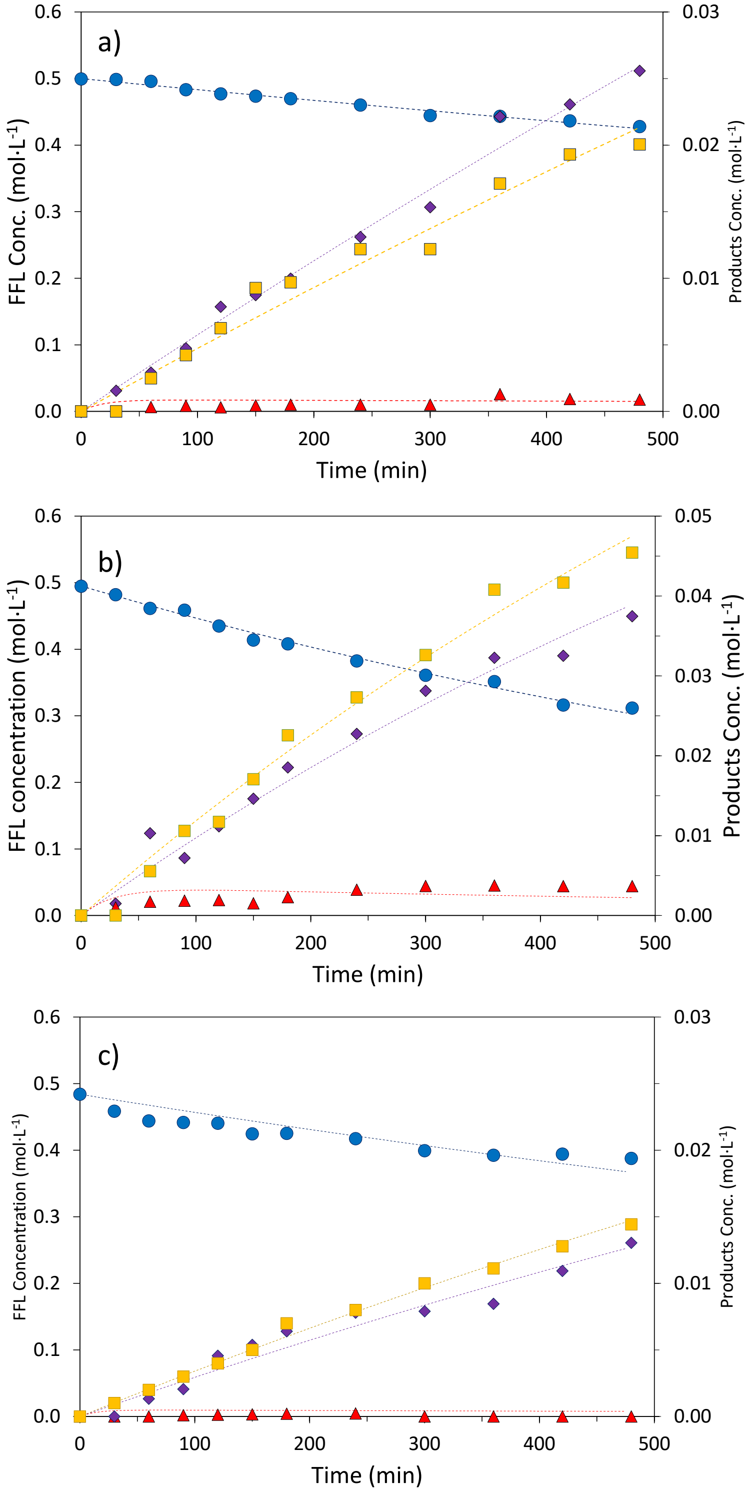

Figure 4.70. Comparison between experimental (symbols) and fit values (broken lines) obtained for the temporal evolution of the furfural oxidation catalyzed by Au/TiO_2 at: (a) 100 °C, 20 bar; (b) 120 °C, 20 bar; and (c) 100 °C, 25 bar. Symbols: FFL (●), FCA (◆), MA (▲), and FA (■)

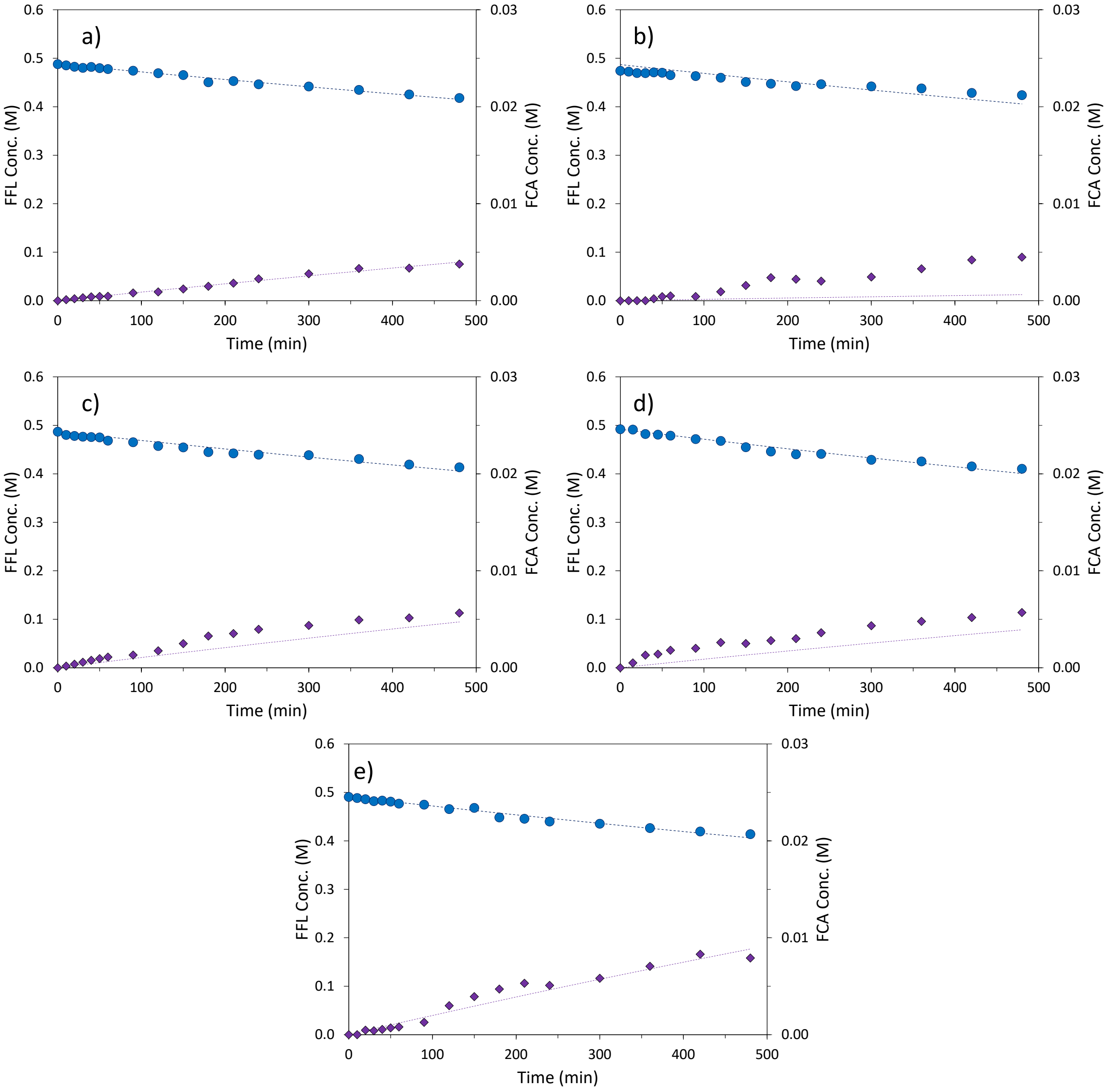

Figure 4.71. Comparison between experimental (symbols) and fit values (broken lines) obtained for the temporal evolution of the furfural oxidation catalyzed by Au/MgAl at 80 ºC as a function of the O_2 pressure: (a) 5 bar, (b) 10 bar, (c) 15 bar, (d) 20 bar, and (e) 25 bar. Symbols: FFL (●), FCA (◆)

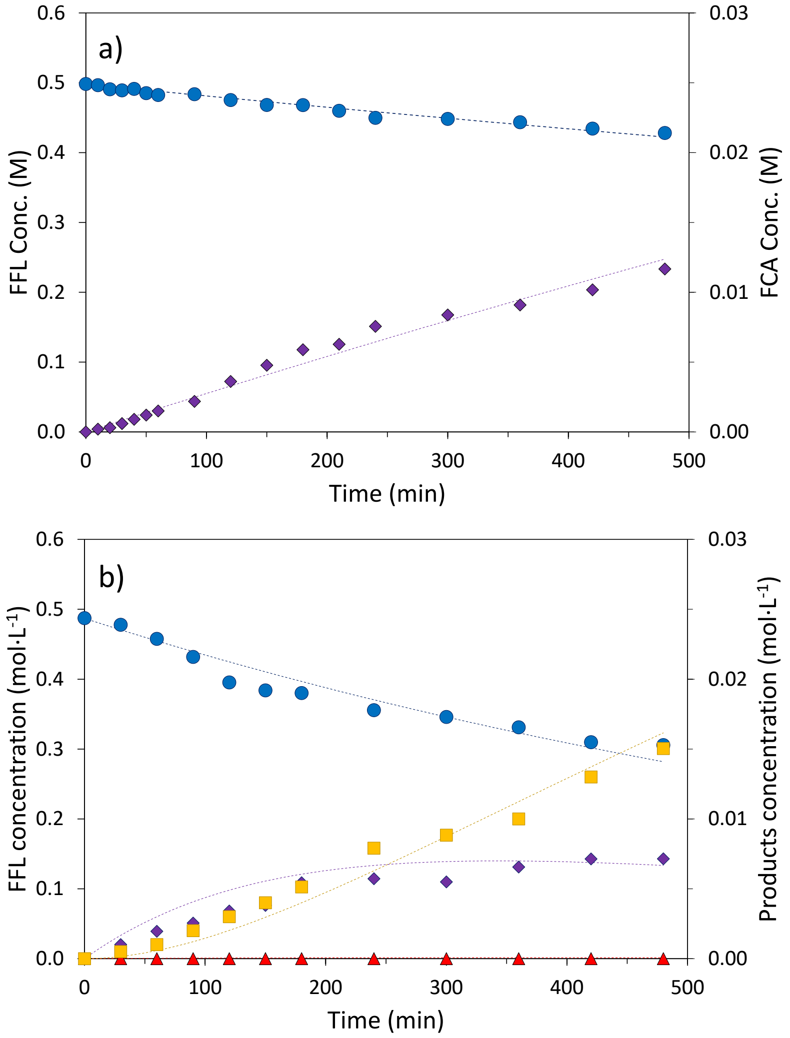

Figure 4.72. Comparison between experimental (symbols) and fit values (broken lines) obtained for the temporal evolution of the furfural oxidation catalyzed by Au/MgAl at: (a) 100 ºC, 20 bar; (b) 100 ºC, 25 bar; and (c) 100ºC, 25 bar. Symbols: FFL (●), FCA (◆), MA (▲), and FA (■)

As analyzed in **Figure 4.73**, using Au/TiO$_2$ at the lowest temperature (80ºC), the direct production of FCA from furfural (k'_1) does not depend on the oxygen pressure, obtaining very similar rate constant values at all the studied pressures. This fact suggests that oxygen surface concentration is large enough for not being a limiting reactant and does not lead to any kind of inhibition or modification of furfural adsorption sites. However, a different trend was observed at higher temperatures (100-120 ºC), observing that total pressure negatively affects this step (Table 19). This result suggests that oxygen hinders the oxidation reaction at these conditions, that could be at first insight, unexpected for an oxidation reaction. This apparent contradiction can be explained by two different causes: a competitive adsorption of oxygen and furfural at higher temperatures (plausible if temperature has a more marked negative effect on furfural adsorption than for oxygen adsorption) or that higher oxygen concentrations at the highest studied temperatures can lead to an overoxidation of the Au atoms, decreasing its intrinsic activity for this reaction.

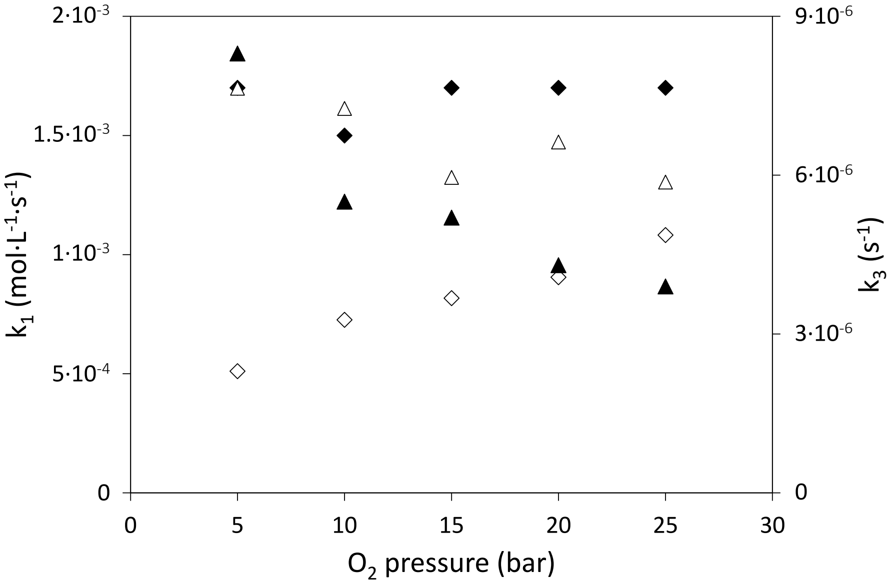

Figure 4.73. Evolution of k_1 (diamonds) and k_3 (triangles) with the O_2 pressure. Data corresponding to Au/TiO_2 (black) and Au/MgAl (white)

A decreasing trend with total oxygen pressure is observed for the furfural oligomerization (k'_3). According to the initial comparison of results in the absence of a catalyst and using the different supports, the furfural oligomerization has a relevant homogeneous component, but the solid catalysts also contribute to this reaction (mainly catalysts with acid properties). Both mechanisms have been previously identified in the literature [67, 73, 76]. The evolution of k'_3 (constant that involves both mechanisms) with the pressure indicates that the furfural oligomerization is inhibited by the presence of oxygen. If this analysis is extended to higher temperatures, the comparison between kinetic rates obtained at 20 and 25 bar demonstrates that the role of oxygen concentration cannot be discarded. Thus, minor discrepancies are obtained, with slightly higher values at 20 bar in comparison to the same step at 25 bar and the same temperature. In global terms, working with high pressure enhances the selective FCA production with k_1/k_3 ratios from 206 to 430, at 5 and 25 bar, respectively.

In the case of the reactions catalyzed with Au/MgAl, the kinetic study demonstrates a positive effect of the oxygen pressure enhancing the target reaction, with increasing k'_1 values with increasing O_2 pressures at all the studied temperatures. This trend is the opposite of that observed for Au/TiO_2 catalysts and suggests that oxygen surface concentration can be limiting for this step when working with Mg-Al supported catalysts. It should be noted that the absence of redox properties of the MgAl support hinders oxygen mobility from metal sites where O_2 is activated to the support (several authors suggest that furfural can be adsorbed in basic sites of the support in this kind of materials [77]). This fact makes surface oxygen concentration more limiting and justifies that increasing pressures lead to higher reaction rates. The chemical differences between Mg-Al oxide (with a higher concentration of basic sites that can promote furfural adsorption but inactive for activating oxygen) and TiO_2 (which has a lower affinity for furfural adsorption but higher electron mobility that can promote overoxidation of the metal sites at the highest temperatures) appear to be responsible for the differential effect of oxygen pressure.

Regarding the furfural oligomerization, the second relevant reaction with this material, the decreasing trend defined for Au/TiO_2 is also observed, with slightly higher values. This result is in good agreement with the role of acid sites promoting oligomerization [76]. With this catalyst, the other steps are only significant when working in the most severe conditions, not obtaining data enough to complete a deep analysis.

As to the influence of the temperature, both at 20 and 25 bar, kinetic rates demonstrate a clear increasing trend, coherently with an Arrhenius dependence. This correspondence verifies the initial assumptions considered when deciding which steps follow an exponential model and which adsorption constants are relevant (opposite behavior of kinetic rates and adsorption constants with the temperature). Although not all the steps are relevant at mild conditions, all the rates obtained were adjusted to the Arrhenius model, obtaining the activation energies summarized in **Figure 4.74**. Although the activation energy should be independent of the pressure, it must be noted that the analysis is done considering the apparent kinetic constants, which involve the oxygen pressure.

The highest activation energy is obtained for the FCA decomposition (k'_5), in good agreement with the fact that this step is only relevant at the most severe conditions. No relevant differences were obtained with the two parallel steps involving the furfural to produce FCA and MA (k'_1 and k'_2, respectively), with typical values of catalytic reactions. Quite similar activation energies are also obtained for the FFL oligomerization (k'_3) and MA total oxidation (k'_4), but in this case with values congruent with a non-catalytic character of these steps.

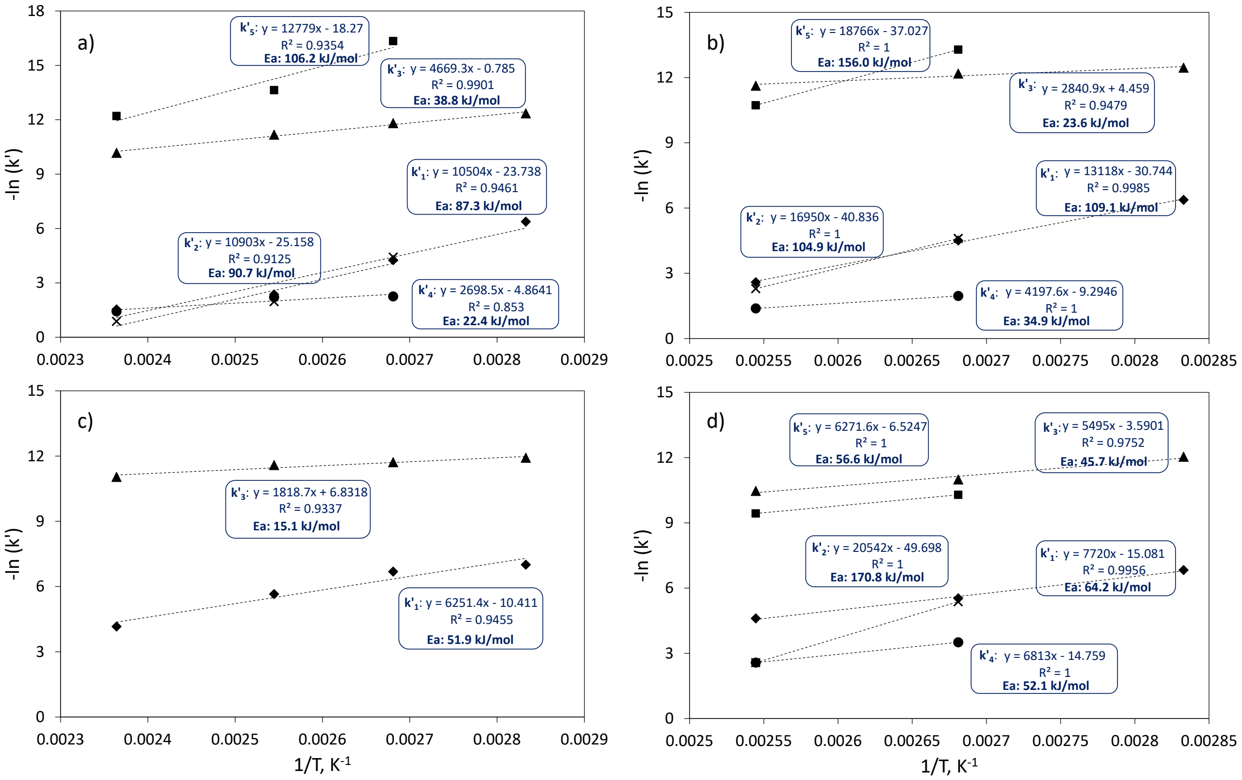

Figure 4.74. Activation energy (Ea) values according to the Arrhenius model (N/A = non available). Data corresponding to (a) Au/TiO_2 20 bar; (b) Au/TiO_2 25 bar; (c) Au/MgAl 20 bar; (d) Au/MgAl 25 bar. Symbols: k'_1 (◆); k'_2 (×); k'_3 (▲); k'_4 (●); k'_5 (■)

The activation energies obtained with this material are lower than those obtained with Au/TiO_2. These results suggest that the slower kinetics obtained are due to significantly lower values of the pre-exponential constants, values related to the probability of constructive interactions between both reactants.

To sum up, the oxygen availability in the vicinity of adsorbed furfural is suggested as the main factor controlling the kinetics of the furfural oxidation to produce furoic acid when using Au/MgAl, obtaining significantly better results when working with Au/TiO_2 because of the higher oxygen mobility in the support. Thus, at the same conditions, FCA productions 160 % higher than those obtained with Au/MgAl are reached when using TiO_2 as support.

4.4.5. Catalyst reusability

Activity studies performed with Au/TiO_2 working under controlled pH conditions (buffered solution) demonstrate that this new approach allows obtaining a relevant increase in terms of furoic acid selectivity (100% in the liquid phase except when working at too high temperatures) concerning previous literature at pH 14 [56, 78] Moreover, the relevance of humins production is reduced. However, to compare this configuration with the base-free one, stability is a key factor to consider. Literature under uncontrolled pH demonstrates a high FCA selectivity but a strong deactivation due to the permanent adsorption of this acid and the catalytic leaching due to the low pH [46, 65, 70, 71].

To study the catalytic stability, the catalyst after the reaction with Au/TiO_2 at 100 °C and 20 bar was recovered by filtration, washed with water, and introduced in subsequent cycles with fresh solutions of furfural without any previous reactivation. Results obtained after 8h of reaction are summarized in **Figure 4.75**, in terms of furfural conversion, furoic acid selectivity, and carbon balance closure. Strong stability is observed, with negligible decreases in the furfural conversion (14.6% after the fourth cycle) and constant furoic acid selectivities of 35%. The slight increase in the carbon balance closure suggests that the humins formation is slightly hindered, maybe because of the permanent adsorption of these solids on the active catalytic sites.

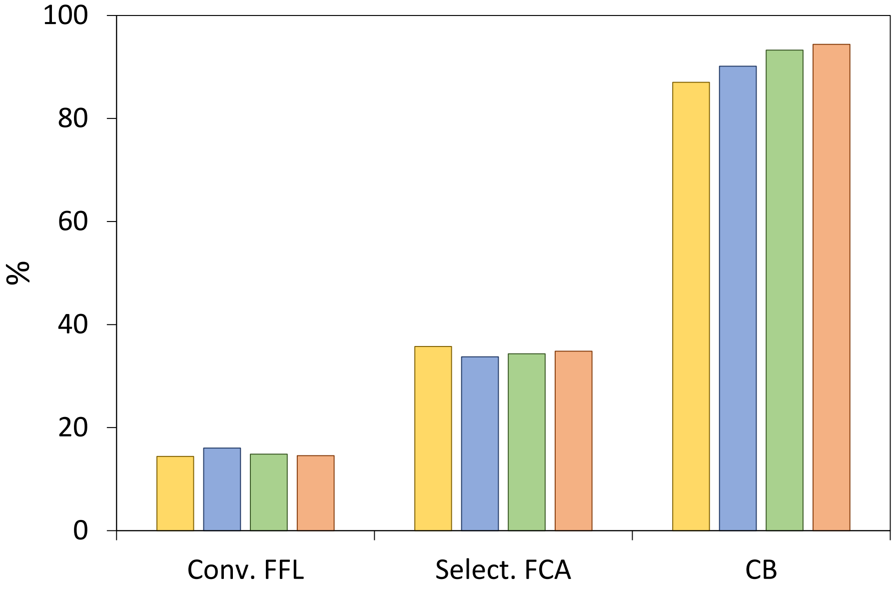

Figure 4.75. Stability results obtained with Au/TiO2 at 100 °C and 20 bar. Results corresponding to data after 8h with the first (yellow), second (blue), third (green), and fourth (orange) cycle

These results demonstrate that the catalytic leaching and the deactivation by permanent adsorption of FCA are prevented by working with a buffer solution at pH 8. This strong stability contrasts with the results published when working under uncontrolled pH, which is a clear advantage of this configuration.

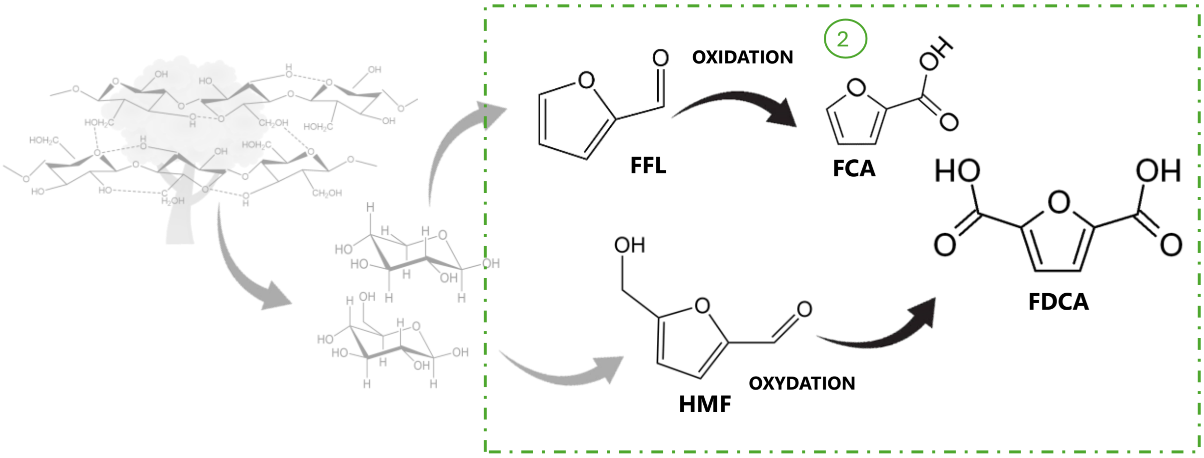

4.5. PRODUCTION OF 2,5-FURANDICARBOXYLIC ACID BY OXIDATION OF 5-HYDROXYMETHYLFURFURAL AND FRUCTOSE

This study aims to conduct a comprehensive analysis of the impact of various reaction conditions (including temperature, oxygen pressure, NaOH:HMF ratio, and HMF initial concentration) on the oxidation of HMF to FDCA over Au/TiO_2 catalysts. The objective is to identify the optimal conditions that achieve a balance between activity, selectivity, and sustainability. Subsequently, we evaluate the feasibility of directly producing FDCA from fructose in a one-pot configuration. This evaluation involves assessing whether the conclusions drawn from the study using commercial HMF remain applicable when using biomass-related feedstocks.

The analyses of the reactions are present in terms of conversion, selectivity, and carbon balance closure, according to the following expressions:

$$x\ (\%) = \frac{C_{i,0} - C_{i,t}}{C_{i,0}} \cdot 100 \qquad \textbf{[4.29]}$$

$$S_i\ (\%) = \frac{n_j \cdot C_j}{(C_{i,0} - C_{i,t})} \cdot 100 \qquad \textbf{[4.30]}$$

$$Yield\ (\%) = = \frac{n_j \cdot C_j}{n_i \cdot C_{i,0}} \cdot 100 \qquad \textbf{[4.31]}$$

$$C.B.(\%) = \frac{\sum(n_j \cdot C_j)}{\sum(n_i \cdot C_i)} \cdot 100 \qquad \textbf{[4.32]}$$

where "n_i" and "C_i" are the number of carbons and the molar concentration of each reactant and "n_j" and "C_j" are the number of carbons and the molar concentration of each compound.

As preliminary studies, the possible HMF oxidation and/or degradation promoted by basic conditions has been tested considering two different configurations, both in the absence of any solid catalyst. On the one hand, the HMF self-degradation was evaluated at room temperature and atmospheric pressure using the most basic conditions considered in this work (0.04 M NaOH, 4:1 NaOH/HMF). After 24 h, more 50% of the initial HMF disappears but no products are detected, with the subsequent decrease in the carbon balance (47.5%). The dark color of the solution is congruent with these results, suggesting a high HMF polymerization trend (humins formation), even in the absence of oxidizing conditions. Humins remain soluble at high pH levels due to their coiled conformations, which are cross-linked by weak forces such as Van der Waals bonds [79, 80].

The same experiment was also performed under oxidizing condition (20 bar of O_2). After 1h, 98.4% of HMF conversion is reached, but the carbon balance decreases to 6.8%, suggesting that the HMF oligomerization, the only reaction taking place at these conditions, is significantly promoted by oxidizing conditions. No products were detected by increasing the temperature to 80 ºC.

Both experiments indicate the need for a metal catalyst to steer the reaction toward the production of FDCA by activating the oxygen dissociation required for oxidation steps [79, 81-83]. The systematic study about the reaction conditions that allow reaching the maximum FDCA yield with the minimum severity is then studied using in all the cases Au/TiO_2 (2 $g{\cdot}L^{-1}$).

4.5.1. Influence of the reaction temperature on the 5-hydroxymethylfurfural oxidation

Figure 4.76 shows the temporal profiles obtained in the aerobic oxidation of a 0.1M HMF solution as a function of the temperature (range studied 60-100 ºC). The high O_2 pressure chosen (20 bar) ensures the theoretical excess of this reactant, whereas the fast stirring (700 rpm) promotes the oxygen transfer from the gas to the liquid phase, discarding mass transfer limitations as relevant in the discussion of the results. The NaOH:HMF ratio (4:1) has been chosen considering the literature [81] to promote the reaction and to keep the humins soluble, preventing their precipitation on the catalyst surface, with the subsequent catalytic deactivation by pore blockage.

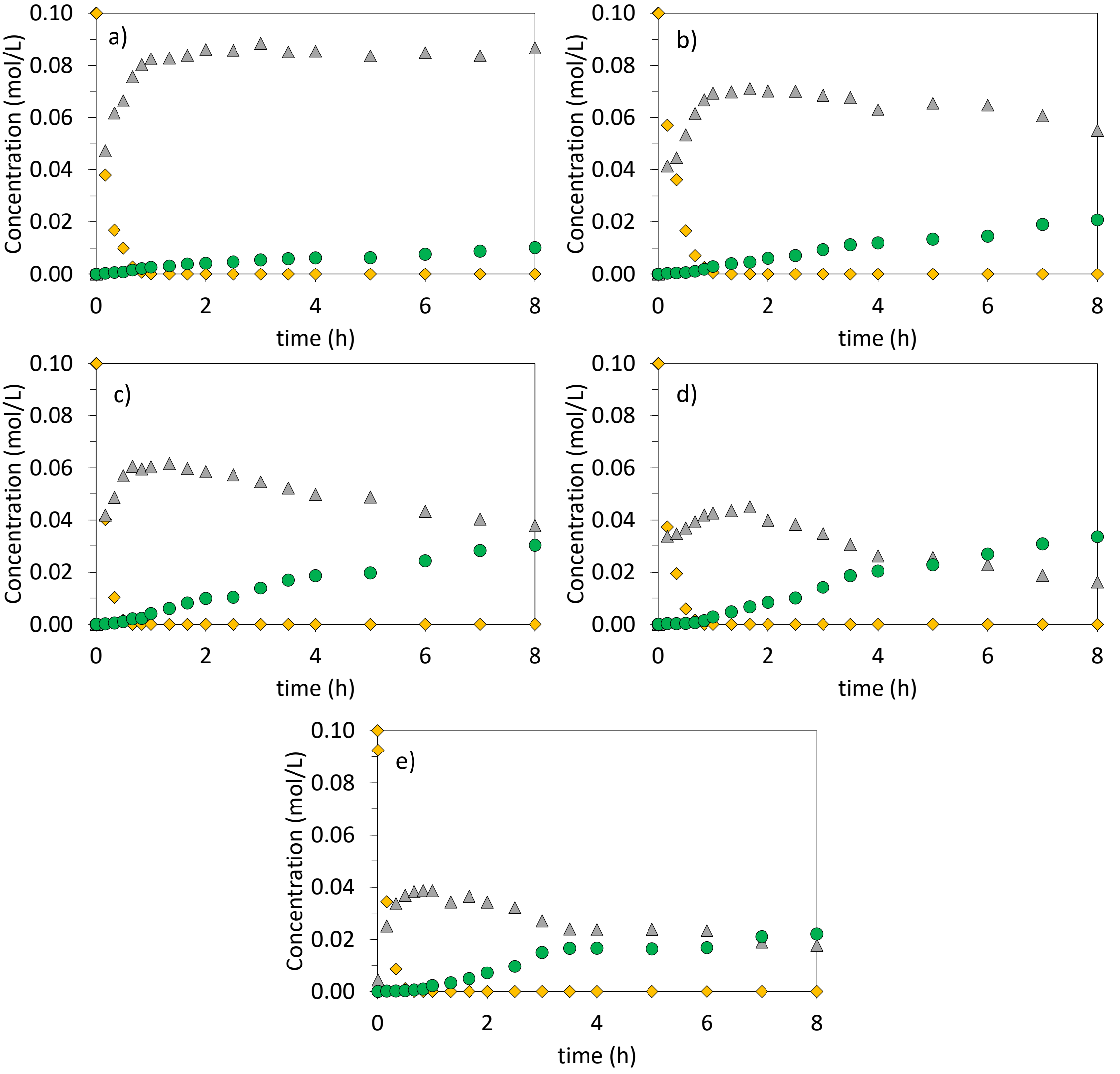

Figure 4.76. Temporal evolution of all the compounds involved in the 0.1 M HMF oxidation as a function of temperature at 20 bar and NaOH:HMF 4:1 ratio over Au/TiO_2 (2 g·L^{-1}). Legend: (a) 60 ºC, (b) 70 ºC, (c) 80 ºC, (d) 90 ºC, and (e) 100 ºC. Symbols: HMF (◆), HMFCA (▲), and FDCA (●)

Total HMF conversion is reached in less than 1 h, regardless of the temperature. HMFCA is the first component detected, discarding the parallel route of DFF. This intermediate has the typical profile of a primary reaction product, reaching its maximum in less than one hour, with concentrations that correspond to more than 80% of the HMF converted at 60 ºC. As the temperature increases, the maximum decreases (70% at 70 ºC, 67% at 80 ºC, 44% at 90 ºC, 38% at 100 ºC), suggesting a higher relevance of humins formation. Reaction at 60 ºC has not severity enough to promote the second oxidation step, FDCA being obtained in traces (<10% after 8 h). Increasing the temperature, HMFCA decreases because of the formation of FDCA. There is total correspondence between the HMFCA disappeared and the FDCA formation, which suggests that HMF is the only humins precursor. Consequently, the carbon balance has been constant since the first hour, obtaining a well-marked decreasing trend with the temperature, from 97% at 60 °C to 40% at 100 °C. This parameter, as well as the selectivity distribution obtained after 8h are compared in **Figure4.77.**

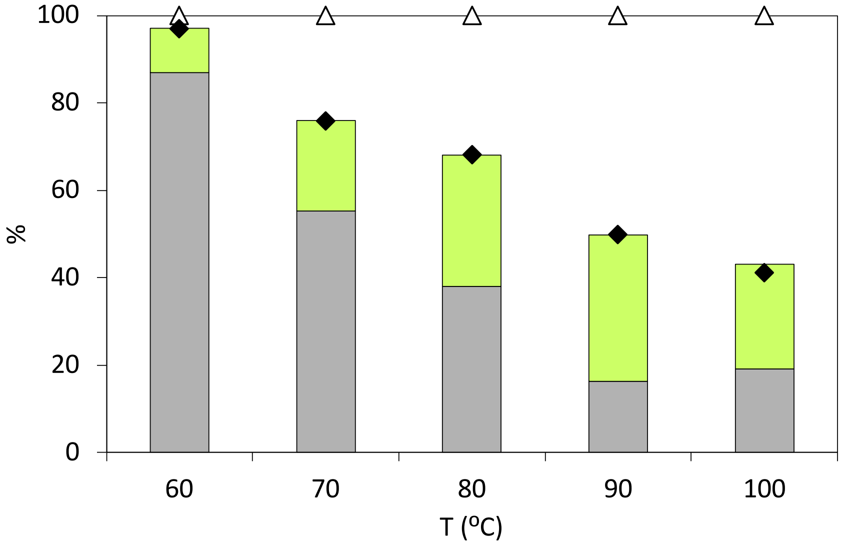

Figure 4.77. HMF conversion (△), carbon balance (◆), and selectivity distribution (bars) obtained after 8 h of 0.1 M HMF oxidation at different temperatures (60-100 °C) over Au/TiO_2 (2 g·L^{-1}) at 20 bar and 4:1 molar ratio NaOH:HMF. Legend: HMFCA (grey) FDCA (green)

The comparison after 8 h reaction time reflects that the second oxidation is not enough promoted at temperatures below 80 °C, being the solution enriched in HMFCA. The maximum FDCA selectivity is observed at 90 °C (33.5% of the total HMF converted, a value that represents 67.3% of the products detected in the liquid phase). However, the carbon balance (49.8%) obtained at this temperature indicates that these conditions are also favourable for the humins formation. This effect is even more relevant at 100 °C. The balance between maximizing the activity and minimizing the humins formation seems to be obtained at 80 °C. Although after 8h the relative selectivity of FDCA is only 44%, the higher carbon balance closure (67%) and the temporal profiles suggest that longer times could significantly improve this value with a limited humins formation. These conditions are considered as the base case for further studies. This study allows concluding some relevant aspects that condition the following studies: (1) humins are generated by the polymerization of HMF but other oxidized compounds are not involved; (2) although temperature promotes both reactions, humins formation is more sensitive to this factor than the oxidation steps, being required to modify other parameters to maximize the FDCA yield, and (3) Minimizing humins formation should be prioritized over maximizing FDCA yield as the primary criterion when selecting optimum conditions to prevent catalytic deactivation (decreasing as much as possible the NaOH usage for avoiding humins precipitation).

4.5.2. Influence of O_2 pressure on the 5-hydroxymethylfurfural oxidation

The optimization of O_2 pressure is interesting because of two opposite aspects. On the one hand, since 20 bar of O_2 represents a high excess concerning the theoretical consumption required to promote the complete oxidation of HMF, trying to minimize the pressure would represent an effort to improve the economy of the process. On the contrary, higher O_2 pressure could enhance the interaction of this molecule with the metal sites, promoting oxygen dissociation and, subsequently, the oxidation pathway over the humins formation. The influence of O_2 pressure was studied from 15 to 30 bar of O_2, keeping constant the optimum temperature at 80 ºC. Temporal profiles, shown in **Figure 4.78**, demonstrate that the reaction mechanism remains unaltered. Thus, total HMF conversion is reached after 1 h and HMFCA is the only intermediate detected. However, the product distribution changes significantly, also affecting the carbon balance, which indicates that the pressure of oxygen plays a key role in the process, despite the large excess theoretically used in all the cases. To facilitate the discussion of this effect results after 0.5 h (before reaching total HMF conversion) and 8 h are compared in **Figure 4.79**.

As anticipated, the decrease in the carbon balance occurs during the first 0.5 h of the reaction, no observing more evolution once the HMF conversion is complete. This fact indicates that HMF plays a crucial role in humins formation. From 15 to 25 bar, results after 0.5 h indicate a positive effect of O_2 pressure tuning the reaction to the desired oxidation, reducing the humins formation, and observing an increase in the carbon balance from 50% to 63%. Considering the short reaction time evaluated, the almost total selectivity of the HMFCA is explained by its character as a primary compound (not enough time to promote the second step). Results obtained at 30 bar suggest a possible inhibition effect that could indicate that all the Au sites are covered by O_2 molecules, disturbing the HMF adsorption. Thus, there is less HMF adsorbed, reducing the frequency of interaction between the two reactants (lowest HMF conversion). This effect would be more relevant at increasing pressures, discarding this approach.

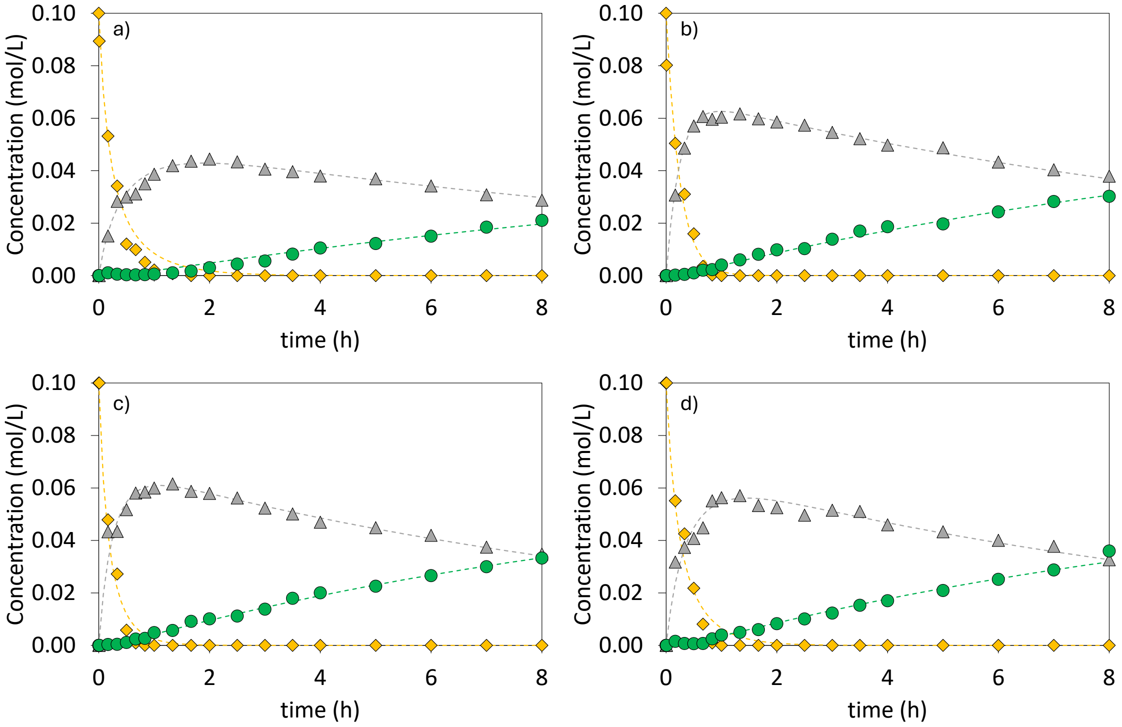

Figure 4.78. Temporal evolution of all the compounds involved in the HMF oxidation as a function of pressure at 80 ºC and 4:1 ratio NaOH:HMF. Legend: (a) 15 bar, (b) 20 bar, (c) 25 bar, and (d) 30 bar. Symbols: HMF (◆), HMFCA (▲), and FDCA (●). Broken lines represent the kinetic model

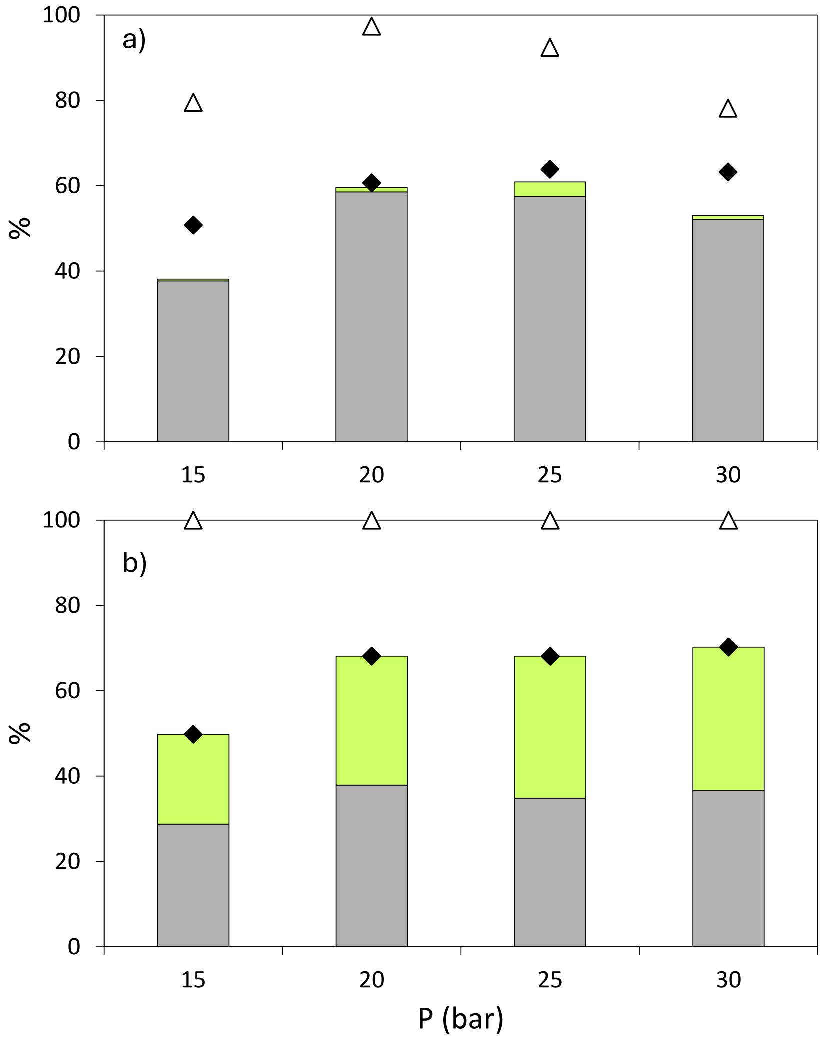

Figure 4.79. HMF conversion (△), carbon balance (◆), and selectivity distribution (bars) obtained after (a) 0.5 h and (b) 8 h of 0.1 M HMF oxidation at 80 ºC as a function of the O_2 pressures using Au/TiO_2 and a NaOH:HMF molar ratio of 4:1. Legend: HMFCA (grey) FDCA (green)

The expected evolution to the second step is observed after 8 h. The analysis of these results suggests a lower effect of O_2 pressure on the second step, and the ratio FDCA/HMFCA increases from 0.4 at 15 bar to 0.5 at 25 bar. As in the previous analysis, this trend is not observed at 30 bar, reinforcing the inhibition.

Comparing the results at 0.5 and 8 h, a slight increase in the carbon balance is observed, except when working at 15 bar: from 60.7 to 68.1%, from 63.9 to 68.4%, and from 63.2 to 70.2%, respectively. Reversible HMF adsorption is discarded as the main reason for this effect since the increase is more relevant at 30 bar, conditions at which the O_2 adsorption competes with the HMF one. Then, this fact suggests certain reversibility of the oligomers formation. The decomposition of soft humins under an oxidizing atmosphere at mild conditions has been previously considered in the literature [84]. Thus, once there is no more HMF in the reaction medium (1 h), the HMFCA is still produced by the decomposition of these "weak" oligomers. This hypothesis is supported by several pieces of evidence, mainly at 30 bar: (1) there is no correspondence between the HMF disappearance and the HMFCA maximum, this point being displaced to 80 minutes, and (2) the total yield of HMFCA and FDCA increases with the time, suggesting a continuous incorporation of more HMFCA, and not only the transformation observed in the other cases.

To reinforce this discussion, a simplified kinetic analysis of results obtained at different pressures has been performed. The experimental results are consistent with a reaction mechanism composed of two consecutive oxidation steps, with HMFCA being the unique intermediate detected in the FDCA formation. Irreversible first-order kinetics has been observed for both successive steps. The high excess of oxygen in all the experiments (the fast stirring and the pressure excess guarantees the saturation) allows considering constant oxygen concentration in each experiment, the effect of oxygen on reaction kinetic being embedded in the apparent kinetic rate constant. With these stablished premises, the kinetic modelling was performed using the following mass balance equations:

$$\frac{d[HMF]}{dt} = -k_1 \cdot [\mathrm{HMF}] - k_3 \cdot [HMF]^2 \qquad \textbf{[4.33]}$$

$$\frac{d[\mathrm{HMFCA}]}{dt} = k_1 \cdot [\mathrm{HMF}] - k_2 \cdot [\mathrm{HMFCA}] \qquad \textbf{[4.34]}$$

$$\frac{d[\mathrm{FDCA}]}{dt} = k_2 \cdot [\mathrm{HMFCA}] \qquad \textbf{[4.35]}$$

In these equations, the effect of undesired consumptions because of the HMF transformation into insoluble compounds (humins) is considered in the "k_3" term, proposing a second-order reaction, which corresponds to a bimolecular process. First-order oligomerization kinetics was also evaluated, obtaining a poorer model prediction. **Table 4.21** summarizes the apparent kinetic rate constants obtained for experiments at different pressures, as well as the corresponding regression coefficients. The high values obtained (>0.98 in all the cases) indicate good correspondence between the theoretical model proposed and the experimental data. This fact is also corroborated by the good fit observed in all the graphs including temporal profiles (Fig 4.78), the theoretical values being plotted with broken lines.

Table 4.21. Apparent reaction rate constants based on reaction mechanism for Au/TiO_2 catalyst (2 g·L^{-1}) as a function of different O_2 pressures when using 0.1 M of initial HMF concentration and a 4:1 NaOH:HMF ratio

P (bar)	**k'₁** (h^{-1})	**k'₂** (h^{-1})	**k'₃** (L·mol^{-1}·h^{-1})	**r^2**
15	1.52	0.065	25.9	0.9892
20	2.76	0.080	28.3	0.9893
25	2.96	0.088	32.5	0.9913
30	1.98	0.090	25.2	0.9871

Since all the experiments were performed at the same temperature and oxygen is at large excess (close to saturation concentration), oxygen concentration can be considered as a constant at a given pressure. However, this concentration increases as operation pressure increases, allowing to correlate reactivity trends with oxygen concentration. The significant differences observed corroborate the role of this reactant, with different impacts in three evaluated reactions. Thus, each apparent kinetic constant can be expressed as a function of the oxygen concentration according to this expression, estimating oxygen concentration with the Henry law for the oxygen-water system:

$$k_i = k'_i \cdot [O_2]^n \qquad \textbf{[4.36]}$$

The linearization of this expression is shown in **Figure 4.80**. The value of k_1 obtained at 30 bar was excluded from this analysis since experimental results demonstrate an inhibition effect of the oxygen adsorbed when working at so high pressure, shielding the effect on the reaction rate.

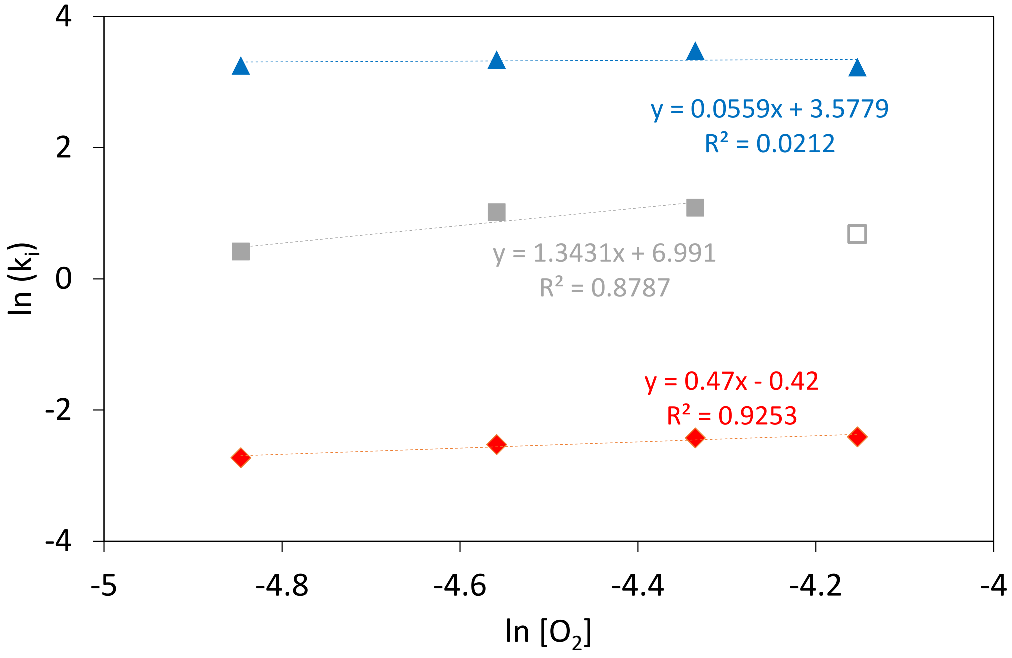

Figure 4.80. Evolution of kinetic constants with the O_2 when performing the HMF oxidation with 2 $g\cdot L^{-1}$ of Au/TiO_2 at 80 ºC with a NaOH:HMF ratio of 4:1. Legend: (■) k_1; (◆) k_2; (▲) k_3

Results indicate a more relevant effect of the oxygen in the first step of the reaction (HMFCA formation), whereas the HMFCA oxidation is less sensitive to oxygen concentration. Considering the few points available for fitting the first step (complete conversion in 1 h), the kinetic order of the second step (0.5) is considered more robust than the corresponding one for the first step (1.3 which could correspond to a real 1.5). In both cases, the oxygen adsorption and subsequent dissociation seem to be relevant, explaining these reaction orders. As suggested in the discussion of experimental results, a negligible role of oxygen in the humins formation is demonstrated. The intrinsic kinetic rate values obtained ($k_1 = 1090\ L^{1.5}\cdot mol^{-1.5}\cdot h^{-1}$; $k_2 = 0.66\ L^{0.5}\cdot mol^{-0.5}\cdot h^{-1}$; and $k_3 = 36\ L\cdot mol^{-1}\cdot h^{-1}$) are in good agreement with the literature [85, 86]. Thus, the first step is significantly faster than the second one, being promoted by NaOH (the direct comparison is not possible because of the different kinetic orders).

4.5.3. Influence of NaOH and 5-hydroxymethylfurfural concentration

Results at different pressures and temperatures suggest that longer times could improve the FDCA yield. However, longer times could increase the complexity of humins, resulting in heavy compounds insoluble even at high pH values. This fact is a potential inconvenience that discourages this option, highlighting the importance of optimizing other operating conditions that may prevent the original formation of these humins.

Strategies to reduce their formation require analyzing the effect of working at different initial HMF concentrations (in good agreement with the second reaction order of the humins formation step, reducing the HMF concentration could decrease the relative weight of their formation) or NaOH:HMF ratios (a relevant effect would suggest that humins formation is homogeneously catalyzed). The effect of the HMF concentration has been studied considering two reactions with lower initial HMF concentration (0.05 and 0.01 M) but keeping constant the NaOH:HMF ratio (4:1). This study was performed at 80 ºC and under 25 bar of O_2. Temporal profiles are detailed in **Figure 4.81**.

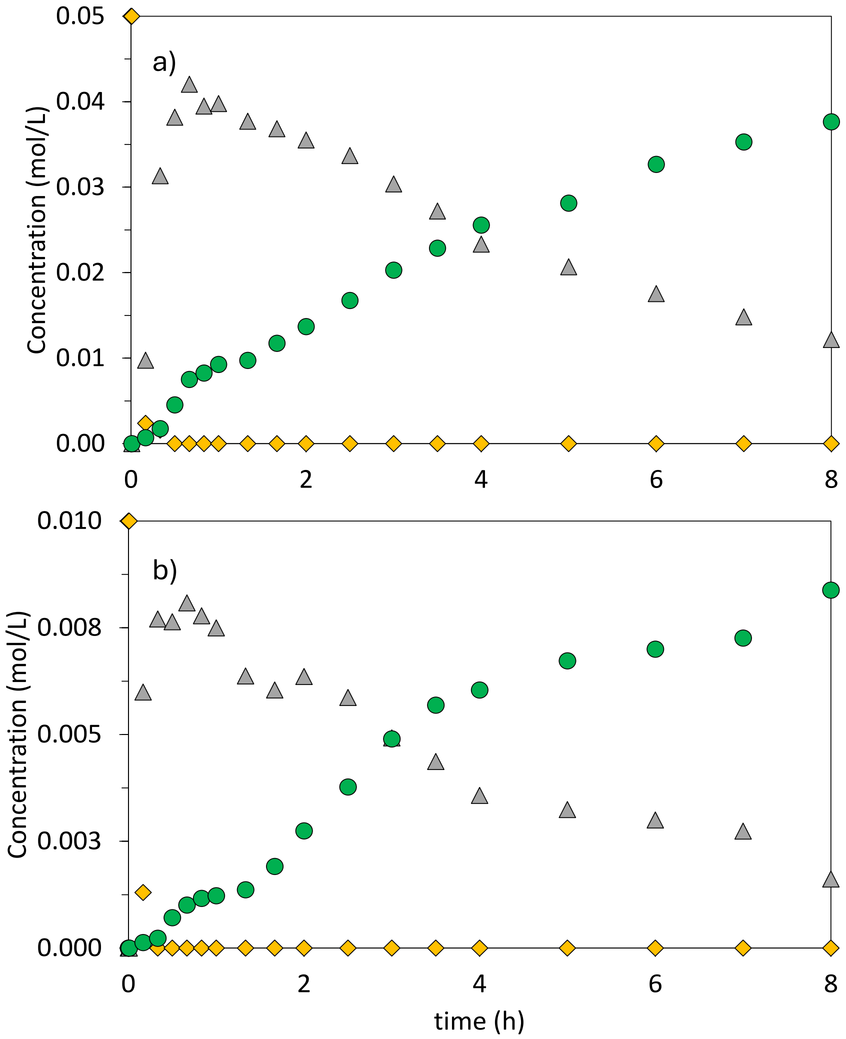

Figure 4.81. Temporal evolution of all the compounds involved in the HMF oxidation at 25 bar, 80 ºC, and 4:1 ratio NaOH:HMF as a function of HMF concentration. Legend: (a) 0.05M HMF, and (b) 0.01M HMF. Symbols: HMF (◆), HMFCA (▲), and FDCA (●)

As anticipated, total HMF conversion was reached at shorter times, after 30 and 20 minutes, respectively, times that correspond to the maximum HMFCA. Longer times are required to transform this intermediate into the FDCA, obtaining a continuous increase and final yields after 8 h of 75.3% and 83.8%, respectively, see **Figure 4.82**.

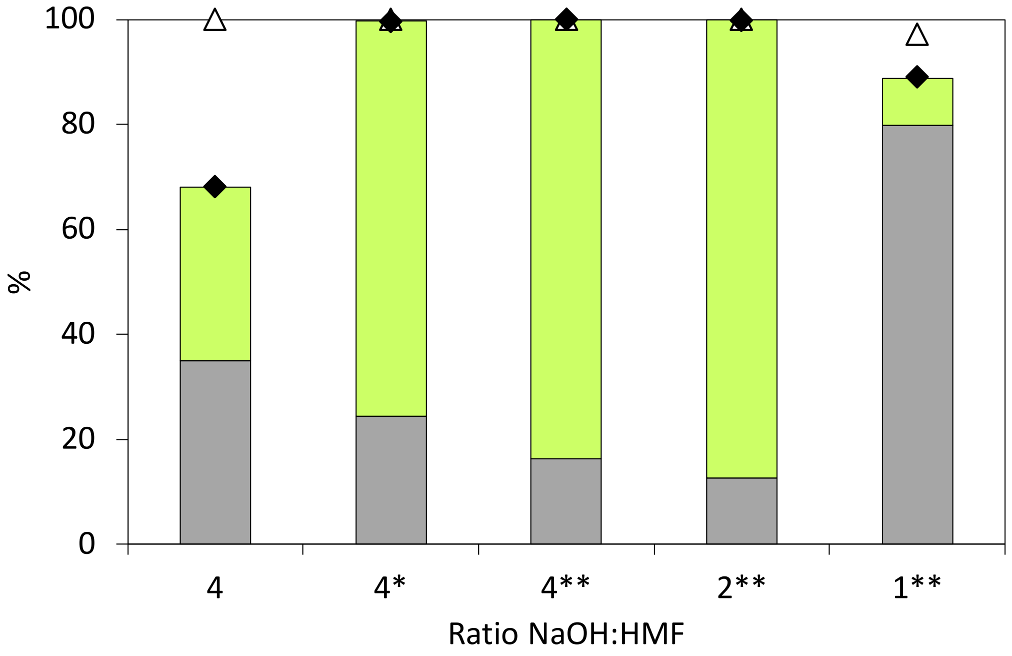

Figure 4.82. HMF conversion (△), carbon balance (◆), HMFCA selectivity (grey bars), and FDCA selectivity (green bars) obtained after 8h of HMF oxidation at 80 ºC over Au/TiO$_2$ (2 g·L^{-1}) with 25 bar of O$_2$ as a function of the NaOH:HMF ratio. (*) initial HMF concentration 0.05 M; (**) initial HMF concentration 0.01M. Base case (4): 80 ºC, 25 bar, 0.1 M of HMF and NaOH:HMF 4:1

The most relevant result of this study is the total disappearance of humins, with carbon balances higher than 99.7% during all the experiments. This fact is congruent with a predominance of oxidation over oligomerization at diluted conditions (higher oxygen/HMF ratios), promoting oxidative pathways. In the same way, lower HMF concentrations also lead to lower humins formation (second-order dependence).

Based on these results, the role of NaOH in promoting the humins is clear. However, the literature indicates that an alkaline pH is required to promote oxidation stabilizing the intermediates. Considering that the use of alkaline solutions is against the Principles of Green Chemistry because of the wastewater generated, the possibility of reducing the excess of NaOH is considered a good practice. For this study, an initial concentration of HMF of 0.01M was used, due to the maximum FDCA yield obtained with these diluted conditions. Temporal profiles working with 4:1, 2:1, and 1:1 ratios (values that correspond to initial pH of 14, 14, and 10, respectively) are plotted in **Figure 4.83**, whereas results after 8 h are summarized in Fig. 4.82 for a better comparison.

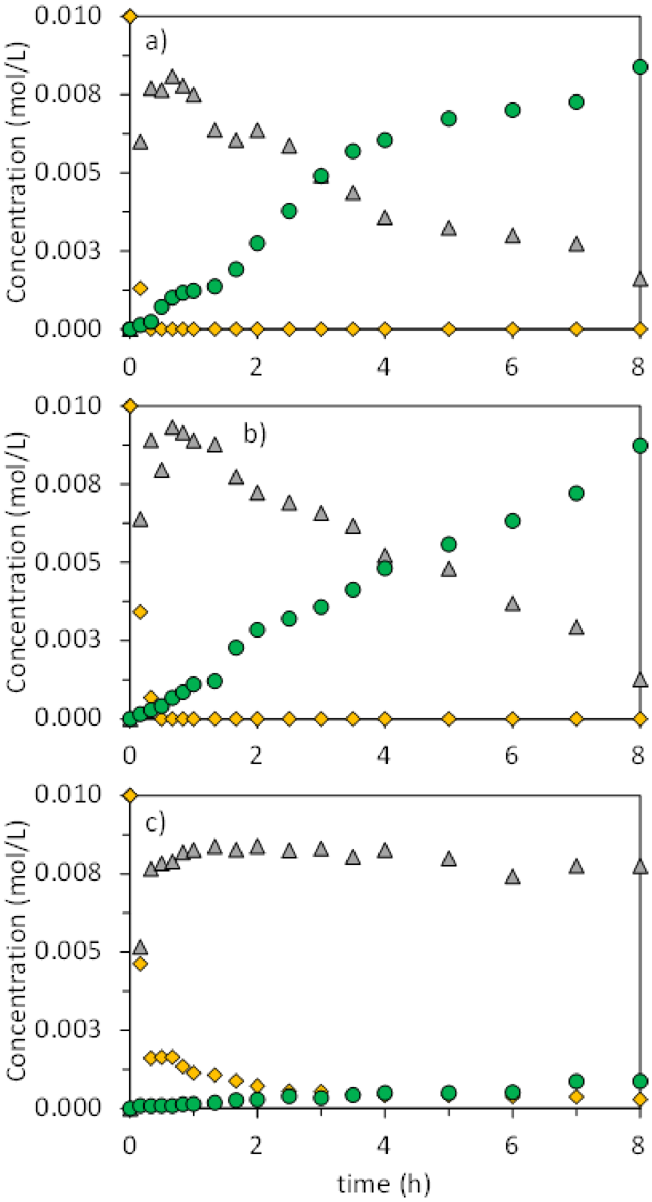

Figure 4.83. Temporal evolution of the compounds involved in the HMF oxidation as a function of NaOH concentration over Au/TiO_2 (2 g·L^{-1}) at 25 bar O_2, 80 ºC, and 0.01M HMF. Legend: (a) 0.04M, (b) 0.02M, and (c) 0.01M. Symbols: HMF (◆), HMFCA (▲), and FDCA (●)

In terms of the HMF evolution, a negligible effect of reducing the NaOH excess from 4:1 to 2:1 is observed, with total conversion in 20 minutes. However, working with equimolar amounts of both compounds significantly reduces the HMF oxidation rate, requiring more than 3h to obtain more than 90% of conversion. Even after 8h, traces of HMF are detected

(97% of conversion). HMFCA and FDCA are the only compounds detected, discarding a different mechanism because of the different pH. At 2:1 condition, the carbon balance remains close to 100% during all the reactions, and more than 87% of FDCA is reached after 8h. On the contrary, at 1:1, the low alkalinity prevails in the second oxidation step, HMFCA being the main product detected (80% after 8h). At these conditions, there is a soft but continuous decrease in the carbon balance, with final values of 89%. This result could be explained by the permanent adsorption of HMFCA or FDCA on the catalytic surface because the pH is not alkaline enough to promote their desorption.

Based on these results, 80 ºC and 25 bar of O_2, working with an initial HMF concentration of 0.01M and a NaOH:HMF ratio of 2:1 are defined as the optimal conditions when using pure HMF as a reactant. However, isolating HMF from sugar hydrolysis is quite complex because of the high HMF reactivity that promotes its rehydration into levulinic and formic acid. Considering this bottleneck, the possibility of integrating as a one-pot reaction the hydrolysis and oxidation was evaluated. It is expected that promoting the HMF oxidation limits its degradation. Obtaining good results in this approach could imply a relevant improvement in the economic feasibility of the process, considering the cost savings derived from the one-pot configuration.

4.5.4. One-pot synthesis of 2,5-furandicarboxylic from fructose

Fructose is used as the model sugar to evaluate the one-pot configuration. This sugar is present in biomass, can be obtained from cellulose through hydrolysis and inversion reactions, and is the direct precursor of HMF. There are many references analyzing the dehydration of fructose to obtain HMF, mainly using HCl as a catalyst [1, 4, 87]. Based on our previous studies, a one-pot approach is proposed considering a first step under dehydration conditions of 3 h (time at which the maximum HMF was reached) [4]. After 3h at 120 ºC under an inert atmosphere (20 bar of N_2), a solution of NaOH was added to the reaction medium to neutralize the previous acidic conditions and to reach a 2:1 theoretical ratio (based on the expected HMF concentration). In this solution, the required amount of Au/TiO_2 was suspended to guarantee the presence of Au nanoparticles required to promote the oxidation. The temperature is then decreased to 80 ºC, introducing an oxidizing atmosphere of 25 bar of O_2. The main results are summarized in **Figure 4.84**.

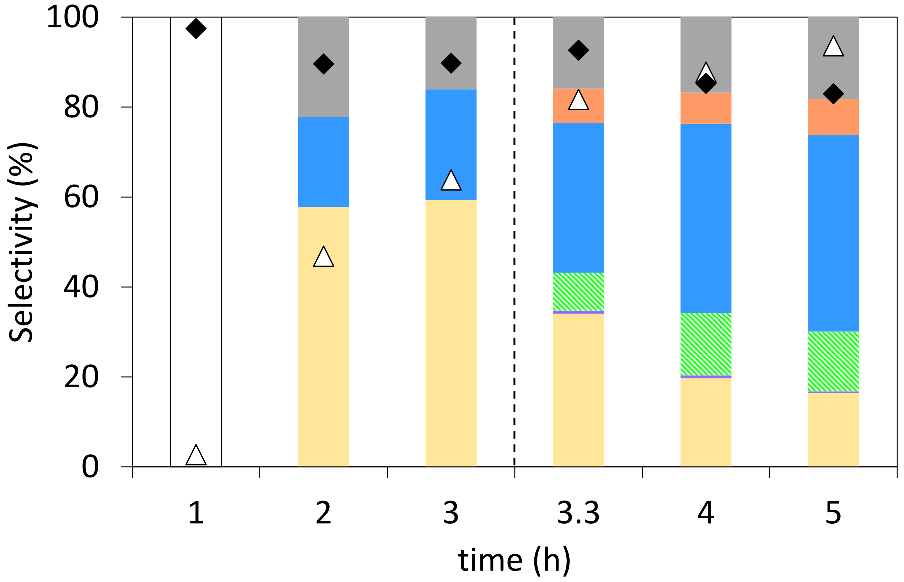

Figure 4.84. Fructose conversion (△), carbon balance (◆), and selectivity distribution of products obtained in dehydration of fructose combined with oxidation of HMF. Legend: HMF (yellow), HMFCA (purple), FDCA (dashed green), LA (blue), FA (orange), and others (grey). The broken line indicates the change from dehydration to oxidation conditions

After 1h, there is a total correspondence between fructose conversion and carbon balance closure (2.7% and 97.5%). However, no products in the liquid phase were detected, suggesting a partial fructose oligomerization. After 3 h (still under hydrolytic conditions), fructose conversion reaches 64% and HMF is obtained with more than 59% selectivity. This time was chosen to switch to oxidizing conditions since levulinic acid is already obtained with 25% of selectivity and longer times are expected to increase this value. The carbon balance at this point is 90%, which is congruent with the lack of signal of formic acid (the acid that is simultaneously produced with levulinic acid). It is suggested that this acid could be decomposed or incorporated into the sugar oligomer's structure as a part of the humins precursor.

Once under oxidizing conditions, only traces of HMFCA are observed (selectivity lower than 1% during all the reaction), but the total oxidation is observed, yielding 14% of FDCA after 4 h. Longer times do not improve this selectivity because of the formation of levulinic and formic acids, reaching up to 44% and 9%, respectively. The effect of high pH promoting levulinic acid formation has been previously reported in the literature [1].

The kinetic model proposed for HMF oxidation does predict FDCA concentration obtained in the one-pot experiment (0.014 mol/L vs. 0.012 mol/L, theoretical vs. experimental value), with quite good correspondence during all the reactions. However, relevant differences are observed when comparing expected and experimental values for HMF and HMFCA. On the one hand, the kinetic model predicts total HMF conversion, whereas experimental data demonstrate a significant HMF concentration due to the continuous incorporation of more HMF by fructose dehydration. In addition, the kinetic model predicts a stream enriched in the HMFCA intermediate, whereas this compound is negligible in the real sample. This result indicates a different interaction between the reactants (HMF and oxygen) and the catalyst, promoting the step less sensitive to the oxygen adsorbed (HMFCA oxidation to FDCA). This fact could be explained by the high salinity obtained when neutralizing the initial HCl and possible interaction with the oxidizing catalyst, by the interaction of fructose and primary derivatives with the active phase, or by a different nature of the fructose-derived humins leading to a more severe deactivation.

According to these results, the one-pot fructose hydrolysis and HMF oxidation process is feasible, but the optimum conditions proposed for HMF oxidation are not applicable in this system, requiring a particular study to maximize the FDCA yield, promoting the first oxidation step and reducing the relevance of levulinic acid production.

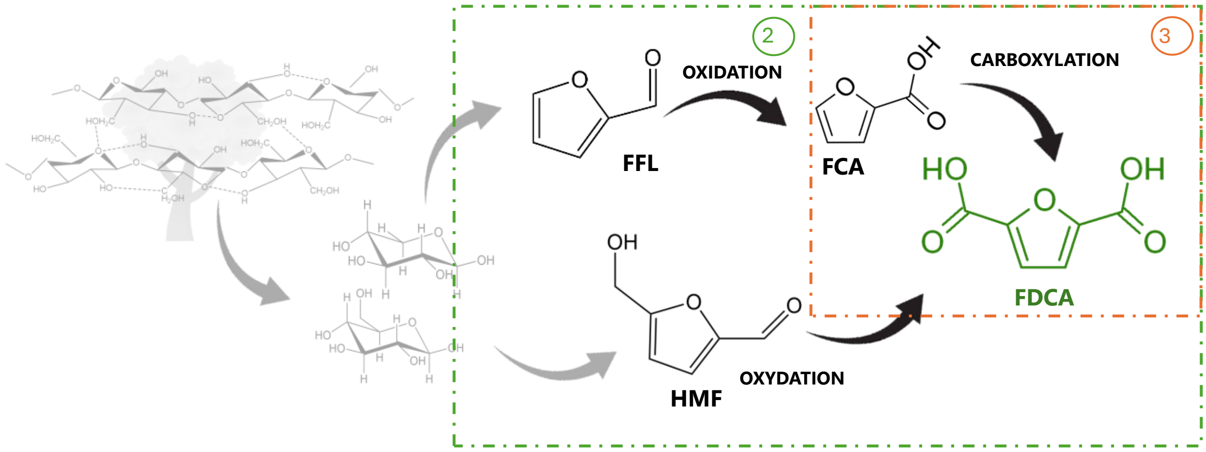

4.6. OXIDATION OF FURFURAL/5-HYDROXYMETHYLFURFURAL MIXTURES TO FURANIC ACIDS OVER AU/TIO$_2$ AND FUROIC ACID CARBOXYLATION

From the perspective of industrial implementation of lignocellulosic biomass waste utilization, the study of simultaneous FFL and HMF oxidation has a key role since both compounds are simultaneously produced by acid hydrolysis. Thus, developing an oxidation process involving both platform molecules would have a positive impact on the total system reducing the purification requirements. However, as discussed in previous sections, the optimum conditions for both oxidations are different. Thus, a new optimization is required, considering the limits due to the instability of HMF (NaOH is required to minimize humins production and other decomposition products) but conditions must be chosen to keep the complex furfural oxidation mechanism under control.

Based on these premises, the joint oxidation of both aldehydes at different NaOH ratios is studied using Au/TiO$_2$ as the catalyst at 30 bar of O$_2$. The analysis focuses on studying the possible effect on the mechanism of working with both aldehydes simultaneously. To understand the possible synergistic or inhibitory effects, preliminary analyses with individual aldehydes at those conditions not considered in previous studies are required. The analyses of the reactions are present in terms of conversion, selectivity, yield and carbon balance closure, according to equations 4.29-32.

4.6.1. Influence of NaOH concentration in individual oxidation of 5-hydroxymethylfurfural and furfural

To study the individual behavior using 1%wt Au/TiO_2 as a catalyst, oxidation experiments were carried out with 30 bar of O_2 at 80 ºC, varying the NaOH:ald. ratio between 2:1 and 4:1. These ratios were chosen, excluding the 1:1 ratio, since this lower ratio was previously tested for the oxidation of HMF as detailed in the previous chapter of this PhD Thesis. It is observed that the oxidation rate at a 1:1 ratio is significantly slower for HMF oxidation. In this case, as FFL is a much more stable compound that does not readily decompose compared to HMF, the study focused on the range between 4:1 and 2:1. Main results are summarized in **Figure 4.86**. During the oxidation of HMF, carbon mass balances above 95% are obtained regardless of the NaOH concentration. However, working with a 2:1 ratio, a 99% carbon balance is achieved and a maximum selectivity of 87% to FDCA, while working with higher concentrations of NaOH results in lower selectivity to the target compound (around 80%).

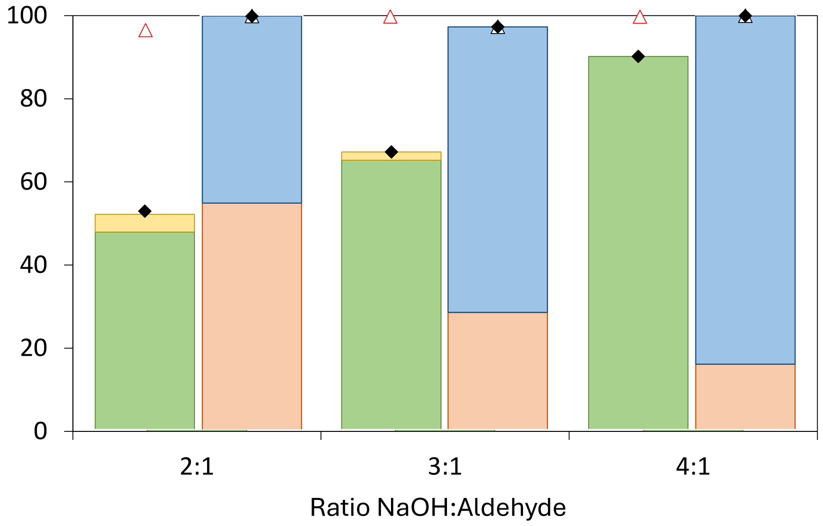

Figure 4.86. HMF conversion (△), FFL conversion (△), carbon balance (◆) and selectivity distribution (bars) obtained in the individual FFL and HMF oxidation at different NaOH:FFL ratios for Au/TiO_2 at 30 bar and 80ºC. Data corresponds to 8h reaction. Legend: HMFCA (orange) FDCA (blue) FCA (green) and FOH (yellow)

During the oxidation of HMF, carbon mass balances above 95% are obtained regardless of the NaOH concentration, defining a ratio 2:1 as the optimum conditions because of the 87% of FDCA selectivity obtained with a 99% of carbon balance.

Regarding FFL oxidation, at low NaOH concentrations (ratio 2:1) the carbon balance achieved is 52%, a value that progressively increases to 90% when working at 4:1. Contrary to the pH-controlled previously proposed configuration for the individual furfural oxidation, working at so high pH (NaOH excess) should promote a Cannizzaro mechanism in which furfural suffers disproportionation, yielding furoic acid but also furfuryl alcohol. In this case, at 2:1 ratio, furfuryl alcohol is produced with a selectivity of 4%, a selectivity that decreases as the NaOH excess increases, with a total disappearance at a 4:1 ratio. This fact is explained by not only the polymerization trend of this alcohol but also the oxidation of this alcohol into furfural, favored by basic conditions and the availability of O_2 in the medium [88]. Consequently, furoic acid is the only compound detected in the liquid phase at 4:1 ratio, but its selectivity is limited to 90% because of the humins formed derived from furfuryl alcohol.

Therefore, considering this analysis, an optimal NaOH concentration applicable to both oxidations is not found (4:1 for furfural, 2:1 for HMF), so it is necessary to conduct the study jointly by directly employing mixtures of FFL and HMF.

4.6.2. Influence of furfural and 5-hydroxymethylfurfural concentration in oxidation of mixtures

A blank test of mixtures oxidation was carried out at 80°C in an aqueous solution using initial concentrations of FFL and HMF of 0.01 M, and 0.04 M NaOH (severe conditions applied) in the absence of any catalyst. No products were detected. However, the carbon balance closure decreased to 81% after 8 hours of reaction due to uncontrolled degradation into humins of both aldehydes in an alkaline medium, as indicated by previous literature [81, 89].

To study the reaction mechanism and the possible inhibition effects due to the use of mixtures of FFL and HMF, catalytic experiments using Au/TiO_2 were performed. In these experiments, the initial concentrations of HMF and FFL varied between 0.01 and 0.02 M, reaching final FFL:HMF ratios of 1:1, 1:1.5, 1:2, and 2:1 while the concentration of NaOH is kept constant at 0.03 M, an intermediate condition between favorable ratios of the individual oxidations of HMF and FFL. Main results after 8 h of reaction are summarized in **Figure 4.87**.

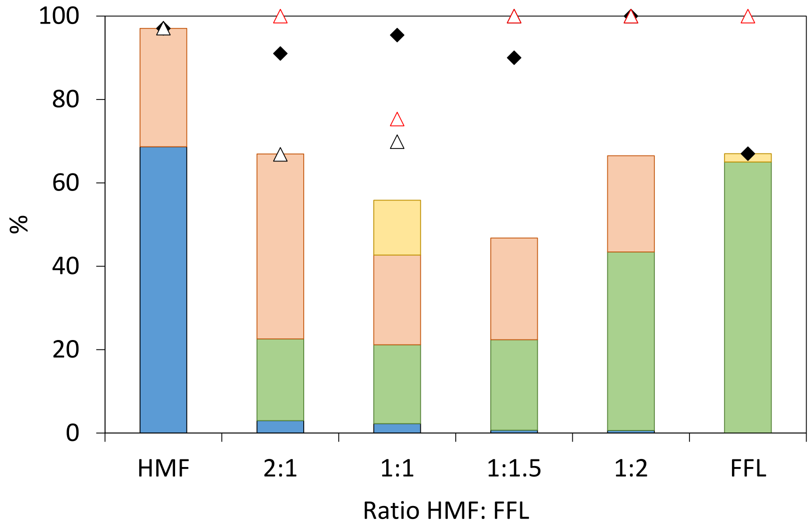

Figure 4.87. HMF conversion (△), FFL conversion (△), carbon balance (◆) and selectivity distribution (bars) obtained in the oxidation of mixtures at different HMF: FFL ratios, and individual oxidations of FFL and HMF. Legend: HMFCA (orange) FDCA (blue) FCA (green) and FOH (yellow). Data corresponds to 8h reaction, 0.03M of NaOH, 30 bar of O_2 and 80ºC

The formation of furoic acid (FCA) is inhibited by the presence of HMF. At the 1:1 ratio of HMF to FFL, the yield of FCA drops significantly from 97% to 14%, as shown in the analogous study of individual furfural oxidation in Figure 4.86. In terms of HMF oxidation, it is even more affected by the presence of FFL, resulting in conversions below 100% and a decrease in FDCA selectivity from 87% (obtained in individual oxidation of HMF) to 2% compared to previous literature and promoting the formation of undesired HFCA. Therefore, humins production decreases (higher carbon balances), suggesting that the heterogeneity of the humins precursors hinders their formation. These results suggest that the interaction of the aldehydes with the metal active sites plays a key role in the reaction rate. Results indicate the prevalence of individual reaction mechanisms previously defined for HMF and FFL oxidation. The reaction pathway considered is illustrated in **Figure 4.88**.

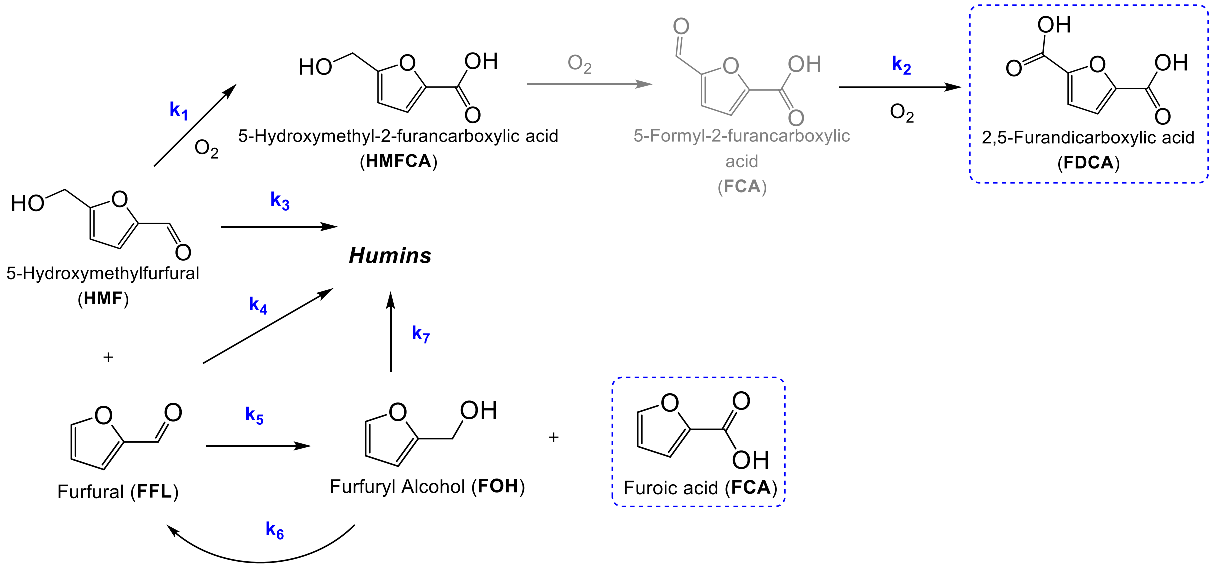

Figure 4.88. Scheme of reaction pathway for HMF and FFL mixtures oxidation in aqueous basic media

In this mechanism, humins are promoted by three different routes, involving the condensation of both reactants and the furfuryl alcohol one. This last option is suggested based on the disappearance of furfuryl alcohol at reaction conditions at which it should be theoretically produced in equimolar amount as furoic acid. Experimental results demonstrate that only furoic acid remains in the liquid phase.

The lower advance of oxidations when working with mixtures in comparison to data obtained with individual reactants suggests a competitive adsorption of both aldehydes on the same active site, aspect that could be anticipated due to their similar structure. HMF adsorption seems to prevail over FFL ones, since the furfural conversion and the production of furoic acid are more limited by the excess of HMF than the HMF oxidation compounds are when working with FFL excess. However, the presence of FFL does limit the second step of the HMF oxidation, resulting in an accumulation of the HMFCA intermediate (23% of selectivity at 1:2 HMF:FFL ratio). This intermediate does not exceed 3% when working under HMF excess conditions.

4.6.3. Influence of NaOH concentration in mixtures oxidation

Previous studies were performed working with 0.03 M of NaOH. However, as demonstrated with the individual reactions, there is not a common optimum NaOH concentration, since best results for furfural oxidation are obtained with a 0.04M NaOH concentration while for HMF oxidation the optimum NaOH concentration is 0.02M. For these studies, an HMF:FFL ratio 1:1, like the theoretical one obtained during the cellulose hydrolysis, was considered. Same studies were performed using an HMF:FFL ratio 1:2, considering the conclusions extrapolated from the studies about the influence of reactants proportions. Remarkable results are presented in **Figure 4.89**.

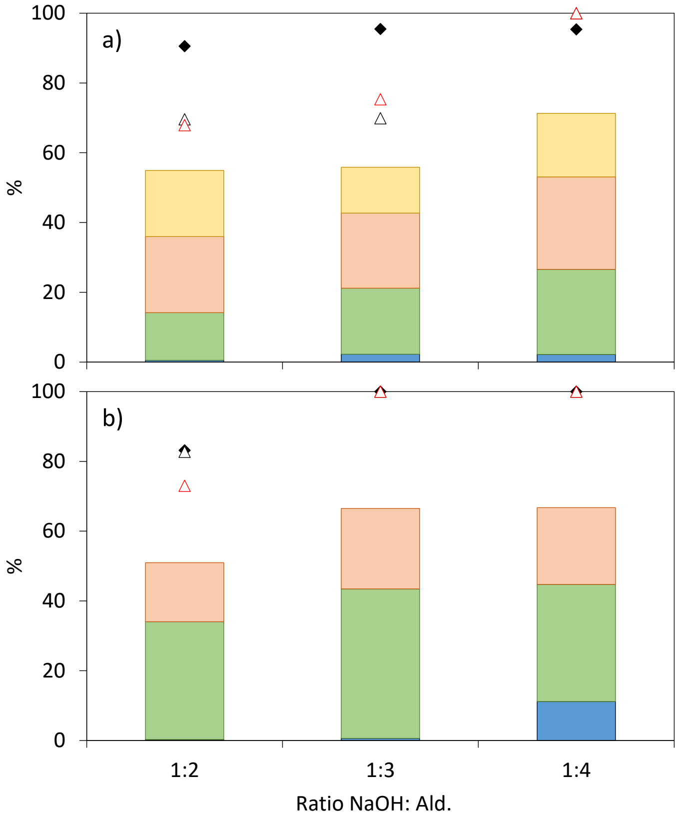

Figure 4.89. HMF conversion (△), FFL conversion (△), carbon balance (◆) and selectivity distribution (bars) obtained in the oxidation of mixtures at different NaOH concentrations. a) 1:1 ratio of HMF and FFL; b) 1:2 ratio of HMF and FFL. Legend: HMFCA (orange) FDCA (blue) FCA (green) and FOH (yellow). Data corresponds to 8h reaction at 80ºC

Focusing on oxidation of mixtures with 1:1 ratio, it is observed that an increase in the concentration of NaOH implies an increase in the selectivity of HMFCA from 22% at 0.02M to 26% at 0.04M. Also, FCA selectivity has an increasing trend obtaining a maximum selectivity (24%) at 0.04M. These results suggest that the basic medium enhances the reactants adsorption. In good agreement, furfural and HMF conversion following a increasing trend, reaching 100% in both cases when working in the most basic conditions tested. The influence of this parameter in the HMFCA oxidation (i.e. FDCA production) is not conclusive, reaching similar selectivity with 0.03 and 0.04 M of NaOH (2.2%). The basicity is also positive for the control of undesired reactions. Thus, there is a clear increasing trend in the carbon balance (higher than 90% in all cases), with the subsequent decreasing relevance of humins production.

As to results obtained with an HMF:FFL ratio 1:2, an increase in the concentration of NaOH from 0.02 to 0.03 M supposes a relative increase in HMFCA selectivity of 36%, but with a negligible amount of FDCA (~0.5%). On the contrary, the desired HMFCA oxidation is clearly observed working with 0.04 M of NaOH, reaching 11% of selectivity, and maintaining an HMFCA selectivity around 22%. An almost constant 20% of FCA is obtained with both 0.03 and 0.04 M of NaOH. At these conditions, the 100% carbon balance indicates that humins production has been totally prevented. The lack of signal related to furfuryl alcohol suggests that, at these conditions, it suffers dehydrogenation, yielding furfural instead of polymerization.

Based on these studies, a ratio 4:1:2 (NaOH:HMF:FFL) is defined as the optimum conditions to perform the oxidation of HMF and FFL mixtures. Despite the selectivities are lower than those obtained with isolate aldehydes (individual optimization), results are promising enough to consider this alternative, which could imply a relevant reduction in purification costs.

4.6.4. Carboxylation of furoic acid to 2,5-furandicarboxylic acid

The last step in the process to obtain FDCA from lignocellulose biomass concerns the furoic acid carboxylation. In should be highlighted that FDCA is directly obtained by HMF oxidation, but in the case of FFL precursor, the oxidized product needs to incorporate an extra carbon. Despite the increase in complexity that the route from furfural could need, this last step implies the incorporation of a CO_2 molecule. Thus, this step could contribute to the depletion of atmospheric CO_2, obtaining a process based on biomass with negative CO_2 emission. In addition, obtaining furfural from biomass is a more controlled process than obtaining HMF due to the higher stability of this aldehyde. Thus, this route cannot be discarded.

Considering the deep analysis of the state-of-the-art of this reaction, see introduction section, carboxylation is still far from being a realistic option in most cases, including the FDCA production. The main drawbacks of this reaction include the challenges associated with carbon capture and utilization (CCU) methods, primarily due to the high CO_2 pressure used in most of these studies. These works use pure CO_2 in conditions difficult and expensive to obtain with atmospheric CO_2. Another issue is related to the solid-gas configuration and the elevated cost of cesium, which is required to form a molten salt during the reaction, enabling ion mobility.

Based on these preliminary results already published in the literature, the experimental effort was focused on two different approaches to this step: (1) optimizing the solid-gas reaction trying to reduce the severe conditions proposed in the literature, and (2) proposing an alternative configuration in the liquid phase.

To identify the range of conditions that could be evaluated, understanding of the thermal stability and decomposition behavior of cesium furoate is crucial. The thermogravimetric decomposition of cesium furoate is illustrated in **Figure 4.90**.

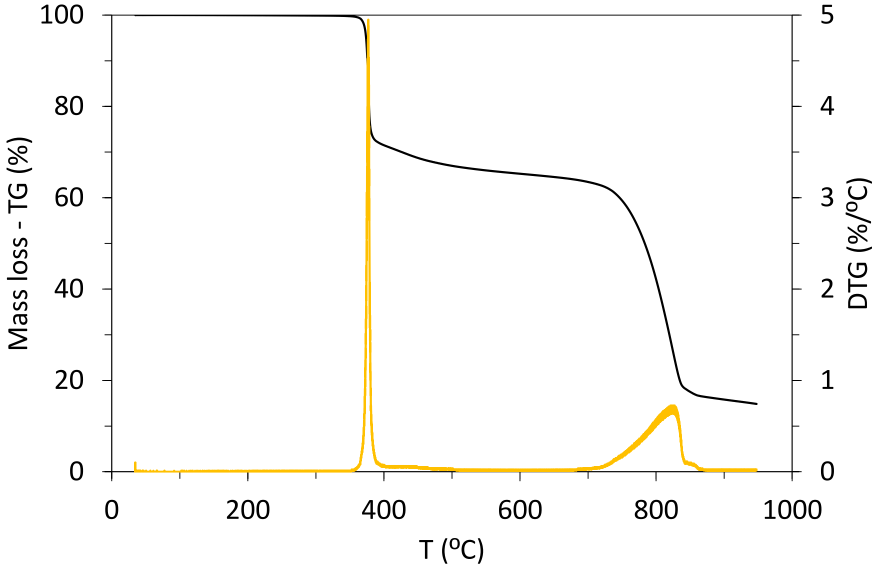

Figure 4.90. TG (black) and DTG (yellow) curves of F-Cs. DGT curve corresponds to secondary axis

The decomposition of cesium furoate under a nitrogen atmosphere reveals two significant mass loss events. The initial mass loss of 27.3% occurs at approximately 390 °C, indicating the possible release of a volatile component or a partial decomposition. This is followed by a substantial mass loss of 55.2% at a final temperature of 850 °C, ultimately leading to the formation of 17.5% ash residue. Therefore, the operating temperature for the proposed experiments is constrained by thermal stability, prompting the design of experiments at temperatures below this threshold of 390ºC. To ensure good contact between O2 and the salt, this last must be melted. This fact introduces a minimum requirement in terms of temperature, and the carboxylation must be studied over 190ºC to ensure the melting state of cesium furoate. The theoretical range (190-390ºC) can be reduced also considering sustainability aspects, trying to prevent harsh conditions that could implied too high energy consumption.

Based on these premises, the solid-gas carboxylation was studied in a temperature range 200-260ºC, working at 10 bar of CO_2 (typical experiments consider pressures up to 60 bar). In these experiments, cesium furoate (F-Cs) was used as a reactant since this salt is the only one melted at the temperature range studied. Main results obtained are summarized in **Table 4.22** considering only the final point (6h) because working in absence of a solvent hinders sampling to see the temporal evolution.

Table 4.22. Influence of reaction conditions on the conversion of F-Cs into FDCA after 6h reaction in gas-solid configuration

T(ºC)	m_o (mol)	m Cs_2CO_3 (mol)	FDCA Yield (%)
200	0.05	0.05	0.6
230	0.05	0.05	1.7
260	0.1	0.1	7

After 6 hours, a maximum 7% yield to FDCA was reached at 260ºC, whereas almost no reaction is observed at lower temperatures. This quite low selectivity is explained by two concomitant effects: on the one hand, the lower pressure, with the subsequent diffusional limitations; and, on the other hand, a possible reactant decomposition due to the heater system. This second cause is suggested based on the appearance of a black solid inside the reactor. This black solid is the reason why higher temperatures were not considered for this configuration.

Trying to prevent this decomposition and facilitate CO_2 diffusion, new experiments were performed in a liquid phase configuration. In the liquid phase, the reactant has a higher dispersion, allowing it to be more accessible to CO_2, which helps mitigate diffusion-related issues. Additionally, the presence of a solvent ensures uniform heat transfer throughout the medium, preventing the formation of localized "hot spots" that can lead to unwanted decomposition reactants. This uniform heat distribution is crucial for maintaining reaction stability and optimizing product selectivity. Working in a liquid phase configuration removes the minimum temperature limitation due to the melting salt, allowing working in more sustainable conditions.

The selection of solvents for carboxylation, specifically DMSO, is based on its ability to ensure high solubility for FDCA and its thermal stability (corroborated by the absence of decomposition signals in the GC). Additionally, water is used in binary systems as it enhances the solubility of cesium furoate, thereby ensuring that the main compounds remain soluble throughout the process. This combination of DMSO and water thus supports both the thermal and solubility requirements necessary for effective carboxylation reactions. Main experimental results are summarized in **Table 4.23**.

Table 4.23. Influence of reaction conditions on FDCA yield after 6h reaction in liquid phase reactions

Reactant	Solvent	T(ºC)	Co (mol/L)	C Cs_2CO_3 (mol/L)	FDCA Yield (%)
FCA	$DMSO/H_2O$	170	0.2	0.4	0
F-Cs	$DMSO/H_2O$	170	0.2	0.2	1.4
$Cu(F)_2$	$DMSO/H_2O$	170	0.2	0.4	0
F-Cs	DMSO	170	0.2	0.2	0
F-Cs	DMSO	200	0.2	0.2	0

An initial experiment was proposed using FCA as the reactant and cesium carbonate in a 1:2 ratio. This configuration is justified since the melting salt (F-Cs) is expected to be not needed since in the aqueous phase the FCA will be always as a furoate. Experimental results discard this approach, not observing any FDCA after 6 h at 170ºC, and demonstrate the crucial role of the alkaline metal in this process, previously suggested in the literature for solid-gas configurations, where Cs is identified as essential to activate the CO_2 and stabile the reaction intermediates [90].

A second approach considered the same system but using F-Cs as a reactant. Results after 6h demonstrate a low but quantifiable activity, with 1.4% of FDCA yield. Trying to reduce the Cs consumption (very expensive reactant), a new approach considering the cupper salt ($Cu(F)_2$) but keeping the Cs_2CO_3 in the medium was performed, but no FDCA was produced. The higher activity of Cs over the Cu one was demonstrated, concluding that, at least at working conditions, doing without Cs is not viable.

The literature also suggests that water can play a negative role in carboxylations. Next studies were focused on analyzing the behavior of DMSO without the aqueous solvent. As in previous cases, no quantitative results were obtained, in this case being assumed to be due to the low solubility of FCA in the solvent.

These preliminary results are far from being optimized and indicate that there is a big space for studying and improving in this step of the process. Results obtained in the solid-gas phase configuration are aligned with the literature (considering the lower pressure and temperatures used in this work) but the liquid phase configuration requires deeper analysis and more research. However, results obtained with F-Cs and the binary system DMSO/water at 170ºC suggest that this configuration is feasible.

4.7. REFERENCES

[1] D. Garcés, L. Faba, E. Díaz, S. Ordóñez, Aqueous-Phase Transformation of Glucose into Hydroxymethylfurfural and Levulinic Acid by Combining Homogeneous and Heterogeneous Catalysis. *ChemSusChem* **2019** (12*)* 924-934. https://doi.org/10.1002/cssc.201802315

[2] L. Faba, D. Garcés, E. Díaz, S. Ordóñez, Carbon Materials as Phase-Transfer Promoters for Obtaining 5-Hydroxymethylfurfural from Cellulose in a Biphasic System. *ChemSusChem* **2019** (12*)* 3769-3777. https://doi.org/10.1002/cssc.201901264

[3] A. Toftgaard Pedersen, R. Ringborg, T. Grotkjær, S. Pedersen, J.M. Woodley, Synthesis of 5-hydroxymethylfurfural (HMF) by acid catalyzed dehydration of glucose–fructose mixtures. *Chemical Engineering Journal* **2015** (273*)* 455-464. https://doi.org/10.1016/j.cej.2015.03.094

[4] D. Garcés, E. Díaz, S. Ordóñez, Aqueous Phase Conversion of Hexoses into 5-Hydroxymethylfurfural and Levulinic Acid in the Presence of Hydrochloric Acid: Mechanism and Kinetics. *Industrial & Engineering Chemistry Research* **2017** (56*)* 5221-5230. https://doi.org/10.1021/acs.iecr.7b00952

[5] M. Ohara, A. Takagaki, S. Nishimura, K. Ebitani, Syntheses of 5-hydroxymethylfurfural and levoglucosan by selective dehydration of glucose using solid acid and base catalysts. *Applied Catalysis A: General* **2010** (383*)* 149-155. https://doi.org/10.1016/j.apcata.2010.05.040

[6] V. Choudhary, R.I. Burnett, D.G. Vlachos, S.I. Sandler, Dehydration of Glucose to 5-(Hydroxymethyl)furfural and Anhydroglucose: Thermodynamic Insights. *The Journal of Physical Chemistry C* **2012** (116*)* 5116-5120. https://doi.org/10.1021/jp2113895

[7] B. Girisuta, L.P.B.M. Janssen, H.J. Heeres, Kinetic Study on the Acid-Catalyzed Hydrolysis of Cellulose to Levulinic Acid. *Industrial & Engineering Chemistry Research* **2007** (46*)* 1696-1708. https://doi.org/10.1021/ie061186z

[8] J. Fan, M. De bruyn, V.L. Budarin, M.J. Gronnow, P.S. Shuttleworth, S. Breeden, D.J. Macquarrie, J.H. Clark, Direct Microwave-Assisted Hydrothermal Depolymerization of Cellulose. *Journal of the American Chemical Society* **2013** (135*)* 11728-11731. https://doi.org/10.1021/ja4056273

[9] S.S. Chen, I.K.M. Yu, D.C.W. Tsang, A.C.K. Yip, E. Khan, L. Wang, Y.S. Ok, C.S. Poon, Valorization of cellulosic food waste into levulinic acid catalyzed by heterogeneous Brønsted

acids: Temperature and solvent effects. *Chemical Engineering Journal* **2017** (327*)* 328-335. https://doi.org/10.1016/j.cej.2017.06.108

[10] D.H. Fockink, J.H. Sánchez, L.P. Ramos, Comprehensive analysis of sugarcane bagasse steam explosion using autocatalysis and dilute acid hydrolysis (H3PO4 and H2SO4) at equivalent combined severity factors. *Industrial Crops and Products* **2018** (123*)* 563-572. https://doi.org/10.1016/j.indcrop.2018.07.017

[11] G. Gliozzi, A. Innorta, A. Mancini, R. Bortolo, C. Perego, M. Ricci, F. Cavani, Zr/P/O catalyst for the direct acid chemo-hydrolysis of non-pretreated microcrystalline cellulose and softwood sawdust. *Applied Catalysis B: Environmental* **2014** (145*)* 24-33. https://doi.org/10.1016/j.apcatb.2012.12.035

[12] Z. Wen, L. Yu, F. Mai, Z. Ma, H. Chen, Y. Li, Catalytic Conversion of Microcrystalline Cellulose to Glucose and 5-Hydroxymethylfurfural over a Niobic Acid Catalyst. *Industrial & Engineering Chemistry Research* **2019** (58*)* 17675-17681. https://doi.org/10.1021/acs.iecr.9b03824

[13] N.V. Gromov, O.L. Ogorodnikova, T.B. Medvedeva, V.N. Panchenko, I.S. Yakovleva, L.A. Isupova, M.N. Timofeeva, O.P. Taran, C. Aymonier, V.N. Parmon, Hydrolysis–Dehydration of Cellulose: Efficiency of NbZr Catalysts under Batch and Flow Conditions. *Catalysts* **2023** (13*)* 9. https://doi.org/10.3390/catal13091298

[14] A.D. French, Idealized powder diffraction patterns for cellulose polymorphs. *Cellulose* **2014** (21*)* 885-896. https://doi.org/10.1007/s10570-013-0030-4

[15] L. Zhang, G. Xi, Z. Chen, D. Jiang, H. Yu, X. Wang, Highly selective conversion of glucose into furfural over modified zeolites. *Chemical Engineering Journal* **2017** (307*)* 868-876. https://doi.org/10.1016/j.cej.2016.09.001

[16] T. Istasse, A. Richel, Mechanistic aspects of saccharide dehydration to furan derivatives for reaction media design. *RSC Advances* **2020** (10*)* 23720-23742. https://doi.org/10.1039/D0RA03892J

[17] J. Gong, J. Li, J. Xu, Z. Xiang, L. Mo, Research on cellulose nanocrystals produced from cellulose sources with various polymorphs. *RSC Advances* **2017** (7*)* 33486-33493. https://doi.org/10.1039/C7RA06222B

[18] Y. Yao, S. Chen, M. Zhang, Sustainable Approaches to Selective Conversion of Cellulose Into 5-Hydroxymethylfurfural Promoted by Heterogeneous Acid Catalysts: A Review. *Frontiers in Chemistry* **2022** (10*)*. https://doi.org/10.3389/fchem.2022.880603

[19] A.A. Rosatella, S.P. Simeonov, R.F.M. Frade, C.A.M. Afonso, 5-Hydroxymethylfurfural (HMF) as a building block platform: Biological properties, synthesis and synthetic applications. *Green Chemistry* **2011** (13*)* 754-793. https://doi.org/10.1039/C0GC00401D

[20] S.S. Chen, L. Wang, I.K.M. Yu, D.C.W. Tsang, A.J. Hunt, F. Jérôme, S. Zhang, Y.S. Ok, C.S. Poon, Valorization of lignocellulosic fibres of paper waste into levulinic acid using solid and aqueous Brønsted acid. *Bioresource Technology* **2018** (247*)* 387-394. https://doi.org/10.1016/j.biortech.2017.09.110

[21] J. Kluska, M. Ochnio, D. Kardaś, Ł. Heda, The influence of temperature on the physicochemical properties of products of pyrolysis of leather-tannery waste. *Waste Management* **2019** (88*)* 248-256. https://doi.org/10.1016/j.wasman.2019.03.046

[22] K. Giannakopoulou, M. Lukas, A. Vasiliev, C. Brunner, H. Schnitzer, Conversion of rapeseed cake into bio-fuel in a batch reactor: Effect of catalytic vapor upgrading. *Microporous and Mesoporous Materials* **2010** (128*)* 126-135. https://doi.org/10.1016/j.micromeso.2009.08.022

[23] F. Cotana, G. Cavalaglio, M. Gelosia, A. Nicolini, V. Coccia, A. Petrozzi, Production of bioethanol in a second generation prototype from pine wood chips. *Energy Procedia* **2014** (45*)* 42-51. https://doi.org/10.1016/j.egypro.2014.01.006

[24] P.N. Trisant, I. Gunardi, Sumarno, The Influence of Hydrolysis Time in Hydrothermal Process of Cellulose from Sengon Wood Sawdust. *Macromol. Symp.* **2020** (391*)* 2000016. https://doi.org/10.1002/masy.202000016

[25] S. Van den Bosch, W. Schutyser, R. Vanholme, T. Driessen, S.F. Koelewijn, T. Renders, B. De Meester, W.J.J. Huijgen, W. Dehaen, C.M. Courtin, B. Lagrain, W. Boerjan, B.F. Sels, Reductive lignocellulose fractionation into soluble lignin-derived phenolic monomers and dimers and processable carbohydrate pulps. *Energy & Environmental Science* **2015** (8*)* 1748-1763. https://doi.org/10.1039/C5EE00204D

[26] C.A. Hubbell, A.J. Ragauskas, Effect of acid-chlorite delignification on cellulose degree of polymerization. *Bioresource Technology* **2010** (101*)* 7410-7415. https://doi.org/10.1016/j.biortech.2010.04.029

[27] J. Shen, S. Zhu, X. Liu, H. Zhang, J. Tan, The prediction of elemental composition of biomass based on proximate analysis. *Energy Conversion and Management* **2010** (51*)* 983-987. https://doi.org/10.1016/j.enconman.2009.11.039

[28] A.A. Marianou, C.M. Michailof, A. Pineda, E.F. Iliopoulou, K.S. Triantafyllidis, A.A. Lappas, Effect of Lewis and Brønsted acidity on glucose conversion to 5-HMF and lactic acid in aqueous and organic media. *Applied Catalysis A: General* **2018** (555*)* 75-87. https://doi.org/10.1016/j.apcata.2018.01.029

[29] G. Yang, E.A. Pidko, E.J.M. Hensen, Mechanism of Brønsted acid-catalyzed conversion of carbohydrates. *Journal of Catalysis* **2012** (295*)* 122-132. https://doi.org/10.1016/j.jcat.2012.08.002

[30] M. Sarno, M. Iuliano, S. De Pasquale, E. Ponticorvo, A new nano-catalyst for sawdust hydrolysis. *Applied Catalysis A: General* **2020** (602*)* 117686. https://doi.org/10.1016/j.apcata.2020.117686

[31] N.M. Clauser, F.E. Felissia, M.C. Area, M.E. Vallejos, S. Gutiérrez, An energy-saving re-use strategy for the treatment of lignocellulosic biomass applied to the production of levulinc acid. *Journal of Cleaner Production* **2020** (257*)* 120549. https://doi.org/10.1016/j.jclepro.2020.120549

[32] A. Kruse, A. Gawlik, Biomass Conversion in Water at 330−410 °C and 30−50 MPa. Identification of Key Compounds for Indicating Different Chemical Reaction Pathways. *Industrial & Engineering Chemistry Research* **2003** (42*)* 267-279. https://doi.org/10.1021/ie0202773

[33] S.S. Toor, L. Rosendahl, A. Rudolf, Hydrothermal liquefaction of biomass: A review of subcritical water technologies. *Energy* **2011** (36*)* 2328-2342. https://doi.org/10.1016/j.energy.2011.03.013

[34] I. Van Zandvoort, Y. Wang, C.B. Rasrendra, E.R.H. van Eck, P.C.A. Bruijnincx, H.J. Heeres, B.M. Weckhuysen, Formation, Molecular Structure, and Morphology of Humins in Biomass Conversion: Influence of Feedstock and Processing Conditions. *ChemSusChem* **2013** (6*)* 1745-1758. https://doi.org/10.1002/cssc.201300332

[35] S.K.R. Patil, J. Heltzel, C.R.F. Lund, Comparison of Structural Features of Humins Formed Catalytically from Glucose, Fructose, and 5-Hydroxymethylfurfuraldehyde. *Energy & Fuels* **2012** (26*)* 5281-5293. https://doi.org/10.1021/ef3007454

[36] T. Rogalinski, T. Ingram, G. Brunner, Hydrolysis of lignocellulosic biomass in water under elevated temperatures and pressures. *The Journal of Supercritical Fluids* **2008** (47*)* 54-63. https://doi.org/10.1016/j.supflu.2008.05.003

[37] J.-W. Lee, T.W. Jeffries, Efficiencies of acid catalysts in the hydrolysis of lignocellulosic biomass over a range of combined severity factors. *Bioresource Technology* **2011** (102*)* 5884-5890. https://doi.org/10.1016/j.biortech.2011.02.048

[38] A. Rodríguez-Chong, J. Alberto Ramírez, G. Garrote, M. Vázquez, Hydrolysis of sugar cane bagasse using nitric acid: a kinetic assessment. *Journal of Food Engineering* **2004** (61*)* 143-152. https://doi.org/10.1016/S0260-8774(03)00080-3

[39] T. Tsoutsos, D. Bethanis, Optimization of the dilute acid hydrolyzator for cellulose-to-bioethanol saccharification. *Energies* **2011** (4*)* 1601-1623. https://doi.org/10.3390/en4101601

[40] X. Li, X. Lan, T. Wang, Selective oxidation of furfural in a bi-phasic system with homogeneous acid catalyst. *Catalysis Today* **2016** (276*)* 97-104. https://doi.org/10.1016/j.cattod.2015.11.036

[41] C.M. Pichler, M.G. Al-Shaal, D. Gu, H. Joshi, W. Ciptonugroho, F. Schüth, Ruthenium Supported on High-Surface-Area Zirconia as an Efficient Catalyst for the Base-Free Oxidation of 5-Hydroxymethylfurfural to 2,5-Furandicarboxylic Acid. *ChemSusChem* **2018** (11*)* 2083-2090. https://doi.org/10.1002/cssc.201800448

[42] N. Alonso-Fagúndez, I. Agirrezabal-Telleria, P.L. Arias, J.L.G. Fierro, R. Mariscal, M.L. Granados, Aqueous-phase catalytic oxidation of furfural with H2O2: high yield of maleic acid by using titanium silicalite-1. *RSC Advances* **2014** (4*)* 54960-54972. https://doi.org/10.1039/C4RA11563E

[43] M.A. Hasnat, M.M. Rahman, S.M. Borhanuddin, A. Siddiqua, N.M. Bahadur, M.R. Karim, Efficient hydrogen peroxide decomposition on bimetallic Pt–Pd surfaces. *Catalysis Communications* **2010** (12*)* 286-291. https://doi.org/10.1016/j.catcom.2010.10.001

[44] H. Yang, T. Zhang, H. Tian, J. Tang, D. Xu, W. Yang, L. Lin, Effect of Sr Substitution on Catalytic Activity of La1-XSrxMnO3 (0≤x≤0.8) Perovskite-Type Oxides for Catalytic Decomposition of Hydrogen Peroxide. *Reaction Kinetics and Catalysis Letters* **2001** (73*)* 311-316. https://doi.org/10.1023/A:1014115508872

[45] B. Geng, S. Zhang, X. Yang, W. Shi, P. Li, D. Pan, L. Shen, Cu2-xO@TiO2-y Z-scheme heterojunctions for sonodynamic-chemodynamic combined tumor eradication. *Chemical Engineering Journal* **2022** (435*)* 134777. https://doi.org/10.1016/j.cej.2022.134777

[46] C.P. Ferraz, S. Navarro-Jaén, L.M. Rossi, F. Dumeignil, M.N. Ghazzal, R. Wojcieszak, Enhancing the activity of gold supported catalysts by oxide coating: towards efficient oxidations. *Green Chemistry* **2021** (23*)* 8453-8457. https://doi.org/10.1039/D1GC02889H

[47] G. Chen, D. Hong, H. Xia, W. Sun, S. Shao, B. Gong, S. Wang, J. Wu, X. Wang, Q. Dai, Amorphous and homogeneously Zr-doped MnOx with enhanced acid and redox properties for catalytic oxidation of 1,2-Dichloroethane. *Chemical Engineering Journal* **2022** (428*)* 131067. https://doi.org/10.1016/j.cej.2021.131067

[48] C. Jiménez-Sanchidrián, J.R. Ruiz, The Baeyer–Villiger reaction on heterogeneous catalysts. *Tetrahedron* **2008** (64*)* 2011-2026. https://doi.org/10.1016/j.tet.2007.11.024

[49] D. Zhao, T. Su, Y. Wang, R.S. Varma, C. Len, Recent advances in catalytic oxidation of 5-hydroxymethylfurfural. *Molecular Catalysis* **2020** (495*)* 111133. https://doi.org/10.1016/j.mcat.2020.111133

[50] G. Papanikolaou, P. Lanzafame, S. Perathoner, G. Centi, D. Cozza, G. Giorgianni, M. Migliori, G. Giordano, High performance of Au/ZTC based catalysts for the selective oxidation of bio-derivative furfural to 2-furoic acid11This paper in honor of Professor James G. Goodwin, Jr., in the occasion of his 75th birthday, to celebrate his outstanding contribution to catalysis sciences and technology. *Catalysis Communications* **2021** (149*)* 106234. https://doi.org/10.1016/j.catcom.2020.106234

[51] R. Ciriminna, L. Albanese, F. Meneguzzo, M. Pagliaro, Hydrogen Peroxide: A Key Chemical for Today's Sustainable Development. *ChemSusChem* **2016** (9*)* 3374-3381. https://doi.org/10.1002/cssc.201600895

[52] D.Y. Murzin, E. Bertrand, P. Tolvanen, S. Devyatkov, J. Rahkila, K. Eränen, J. Wärnå, T. Salmi, Heterogeneous Catalytic Oxidation of Furfural with Hydrogen Peroxide over Sulfated Zirconia. *Industrial & Engineering Chemistry Research* **2020** (59*)* 13516-13527. https://doi.org/10.1021/acs.iecr.0c02566

[53] F. Saleem, P. Müller, K. Eränen, J. Warnå, D. Yu Murzin, T. Salmi, Kinetics and modelling of furfural oxidation with hydrogen peroxide over a fibrous heterogeneous catalyst: effect of reaction parameters on yields of succinic acid. *Journal of Chemical Technology & Biotechnology* **2017** (92*)* 2206-2220. https://doi.org/10.1002/jctb.5248

[54] H. Kumar, M.W. Fraaije, Conversion of Furans by Baeyer-Villiger Monooxygenases. *Catalysts* **2017** (7*)* 6. https://doi.org/10.3390/catal7060179

[55] J. Luo, H. Yuan, H. Liu, J. Li, Y. Wang, Y. Wang, J. Yao, H. Li, One-pot Baeyer–Villiger oxidation of cyclohexanone with in situ generated hydrogen peroxide over Sn-Beta zeolites. *Green Chemical Engineering* **2021** (2*)* 294-300. https://doi.org/10.1016/j.gce.2021.03.003

[56] M. Douthwaite, X. Huang, S. Iqbal, P.J. Miedziak, G.L. Brett, S.A. Kondrat, J.K. Edwards, M. Sankar, D.W. Knight, D. Bethell, G.J. Hutchings, The controlled catalytic oxidation of furfural to furoic acid using AuPd/Mg(OH)2. *Catalysis Science & Technology* **2017** (7*)* 5284-5293. https://doi.org/10.1039/C7CY01025G

[57] C. Jiménez-Sanchidrián, J.M. Hidalgo, R. Llamas, J.R. Ruiz, Baeyer–Villiger oxidation of cyclohexanone with hydrogen peroxide/benzonitrile over hydrotalcites as catalysts. *Applied Catalysis A: General* **2006** (312*)* 86-94. https://doi.org/10.1016/j.apcata.2006.06.031

[58] E. Kertalli, J.C. Schouten, T.A. Nijhuis, Effect of hydrogen and propylene on the hydrogen peroxide decomposition over Pt, PtO and Au catalysts. *Applied Catalysis A: General* **2017** (538*)* 131-138. https://doi.org/10.1016/j.apcata.2017.03.023

[59] L.A. García-Contreras, J.O. Flores-Flores, J.Á. Arenas-Alatorre, J.Á. Chávez-Carvayar, Synthesis, characterization and study of the structural change of nanobelts of TiO2 (H2Ti3O7) to nanobelts with anatase, brookite and rutile phases. *Journal of Alloys and Compounds* **2022** (923*)* 166236. https://doi.org/10.1016/j.jallcom.2022.166236

[60] V. Collins-Martínez, A. López Ortiz, A. Aguilar Elguézabal, Influence of the Anatase/Rutile Ratio on the TiO2 Photocatalytic Activity for the Photodegradation of Light Hydrocarbons. *International Journal of Chemical Reactor Engineering* **2007** (5*)*. https://doi.org/10.2202/1542-6580.1613

[61] A.G. Ilie, M. Scarisoareanu, I. Morjan, E. Dutu, M. Badiceanu, I. Mihailescu, Principal component analysis of Raman spectra for TiO2 nanoparticle characterization. *Applied Surface Science* **2017** (417*)* 93-103. https://doi.org/10.1016/j.apsusc.2017.01.193

[62] A. Banerjee, G.R. Dick, T. Yoshino, M.W. Kanan, Carbon dioxide utilization via carbonate-promoted C–H carboxylation. *Nature* **2016** (531*)* 215-219. https://doi.org/10.1038/nature17185

[63] J.-D. Grunwaldt, M. Maciejewski, O.S. Becker, P. Fabrizioli, A. Baiker, Comparative Study of Au/TiO2 and Au/ZrO2 Catalysts for Low-Temperature CO Oxidation. *Journal of Catalysis* **1999** (186*)* 458-469. https://doi.org/10.1006/jcat.1999.2564

[64] Y. Wang, D. Widmann, M. Heenemann, T. Diemant, J. Biskupek, R. Schlögl, R.J. Behm, The role of electronic metal-support interactions and its temperature dependence: CO adsorption and CO oxidation on Au/TiO2 catalysts in the presence of TiO2 bulk defects. *Journal of Catalysis* **2017** (354*)* 46-60. https://doi.org/10.1016/j.jcat.2017.07.029

[65] Z. Ren, Y. Yang, S. Wang, X. Li, H. Feng, L. Wang, Y. Li, X. Zhang, M. Wei, Pt atomic clusters catalysts with local charge transfer towards selective oxidation of furfural. *Applied Catalysis B: Environmental* **2021** (295*)* 120290. https://doi.org/10.1016/j.apcatb.2021.120290

[66] A.S.K. Hashmi, Gold-Catalyzed Organic Reactions. *Chemical Reviews* **2007** (107*)* 3180-3211. https://doi.org/10.1021/cr000436x

[67] A. Sadier, S. Paul, R. Wojcieszak, Selective Oxidation of Furfural at Room Temperature on a TiO2-Supported Ag Catalyst. *Catalysts* **2022** (12*)* 8. https://doi.org/10.3390/catal12080805

[68] C.P. Ferraz, M.A.S. Garcia, É. Teixeira-Neto, L.M. Rossi, Oxidation of benzyl alcohol catalyzed by gold nanoparticles under alkaline conditions: weak vs. strong bases. *RSC Advances* **2016** (6*)* 25279-25285. https://doi.org/10.1039/C6RA01795A

[69] F. Nocito, N. Ditaranto, D. Linsalata, M. Naschetti, R. Comparelli, M. Aresta, A. Dibenedetto, Selective Aerobic Oxidation of Furfural into Furoic Acid over a Highly Recyclable MnO2@CeO2 Core–Shell Oxide: The Role of the Morphology of the Catalyst. *ACS Sustainable Chemistry & Engineering* **2022** (10*)* 8615-8623. https://doi.org/10.1021/acssuschemeng.2c02341

[70] A. Roselli, Y. Carvalho, F. Dumeignil, F. Cavani, S. Paul, R. Wojcieszak, Liquid Phase Furfural Oxidation under Uncontrolled pH in Batch and Flow Conditions: The Role of In Situ Formed Base. *Catalysts* **2020** (10*)* 1. https://doi.org/10.3390/catal10010073

[71] C.P. Ferraz, M. Zieliński, M. Pietrowski, S. Heyte, F. Dumeignil, L.M. Rossi, R. Wojcieszak, Influence of Support Basic Sites in Green Oxidation of Biobased Substrates Using Au-Promoted Catalysts. *ACS Sustainable Chemistry & Engineering* **2018** (6*)* 16332-16340. https://doi.org/10.1021/acssuschemeng.8b03330

[72] C. P. Ferraz, N.J.S. Costa, E. Teixeira-Neto, Â.A. Teixeira-Neto, C.W. Liria, J. Thuriot-Roukos, M.T. Machini, R. Froidevaux, F. Dumeignil, L.M. Rossi, R. Wojcieszak, 5-Hydroxymethylfurfural and Furfural Base-Free Oxidation over AuPd Embedded Bimetallic Nanoparticles. *Catalysts* **2020** (10*)* 1. https://doi.org/10.3390/catal10010075

[73] V.P. Santos, S.A.C. Carabineiro, P.B. Tavares, M.F.R. Pereira, J.J.M. Órfão, J.L. Figueiredo, Oxidation of CO, ethanol and toluene over TiO2 supported noble metal catalysts. *Applied Catalysis B: Environmental* **2010** (99*)* 198-205. https://doi.org/10.1016/j.apcatb.2010.06.020

[74] H. Shen, H. Shan, L. Liu, Evolution Process and Controlled Synthesis of Humins with 5-Hydroxymethylfurfural (HMF) as Model Molecule. *ChemSusChem* **2020** (13*)* 513-519. https://doi.org/10.1002/cssc.201902799

[75] S. Liu, Y. Zhu, Y. Liao, H. Wang, Q. Liu, L. Ma, C. Wang, Advances in understanding the humins: Formation , prevention and application. *Applications in Energy and Combustion Science* **2022** (10*)* 100062. https://doi.org/10.1016/j.jaecs.2022.100062

[76] L. Filiciotto, A.M. Balu, J.C. Van der Waal, R. Luque, Catalytic insights into the production of biomass-derived side products methyl levulinate, furfural and humins. *Catalysis Today* **2018** (302*)* 2-15. https://doi.org/10.1016/j.cattod.2017.03.008

[77] S. Chen, R. Wojcieszak, F. Dumeignil, E. Marceau, S. Royer, How Catalysts and Experimental Conditions Determine the Selective Hydroconversion of Furfural and 5-Hydroxymethylfurfural. *Chemical Reviews* **2018** (118*)* 11023-11117. https://doi.org/10.1021/acs.chemrev.8b00134

[78] M. Lin, C. Mochizuki, T. Ishida, Y. Zhang, M. Haruta, T. Murayama, Effect of poly(N-vinylpyrrolidone) ligand on catalytic activities of Au nanoparticles supported on Nb2O5 for CO oxidation and furfural oxidation. *Catalysis Today* **2023** (410*)* 143-149. https://doi.org/10.1016/j.cattod.2022.03.034

[79] D. Yan, J. Xin, Q. Zhao, K. Gao, X. Lu, G. Wang, S. Zhang, Fe–Zr–O catalyzed base-free aerobic oxidation of 5-HMF to 2,5-FDCA as a bio-based polyester monomer. *Catalysis Science & Technology* **2018** (8*)* 164-175. https://doi.org/10.1039/C7CY01704A

[80] W. Wei, G. Lyu, W. Jiang, Z. Chen, S. Wu, High-efficiency synthesis of 5-hydroxymethylfurfural and 2,5-diformylfuran from fructose over magnetic separable catalysts. *Journal of Colloid and Interface Science* **2021** (602*)* 146-158. https://doi.org/10.1016/j.jcis.2021.05.161

[81] T. Pasini, M. Piccinini, M. Blosi, R. Bonelli, S. Albonetti, N. Dimitratos, J.A. Lopez-Sanchez, M. Sankar, Q. He, C.J. Kiely, G.J. Hutchings, F. Cavani, Selective oxidation of 5-hydroxymethyl-2-furfural using supported gold–copper nanoparticles. *Green Chemistry* **2011** (13*)* 2091-2099. https://doi.org/10.1039/C1GC15355B

[82] A. Piccolo, P. Conte, A. Cozzolino, Effects of mineral and monocarboxylic acids on the molecular association of dissolved humic substances. *European Journal of Soil Science* **1999** (50*)* 687-694. https://doi.org/10.1046/j.1365-2389.1999.00276.x

[83] S.E. Davis, L.R. Houk, E.C. Tamargo, A.K. Datye, R.J. Davis, Oxidation of 5-hydroxymethylfurfural over supported Pt, Pd and Au catalysts. *Catalysis Today* **2011** (160*)* 55-60. https://doi.org/10.1016/j.cattod.2010.06.004

[84] S.G. Maerten, D. Voß, M.A. Liauw, J. Albert, Selective Catalytic Oxidation of Humins to Low-Chain Carboxylic Acids with Tailor-Made Polyoxometalate Catalysts. *ChemistrySelect* **2017** (2*)* 7296-7302. https://doi.org/10.1002/slct.201701553

[85] H. Cong, H. Yuan, Z. Tao, H. Bao, Z. Zhang, Y. Jiang, D. Huang, H. Liu, T. Wang, Recent Advances in Catalytic Conversion of Biomass to 2,5-Furandicarboxylic Acid. *Catalysts* **2021** (11*)* 9. https://doi.org/10.3390/catal11091113

[86] F. Neațu, R.S. Marin, M. Florea, N. Petrea, O.D. Pavel, V.I. Pârvulescu, Selective oxidation of 5-hydroxymethyl furfural over non-precious metal heterogeneous catalysts. *Applied Catalysis B: Environmental* **2016** (180*)* 751-757. https://doi.org/10.1016/j.apcatb.2015.07.043

[87] X. Liu, D.C.Y. Leong, Y. Sun, The production of valuable biopolymer precursors from fructose. *Green Chemistry* **2020** (22*)* 6531-6539. https://doi.org/10.1039/D0GC02315A

[88] M. Douthwaite, X. Huang, S. Iqbal, P.J. Miedziak, G.L. Brett, S.A. Kondrat, J.K. Edwards, M. Sankar, D.W. Knight, D. Bethell, The controlled catalytic oxidation of furfural to furoic acid using AuPd/Mg (OH) 2. *Catalysis Science & Technology* **2017** (7*)* 5284-5293. https://doi.org/10.1039/C7CY01025G

[89] S. Albonetti, A. Lolli, V. Morandi, A. Migliori, C. Lucarelli, F. Cavani, Conversion of 5-hydroxymethylfurfural to 2,5-furandicarboxylic acid over Au-based catalysts: Optimization of active phase and metal–support interaction. *Applied Catalysis B: Environmental* **2015** (163*)* 520-530. https://doi.org/10.1016/j.apcatb.2014.08.026

[90] G.R. Dick, A.D. Frankhouser, A. Banerjee, M.W. Kanan, A scalable carboxylation route to furan-2,5-dicarboxylic acid, *Green Chemistry* **2017** (19) 2966-2972. https://doi.org/10.1039/C7GC01059A

5. CONCLUSIONES

La presente Tesis Doctoral explora una vía sostenible para la producción de monómeros renovables a partir de biomasa, proceso propuesto en tres etapas de condiciones de operación muy diferentes: hidrólisis ácida, oxidación y carboxilación. Dada la extensión y diversidad de las reacciones estudiadas, las conclusiones se organizan en conclusiones parciales derivadas del estudio de cada etapa. Estos apartados abarcan desde la producción de 5-hidroximetilfurfural (HMF) y furfural (FFL) mediante la hidrólisis de celulosas pretratadas y serrín de pino, hasta la oxidación catalítica del FFL para la producción de ácido furoico (FCA), y el desarrollo de procesos de carboxilación en fase líquida para sintetizar ácido 2,5-furandicarboxílico (FDCA) a partir de fuentes renovables. En cada etapa se señalan las condiciones óptimas y las posibles aplicaciones industriales de estas reacciones.

Producción de 5-hidroximetilfurfural mediante hidrólisis de celulosas pretratadas

Se ha verificado la eficacia del sistema bicatalítico (HCl y beta zeolita) en la hidrólisis de celulosa microcristalina. Como resultado, se produce HMF debido a la sinergia entre los centros de Brønsted (que favorecen la hidrólisis) y los centros de Lewis (que facilitan la deshidratación de azúcares a través de la isomerización previa de glucosa a fructosa).

El análisis en términos de severidad (CSF) descarta un efecto preferente de la temperatura, el tiempo de reacción o la concentración de ácido, obteniéndose selectividades similares para factores de severidad combinada iguales. Basado en este análisis, se definen

140 ºC y 0,02% de HCl como los parámetros óptimos para maximizar la producción de HMF (19% de selectividad). Sin embargo, estos resultados están limitados por la baja reactividad de la celulosa (carácter recalcitrante). Debido a esto, la obtención de HMF requiere altas temperaturas y tiempos de reacción tan prolongados que el control de la reacción es deficiente y se obtiene una concentración relevante de ácidos (degradación de HMF).

Se propusieron tres pretratamientos químicos (HCl, H_2O_2 y HNO_3) para resolver este inconveniente. La suavidad de estos pretratamientos (a temperatura ambiente) no permite una alteración completa de la estructura cristalina, pero genera una superficie más reactiva (principalmente después del tratamiento con HNO_3) que produce un aumento significativo en la producción de HMF, logrando selectividades de HMF superiores al 50%.

Las pruebas de reutilización indican que la zeolita permanece activa una vez que la celulosa no reaccionada se elimina por calcinación, obteniéndose una correspondencia perfecta en conversión y distribución de productos (49% de conversión de celulosa, >44% de selectividad de HMF).

Producción de 5-hidroximetilfurfural y furfural mediante hidrólisis de serrín de pino

La lignina limita fuertemente la hidrólisis del serrín de pino, requiriendo condiciones tan fuertes que la producción de huminas restringe el proceso. Las deslignificaciones reductiva y oxidativa producen un efecto positivo, marcado por una productividad de TRS 140 veces mayor que con el serrín fresco y una disminución relevante en la producción de huminas. Los mejores resultados obtenidos son 3.2 g/L de ácido levulínico con una selectividad del 86% después de 7 h de reacción a 220 ºC y 1000 ppm de HCl aplicando el pretratamiento oxidativo, y 1.2 g/L de aldehídos (selectividad del 35.4 %) en menos de 1 h, con el pretratamiento reductivo.

Producción de ácido furoico mediante oxidación catalítica de furfural con H_2O_2

La oxidación parcial del FFL utilizando H_2O_2 es una reacción compleja en la que la conversión y las selectividades están definidas por una combinación de contribuciones homogéneas y heterogéneas, incluyendo acidez (para promover la oxidación), basicidad (para estabilizar los ácidos orgánicos evitando su descomposición total en CO_2), la actividad particular de cada metal utilizado (Pd, Pt o Au) y un efecto sinérgico entre el metal y el soporte, principalmente cuando el soporte tiene propiedades redox.

La máxima selectividad hacia ácido furoico se obtiene con Au/TiO_2 (42%). En términos de rendimiento del producto, Au/MgAl (8.5%) también es un buen candidato para su producción. La hipótesis de que la producción del ácido furoico está favorecida por el Au con un papel secundario del soporte fue corroborada, definiendo un tamaño de partícula óptimo de 5-7 nm. Este tamaño promueve la quimisorción necesaria de FFL y peróxido de hidrógeno en las partículas metálicas, reduciendo la relevancia de las reacciones paralelas (el mecanismo de B-V).

Producción de ácido furoico mediante oxidación catalítica de furfural con O_2

Se propone un nuevo enfoque para obtener ácido furoico mediante oxidación parcial en fase acuosa de FFL trabajando con una solución tampón a pH controlado = 8 y utilizando una baja carga catalítica. Se probaron diferentes catalizadores, involucrando soportes (TiO_2, MgAl y CeO_2) y metales activos (Au, Pd, Pt), con un exhaustivo cribado de las condiciones de reacción. Los resultados experimentales demuestran la alta actividad oxidante del Au, así como un efecto sinérgico con TiO_2 para activar el oxígeno, obteniéndose los resultados más prometedores al trabajar a 100 ºC y 20 bares: 100% de selectividad de ácido furoico en fase líquida, 16% de conversión de FFL, y 35,8% de selectividad total de ácido furoico, reduciendo la producción de huminas. Los resultados experimentales se ajustaron a un mecanismo común de reacción condicionado por la adsorción de FFL, concluyendo que la temperatura y las propiedades del soporte juegan un papel clave en la producción de ácido furoico.

Este estudio introduce un camino muy prometedor para obtener precursores poliméricos por una vía sostenible, obteniendo un buen equilibrio entre las ventajas de las configuraciones anteriores propuestas en la literatura (pH fuerte usando NaOH y pH no controlado) y reduciendo los inconvenientes de ambos procedimientos. Así, el ácido furoico se puede producir selectivamente en condiciones suaves (una mejora clara respecto al mecanismo de Cannizzaro obtenido al trabajar a pH 14), se reduce significativamente la relevancia de la producción de huminas y se obtienen resultados muy interesantes en términos de estabilidad catalítica (un inconveniente muy relevante de la configuración de base libre).

Producción de ácido 2,5-furandicarboxílico mediante oxidación de 5-hidroximetilfurfural y fructosa

Este estudio demuestra la influencia crítica de las condiciones de reacción en la síntesis catalítica de FDCA a partir de HMF. La temperatura influye significativamente en la cinética de la reacción, principalmente en el segundo paso de oxidación, que requiere un mínimo de 80ºC para obtener el FDCA en cantidades significativas. Esta selectividad aumenta con la temperatura, pero la formación de huminas prevalece sobre la ruta oxidativa, requiriendo de un equilibrio. Los estudios a diferentes presiones demuestran que un exceso de presión de O_2 sobre las condiciones estequiométricas garantiza la adsorción disociativa de oxígeno en la superficie de las nanopartículas de Au, activando la carboxilación y, consecuentemente, reduciendo la formación de huminas.

Las huminas se producen principalmente a través de una ruta catalítica homogénea, reduciendo la concentración inicial de HMF disponible para la oxidación. Trabajar con un bajo exceso de NaOH es crucial para reducir su relevancia y aumentar el carácter sostenible de esta ruta. A 80 ºC, utilizando una proporción de NaOH de 2:1 y una presión de oxígeno de 25 bares, la selectividad de FDCA alcanzó el 87% después de 8 horas, con una formación de huminas despreciable, como lo confirmó el análisis del balance de carbono.

Además, el estudio exploró un proceso de un solo paso que integra la hidrólisis de fructosa y la oxidación de HMF, mostrando viabilidad (14% de FDCA obtenido después de 9 horas de reacción), pero destacando los desafíos en la prevención de la degradación del HMF.

Oxidación de mezclas de furfural/5-hidroximetilfurfural a ácidos furánicos sobre Au/TiO_2 y carboxilación de ácido furoico

Con el ánimo de optimizar un proceso que suponga la oxidación simultánea de ambas moléculas plataforma, se realizó un estudio comparativo de las oxidaciones de los aldehídos individualmente, intentando fijar condiciones óptimas comunes. Sin embargo, estos resultados demuestran la inexistencia de estas condiciones óptimas, debida a la dispar reactividad de estos aldehídos. Así, la oxidación de HMF alcanza un balance de carbono del 99% y una selectividad máxima del 87% para FDCA al usar una concentración de NaOH en una proporción de 2:1. Por otro lado, la oxidación de FFL mostró solo un balance de carbono del 52% a bajas concentraciones de NaOH, que mejoró con el aumento de los niveles de NaOH, alcanzando una selectividad del 90% para el FCA a mayor basicidad.

Consecuentemente, el análisis de oxidación de mezclas requiere una nueva optimización para determinar las condiciones de equilibrio entre ambas situaciones. Los resultados indican que una proporción de 1:1 entre HMF y FFL reduce drásticamente el rendimiento de FCA del 97% al 14%, lo que destaca un notable efecto inhibitorio de HMF sobre la producción de FCA. Además, durante la oxidación de mezclas, se observa que la concentración de FFL limita la producción de FDCA.

Basado en estos estudios, se define una proporción de 4:1:2 (NaOH:HMF:FFL) como las condiciones óptimas para realizar la oxidación de mezclas de HMF y FFL obteniendo una selectividad del 12% de FDCA y del 34% de FCA. A pesar de que las selectividades son menores que las obtenidas con aldehídos aislados (optimización individual), los resultados son lo suficientemente prometedores como para considerar esta alternativa, lo que podría implicar una reducción relevante en los costos de purificación

Los resultados de los ensayos de carboxilación de FCA para producir FDCA demuestran que, en fase líquida, es posible lograr una selectividad del 1.4% para FDCA después de 6 horas a 170ºC. Aunque estos resultados aún no están optimizados, proporcionan un punto de partida prometedor para el desarrollo de una síntesis completamente en fase líquida de FDCA a partir de biomasa.

6. CONCLUSIONS

This PhD Thesis explores a sustainable pathway to produce renewable monomers from biomass, with a proposed process consisting of three stages with different operating conditions: acid hydrolysis, oxidation, and carboxylation. Given the scope and diversity of the reactions studied, the conclusions are organized into partial conclusions derived from the study of each stage. These sections cover diverse topics, from the production of 5-hydroxymethylfurfural (HMF) and furfural (FFL) through hydrolysis of pretreated celluloses and pine sawdust, to the catalytic oxidation of FFL for furoic acid production, and the development of liquid-phase carboxylation processes to synthesize 2,5-furandicarboxylic acid (FDCA) from renewable sources. Each segment provides insights into the optimal conditions.

Production of 5-hydroxymethylfurfural by pretreated celluloses hydrolysis

The effectiveness of the bicatalytic system (HCl and beta zeolite) in the hydrolysis of microcrystalline cotton cellulose has been verified. As a result, HMF is produced due to the synergy between Bronsted centers (favoring hydrolysis) and Lewis centers (facilitating sugar dehydration through prior isomerization of glucose into fructose).

Analysis in terms of severity (CSF) rules out a preferential effect of temperature, reaction time, or acid concentration, yielding similar selectivities for equal combined severity factors. Based on this analysis, 140 °C and 0.02% of HCl are defined as the optimal parameters to maximize HMF production (19% of selectivity). However, these results are limited by the low reactivity of the cellulose (recalcitrant character). Due to this, obtaining HMF requires high temperatures and reaction times so long that the control of the reaction is poor, and a relevant concentration of acids is obtained (HMF degradation).

Three chemical pretreatments (HCl, H_2O_2, and HNO_3) were proposed to solve this drawback. The mildness of these pretreatments (room temperature) does not allow for complete alteration of the crystalline structure but generates a more reactive surface (mainly after treatment with HNO_3) that produces a significant increase in HMF production, achieving HMF selectivities higher than 50%.

Reusability tests indicate that the zeolite remains active once the unreacted cellulose is removed by calcination, obtaining a perfect correspondence in conversion and product distribution (49% of cellulose conversion, >44% of HMF selectivity).

Production of 5-hydroxymethylfurfural and furfural by pine sawdust hydrolysis

Lignin strongly limits the hydrolysis of pine sawdust requiring so strong conditions that humins production restricts the process. Reductive and oxidative delignifications produce a positive effect, marked by a productivity of TRS 140 times higher than with the fresh sawdust and a relevant decrease in humins production. The best results obtained are 3.2 g/L of levulinic acid with a selectivity of 86% after 7 h of reaction at 220 ºC and 1000 ppm of HCl applying the oxidative pretreatment, and 1.2 g/L of aldehydes (selectivity of 35.4 %) in less than 1 h, with the reductive pretreatment.

Furoic acid production by catalytic oxidation of furfural with H_2O_2

The partial oxidation of FFL using H_2O_2 is a complex reaction in which the conversion and the selectivities are defined by a combination of homogeneous and heterogeneous contributions, including acidity (to promote the oxidation), basicity (to stabilize the organic acids preventing their total decomposition into CO_2), the particular activity of each metal used (Pd, Pt or Au) and a synergetic effect between the metal and the support, mainly when the support has redox properties.

As to furoic acid, the maximum selectivity is obtained with Au/TiO_2 (42%). In terms of product yields, Au/MgAl (8.5%) is also a good candidate for its production. The hypothesis that furoic acid is promoted by Au with a secondary role of the support was corroborated, defining and optimum particulate size of 5-7 nm. This size promotes the required chemisorption of FFL and hydrogen peroxide on the metal particles, reducing the relevance of the parallel reactions (the B-V mechanism).

Furoic acid production by catalytic oxidation of furfural with O_2

We propose a new approach for obtaining furoic acid by aqueous-phase partial oxidation of FFL working with a buffer solution at controlled pH = 8 and using a low catalytic loading. Different catalysts were tested, involving supports (TiO_2, MgAl, and CeO_2) and active metals (Au, Pd, Pt), with a thorough screening of reaction conditions. Experimental results demonstrate the high oxidation activity of Au, as well as a synergetic effect with TiO_2 to activate the oxygen, obtaining the most promising results when working at 100 ºC and 20 bar: 100% of furoic acid selectivity in the liquid phase, 16% of FFL conversion, and 35.8% of furoic acid total selectivity, reducing the humins production. All these results were fit to a common reaction mechanism conditioned by FFL adsorption, concluding that temperature and the support properties play a key role in furoic acid production.

This study introduces a very promising path to obtain polymer precursors by a sustainable route, obtaining a good equilibrium between the advantages of the previous configurations proposed in the literature (strong pH using NaOH and uncontrolled pH) and reducing the drawbacks of both procedures. Thus, furoic acid can be selectively produced at mild conditions (a clear improvement with respect to the Cannizaro mechanism obtained when working at pH 14), the relevance of humins production is significantly reduced, and very interesting results in terms of catalytic stability are obtained (a very relevant drawback of the free-base configuration).

Production of 2,5-furandicarboxylic acid by oxidation of 5-hydroxymethylfurfural and fructose

This study demonstrates the critical influence of reaction conditions on the catalytic synthesis of FDCA from HMF. Temperature significantly influences the reaction kinetics, mainly the second oxidation step, requiring a minimum of 80 ºC to obtain FDCA as the main product. This selectivity increases with the temperature, but the humins formation prevails over the oxidizing route. A high excess of O_2 pressure is required to guarantee the oxygen dissociative adsorption on the total amount of Au nanoparticles, a fact which reduces the humins formation enhancing the oxidation. Humins are mainly produced by a homogeneous catalytic route, reducing the HMF initial concentration. Working with a low NaOH excess is crucial to reduce their relevance and to increase the sustainability character of this route. At 80 ºC, using a NaOH:HMF ratio of 2:1 and 25 bar oxygen pressure, FDCA selectivity reached 87% after 8 hours, with negligible humins formation, as confirmed by carbon balance analysis. Furthermore, the study explored a one-pot process integrating fructose hydrolysis and HMF oxidation, showing feasibility (14% of FDCA obtained after 9 h of reaction) but highlighting challenges in preventing HMF degradation.

Oxidation of furfural/5-hydroxymethylfurfural mixtures to furanic acids over Au/TiO_2 and carboxylation of furoic acid

To optimize a process that involves the simultaneous oxidation of both platform molecules, a comparative study was conducted on the individual oxidations of the aldehydes, aiming to establish common optimal conditions. However, these results demonstrate the absence of such optimal conditions due to the differing reactivity of these aldehydes. Thus, the oxidation of HMF achieved a carbon balance of 99% and a maximum selectivity of 87% for FDCA when using a NaOH concentration in a 2:1 ratio. On the other hand, the oxidation of FFL showed only a 52% carbon balance at low NaOH concentrations, which improved with increasing NaOH levels, reaching a selectivity of 90% for FCA at higher basicity.

Consequently, the oxidation analysis of mixtures requires new optimization to determine the equilibrium conditions between both situations. The results indicate that a 1:1

ratio between HMF and FFL drastically reduces the FCA yield from 97% to 14%, highlighting a significant inhibitory effect of HMF on FCA production. Additionally, during the oxidation of mixtures, it is observed that the concentration of FFL limits FDCA production.

Based on these studies, a 4:1:2 ratio (NaOH:HMF:FFL) is defined as the optimal condition for oxidizing mixtures of HMF and FFL, achieving a selectivity of 12% for FDCA and 34% for FCA. Although the selectivities are lower than those obtained with isolated aldehydes (individual optimization), the results are promising enough to consider this alternative, which could lead to a significant reduction in purification costs.

The results of FCA carboxylation trials to produce FDCA demonstrate that, in the liquid phase, it is possible to achieve a selectivity of 1.4% for FDCA after 6 hours at 170ºC. Although these results are not yet optimized, they provide a promising starting point for the development of a fully liquid-phase synthesis of FDCA from biomass.

7. ANEXOS

LISTA DE ABREVIATURAS

List of abbreviations

AB	Acrilonitrilo butadieno
AHG	Anhydroglucose
ALD	Aldehydes
ASA	Acrilonitrilo estireno acrilato
BEI	Backscattered Electron Image
BET	Brunauer, Emmet y Teller
BFA	Ácido β-formilacrílico
BJH	Barret, Joyner y Halenda
B-V	Baeyer-Villiger
CB	Carbon balance
CCU	Procesos de captura y utilización de CO_2
CMNUCC	Convención Marco de las Naciones Unidas sobre el Cambio Climático
COP	Conferencia de las partes
CSF	Combined severity factor
$Cu(F)_2$	Difuroato de cobre
DAD	Detector de absorción a diferentes longitudes de onda
DFF	Diformilfurano
DME	Dimetil éter
DMSO	Dimethildulfoxide
DRIFT	Espectroscopía infrarroja de reflexión difusa por transformada de Fourier
DRX	Difracción de Rayos X
DP	Grado de polimerización
EDS	Energy Dispersive Spectrometer
FA	Ácido fórmico
FCA	Ácido Furoico

F-Cs	Furoato de cesio
FDCA	Ácido 2,5-furandicarboxílico
FFL	Furfural
FN	2-(5H)-furanona
FOH	Furfuryl alcohol
FTIR	Espectroscopía Infrarroja por Transformada de Fourier
FTIR	Fourier transform infrared
FUM	Ácido fumarico
GC	Cromatografía de gases
GC-MS	Cromatografía de gases acoplada a espectrometría de masas
GEI	Gases de efecto Invernadero
HDPE	Polietileno de alta densidad
HF	2-hidroxifurano
HFN	5-hidroxi-2(5H)-furanona
HMF	5-Hidroximetilfurfural
HMFCA	Ácido 5-hidroximetil-2-furancarboxílico
HPLC	Cromatografía líquida de alta eficiencia
ICP-MS	Espectrometría de masas con plasma acoplado inductivamente
LA	Ácido levulínico
LDPE	Polietileno de baja densidad
MA	Ácido maleico
MAL	Ácido málico
MCC	Celulosa microcristalina
MCT	Mercury-Cadmium-Telluride detector
MS	Espectrometría de masas
ODEs	Ecuaciones diferenciales ordinarias
ODS	Objetivos de Desarrollo Sostenible
ONU	Organización de las Naciones Unidas

PE	Polietileno
PEF	Furanoato de polietileno
PET	Tereftalato de polietileno
PP	Polipropileno
PS	Poliestireno
PTA	Ácido tereftálico
PUR	Poliuretano
PVC	Cloruro de polivinilo
RID	Detector de índice de refracción
SEI	Secundary Electron Image
SEM	Microscopía electrónica de barrido
TCD	Detector de conductividad térmica
TEM	Microscopía electrónica de transmisión
TGA	Thermal gravimetric analyzer
TPD	Desorción a temperatura programada
TPO	Oxidación a temperatura programada
TPR	Reducción a temperatura programada
TRS	Total reduced sugars
XPS	Espectroscopía electrónica de rayos X

LISTA DE SÍMBOLOS

List of symbols

β	Anchura a media altura del pico (radianes)
γ	Dispersión metálica (%)
η	Rendimiento
θ	Ángulo de difracción o ángulo de Bragg
λ	Longitud de onda de la radiación incidente (nm)
hv	Energía de fotones
ρ	Densidad del metal
%C	Mass percentage of carbon in the sawdust
A_{sm}	Área activa por gramo de metal puro
C_{ac}	Amount of formic and levulinic acid (g/L)
C_{adl}	Sum of HMF and FFL (g/L)
C_D	Dimer concentration detected in liquid phase (g/L)
$C_{FFL,0}$	Concentración de furfural a t=0
$C_{FFL,t}$	Concentración de furfural a tiempo t
$C_{H_2O_2,0}$	Concentración de H_2O_2 a t=0
$C_{H_2O_2,t}$	Concentración de H_2O_2 a tiempo t
C_i	Molar concentration of each compound detected in liquid phase
C_M	Monomer concentration detected in liquid phase (g/L)
C_P	Sum of hemicellulose and cellulose in the sawdust (g/L)
d	Tamaño de cristalita (visto en quimisorción)
d	Distancia entre planos de átomos del cristal (visto en DRX)
Dp	Diametro de poro (m)
Ea	Energía de activación
EK	Energía cinética

EL	Energía de enlace de electrones del electrón expulsado
F_s	Factor estequiométrico en quimisorción
k_i	Constante cinética
K	Constante de Scherrer
K_i	Constante de adsorción del compuesto i
L	Tamaño medio de los cristales
M	Porcentaje de metal activo expresado en gramos de metal activo por cada gramo de muestra
m/z	Relación masa/carga
$m_{cellulose}$	Mass of cellulose introduced in the reactor
$M_{cellulose}$	Molar mass of cellulose (162 g/mol)
$m_{sawdust}$	Mass of delignified sawdust introduced in the reactor at the initial point
MW_C	Molar mass of carbon
n	Número entero
n_i	Number of carbons in the molecule of compound *i*
P	Presión real de N_2 en los ensayos de fisisorción (Pa)
P_o	Presión de saturación de N2 en los ensayos de fisisorción (Pa)
S_i	Selectivity of compound i in liquid phase
t	Reaction time of hydrolysis in minutes
T	Reaction temperature
V	Total reaction volume
V_m	Volumen de gas quimisorbido (cm_3/g)
V_{mol}	Volumen molar de gas quimisorbido (cm_3/g)
V_{meso}	Volumen de mesoporos
V_{micro}	Volumen de microporos
W_a	Peso atómico del metal activo
X	Conversion
X_c	Liquid-phase carbon conversion